Development of topographically controlled electrospun scaffolds to stimulate wound healing for skin tissue engineering

David Hiram Ramos Rodriguez

A thesis submitted to the University of Sheffield in fulfilment of the requirements for the degree of

Doctor of Philosophy

The School of Clinical Dentistry

Faculty of Medicine, Dentistry, and Health

October 2021

Acknowledgments

I would like to recognize all the people that were with me over these 4 years. To you, I say thank you. Thank you for your time, your patience, your support, and your help. To my friends Ale, Sara, Ana Isabel, Xavi, Ana Jimenez and Sergio. To my colleagues at the Kroto research institute and school of clinical dentistry Tom, Anthony, Sabi, and Serkan. To my supervisors, Dr. Ilida, Prof. Sheila, and Dr. Fred. To all of you, thanks.

I would also like to say *gracias* to my family that has been there for me always. My mom, my dad, and my brother, this is as much my achievement as it is yours. Even far away from home, I have always felt supported and loved by you.

Finally, but of course not less important, to Ana, my partner, my friend, my confidant, my companion, my accomplice, and the reason I wrote these acknowledgments. Let this be a record that you and I met and fell in love during this time, that being together was and would always be an adventure.

"It's a dangerous business, going out your door. You step onto the road, and if you don't keep your feet, there's no knowing where you might be swept off to."

J.R.R Tolkien

Table of contents

Abbreviations

2dDr	2-deoxy-D-ribose
2dDr-P	2-deoxy-D-ribose 1-phosphate
3D	3 dimensional
ADP	Adenosine diphosphate
AdSC	Adipose derived stem cells
AM	Additive manufacturing
AP	Air Plasma
AV	Aloe vera
bFGF	Basic fibroblast growth factor
BAT	Brown adipose tissue
CAD	Computer aided design
CAM	Chicken chorioallantoic membrane
DAPI	4',6-diamidino-2-phenylindole
DCM	Dichloromethane
DD	Development day
DEJ	Dermal-epidermal junction
DED	De-epidermized dermis
dH$_2$O	Distilled water

DMEM	Dulbecco's modified eagle's medium
DMF	Dimethylformamide
DMSO	Dimethyl sulfoxide
DSC	Differential scanning calorimetry
E2	17β-estradiol
ECM	Extracellular matrix
EGF	Epidermal growth factor
EMA	European medicines agency
ER	Estrogen receptor
FDA	Food and drug administration
GAG	Glycosaminoglycan
HA	Hyaluronic acid
HDF	Human dermal fibroblasts
HDK	Human epidermal keratinocytes
HFSC	Hair Follicle stem cells
HMDS	Hexamethyldisilazane
IGFs	Insulin like growth factors
IL-6	Interleukin-6
KGF	Keratinocyte growth factor
KSCs	Keratinocyte stem cells

LDH1	Lactate dehydrogenase 1
MCS	Melanocyte stem cell
NAD^+/NADH	Nicotinamide adenine dinucleotide
NF-κB	Nuclear factor kappa β
NOX2	NADPH oxidase 2
NRP	Neuropilin
PBS	Phosphate buffer saline
PCL	Polycaprolactone
PDGF	Platelet derived growth factor
PEO	Polyethylene oxide
PHBV	Poly(3-hydrroxybutyrate-co-3-hydroxyvalerate
PGA	Poly(glycolic acid)
PGE_2	prostaglandin E_2
PLA	Poly(lactic acid)
PLGA	Poly(lactic-*co*-glycolic) acid
PLGF	Placental growth factor
PPM	Parts per million
RES	Random electrospun scaffold
ROS	Reactive oxygen species
RT	Room temperature

SEM	Scanning electron microscopy
SHH	Sonic hedgehog
SLA	Stereolithography
TBSA	Total body surface area
TCES	Topographically controlled electrospun scaffold
TCP	Tissue culture plate
TGFβ	Transforming growth factor-β
TNF	Tumor necrosis factor
TP	Thymidine phosphorylase
TRITC	Tetramethylrhodamine isothiocyanate
UTS	Ultimate tensile strength
UV	Ultraviolet
UVR	Ultraviolet radiation
VEGF	Vascular endothelial growth factor
WAT	White adipose tissue
Wt%	Weight percent

List of figures

xviii

List of tables

List of equations

Publications and presentations

- **Publications**

Ramos-Rodriguez, D.H., MacNeil, S., Claeyssens, F. and Ortega Asencio, I., 2021. Fabrication of Topographically Controlled Electrospun Scaffolds to Mimic the Stem Cell Microenvironment in the Dermal-Epidermal Junction. *ACS Biomaterials Science & Engineering*, 7(6).

Ramos-Rodriguez, D.H., MacNeil, S., Claeyssens, F. and Asencio, I.O., 2021. The Use of Microfabrication Techniques for the Design and Manufacture of Artificial Stem Cell Microenvironments for Tissue Regeneration. *Bioengineering*, *8*(5), p.50.

Ramos-Rodriguez, D.H., MacNeil, S., Claeyssens, F. and Ortega Asencio, I., 2021. Delivery of bioactive compounds to improve skin cell responses on microfabricated electrospun microenvironments. *Bioengineering*, *8*(8), p.105.

- **Oral presentations**

Tissue Engineering and Regenerative Medicine International Society (TERMIS) 2021. "Topographically controlled nanofibrous membranes to mimic the epidermal stem cell microenvironment of the Rete ridges".

World Biomaterials Congress 2020. "Fabrication of topographically controlled electrospun scaffolds to mimic stem cell microenvironment in the dermal-epidermal junction".

Biomaterials and Tissue Engineering Group 2020. "The inclusion of microtopographical cues in electrospun scaffolds to mimic the rete ridges stem cell microenvironment".

UKSB 2020. "Introducing microfabricated electrospun membranes to mimic the stem cell microenvironment in the dermal-epidermal junction".

TCES 2019. "Development of hierarchical topographically controlled electrospun scaffolds to deliver proangiogenic agents for wound healing.

Chapter I. Introduction

During the last two decades, the understanding of the role of stem cells in tissue regeneration and homeostasis has been a promising but challenging task. Stem cells were once considered a potential supply for numerous regenerative medicine applications; however, stem cells are now subject to scientific debate due to how they are sourced, and the risks related to their differentiation methods. Although strategies have been developed to overcome some of the challenges posed by the use of embryonic and fetal stem cells, adult stem cells have emerged as an attractive alternative due to their limited capacity to differentiate and their relatively simple isolation methods.

Adult stem cells are multipotent stem cells that only differentiate to cell lines related to the tissue in which they reside. To preserve the stemness of the cells throughout the life cycle of the tissue, adult stem cells are located in highly specialized microenvironments known as stem cell niches. These niches use physical and chemical cues to maintain a healthy environment in which stem cell activity can be regulated according to the regenerative profile of each specific tissue. For example, tissues with high regenerative profiles such as the epidermis, cornea, or intestine require a continuous replenishment of cells to supply their self-renewal cycle or in case of injury.

In human skin, there are two defined stem cell microenvironments in the form of the hair bulge and at the bottom of the ridged topography between the epidermal and dermal layers known as rete ridges. The rete ridges are microstructures with an average size of 50 µm in depth to 400 µm in width. These microenvironments have been studied for their role in keratinocyte stratification and regeneration of the epidermal layer. The effects of losing this structure due to aging or skin injury can limit or impair the healing process [1], [2].

In recent years, several attempts have been made to study these structures *in vitro* using microfabrication techniques. The first attempts of studying stem cells on rete ridge-like structures were performed by creating undulating surfaces on solid surfaces. However, this approach neglects the effect of the 3D fibrous extracellular environment present on native tissue. New developments in tissue engineering and microfabrication have led to the introduction of complex microtopographies on hydrogels and fibrous scaffolds, with both approaches aiming to mimic the nano and macro components of the rete ridges.

Another key issue to consider when working on skin tissue engineering applications is vascularization; in fact, construct vascularization is often a challenge that hinders tissue viability due to the resulting lack of nutrients on the newly formed tissue. Moreover, the lack of vasculature is often followed by rejection or infection of tissue engineered constructs. Additionally, other pathological conditions such as chronic inflammation can alter the vascularization process during wound healing. Fabrication of a multifunctional device that can introduce structural cues while improving vascularization is a challenging but attractive strategy for skin tissue regeneration. The work presented here has the potential to generate a versatile fibrous construct able to aid skin regeneration via the introduction of native-like topographical cues as well as offering a platform technology that can release key bioactive agents (e.g., angiogenic compounds) in a controlled manner.

Chapter II. Literature Review

1.   Superficial and chronic wounds as a health problem

The human skin provides the first protective barrier against environmental factors and is subject to constant wear and damage related to basic daily activities or unintentional exposure to abrasion, heat, chemical contamination, and high energy electromagnetic radiation (UVB). The destruction of at least 15% of the total surface area of the skin can become life-threatening [3]. In nature, incisional wounds are the most common skin injuries, and their severity is evaluated by the amount of tissue that was lost during the incision. These incisional wounds range from small or imperceptive injuries in the upper layer of the skin to disruptive wounds in which a large volume of dermal tissue is damaged and blood supply to the injury is compromised.

There are several categories in which skin wounds can be classified for their study and treatment. These categories evaluate; the cause of the injury (cuts, lacerations, burns, avulsions), the skin layers disrupted by the injury (superficial, partial-thickness, or full-thickness), or the nature of their healing process (chronic and acute). Although all these categories provide useful information about the wound, categorizing the injuries by superficial, partial-thickness or full-thickness allows clinicians to describe the damage in terms of tissue structure and thus early identify possible treatments [4]. Superficial injuries are those that have caused the loss of the epidermal outer layer. Partial-thickness injuries have lost the epidermal layer and a section of the dermal component. Additionally, full-thickness wounds involve the loss of the epidermal, dermal, and hypodermal layers, with possible damage to the bone in the most severe cases [5].

The capacity of a skin wound to regenerate is important to determine medium- and long-term treatments. Acute wounds are defined by their capacity to heal completely with minimal scarring, while chronic wounds heal slowly causing prolonged inflammation, and constant infection [6]. Is estimated that 20 million patients have suffered from chronic wounds, having an economic impact of billions of dollars. In the United States only, 6.5 million patients suffered from chronic wounds [7]. Furthermore, a high incidence of chronic wounds is usually associated with high-profile public health problems such as diabetes and obesity [7], [8].

In humans, burns are the most extensive forms of acute soft tissue injuries that can occasionally result in chronic wounds. In some extreme cases, burns can lead to death primarily due to fluid loss, and infection of the burned dead tissue [5], [9]. Burns can also be responsible for severe emotional distress due to the physical and mental harm caused by procedural pain, excessive scarring, and skin contractures [10]. Because burns and scalds have the potential to cause extensive and rapid deep wounds, treating burn wounds is a complex process that requires specialized treatment. The treatment of wounds caused by burns depends on several factors, such as the degree of burn, and cause of the burn (thermal or chemical) [11].

The degree of a burn is determined by the depth of the damaged area. First-degree burns are those that have caused superficial thermal irritation, second-degree burns have damaged the epidermis and the upper section of the dermis, and finally, third-degree burns have carbonized the epidermis and destroyed the dermal component. Burns that have caused damage beyond the dermal layer, for example to bone or muscles, are usually referred to as fourth-degree burns [12], [13].

The world health organization states that 180,000 deaths are caused every year by burns, the majority occurring in developing countries. Approximately 67 million fire or heat-related injuries

were registered in 2015 with 6 million people requiring medical attention for burn-related wounds every year [14]–[17]. However, defects resulting from acute burns in adults have not a significant impact in most developed countries due to advances in burn care and social development [18]. In contrast, burns are the second most common cause of accidental death in developed countries for children under five years.

Infants mostly suffer from superficial burns and scalds commonly caused by hot liquids or hot coals in house kitchens [19], [20]. In the United Kingdom, it is estimated that there are 25,000 pediatric cases of injuries caused by burns and scalds per year [21]. The treatment of burns in children requires special considerations as scar tissue and skin grafts can overreact and create a hypertrophic scar and risk impaired mobility [20]. However, the contraction and scarring can be overcome by accelerating the healing process of the wound [22].

Wound excision and skin grafting are common clinical practices that have significantly improved the outcomes for severe burn patients by reducing the mortality rate and days of hospital stay. However, the treatment of wounds caused burns to have two main challenges: The shortage of autologous skin transplantation when the defect exceeds 50-60% of the total body surface area (TBSA); and the drawbacks of conventional (and gold standard) skin grafting techniques. Because the skin grafting technique requires the removal of necrotic tissue from the wound side, a split-thickness or full-thickness transplant of autologous healthy tissue is taken from the patient or donor, causing donor site morbidity. Normally, the autologous skin graft consists of both epidermis and dermis for the full thickness graft, and the full epidermis and upper section of the dermal layer in the case of the split-thickness graft [23]–[25]. Furthermore, there are critical additional challenges specific for burn injuries such as infection, pain, and hypertrophic scarring [25].

There are specific problems that burned patients face during recovery such as controlling the inflammatory response that can compromise the regenerative process [11]. Burns are primarily healed by the endogenous process of regeneration as other skin injuries. Therefore, the understanding of skin anatomy and the wound healing process is crucial in the context of creating new dressings and strategies that overcome the challenges for optimal skin regeneration.

2. Skin anatomy and composition

The skin is the organ with the highest surface area in the human body. It serves as a protective barrier that creates an interface between the surrounding environment and the human body as well as being a sensory organ (temperature, pressure, and pain) and controlling the synthesis of vitamin D after exposure to sunlight [16]. Human skin can be divided into glabrous (hairless skin) and hair-bearing skin. Glabrous skin lacks sebaceous glands and hair follicles and has a characteristic grooved surface created with alternating ridges and sulci with unique markings or patterns known as dermatoglyphics. In contrast, hair-bearing skin shows sebaceous glands and hair follicles [26].

The skin protects the organs from biological entities such as microorganisms and pathogens, from ultraviolet light, and mechanical, chemical, or thermal disturbances [27]. Structural proteins such as keratin, collagen, and elastin give the skin a tough, yet flexible structure that provides resistance and adaptation during body movement [28]. Because of its constant exposure to environmental factors, the skin has developed a healing mechanism that allows for constant regeneration or repair in the case of trauma [9]. Most of the elements that control the regenerative cycle and healing process of the skin can be found on the dermal and epidermal layers. Other components such as hair follicles, sweat glands, and nails help to maintain and protect the skin as well as playing part in the regenerative process [29].

The human skin is capable of retaining and regulating the amount of water that is absorbed and released. This characteristic is highly related to the ability of the skin to thermoregulate itself through cutaneous nerves sensing the surface temperature of the human body. Skin thermoregulation is also responsible for cutaneous vasodilation and cutaneous vasoconstriction, which are autonomic temperature changes against aggressive heat and cold environments respectively [30]. The skin has an average pH of 5 created by a protective film that contains antimicrobials called the acid mantle. This acidic environment in conjunction with its relatively dry surface controls the growth of bacteria and fungi colonies in the skin and creates a homeostatic barrier [9], [31].

The human skin is composed of two main layers called the epidermis and dermis (Figure 1). In adult skin, these layers are composed of topographical cues, appendages, and approximately 20 different cell types that give the skin its mechanical, physiochemical, and biological properties and functions [32]. The average thickness of each layer varies depending on the body region and it is often related to the physical forces and environmental wear to which the area is commonly exposed. For example, thicker skin can be found in areas such as the palms of the hands and soles of the feet that are often exposed to mechanical wear. This difference in thickness translates to changes in the skin anatomy, with thicker skin for example showing an extra layer, *stratum lucidum*, in comparison with thin skin that lacks such a layer [33].
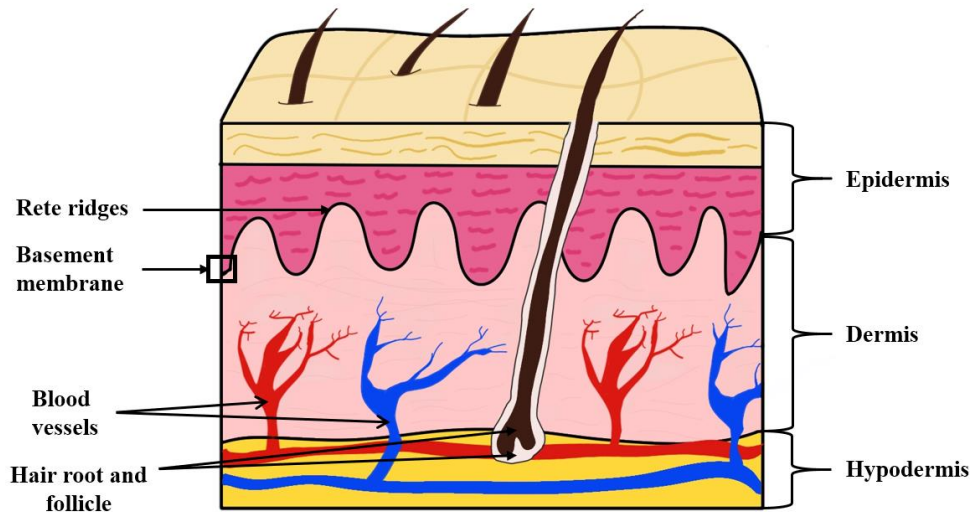
Figure 1. Anatomy of human skin. The three main epidermal, dermal, and hypodermal layers, their interconnections and components are highlighted.

2.1. The epidermis

The epidermis is the outer, avascular layer of the skin, which is mainly composed of several cell types that form a stratified squamous epithelium. This 120 µm thick layer is segmented into five distinct layers (*stratums*) called *basale, spinosum*, *granolosum*, *lucidum,* and *corneum* that provide different microenvironments that control cell behavior and dictate the highly efficient renewal system of the epidermis [9], [34]. Additionally, each layer presents sub-layers of cells (except for the *stratum basale*) that have specific biochemical cues and have a distinctive role in the regenerative cycle of the epidermis [33].

To ensure a homeostatic balance, the epidermis has an active population of keratinocytes that are continuously replaced from basal cells located at the bottom of the epidermal layer. These basal keratinocytes are often the only ones that divide, and it is their progeny that migrates through the epidermal layers that exposes them to different biochemical cues and regulates their differentiation

[35], [36]. This regenerative cycle is described in more detail when discussing the cellular and proteic components of the skin (section 2.5).

The interface between the epidermis and dermis is a complex biochemical and mechanical junction called the basement membrane zone. This specialized structure is crucial to anchor the epidermis with the dermis and to create a permeability barrier, and control the migration of cells and molecules [37]. Composed of the plasma membrane, *lamina lucida*, *lamina densa*, and *lamina reticularis*; the basal layer of the epidermis attaches to the dermis using anchoring structures called hemidesmosomes present in the basement membrane (BM). The BM contains stem cells that move up to the outer layer to differentiate and support epidermal maintenance and tissue regeneration [38], [39].

The dermal-epidermal junction (DEJ) consists of a network of interacting proteins that reside on specialized dermal papillae protrusions called rete ridges. These topographical structures are only present in humans and swine, and create microenvironments that range from 50 µm to 200 µm in depth and 50 µm to 400 µm in width, and have several biochemical and mechanical functions related to homeostasis and structural cohesion between the epidermis and dermis [35], [38], [40].

2.2. Rete ridges

The rete ridges are topographical cues that fully developed during the mid-stages of human gestation. The rete ridges have mechanical and biological functions in human skin, their structure (Figure 1) increases the contact area between the epidermis and the dermis, improving shear resistance and creating a more efficient system for nutrient diffusion from the surrounding microvasculature [40]. The dimensions of the rete ridges play a key role in their functions; for example, as they decrease in depth as skin ages, the microfeatures that affect cell behavior and cell

9

proliferation are lost. Morphology of the rete ridges can be disrupted by hyperproliferative disorders, such as psoriasis, which have an inverse effect in the morphology of the rete ridges in comparison with aging, as they become thin and elongated [1], [2]. Additionally, it has been found that darker skin is more densely packed with larger rete ridges than lighter skin. The average density of rete ridges on human forehead skin is approximately 82/mm^2 [41], [42].

However, the dimensions of the rete ridges are not homogenous among the skin [43]. Areas exposed to less friction such as the foreskin, and scalp present wider and shallower microfeatures in comparison with areas such as, the palms of the hands that present narrow and deep rete ridges. These dimensional differences of the ridges influence the expression of integrins and cytokeratins, and epidermal stem cell proliferation [43] [44], [45]. The 3D microstructures of the rete ridges create cellular microenvironments that have been studied for their effects in cell proliferation and differentiation, focusing on the high production of integrin β1 (Iβ1) and their relation with keratinocyte adult stem cells located at the base of the rete ridges [1], [40], [44].

2.3. The dermis

The dermal layer is composed of irregular dense connective tissue made of fibrous proteins (collagen and elastin), blood vessels, lymph vessels, and specialized cells. Collagen is the most abundant extracellular matrix (ECM) protein of the dermal component with 90% of the dry weight of the dermis [46]. This skin layer is about 1 mm to 4 mm in thickness and it is structured in papillary and reticular layers. The main differences between these layers are the arrangement and dimension of the collagen fibers and collagen bundles, and the presence of specific structural proteins such as elastin and proteoglycans [47]. The papillary dermis is located on the upper section close to the epidermal layer; it comprises about 10% of the dermis. The collagen fibrils present in

the papillary layer are packed together to create thicker collagen fibers about 0.3 µm to 3 µm in diameter, and collagen bundles of less than 10 µm. The lower section of the dermis contains the reticular layer, which is composed primarily of entangled collagen type I fibers of 10 µm – 40 µm in diameter, these fibers form bundles about 50 µm in diameter [48].

2.4.   Hypodermis and adipose tissue

The hypodermis is a highly vascular underlayer composed of areolar and adipose tissue, the main function of which is insulation and energy source. Skin appendages such as hair follicles, sweat glands, and sebaceous glands are located throughout or interact with multiple skin layers. These appendages have different functions related to hormone production, wound healing, and stem cell development [23], [49]. Hair follicles stand as multifunctional appendages that generate new hair, aid in thermal regulation, and work as physiological connections with sensory neurons. Regeneration of hair follicles is regulated by melanocyte stem cells and hair follicle stem cells (HFSCs), located in microniches known as the bulge and the hair herm [50].

The main function of adipose tissue is to store energy as lipids and can be found around other organs and assume different functions accordingly. In mammals, adipose tissue is divided into white adipose tissue (WAT), and brown adipose tissue (BAT) [51]. Subcutaneous WAT is located in several regions of the human body such as the deep and superficial abdomen, and gluteofemoral areas. Dermal WAT plays a key role in processes such as the hair follicles regeneration cycle [51], and angiogenesis [29], [52].

2.5. Cellular and proteic components of the skin

Across all skin composition, fibroblasts, melanocytes, and keratinocytes are the most common cell types. Keratinocytes and melanocytes are the main cell types of the epidermal layer. Melanocytes constitute the lower layer of the epidermis and provide pigmentation to the skin through the secretion of melanin, a pigment that also provides protection by absorbing ultraviolet radiation (UVR), thus protecting the DNA [53]. Keratinocytes constitute about 95% of the epidermis composition. These cells produce a dense cytoskeletal structure of 10 nm composed of keratin that protects the skin from physical damage [50]. Dendritic cells (Langerhans cells) and sensory receptors (Merkel cells) are also present in the epidermis as part of the immune and nervous systems respectively [39].

Keratins are the major structural proteins present on the epidermis. They constitute a subfamily of heteropolymeric proteins that work as an adaptable scaffold of intermediate filaments. The family of intermediate filament (IF) proteins is divided into six different types of 10 nm structural proteins. Type I and type II IF proteins are constituted by 28 and 26 different keratins, respectively. Keratins play a key role in protecting epithelial cells from mechanical and non-mechanical stresses, regulating cell growth, migration, and differentiation [50], [54], [55]. The expression of keratin in the skin is not homogenous. The stratified composition of the epidermis has characteristic keratins and other protein markers that modulate cell behavior in a process called cornification (defined by the formation of corneocytes) [56]. Figure 2 shows the characteristic keratin expression patterns of the epidermis. Disturbances such as wound healing, hyperproliferative diseases, or infection can alter or induce the expression of specific keratins such as K6, K16, and K17 [57].
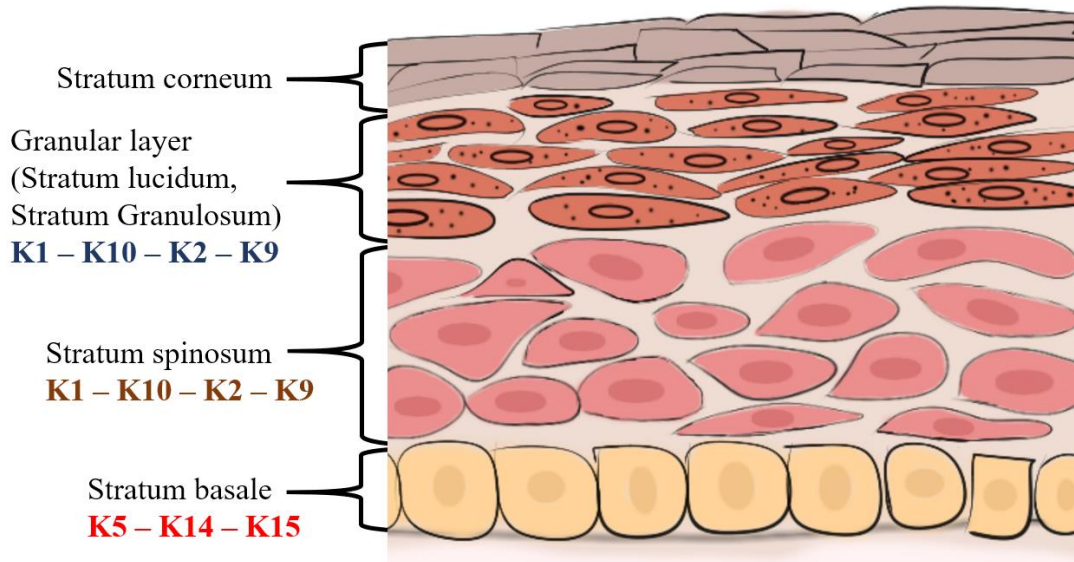
Figure 2. Characteristic keratin expression pattern in the human epidermis.

In the epidermal layer, stem cells can be found in the *stratum basale* and the dermal BM, playing a key role in the maintenance and repair of the upper *stratums*. Epidermal stem cells (ESC) and keratinocyte stem cells are capable of expressing high levels of integrins and adhere to collagen type IV, and fibronectin [45]. In normal conditions, these stem cells consist of up to 10% of the basal layer.

The lower dermal layer fibroblasts are responsible for the production of rich collagen and elastin ECM, which contributes to the strength and flexibility of the skin [24], [34]. The ECM plays a key role in cellular development, signaling, and organization, this complex structure controls cellular behavior through biochemical cues that mediate cell adhesion, cell migration, and cell differentiation [34]. ECM composition includes proteins, proteoglycans such as heparin and chondroitin sulfate, and glycoproteins[58]. The ECM produced in the skin is especially rich in glycosaminoglycans (GAGs), such as hyaluronic acid (HA), that play an important role in controlling hydration and moisture [34].

Collagens are a family of proteins that compose about 30% of the total protein mass in mammals. Collagens consist of polypeptide α chains that form a triple helix structure and enable collagen to resist high strain deformation. In the human dermis, dermal fibroblasts synthesize, maintain, and organize collagen [46]. Although there are 28 types of collagen reported in vertebrates, Collagen type I (COL1) is the most abundant in humans, with type III (COL3) and IV (COL4) being critical for the mechanical properties of the skin [59].

COL1 is composed of two α1 and one α2 chains that create the characteristic triple helix structure due to interactions between its characteristic amino acids: proline, hydroxyproline, and glycine. Generally, COL1 molecules pack together to form fibrils with an average diameter of 50 nm -200 nm and a length of 300 nm [59], [60]. Specific sequences of the collagen fibrils promote cellular proliferation and differentiation due to their chemotactic nature [61]. COL4 is a unique type of collagen composed of six distinctive α chains only expressed in the BM. Although COL4α1 and COL4α2 are present in the BM of several tissues, other chains are exclusive to certain tissues, such as COL4α5 and COL4α6 for the BM of the skin [62]. The chemical characteristics of COL4 produced a non-fibrillar sheets that works as a scaffold for protein deposition [63].

Adipose-derived adult stem cells (AdSCs) are mesenchymal stem cells present in the subcutaneous WAT. AdSCs are considered important for the skin regeneration process due to their role in secreting growth factors such as basic fibroblast growth factors and vascular endothelial growth factors [64]. Other sources of stem cells in the human skin include hair follicles (melanocyte stem cells and HFSCs), and sebaceous gland stem cells [39], [40]. Understanding the relation of all these structural, cellular, and biochemical components of the skin is critical when studying stem cell behavior and the effects of altering the stem cell microenvironment.

14

3. The stem cell microenvironment

Stem cells are vital for the regenerative cycle of human skin. In general, stem cells are characterized by their high capacity for self-renewal and differentiation throughout their life cycle. Early attempts to characterize what defines stem cells used the term "stromal cells" to describe cells that reside in the bone marrow stroma. Since then, stromal cells have been misused to describe stem cells in general. Nonetheless stromal cells only referred to mesenchymal stem cells [65].

Stem cells are classified according to their original source into embryonic, fetal, or adult stem cells. In contrast with embryonic and fetal stem cells, adult stem cells are present throughout the adult life of the host, but with a limited potential to differentiate, as they produce cells that are needed to maintain a healthy cell pool in their specific tissues [66], [67]. Adult stem cells reside in complex microenvironments often referred to as stem cell niches. These microenvironments protect the stem cells as well as provide biochemical, spatial, and mechanical cues that control stem cell fate [68]. The prototypical components of a stem cell niche are shown in Figure 3 and can be grouped as microenvironmental (spatial distribution, size, physiological and biological cues) or biochemical (soluble factors, ECM proteins).
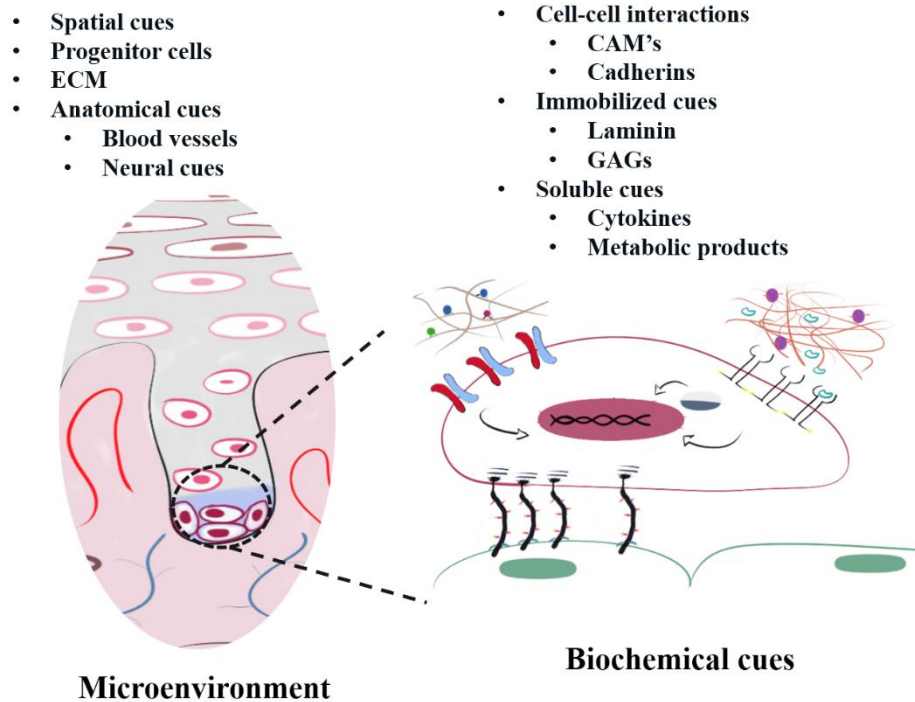
Figure 3. Microenvironmental and biochemical cues of a prototypical stem cell niche. Adapted from Lutolf & Blau [69].

Stem cell fate in adult tissues is governed by complex chemical and physical interactions within their enclosed microenvironment and by external stimuli. Figure 4 shows the possible outcomes for stem cell fate. The stem cell niche creates a microenvironment that encourages close-range interactions and signals such as changes in pH, ECM components, integral proteins, and soluble factors [70]. The cellular organization that surrounds the niche is also critical to its function as autocrine and paracrine signals and cell-cell contact influence stem cell activity [71].
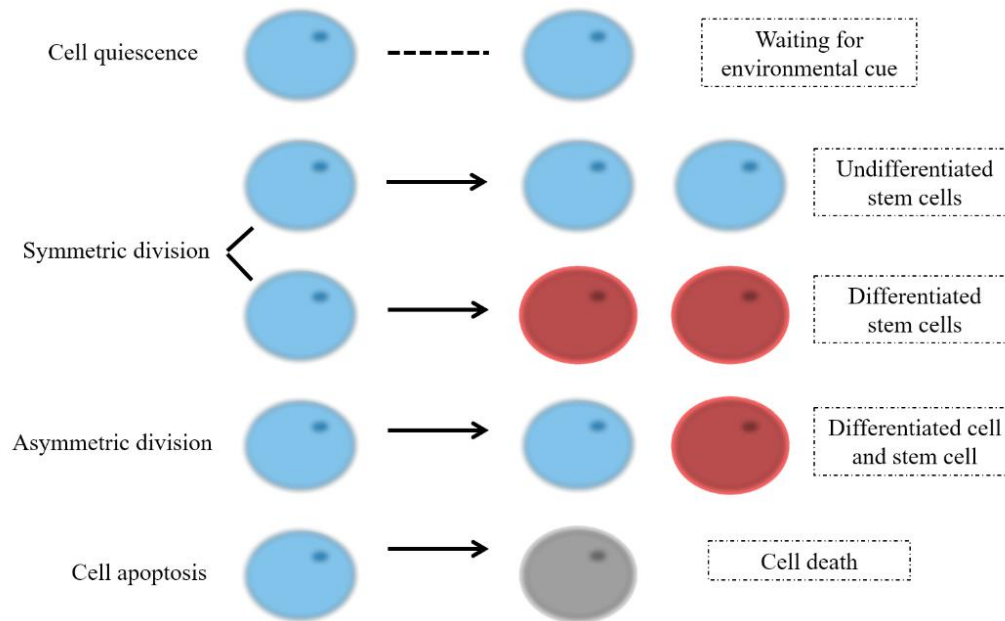
Figure 4. Possible outcomes for stem cell fate. Undifferentiated stem cells (blue) are normally quiescent within their niche unless an external cue activates them in response to trauma or homeostatic regulation. Symmetric or asymmetric division results in differentiated stem cells (red) and is controlled by internal or external cues in their microenvironment such as stress or loss of their niche.

The organization of the stem cell niche has been proposed to protect from gene mutations that could lead to malignant transformation [72]. In recent years, studies have shown the impact of deregulated and aged stem cell niches *in vivo*. However, the relation between the loss or disruption of the niche and pathologies associated with premature aging, tumorigenesis, and tissue regeneration remains controversial [73], [74], [75].

Tissues that have a high proliferative profile and require and continuous replenishment of cells, such as the epidermis, intestine, hematopoietic system, or cornea, have a need for active stem cell niches to modulate this high self-renewal cycle [76]. In comparison, tissues such as the skeletal

17

muscle require a dormant stem cell niche that can preserve a quiescent stem cell population that can be activated under specific conditions [73], [77]. The epidermal stem cell microenvironments of the hair bulge and rete ridges are clear examples of high proliferative niches that provide physical protection and preserve an undifferentiated stem cell phenotype [78]. Table 1 shows a summary of stem cell microenvironments that have been studied for their importance in tissue regeneration.

Table 1. Stem cell niches that have been located and studied to understand and control stem cell behavior [79].

Tissue/System	Location	Stem cell population	Ref
Skin	Hair follicles	Melanocyte stem cells, hair follicle cells	[78], [80]
	Rete ridges	Epidermal stem cells	[81]
		Keratinocyte stem cells	[82]
Hematopoietic system	Bone marrow	Hematopoietic stem cells (HSCs)	[83]
		Mesenchymal stem cells (MSC)	[84]
Small intestine	Epithelium of the small intestine	Intestinal stem cells, non-epithelial stromal cells, myofibroblasts.	[85]

Heart	Epicardial lining	Cardiac stem cells (CSC)	[86]
	Myocardium		
Cartilage	Articular cartilage	Bone marrow mesenchymal stem cells (BMSC), Cartilage-derived mesenchymal progenitors	[87]
Eye	Corneal limbus / Palisades of Vogt	Limbal epithelial stem cells	[88]
Neural system	Subventricular zone	Neuronal stem cells (NSC)	[89], [90]
	Hilus of the dentate gyrus	Radial neural stem cells, Dentate gyrus neural stem cells	[91]
Lung	Lung epithelium / tracheal submucosal glands	Basal cells, club cells, and ATII cells	[92], [93]
Primary or permanent teeth	Dental pulp tissue	Human dental pulp stem cells, MSCs, BMSCs.	[94], [95]

3.1. The keratinocyte stem cell microenvironment

The balance between differentiation, proliferation and programmed cell death of keratinocytes is critical to maintaining epidermal homeostasis and regeneration [80]. The BM contains a basal layer of proliferative keratinocytes, which are periodically detaching from the BM and initiating a

terminal differentiation process known also as cornification This keratinocyte differentiation induces cell migration towards the skin surface and creates the three distinctive *stratums* of the epidermis (*spinosum*, *granulosum,* and *corneum*). The cell undergoes several morphological changes controlled by organellar and molecular mechanisms until eventually their cell nuclei is lost (becoming corneocytes) and they are shed from the skin [56]. Keratinocyte stem cells (KSCs) play a key role in epidermal homeostasis and tissue regeneration as they can generate differentiated cell linages that build mature tissue [80].

In comparison with the KCS found in the hair follicle, and sebaceous glands, the location of the KCS on the BM, specifically within the base or the tip of the rete ridges remains controversial [80], [82], [96]. The epidermal proliferative unit (EPU) model establishes that a single slow-cycling stem cell in the basal layer produces a column of transit-amplifying and committed cells [39]. The location of the EPU within the rete ridges has been studied using stem cell markers such as integrin α6 and Iβ1 [82], [96]. However, other markers for cell stemness such as Ki67, p63, K14, K15 have been used to study the distribution of the stem cells across the BM [68], [80], [97].

Changes in the organization of the rete ridges can alter the biomechanical and therefore biochemical properties of the skin as the ridges interact with proteins expressed on the DEJ such as laminin-111, COL1, and COL4 [98], [99]. Other studies have shown the effect of the rete ridges on the maintenance of mature Merkel cells by stem cells [100] and the relation between aging and flattened ridges due to changes in the expression of Iβ4, COL4, COL7, and COL12 [101]–[103].

A recent study by Hirobe et al. theorized a relation between the rete ridges and the melanocyte and melanoblast population. Even though there was an increase in the average number of melanocytes on the rete ridges, the study remains inconclusive, and more work is needed to clarify the difference

between flat and ridged dermis. The main theory behind this behavior is that the high production of cytokines and growth factors within the niche induced the proliferation and differentiation of melanocytes and melanoblasts [104]. These findings further support the idea that the rete ridges not only support skin regeneration and homeostatic balance, but that also play a key role in regulating other processes within the dermis.

4. Skin wound healing

The skin wound healing process is a complex biological response to restore the structural integrity and function of the damaged tissue [58]. Despite the severity of the incised injury or burn, several overlapping phases take place during the wound healing process. The stages of inflammation, cell recruitment, matrix synthesis and deposition, epithelialization, remodelling of the ECM, and angiogenesis are critical for the regulation and healing of skin injuries [25], [105]. The wound healing process is divided into four main phases: homeostasis, inflammation, proliferation, and remodelling (also known as the maturation phase) [18].

The conventional skin healing process starts within the first seconds after the injury with the homeostasis phase. Upon stimulation of sensory neurons that trigger pain, cutaneous neurogenic inflammation promotes microvascular permeability and initiates the formation of a fibrin clot that plugs the wound while the subsequent stages of healing are initiated. The function of this clot is to shield the damaged tissue, storage of cytokines and growth factors, and provide a provisional interface in which cells can migrate during the regeneration process. This early mixture of growth factors proves a "starting" signal for sedentary cell lines and inflammatory cells to migrate to the wound side [106], [107].

The inflammation phase triggers monocytes and neutrophils to migrate from the circulating blood to the wound site. The arrival of neutrophils to the wound has been related to the elimination of bacteria and the production of pro-inflammatory cytokines that have a role in the early stage of fibroblast and keratinocyte migration. After macrophages remove the remaining pathogenic organisms, ECM, and cellular debris in the wound, several cytokines and growth factors are synthesized to amplify the signals released by platelets and neutrophils, leading to the stage of re-epithelialization [106].

Once fibroblast and endothelial cells have proliferated, platelets regulate the expression of transforming growth factors-β (TGFβs), epidermal growth factor (EGF), and platelet derived growth factors (PDGF) [58]. Fibrin, fibronectin, and collagen support the structural integrity of the ECM during the phases of tissue repair. The interaction between fibronectin and fibrin creates a provisional matrix that allows cell adhesion and migration during wound healing. This provisional matrix is replaced by fibroblasts with granulated tissue composed of collagen and fibronectin. Endothelial cells migrate to the wound side to create a vascularized network [108], [109]. In order to vascularize the wound, complex signaling is required to trigger vasodilatation, the degradation of the BM, and activate endothelial cell migration and proliferation [110]. This critical stage of wound healing is defined as revascularization and angiogenesis and is described in detail in section 5.

As revascularization is performed, fibroblasts differentiate into myofibroblasts, these cells produce cytokines and metalloproteinases that remodel the ECM and have an active role in the inflammatory response [108], [109]. Myofibroblasts also express α-SM (smooth muscle) actin in the form of microfilament bundles; these α-SM actin complexes allow contraction and maturation of the granulation tissue [108]. Production of fibronectin granulation tissue provides a vasculature

22

that leads to further collagen deposition in the wound side, and collagen fibrils bundle and cross-link as the new tissue is remodeled [109]. Figure 5 shows an overview of the skin wound healing process with is four main stages.
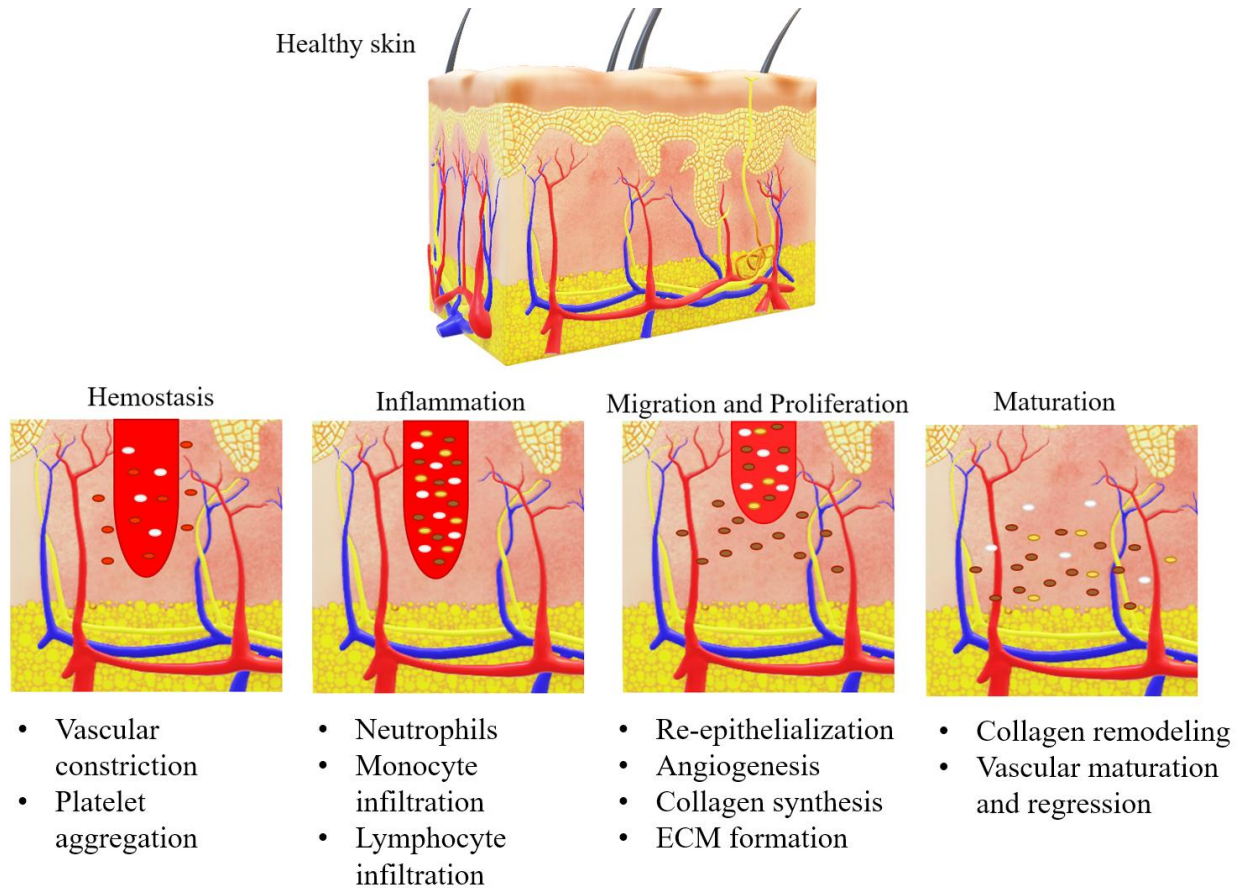
Figure 5. Overview representation of the key events of the skin wound healing process: hemostasis, inflammation, migration and proliferation, and maturation (adapted from Dias et al. [16]). Each stage of wound healing requires the activation production of specific cell types and biomarkers.

Although minor skin lesions are healed efficiently during the first or second week, the new tissue is usually not aesthetically or completely functional. Severe wounds also affect epidermal appendages that do not regenerate and leave a scar of connective tissue [106]. The presence of hair follicles in the wound has a large impact on the regeneration of the epidermis, as they act as

23

epidermal wound edges and allow for regeneration from these focus points, providing storage of cells to replace the lost tissue during the injury. Researchers have suggested that the proliferative capacity of the hair follicles is related to the presence of epidermal stem cells [106], [111].

Scarring is the consequence of the body trying to reconstruct the damaged tissue without the original composition, and distribution of the collagen fibers in the skin. Wound contraction is characteristic of scarring tissue and is caused by the presence of myofibroblasts that have developed characteristics of smooth muscle cells, such as the ability of contraction due to calcium signaling [23], [108]. Myofibroblast contractive nature is related to cytoskeletal features that create strong connections with the ECM. These protein complexes provide a means for the myofibroblasts to contract and remodel the ECM [23]. In the case of skin grafts, if the dermis layer remains, interactions in the epidermal-dermal junction promote the re-epithelialization of keratinocytes, increasing the resistance to scarring and wound contraction [112].

Growth factors are essential in the wound healing process, as they activate cell surface receptors to encourage development, cell differentiation, and cell migration. Once the growth factor has reached its receptor, it transduces extracellular signals to activate intracellular carriers. In the case of wound healing, basic fibroblast growth factor (bFGF), vascular endothelial growth factor (VEGF), EGF, PDGF, and TGF-β1, have active roles in different stages of the regeneration of damaged tissue [113], [114].

EGF activates cell proliferation, accelerates re-epithelialization, and induces cell migration and expression of keratin in keratinocytes [114], [115]. bFGF is a family composed of 23 factors, being FGF-2, FGF-7, and FGF-10 the most relevant for dermal wound healing. These factors are related to the formation of granulated tissue, re-epithelialization, tissue remodeling, and the production of

ECM components that improves the migration of fibroblasts and the production of the enzyme responsible for the rupture of collagen, collagenase. TGF-β1 is critical in the inflammatory phase, angiogenesis, re-epithelialization, regeneration of connective tissue. TGF-β1 has been identified as an inhibitor in re-epithelialization and capable of inducing fibrosis, when is overexpressed in burn injuries [115].

PDGF is a biochemical mediator of the wound healing process that is released at the time of the injury and later by macrophages in the wound healing process. PDGF is a chemotactic agent for smooth muscle cells, fibroblasts, neutrophils, and monocytes, its expression improves dermal regeneration, promotes collagen synthesis, encourages endothelial migration. PDGF also plays a key role in angiogenesis by stimulating the production of angiogenic factors or through the activation of vascular endothelial cells [116].

VEGFs are a family of secreted polypeptides that are studied for their role in vascular development. In humans, VEGF-A is one of the main mediators that induce the appearance of capillaries that invade the wound and ensure that the healing process maintains a nutrient and oxygen gradient. VEGF controls the proliferation and chemotaxis of endothelial cells and induces vascular permeability when it is released by activated platelets upon injury, promoting the initial stages of angiogenesis [110], [115].

Clinical conditions such as diabetes, venous hypertension, and immune deficiency can compromise the endogenous healing process. The specific challenges of each condition often require specific pharmacological agents or procedures to aid wound healing. However, vascular insufficiency, infection, and acute inflammation remain challenges for clinicians and tissue engineering applications.

Furthermore, wound healing is also affected by the changes in pH, leading to inhibition or structural changes of some of the proteins involved in the remodeling of the tissue [117]. Other factors such as calcium concentration (a contributor to skin homeostasis and keratinocyte proliferation and differentiation) [118], and oxygen levels [119] severely compromising the healing process. Additionally, severe burns also stimulate a stress response and a hypermetabolic condition. These pathophysiological changes affect the pharmacological response of several drugs and are key in the treatment of chronic or acute wounds [25].

5. Vascularization and angiogenesis

Skin microcirculation consists of two vascular networks (or plexuses), one located on the deeper dermal layers close to the hypodermis (lower plexus), and another located close to the epidermal layer on the papillary dermis (upper plexus). Skin microcirculation plays a significant role in thermoregulation, homeostasis, blood pressure, and the inflammatory response. Furthermore, skin microcirculation allows for nutrient diffusion from arteries to small capillaries close to the epidermis (upper plexus), and other relevant appendages such as hair bulbs and sweat glands (lower plexus). Injuries and other conditions such as coagulation disorders, hypoxia, temperature, and aging can affect skin microcirculation [120]–[122].

Angiogenesis is the growth of blood vessels from pre-formed vasculature. This process of new blood vessel formation is uncommon in the human body, occurring only during the highly controlled process of wound healing and the female reproductive cycle. However, regions that have experienced an increase in metabolic activity due to poorly perfused conditions such as cancer can also trigger angiogenesis [123]. The levels of nutrients and oxygen controlled the activation of angiogenesis. Hypoxic conditions in tissues activate vascular growth by secreting growth factors

and chemokines [124]. Furthermore, endothelial cell proliferation and new blood vessel formation are key steps of the proliferative phase of wound healing.

Angiogenesis in the skin usually involves the remodeling and creation of a stable vessel network from the upper plexus controlled by endothelial cell migration (sprouting angiogenesis) [125]. Unless angiogenic signals are activated, endothelial cells remain dormant under normal physiological conditions. Sprouting angiogenesis starts with endothelial cell migration from pre-existing vessels and coordinates branching and sprouting to perfuse the hypoxic tissue to meet the oxygen demand [124].

The hypoxic conditions trigger neovascularization by stimulating the release of angiogenic factors FGF, TGF-β1, PDGF, and VEGF from endothelial cells, keratinocytes, fibroblasts, and macrophages [107], [126]. After the degradation of the vascular BM, pericyte loss and sprouting of capillaries are followed. The sprouting is control by migratory tip cells that guide the new sprout using VEGF as an endothelial cell chemoattractant. Finally, stalk cells elongate the sprout, quiescent phalanx cells form the lining of the vessel, and mural cells cover the mature vessel with a BM [107].

Vascularization of the tissue constructs is required to provide nutrients and oxygen to the inner tissue. Infection, loss of function, rejection of the skin substitute, and necrosis are challenges that result from an insufficient vascular network. Tissue engineers have explored the use of angiogenic and prevascularization (also called inosculation of blood vessels) strategies to aid the generation of a suitable vascular network by decreasing the time needed to vascularize a tissue construct [127], [128]. Prevascularization techniques aim to create a microvasculature within the tissue prior to implantation, while angiogenic approaches aim to stimulate the ingrowth of blood vessels in tissue

constructs from an existing vasculature [129]. As angiogenic approaches depend on the slow growth rate of neovasculature (approximately 5µm/h) [130] they are not considered appropriate for vascularization of large implants. This low growth rate becomes more relevant when considering that tissue constructs cannot grow beyond the diffusion limit of oxygen of 100 µm – 200 µm [128].

Three dimensional scaffolds have been used as effective templates for dermal regeneration when treating full thickness skin defects caused by burns, chronic diseases, or trauma. When the integrity of the skin is compromised, the acceleration of angiogenesis increases the post transplantation healing time of thin skin grafts and decreases the risk of the infection improving healing [58]. However, as described before, the ingrowth of newly formed blood vessels is a complex process that requires the activation of the host microvasculature near the implantation site. After implantation, the surrounding cells of the tissue construct react to the hypoxic conditions and stimulate the invasion of blood vessels to create a pseudo vascular network [128].

6. VEGF: Challenges and novel alternatives

Proangiogenic growth factors such as VEGF or bFGF, are key regulators produced by cells of the host tissue in response to inflammation or injury due to the implantation procedure. Discovered in 1989 by Ferrara and Henzel [131], VEGFs are a family of five polypeptides that includes VEGF-A, VEGF-B, VEGF-C, and VEGF-D, and placental growth factor (PLGF) [132]. VEGF-A (commonly referred to just as VEGF) is the most biologically relevant for its role in the regulation of angiogenic activity in several biological processes such as embryogenesis, skeletal growth, wound healing, and reproductive functions [132].

VEGF gene expression is primarily controlled by oxygen tension via the oxygen sensor hypoxia-inducible factor (HIF-1) [133]. Once activated, the angiogenic process induces a signaling cascade that promotes the growth of vascular endothelial cells from arteries and veins [127][134]. VEGF also mediates unregulated pathological angiogenic activity such as arthritis, metastasis, tumorigenesis, and ocular neovascularization [134][135][136]. The major roles of VEGF in the angiogenic process include increasing microvascular permeability, secretion of metalloproteinases, and inducing endothelial cell migration, survival, and proliferation [137].

Secreted as homodimers, the VEGF family interacts with a group of three tyrosine kinase receptors VEGFR1, VEGFR2, VEGFR3, with VEGF-A binding to both VEGFR1 and VEGFR2 [138]. Nonetheless, VEGF-A primarily binds VEGFR2 to activate endothelial cell proliferation, migration, and vascular permeability. The VEGF signaling pathway induces the production of vasodilatory mediators through the increase of nitric oxide (NO) [139]. Once VEGF binds to VEGFR2 it goes under an autophosphorylation process that activates the phospholipase-Cγ/protein kinase C pathway and increases the level of intracellular calcium by phosphatidylinositol-3 kinase (PI3K/Akt) interactions [137], [140]. The increase in calcium promotes calmodulin binding on nitric oxide synthase (NOS) and induces the production of NO. This increase in NO production promotes endothelial cell survival and vascular permeability [141]. Figure 6 shows a schematic representation of the VEGF family and its receptors.
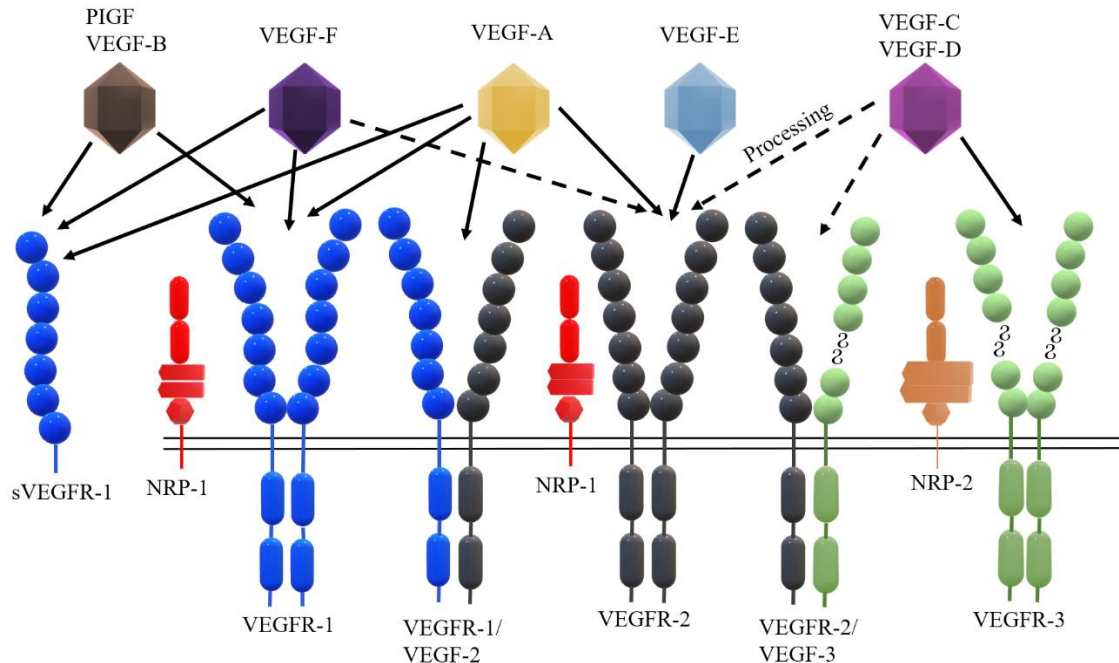
Figure 6. Schematic of the VEGF family binding mechanism. The different members of the VEGF family bind to different VEGFRs. VEGF-A signalling through VEGFR2 is the main pathway that activates angiogenic activity. The mature forms of VEGF-C and VEGF-D can also bind to VEGFR2. VEGF-B is primarily expressed in skeletal muscle, cardiac tissue, and BAT. The other two members VEGF-E and VEGF-F are less biologically relevant [140], [142].

Clinical studies have used infusions and injections of VEGF in solution for therapeutic purposes. Furthermore, applications in tissue regeneration have aimed for the effective delivery of VEGF through controlled release scaffolds [143] or tissue engineered constructs [144], [145]. Complex delivery systems that use heparin have been proposed to stabilize VEGF when loaded in polymeric scaffolds [146], [147], however, the process of binding is still in the early stages of optimization.

However, there is controversy about the use of VEGF in clinical applications. Pathologies caused due to high levels of VEGF such as vascular leakage, vasodilatation, formation of dense but non-functional vessels, and hypotension have limited the use of VEGF in tissue engineered constructs

30

[134], [148]. Other studies have raised concerns about extended time of exposure to VEGF, spatial distribution in the target tissue, gradient concentration, and short half-life [148]–[150]. These drawbacks, in conjunction with a high production cost, have raised the demand for alternatives to VEGF in clinical applications. Table 2 shows novel proangiogenic agents that are being studied to overcome some of the limitations of VEGF.

Table 2. Novel proangiogenic factors that are being studied and integrated into tissue engineering applications.

Proangiogenic factor	Description	Ref
Hh genes, Sonic hedgehog (Shh)	Morphogen that regulates mesenchymal/epithelial interactions and stimulates angiogenesis characterized by large-diameter vessels.	[151], [152]
Apelin	Endogenous ligands of the G-protein-coupled receptor APJ present in the brain, retina, and heart, that stimulates angiogenic activity in retinal endothelial cells and myocardial infarction	[153], [154]
Extracellular matrix/stromal vascular fraction	Adipose-tissue-derived gel use for mesenchymal stem cell therapy that has shown angiogenic effects in wound healing model.	[155]

Polyphenols (Eg. Flavonoids, and phenolic acids)	Polyphenols have been investigated for their effects in the angiogenesis signaling pathway through the activation of vascular extracellular growth factor receptors.	[156]

Sugars and hormones have been studied by our research group as potential proangiogenic agents that can be integrated into polymeric scaffolds [157]–[159]. For this study, 2-deoxy-D-ribose and 17-β estradiol were studied as promising regulators of angiogenic activity to introduce fibrous scaffolds. Additionally, the use of aloe vera as a natural multifunctional angiogenic compound was explored further in this thesis.

6.1.   2-deoxy-D-ribose

2-deoxy-D-ribose (2dDr) is a five-carbon sugar that is produced *in vivo* by the catalytic action of thymidine phosphorylase (TP) over thymidine. 2dDr is a D-isomer discover in 1930 mostly known for its role on DNA structure [160]. The biologic relation between thymidine phosphorylase, thymidine, and thymine with 2dDr has been documented by several authors [123], [161], [162]. However, the mechanism behind the angiogenic potential of 2dDr and its derivatives is not completely understood [163], [164] and remains controversial due to its relation resistance to hypoxia-induced apoptosis, and metastasis [163], [165]. Recent studies by our research group have shown that µM concentrations are capable of inducing angiogenesis *in vivo*, *in vitro,* and in an *ex-ovo* assay [166]–[171]. Figure 7 shows the chemical linear structure of 2dDr.
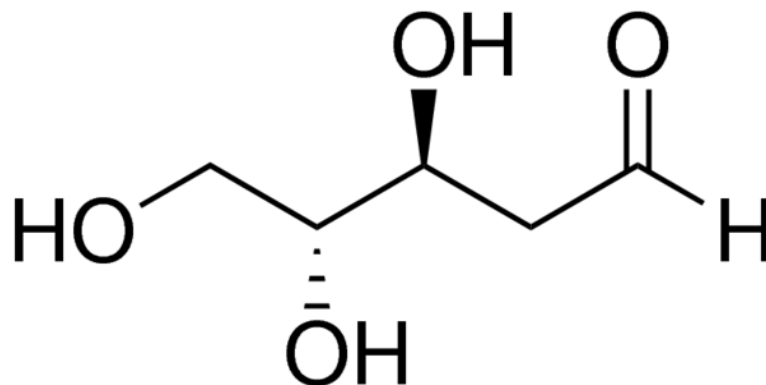
Figure 7. Linear chemical structure of 2dDr.

The most accepted theories behind 2dDr angiogenic nature are: 1) the production of VEGF and interleukin 8 (IL-8) through the increase in oxidative stress due to the production of 2dDr by enzymatic degradation of thymidine to thymidine via TP [123], [165] and 2) the activation of NADPH oxidase 2 (NOX2) that upregulates VEGFR2 through transcription of nuclear factor kappa B (NF-κB) [161], [169], [172]. The mechanism in which 2dDr initiates endothelial-cell migration has been compared with the glucose chemoattractant properties, as in contrast with the majority of endothelial-cell chemoattractants, 2dDr appears to lack a specific cell receptor [123].

In vivo, the catalytic action of TP over thymidine produces the nucleobase thymine, and the sugar 2-deoxy-D-ribose 1-phosphate (2dDr-P), which can leave the cell after being dephosphorylated and has been reported as angiogenic when released by macrophages, platelets, and cancerous cells [161]. The migration of thymidine into the cell does not require any energy and is mediated through the salvage pathway that ensures a suitable concentration of nucleotides for the maintenance of DNA. Therefore, if TP has a constant supply of substrate thymidine, the production of 2dDr increases [123].

A comparative study by Yar et al. has compared the proangiogenic effect L and D isomers of deoxy-sugars when loaded into chitosan/collagen hydrogels [157]. The results showed the promising effects of 2dDr when compare with its L isomer, fucose, and rhamnose. However, the use of deoxy-sugars in wound healing may induce microbiological activity from *Pseudomonas aeruginosa*, as this strain was able to metabolize 2dDr [157].

6.2. 17-β Estradiol

17-β estradiol (E2) is an endogenous estrogen (Figure 8) that plays a major role in the menstrual cycle and is also responsible for inducing cardiovascular activity, cell migration, and collagen synthesis [158], [173]. During the menstrual cycle, the lining of the uterus (endometrium) exhibits angiogenic activity in the form of dense networks of mature blood vessels. This rapid growth of vasculature in the endometrium is control by the female reproductive cycle and the release of sex steroid hormones. The hormones released during the female cycle activate the endometrium cells including, endothelial, epithelial, stromal, and immune cells. The proliferative phase of the female reproductive cycle is characterized by an increase of E2 levels that mediate tissue growth. The secretory and menstrual phases also present a certain level of angiogenic activity, although the majority of the angiogenic activity is expressed during the proliferative phase. Although most of the effects of estrogen on the skin are associated with post-menopausal women such as altering skin thickness, collagen production, elasticity, and water content, they also protect against photoaging, development of chronic wounds, and reduce the risk of skin tumors [174], [175].
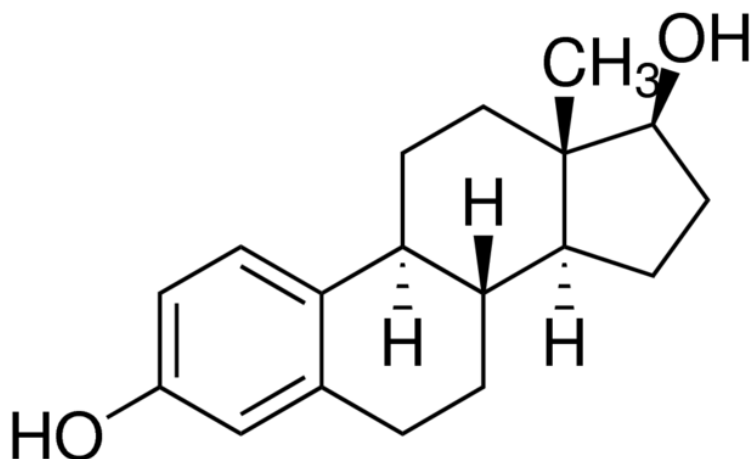
Figure 8. Chemical structure of E2.

Elevated levels of E2 signal the initial expression of VEGF, which is the primary proliferative factor related to vascularization during the female reproductive cycle [175], [176]. However, the relation between endothelial cell proliferation, VEGF signaling, and E2 has not been fully characterized. Herve et al. showed that E2 can upregulate VEGFR-2 through the activation of estrogen receptors (ER) ERα and ERβ using an *in vivo* animal model [177] [178]. Studies have reported that E2 upregulates the production of the VEGF gene in human endometrial cells [179]. *In vitro* treatment with E2 has shown an increase in NO2 concentration and eNOS expression [180]. Albrecht et al. explored the potential of E2 to induce proangiogenic activity growth of vascular endothelial tubes, using human epithelial cells or stromal cells with human myometrial microvascular endothelial cells [181].

The suitability of E2 in regenerative medicine applications has been explored by Mangir et al. and Shafaat et al. by introducing E2 into biocompatible materials to improve tissue integration for urogynaecological applications [158], [159]. Pence et al. reported a covalent immobilization of E2 in a collagen based biomaterial [175]. Sekiguchi et al. introduced E2 into a gelatin hydrogel to

induce differentiation of neural stem cells to intro endothelial cells and improving motor nerve repair [182]. A study by Toutain et al. explored the use of E2 as an alternative to FGF and VEGF to prevent necrosis on skin flaps (full thickness transplants) by revascularization [183]. Crompton et al. used E2 on a lipopolysaccharide bacterial infection model and reported re-epithelialization, reduction in local inflammation, and collagen deposition [184]. These studies have proved the feasibility of E2 as a novel proangiogenic alternative to VEGF.

6.3. Aloe Vera

Aloe barbadensis (commonly known as *aloe vera*) is a succulent perennial and drought resistant plant known for its biomedical properties as an antioxidant, anti-inflammatory, anti-aging, and anticancer agent [185]. Aloe vera (AV) can stimulate cell proliferation through the production of amino acids, that promotes regeneration at the deepest layers of the skin preventing scar formation, and encourage the production of antibodies and release of growth factors, thus accelerating the wound healing process [186], [187].

The composition of AV varies significantly depending on the part of the plant that is extracted and the technique used to process the whole leaf is critical to determine the potential healing effects. From the three layers of the AV leaf (gel, fillet, and rind), the gel of the AV has the highest amount of nutrients and bioactive compounds [188]. Polysaccharides, sugars, and inorganic electrolytes such as potassium, sodium, zinc, and calcium represent about 88% of the entire gel composition [186], [189]. Table 3 shows the chemical composition of the whole AV leaf.

Table 3. Summary of chemical and bioactive compounds present in AV [186],[190]–[192].

Class	Compounds
Amino acids	Alanine, arginine, aspartic acid, cysteine, glutamic acid, glycine, histidine, hydroxyproline, leucine, lysine, methionine, proline, phenylalanine, threonine, serine, tyrosine, and valine
Anthraquinone	Aloe-emodin, aloetic acid, anthranol, aloin A, aloin B, anthracine, anthranon, barbaloin, emodin, ethereal oil, ester of cinnemonic acid, isobarbaloin, and resistannol
Carbohydrates	Lignins, and sugars such as arabinose, cellulose, fructose, fucose, galactose, glucose lactose, maltose, mannose, rhamnose, sucrose, uronic acids, and xylose
Chromones	8-C-glucosyl-(2'-O-cinnamoyl)-7-O-methylaloediol A, 8-C-glucosyl-(S)- aloesol, 8-C-glucosyl-7-O-methyl-(S)-aloesol, 8-C-glucosyl-7-O-methylaloediol, 8-C-glucosyl-noreugenin, isoaloeresin D, isorabaichromone, and neoaloesin A
Enzymes	Alkaline phosphotase, amylase, carboxypeptidase, catalase, cellulase, cyclooxidase, cyclooxygenase, lipase, oxidase, peroxidase, phosphoenolpyruvate carboxylase and superoxide dismutase

Inorganic compounds	Calcium, chlorine, chromium, copper, iron, magnesium, manganese, phosphorous, potassium, sodium, and zinc
Proteins and hormones	Lectuin, auxins, and gibberllins
Sterols	Cholesterol, campesterol, lupeol and β-sitosterol
Vitamins	A, C, E, B1, B2, B6, B9, and β-carotene

Although several components of the AV leaf have been studied individually there is a consensus that the bioactivity of AV is mainly due to the synergistic interaction of the compounds [190]. The anti-inflammatory and pain relief effects of AV are related to the presence of anthraquinones, chromones, and the inflammatory mediator of bradykinin [193], [194]. Antibacterial activity of AV has been analyzed against *S. aureus*, *S. pyogenes*, *P. aeruginosa,* and *E. coli*. Where maximum growth suppression was observed in *S. pyogenes* and *P. aeruginosa* [195]. Aside from the conventional topical application, aloe vera has been rarely used in wound healing. Recent studies have loaded AV in nanofibrous scaffolds [196], and hydrogel films [197], with promising advantages over the topical route for wound healing applications.

The angiogenic activity of AV has been reported as an effect of β-sitosterol [198]. However, the mechanism behind the angiogenic potential of AV remains unclear. The most accepted theory suggests that β-sitosterol induces the gene expression of bFGF and VEGF [198]. Interestingly, aloin and β-sitosterol have been studied for their properties to inhibit the angiogenic response of VEGF and the levels of E2, respectively. Both aloin and β-sitosterol have been used to inhibit

tumor growth of colorectal and breast cancer respectively [199], [200]. This duality of cancer inhibition and angiogenesis reinforces the theory of a complex interaction between the compounds present in AV.

As discussed in chapter I section 4, skin wound healing is a complex process that requires a constant exchange of nutrients and signaling molecules to control the phases of the healing process. For example, conditions such as infection and impaired healing that compromise the integrity of the surrounding healthy tissue can be overcome by introducing anti-microbials, anti-inflammatory, or proangiogenic agents into wound dressings or tissue engineered constructs.

Inducing vascularization is critical for tissue engineering applications and choosing the appropriate angiogenic agent to deliver to the wound side is a key aspect to improve wound healing. However, the biomaterials and the architecture of the wound dressing or scaffold play a very important role as well. In recent years, new strategies have been developed to improve skin regeneration. The current challenges and novel strategies of skin tissue engineering are described in detail in the next section.

7. Skin substitutes and tissue engineering approaches

Limited donor sites and the need for reducing surgical procedures have encouraged the development of tissue engineering matrices and scaffolds using biocompatible and biodegradable polymers. The principles of tissue engineering describe the ideal scaffold as the structure capable of supporting cellular activities that degrades at the same rate as the tissue is being regenerated. In the case of skin, the design of an ideal wound dressing aims to imitate the structure and biological functions of the components of the ECM, while providing a barrier layer of renewable keratinocytes, and allowing for proper vascularization of the construct. Mechanical strength and

porosity are also required to enable cellular infiltration and growth, and to provide elasticity and structural support for skin [34], [58], [201].

Dermal substitutes and scaffolds can be classified according to their composition; as natural or synthetic [58]; or according to their biological function as temporary, semi-permanent, and permanent [202]. In comparison to dermal substitutes or scaffolds, the main function of a wound dressing is to cover the wound from external damage, aid in the re-epithelialization, and avoid infection. Wound dressings are divided into four groups according to their chemical nature or bioactivity. These are biological dressings, biosynthetic dressings, antimicrobial, and conventional dressings [25].

Furthermore, other examples of skin substitutes include Biobrane ®, which consists of 2 layers of nylon filled with type I porcine collagen, covered with silicone [203]; and integra dermal regeneration template, which is composed of bovine collagen, chondroitin-6-sulfate in a silicone lamina [204]. Nevertheless, high risk of infection and difficulty of wound adherence limits the performance of these skin substitutes. In addition, even though the role of growth factors in skin wound healing has been investigated, they have not been included in commercially available skin substitutes, as cell-based skin substitutes rely on the production of growth factors, such as epidermal growth factor (EGF), from the cells present on the skin substitute [205].

Biological dressings are commonly used by clinicians, these include cadaveric allografts and xenografts. However, their inconsistency in quality, the risk of pathogen transfer, rejection, and limited supply, are challenges that need to be addressed regarding these biological dressings. In comparison, conventional dressings (without antibiotics or drugs) such as silicone sheets or gauze dressings, are easier to control in terms of consistency and quality, also their availability is higher,

and their cost of production is lower. The drawback of conventional dressings is that they are used mostly for the protection of the wound during re-epithelialization, and they have a tendency of damaging the newly formed epithelia, as they adhere to the wound surface and need to be frequently changed [25].

Biosynthetic dressings are designed to mimic the function and the structure of the epidermis and dermis, using biomaterials and, in some cases loading them with chemical agents to aim the regeneration of the damaged tissue. Commercially available products can be divided into cellular dermal matrices including bilayered living cellular constructs (Apligraf®), and collagen dermal matrix (Dermagraft®); and acellular dermal matrices such as Integra dermal regeneration template and Poly-N-acetyl glucosamine fibrous matrix [206].

Additionally, novel techniques are being developed to explore the use of both angiogenic and prevascularization strategies using additive manufacturing techniques, scaffold design, and the introduction of new angiogenic agents. According to the application, size, and nature of the tissue engineering construct either prevascularization or angiogenesis could be suitable approaches to achieve vascularization. However, for most clinical applications, VEGF remains the gold standard to induce rapid and efficient vascularization. Table 4 shows an overview of established and novel strategies used to achieve vascularization in tissue constructs.

Table 4. Overview of techniques and products that have been used to stimulate prevascularization or angiogenesis in skin substitutes.

Approach	Product / technique	Description	Ref

Angiogenesis	Integra® Crosslinked collagen and GAGs	Vascularization achieves by controlling pore size and interconnectivity. Pore size between 20 -125µ and 20-150 µm respectively	[129], [207]
	Matriderm® bovine lyophilized dermis		
	Plasma treatment	Collagen-elastin matrix scaffold treated using plasma surface activation with cold low-pressure argon/hydrogen	[208]
	poly-N-acetyl glucosamine nanofibers	Nanofibrous scaffolds developed from microalgae poly-N-acetyl glucosamine	[209]
	Bilayer PLLA fibrous scaffold	Scaffolds designed with ~ 220 and 250 µm thickness. Different fiber arrangements to create larger pore size scaffolds	[210]
	Covalently immobilized VEGF	Porous collagen scaffold prepared with low (~14 ng) and high (~97 ng) immobilized VEGF concentrations	[211]
	Poly (lactic-co -glycolic acid) microspheres loaded with bFGF	Controlled delivery of bFGF from microspheres loaded on alginate composite scaffolds.	[212]

	Adenoviral-gene transfer to deliver growth factors	PDGF-β delivers through adenoviral vector as an alternative topically applied growth factor in ulcers.	[213], [214]
Pre-vascularization	3D printing	Laser-assisted bioprinting to create skin substitutes using fibroblasts and keratinocytes on top of Matriderm®	[215]
	Microfluidics	Interconnected microporous gel scaffolds seeded with fibroblasts and stem cells.	[216]
	Vessel-forming cells used in 3D scaffolds	Human reconstructed skin combining fibroblasts, keratinocytes, and endothelial cells in a collagen-GAG-chitosan polymer	[217]
	Network of organotypic capillaries	3D capillary networks of human microvascular endothelial cells seeded into fibrin hydrogels	[218]

A key component in tissue engineering and some regenerative medicine applications is the use of biomaterials. Biomaterials are natural or synthetic materials that are intended to interface with biological systems to treat, evaluate, augment or replace any function, organ, or tissue of the body

[219]. These biomaterials are often exposed to post-processing or specific manufacturing techniques to achieve certain physical, structural, or chemical characteristics.

7.1. Polymeric scaffolds

The selection criteria for a biomaterial are highly associated with the intended end application. However, regarding the tissue or application, biocompatibility, biodegradability, manufacturing technology, and mechanical properties should be considered when selecting an effective biomaterial. Due to the composition of the human skin, the most commonly used biomaterials for dermal replacement and wound healing include: natural human or porcine dermal collagen, extracted animal collagen, and polyglycolic acid scaffolds [201], [206]. These materials share characteristics of high biocompatibility and fast degradation. Although many polymers have been proved suitable for wound healing and skin tissue engineering applications, this work was focused on studying the use of either poly(lactic-*co*-glycolic) acid or polycaprolactone to create a fibrous scaffold.

Poly(lactic-*co*-glycolic) acid (PLGA) is a biocompatible synthetic linear copolymer that is synthesized from lactic acid and glycolic acid (Figure 9). Poly(lactic acid) (PLA) chemical structure contains an α-carbon that produces D and L forms of PLGA [220]. Different ratios of these monomers can lead to different effects on the mechanical and biological properties of the final polymer. The amount of methyl side groups present in PLA produces a hydrophobic polymer that absorbs less water and degrades at a slower rate [220]. The degradation profile of PLGA is mediated by hydrolysis of ester linkages and is defined by its poly(glycolic acid) (PGA) and PLA monomer composition, which can be metabolized in physiological conditions by the Krebs cycle [5]. The versatility of PLGA allows controlling the degradation rate to meet different clinical

applications. Other factors that influence the degradation of PLGA constructs include sterilization, residual solvents, surface properties, temperature, porosity, and molecular weight [221].
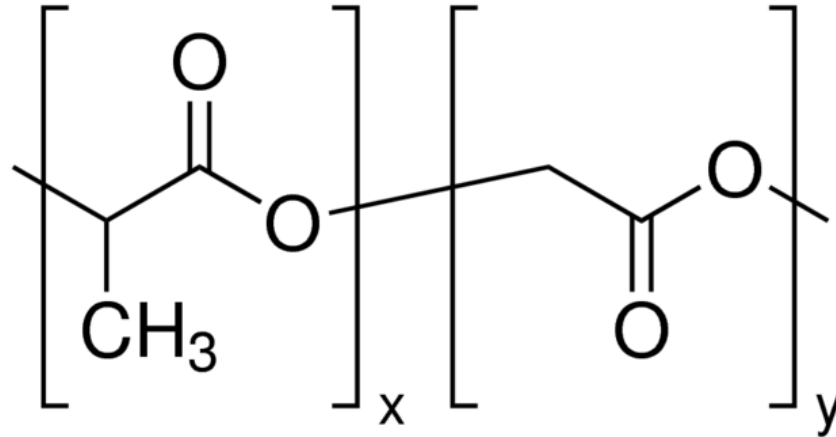
Figure 9. Chemical structure of PLGA. X represents the lactic acid units and Y the glycolic acid. Different ratios between these units give PLGA different mechanical and degradation properties.

In wound healing, the degradation of PLGA in lactate integrates into the hypoxic stage of the healing process. Hypoxic conditions caused a metabolic adaptation in the host, encouraging the production and accumulation of lactic acid, which signals collagen synthesis and deposition [222], [223]. The overexpression of lactate changes the NAD+/NADH ratio increasing the concentration of NADH metabolite and activating the enzyme collagen prolylhydroxylase. This change in NADH causes a substrate competition between lactate dehydrogenase 1 (LDH1) and ADP-ribosyl polymerase, encouraging a transduction cascade that is regulated by ROS. The end products of this process trigger the transcription of procollagen and VEGF in fibroblasts; and the release of bFGF and VEGF receptors by endothelial cells [5], [222]–[224].

PLGA and PCL DEGRADATION.

PLGA has been introduced in several commercial products due to its certification as a biocompatible material from the Food and Drug Administration (FDA) and the European Medicines Agency (EMA) [5]. Researchers have used PLGA to improve the bioactive and mechanical properties of collagen scaffolds [225]; used as degradable hydrogels, nanoparticles, fibrous mats, and microspheres, as delivery carriers for bioactive compounds [5], [226], such as bFGF [227] and VEGF [145], [228]; and into composite scaffolds for bone [229] and skin tissue engineering [230]. The versatility of PLGA as a drug delivery carrier and its recognition as a biocompatible, bioresorbable, and bioactive material makes it a promising candidate to design a wound dressing that can be used for clinical applications.

Polycaprolactone (PCL) is a semi-crystalline linear polymer. The capacity of PCL to be biodegradable is due to the susceptibility of the aliphatic ester linkage to hydrolysis (Figure 10). The products of the PCL degradation are metabolized by either renal secretion or the tricarboxylic acid cycle. PCL has been approved by the FDA to be used in several drug delivery and medical devices. Applications of PCL included but are not limited to resorbable and bioactive sutures [231], tissue engineering scaffolds [232], bone graft substitutes [233], and nerve guide conduits [234]. However, the hydrophobic nature and low bioactivity of PCL have limited its applications due to the slow degradation and resorption kinetics compared to other aliphatic polyesters [235].
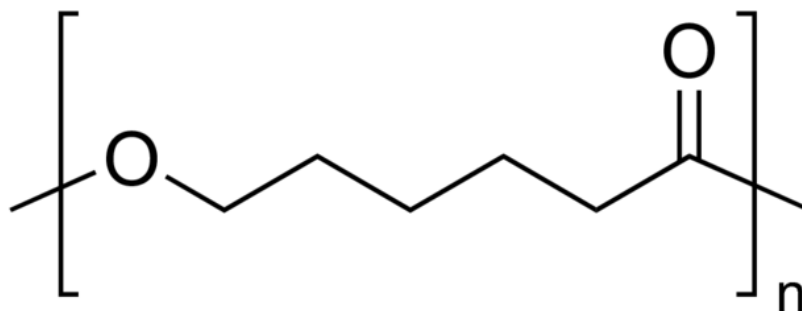
Figure 10. Chemical composition of PCL.

Degradation of PCL is primarily mediated by lipase cleavage of ester groups followed by intracellular degradation controlled by macrophages once PCL has a low molecular weight. The average molecular weight of PCL ranged from 3,000 to 80,000 g/mol [236]. Total degradation of PCL can take between two to four years depending on the starting molecular weight of the device [237]. Additionally, the rate of hydrolysis on PCL constructs can be altered by introducing lactones or glicolides via copolymerization [238].

In order to overcome the hydrophobic nature of PCL, several strategies have been developed to functionalize its surface to induce cell attachment without altering the mechanical properties or degradation profile of the material. Among these techniques, plasma treatment (or plasma deposition) is one of the most attractive and versatile techniques. Plasma treatment does not require any chemical crosslinking nor complex activation method to incorporate functional groups into the surface of PCL constructs [239], [240]. This technique is based on the exposure of the polymer construct to an ionized gas. The nature of the gas would dictate the chemical properties of the nm coating created on the surface. For example, oxygen plasma would generate a hydrophilic surface due to the deposition of OH groups, whereas fluorine plasma generates a hydrophobic surface [241].

Regarding skin applications, PCL has been mostly used in conjugation with natural components such as collagen, and elastin [242]. However, the development of ultra-thin wound dressings [243] and the incorporation of bioactive compounds [244] [245] have proved that PCL has the potential to be used as a non-adhesive and non-absorbent wound dressing.

In recent years, the introduction of micro and nano topographies within tissue engineering scaffolds has become more relevant to mimic as closely as possible the tissue structure and cell microenvironment. Microfabrication techniques have allowed scientists to introduce complexity within the scaffolds to study and improve certain aspects of tissue regeneration. Here electrospinning and microstereolithography were chosen to fabricate tissue engineered scaffolds with stem cell-like microenvironments.

8. Microfabrication for tissue engineering

Microfabrication techniques involve the construction of structures, patterns, or topographies that range in the micrometric scale (or nanometric for several applications). The first attempts at controlling and understanding the relation of spatial distribution and cell behavior started with the introduction of fibrous environments to mimic the ECM [246], [247]. The most common fabrication techniques include soft-lithography, phase separation, additive manufacturing, and electrospinning. Each of these techniques provides advantages and challenges such as available materials, versatility for 3D constructs, and production cost to consider when fabricating tissue engineering scaffolds [248], [249].

8.1.   Electrospinning: A fabrication technique for fibrous scaffolds

Electrospinning is an advanced manufacturing process (from the electro-hydrodynamic techniques family) derived from the technique known as electrospraying, in which high electrostatic forces are used to form solid polymer droplets. In comparison with electrospraying, the electrospinning process generates fibers from a range of micro and nanometres. The electrospinning process involves electrohydrodynamic interactions within a liquid droplet to generate a jet, followed by stretching and elongation to create a fiber. At the beginning of the electrospinning process, the liquid is extruded to generate a pendant droplet as a result of the surface tension of the liquid. By electrifying the droplet, the electrostatic repulsion on the surface charges and deforms the droplet to finally being ejected [250], [251].

The basic electrospinning set up consists of a high voltage source with positive polarity and negative polarity connected to a grounded collector, and a polymer solution loaded into a capillary through which a syringe pump would feed the liquid to form a pendant drop at the tip at a constant and controllable rate [250], [252]. Figure 11 shows a schematic of the basic electrospinning set up.
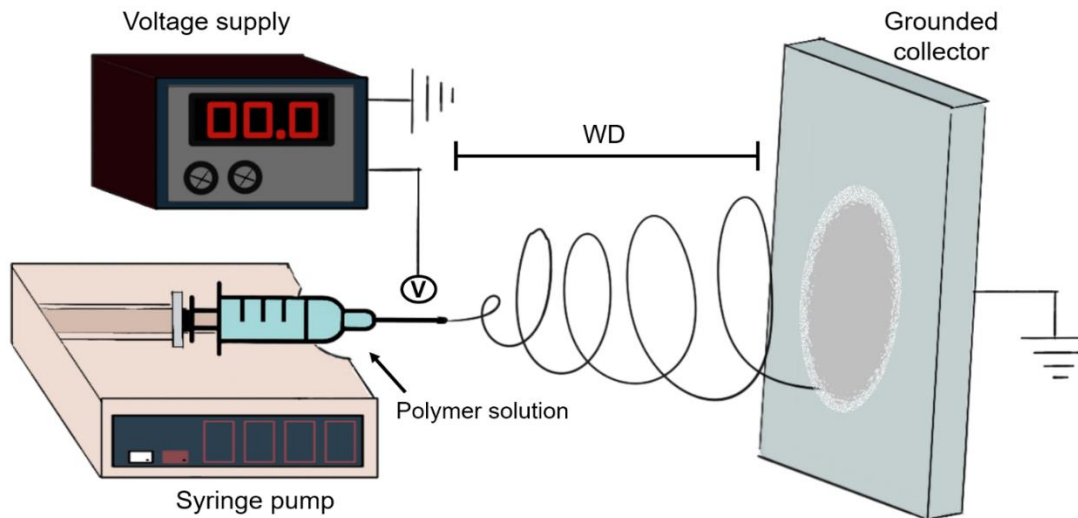
Figure 11. Schematic of a basic vertical electrospinning set up.

As the pendant drop of polymer solution becomes highly electrified by the voltage supply, the induced charges are distributed over the surface. These electrostatic forces deformed the drop into a conical shape known as Taylor cone. The amount of voltage required for this phenomenon is related to the physicochemical properties of the polymer solution. Once the voltage overcomes the threshold value of the polymer solution, the electrical forces disrupt the surface tension of the droplet and create a jet of solution from the tip that is targeted to a grounded metal collector. As the jet travels to the collector, the solvent evaporates and a nonwoven mat is formed [226].

Organic polymers are the most common materials used for electrospinning. To electrospin an organic polymer is necessary to create a dissolution using appropriate solvents to achieve a homogeneous solution without degradation. The use of these basic polymer solutions is referred commonly to as conventional electrospinning or solution electrospinning. The success of solution electrospinning depends on the interactions between the polymer solution and the process parameters. In general, two main requirements are needed to create electrospun fibers from

polymer solution: i) the polymer should have a sufficiently high molecular weight (as low molecular weight limits the chain entanglement), and ii) a suitable solvent to create a homogeneous polymer solution [250].

The parameters of the electrospinning process play a critical role in fiber morphology and distribution; thus, its understanding and control are key to achieve specific distributions and mimic the structure of the tissue. These parameters are classified into solution, process, and ambient parameters, and separately they control different outcomes in the electrospun fibers. However, the complex physicochemical polymer-polymer and polymer-solvent interactions (viscosity, surface tension, conductivity) in both the polymer solution and the tip of the needle, create a dynamic environment that does not make it possible to standardize a formula for all electrospinning processes [253].

Additionally, because of their high surface area, electrospun fibers are exceptional drug delivery carriers that enable encapsulation, adsorption, or basic functionalization. Specifically, encapsulating drugs is an efficient delivery method that commonly releases from the bulk matrix of the fibers and can be controlled by diffusion/degradation mechanisms of the polymer and the drug. Moreover, due to the high porosity and pore interconnectivity of the fibrous electrospun, drugs can diffuse from the construct after release [254]. These advantages over the traditional single dosage make electrospun fibers attractive carriers for the sustained delivery of drugs in tissue engineered scaffolds [251], [255], [256], wound dressings [257]–[259], and buccal or cardiac patches [260]–[262].

Electrospinning has been used for several applications including nanosensors, drug delivery, enzyme immobilization, protective military equipment, cosmetic industry, and scaffolds for tissue

engineering technologies [226]. Research in tissue engineering has explored alternatives to regenerate tissue by mimicking the fibrous components of the cellular environment. ECM fibers exhibit diameters between 10 nm and 300 nm, making possible to create biocompatible fibrous matrices made from electrospinning to produce a more complex 3D environment. These fibrous scaffolds showed advantages in comparison with 2D cultures in regard of cell behaviour [254]. Although these nanometric diameters are difficult to achieve with conventional electrospinning, fibroblast and keratinocyte migration and adhesion have been reported with the most achievable fiber diameters of 1-10 µm [34], [230].

The high porosity and structural properties of nanofibers have been proved to enhance cell differentiation, adhesion, and proliferation. Synthetic and naturally derived materials can be processed to achieve different physicochemical properties, biodegradability rates, compatibility, and mechanical strength. However, high molecular weight above the electrospun threshold and problems with solubility are challenges in the electrospinning of most natural polymers [263].

8.2. Stereolithography

The incorporation of novel 3D micro-additive manufacturing techniques such as stereolithography, 3D printing, and fused deposition modeling, has allowed scientists to create pattern surfaces for several applications. Stereolithography (SLA) was introduced as a micrometer resolution technique in 1993 by implementing a laser spot of a few micrometers. This UV laser radiates the UV-curable photopolymer, solidifying it and creating layer thickness of 1-10 µm [264], [265]. From this general method, two different techniques have been established, the laser based method and the digital light projection. The average resolution of most commercial STL systems is about

50 µm with techniques such as 2-photon polymerization being capable of features smaller than 500 nm [266] [267].

Laser-based methods are often referred to as additive manufacturing (AM) techniques and are based on CAD layer-by-layer processes. In the case of stereolithography, a photosensitive polymerization resin is used in conjugation with UV light [265]. The use of STL for biodegradable devices was first reported by Masuda et al. using photocurable PCL and trimethylene carbonate to create microscale features [268].

Patterned surfaces with a resolution of nano or micrometers can be used as collectors for electrospinning, thus creating complex designs that encourage the assembly of electrospun fibers to mimic topographical cues in different tissues. The first attempt of combining AM with other fabrication techniques was reported by Ortega et al. [269], creating PLGA electrospun membranes into collectors that were fabricated using microstereolithography, and present micropockets to enhance corneal repair. Further studies have explored the use of this technique in bone healing applications using modified membranes for mesenchymal stromal cells [270], and topographically control collectors fabricated using selective laser melting and poly(3-hydrroxybutyrate-co-3-hydroxyvalerate (PHBV) electrospun fibers, to mimic the rete ridges in the skin [271]. This approach of controlling the fibrous environment of the scaffold while providing micro topographical cues is a promising strategy to imitate as much as possible the stem cell niche.

9.   Introducing complexity within electrospinning membranes

The basic electrospinning setup uses a static plain collector to create nonwoven mats. Recently, several researchers have reported specialized collectors designed to create electrospun fibers with specific architectures for several applications. Theron et al. was a pioneer in the creation of

orientated and aligned polyethylene oxide (PEO) nanofibers, using a sharp-edged wheel as a collector to create parallel arrays of fibers with defined distances between them [272], [273]. Ma et al. have explored the creation of electrospun scaffolds with microstructural cues for skin regeneation, using a combination of radially-aligned fibers, square arrayed microwells, and structural cues, through the use of stainless steel pins and beads [274]. Table 5 shows different approaches that have been used with electrospinning to introduce topographical cues into tissue engineered scaffolds to mimic the stem cell microenvironment.

Table 5 Summary of tissue engineered scaffolds fabricated with electrospinning to replicate the micro and nano spatial cues of the stem cell niche.

Application	Polymer	Outcome	Ref
Developing fibrous membranes with controlled microenvironments to study MSC behavior	SLM metallic collectors used as templates for PCL fibers	Three different topographies were tested with dimensions 667, 1038, and 1168 µm. Average fiber diameter of $1.8 - 2.2$ µm	[270]
Design artificial limbal stem cell niches using biodegradable electrospun rings containing microfeatures	Polyethylene glycol diacrylate (PEGDA) collectors used with PLGA 50:50 fibers	Constructs of 1.2 cm diameter and of 0.36 mm thickness containing U-shaped micro pockets of 150–300 µm diameter made of microfibers of ~3.5 µm in diameter.	[269]
Use patterned scaffolds to simulate the anisotropic and multiscale architecture of cardiac tissue, to	Teflon-coated silicon wafer patterned collector use with a blend of	Fibrous constructs with an average fiber diameter of 1.2 µ with three different patterns tested: Two arrays of parallel	[275]

promote cardiac cell alignment	poly(glycerol sebacate) (PGS) and PCL	grooves of 10 μm in diameter, and square-shaped features of 100 μm.	
Developing a new *in vitro* model in which to study epithelial stem cell behavior	Poly(3-hydrroxybu-tyrate-co-3-hydroxyvalerate (PHBV) fibers patterned using a PEGDA template	Fibrous bilayer constructs with an average fiber diameter of 750 nm. The micropattern layer was made of square or rectangular features of 200 – 1000 µm in width and 200 – 500 µm in depth.	[271]
Create a platform to mimic the cellular microenvironment of hMSCs	Oxygen plasma treated PDMS microfluidic device with carboxyl group modified PU fibers	Microfluidic chip with randomly orientated nanofibers of 200–500 nm diameter.	[276]
Study the use of a sandwich-type scaffold to promote re-epithelialization	Stainless steel collector coated with plasma treated PCL polymer fibers	Random and aligned fibers with microwells of 200 – 280 µm in depth. No fiber diameter was reported.	[274]
Developing a hybrid scaffold to study chondrogenic differentiation of hMSCs based on protein and gene expression	Composite of a thermosensitive PEG-PNIPAAm gel and PCL fibers	Electrospun scaffold of ~11 µm fiber diameter encapsulated in a mold-less hydrogel.	[277]

Mimicking the *in vivo* anatomy of human skin may reduce healing times due to the interaction of microniches with keratinocytes and their expression of Iβ1. Changes in gene expression have been

identified by comparing keratinocytes seeded on flat membranes against collagen fibril membranes that resemble the morphology of human dermis [40], [44], [278]. These findings are key to understanding how microtopographic features enhance wound healing. Although the creation of multilayer electrospun scaffolds has been previously reported [271], [279], [280], the incorporation of topographical cues and delivery of proangiogenic agents is a novel alternative to address insufficient vascularization and tissue integration.

The versatility of PLGA and PCL fibers as drug delivery systems allows for the incorporation of bioactive compounds that can support skin regeneration during wound healing. Although the concepts of drug delivery and topographically control scaffolds have been introduced individually in tissue engineered constructs, to the best of our knowledge, this is the first attempt to incorporate proangiogenic agents and 3D microfeatures into a multilayer electrospun scaffold. The outcome of this study has the potential to provide an effective and *novel* treatment for wound healing that addresses key challenges of vascularization and wound healing.

10. Hypothesis and general aims

The hypothesis on which this research project was based is that:

- The introduction of topographical cues into electrospun scaffolds to mimic the morphology of rete ridge stem cell niche as well as the delivery of angiogenic and bioactive compounds could significantly improve skin regeneration by creating a 3D environment that cells would be able to repopulate and preserve rete ridges that control keratinocyte stemness.

The general aim of this study is to develop a hierarchical fibrous scaffold for aiding skin tissue regeneration via the introduction of intricate topographies that resemble the rete ridges stem cell niche morphology and via the delivery of proangiogenic agents to enable tissue development and nutrient distribution.

The general specific aims of this research project are:

- To fabricate fibrous scaffolds that mimic to a degree the structure of the ridged topography present in the DEJ, known as rete ridges.

- To assess the *in vitro* effects on metabolic activity and proliferation of human dermal cell lines when exposed to different concentrations of 2dDr, E2, or AV.

- To load 2dDr, E2, or AV into random and topographically controlled fibrous scaffolds and to explore their angiogenic potential of using the chick chorioallantoic membrane assay.

- To test the potential of topographically controlled fibrous scaffolds to generate features that resemble the rete ridges using tissue engineered skin models.

The experimental objectives planned to achieve these aims are described in each of the experimental chapters.

Chapter III. Fabrication and characterization of random and topographically controlled electrospun scaffolds

1. Introduction

Fibrous membranes have been attractive options for tissue engineering constructs due to their capacity to mimic the extracellular (ECM) environment in terms of fiber distribution and size as well as porosity. [281]–[285]. Electrospinning is arguably one of the most used techniques to fabricate fibrous scaffolds with interpore connectivity, high surface-to-volume ratio, and nano-to-micron fiber diameter. A traditional electrospinning setup allows for control of fiber diameter and alignment; however, novel methods have been developed to allow for further control of fiber deposition and morphology. Some of these novel methods have combined additive manufacturing and electrospinning to create fibrous environments that can closely mimic the native stem cell microenvironment [271], [274], [286].

The parameters of the electrospinning technique can be divided into solution parameters and process parameters. A balance between these variables is necessary to achieve the conditions needed to create an electrospun jet. However, most of the electrochemical reactions that produce a stable and constant polymer jet are controlled by the surface tension, electrostatic interactions, and solvent properties. Therefore, the polymer solution plays a key role in fiber morphology, and by selecting specific solvents and polymer combinations, it is possible to load organic and inorganic compounds into the fibers for different applications [287].

The most common method for electrospinning as a drug delivery platform is the use of blend electrospinning which incorporates the drug directly into the solvent system. However, this

technique requires a deep understanding of the drug's stability and solubility. Understanding these parameters is key to achieve a successful electrospinning process and when selecting a solvent system [288]. Although it is possible to electrospun polymers and drugs that are not soluble in the same solvent using emulsion electrospinning (including co-axial electrospinning, or surface modification), introducing the drug directly into the solvent has the highest loading rate compared to other methods [254], [287], [289]. Additionally, co-axial electrospinning or fiber surface modification increases the complexity of the fabrication of the scaffold. Therefore, selecting miscible solvents that can dissolve both the polymer and the bioactive compound is a simple and versatile approach to create electrospun scaffolds that can be fabricated with a conventional electrospinning setup.

A plethora of drugs and bioactive compounds has been loaded into electrospun scaffolds, including growth factors, small sugars, and inorganic compounds. For skin regeneration applications, factors for reducing inflammation, avoiding infection, and aiding vascularization are key for scaffold design [24]. To determine the biological effects of electrospun scaffolds loaded with bioactive compounds, it is important to first select the proper biocompatible material, optimize and determine the maximum amount of bioactive compound that can be electrospun and characterize the effects in the physicochemical properties of the scaffold when these compounds are loaded into the electrospun fibers.

Combining micropatterned collectors and electrospinning to fabricate microtopographical environments within electrospun scaffolds require that the electrospinning jet produces non beaded fibers that can be collected directly on the surface of the collector [290], [291]. Any disturbances in the electrospinning jet could cause polymer aggregates or the accumulation of fibers outside the patterned collector, thus challenging how these fibers mimic the morphology of the collector and

59

limiting the standardization of these scaffolds. Furthermore, because the electrospinning process is also affected by the presence of the collector, it is necessary to further optimize the electrospinning parameters to suit this new application.

The potential of 2-deoxy-D-ribose (2dDr), 17β-estradiol (E2), and aloe vera (AV) as proangiogenic agents has been explored before using random electrospun scaffolds. However, the introduction of bioactive compounds into topographically controlled scaffolds to improve cell response is yet to be developed. This chapter described the development and characterization of topographically controlled electrospun scaffolds (TCES), as well as the fabrication of random electrospun scaffolds (RES) and TCES, loaded with 2dDr, E2, or AV. The *in vitro* effects of these bioactive compounds in solution on skin cell types is described in detailed in Chapter IV as it was critical to first characterize the performance of the scaffolds as drug delivery devices

1.1. Aim and objectives

The aim of this experimental chapter is to study the feasibility of fabricating topographically controlled electrospun scaffolds (TCES) using poly(lactic-*co*-glycolic) acid (PLGA) and polycaprolactone (PCL) to mimic the morphology of the rete ridges in the skin as well to evaluate the use of RES and TCES as drug delivery carriers for 2dDr, E2, and AV; and the effects of plasma treatment on TCES morphology fabricated using PCL. In order to achieve this aim, the following objectives were established:

- Fabricate PLGA and PCL RES with and without 2dDr, E2, or AV.

- Design and fabricate micropatterned 3D printed collectors.

- Fabricate PLGA and PCL TCES with and without 2dDr, E2, or AV.

- Investigate the changes in physical properties of RES when 2dDR, E2, or AV were added.

- Investigate the changes in chemical properties of RES when 2dDR, E2, or AV were added.

- Observe the changes in fiber morphology and diameter when PCL TCES were exposed to air plasma treatment.

- Study changes in fiber morphology and diameter when TCES were loaded with 2dDr, E2, and AV.

- Characterize the release of 2dDR, E2, or AV from PCL and PLGA RES.

2. Materials and Methods

2.1. Manufacture of 3D printed collectors

The ridged topography of the collectors was designed using ThinkerCAD© (AutoDesk, USA) online software. A uniform surface of ridges was drawn on a 20 x 20 mm collector using Equation (1).

$$z(x, y) = \cos\left(\frac{n}{3} \times x\right) \times \cos\left(\frac{n}{3} \times y\right) \times A \qquad (1)$$

Equation 1. Mathematical representation of the patterned collectors designed. *A* and *n* represent constants that control the amount and height of the ridges, respectively.

Several designs were tested to study the performance of the collectors and their capacity to create topographically controlled electrospun scaffolds (TCES) by changing the values of *X*, *Y*, *n*, and *A*, and scaling as required. *X* and *Y* dictate the size of the collector, n controls the number of ridges present on the pattern, and A dictates the height of the ridge (Figure 12).

Table 6 shows the dimensions of all the patterns created for this study. The different sizes fabricated cover the range of 50 – 400 µm and 50 – 200 µm in width and depth, respectively of the native rete ridges fond in human skin. The patterns with features outside this range were used to study the feasibility of the technique.
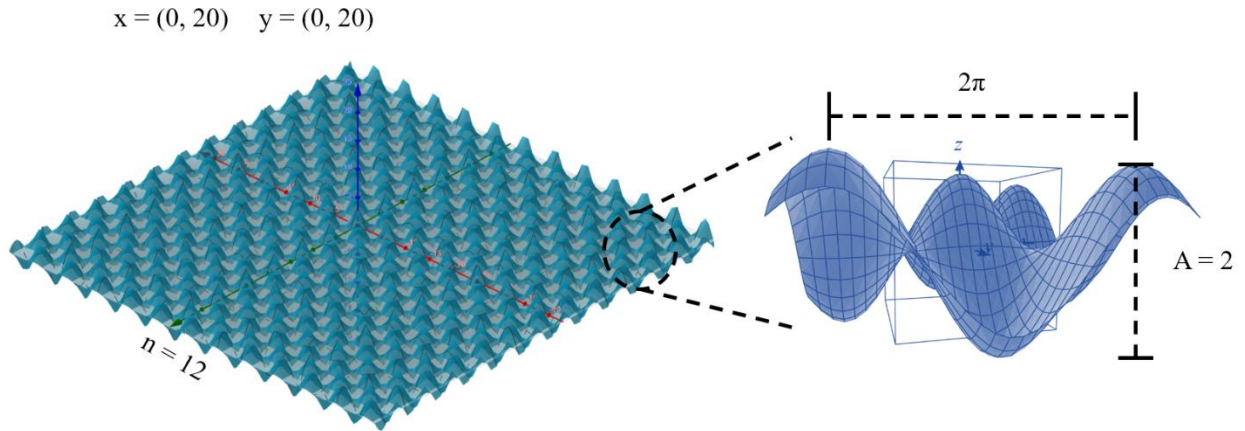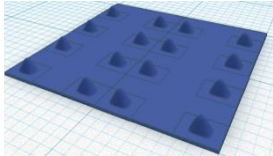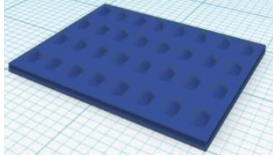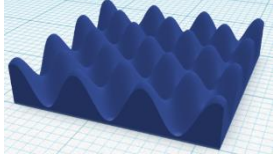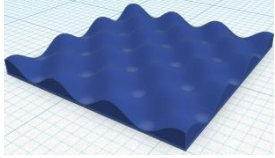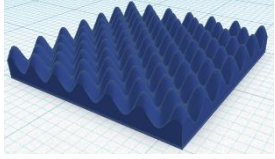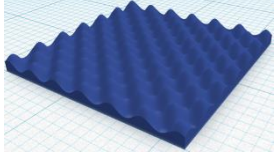
Figure 12. Representation of the 3D surface designed to mimic the ridge topography of the DEJ. The variable n determines the number of ridges while x, y, and A control the size and the height of the surface.

Table 6. Dimensions of 3D printed patterned collectors.

Code	Design	Width	Height
C1		2000 µm	1000 µm
C2		2000 µm	500 µm
C3		1248 µm	800 µm

C4		1248 µm	400 µm
C5		624 µm	400 µm
C6		624 µm	200 µm

A FormLabs 2 SLA printer was used to manufacture the collectors using grey resin methyl methacrylate polymer mixed (RS-F2-GPGR-04, Formlabs, USA). To avoid damage to the microstructure, supports were created at the base of the collectors using the PreForm software (version 3.3.1, Formlabs). Two isopropanol washes of 10 min were performed to remove uncured resin immediately after printing. Collectors were then left to air dry for 10 min followed by a UV curing process ($\lambda = 405$ nm) using a Form cure (FH-CU-01, Formlabs) for 30 min at 60 ℃. After curing, the supports were carefully removed from the base using tweezers.

2.1.1. Scanning electron microscopy (SEM) for patterned collectors

3D printed collectors were coated with a 10 nm gold layer (SC 500A, Emscope) and mounted on aluminum pin stubs (AGG301, Agar scientific) with carbon tabs (AGG3347N, Agar scientific) and analyzed under a HITACHI SEM (FE SEM, JSM-6500F, JEOL; and FE/VP SEM, TM3030Plus, HITACHI). Spot size and voltage were set up at 3.5 nm and 10 kV respectively for all samples. ImageJ software v. 1.48 from NIH (National Institutes of Health, USA) [292], was

used to measure the size of the microfeature on the SEM micrographs. Two independent tests were performed by triplicate for each topography (N = 2, n = 3).

2.2.   Preparation of polymer solutions

2.2.1. Preparation of polymer solutions without bioactive compounds

Polymer solutions of PCL (440744, Sigma-Aldrich) (Mn = 80,000 g/mol), and PLGA with a 50:50 (PURASORB®, 5004A, Corbion) and 75:25 (P1941, Sigma) glycolic:lactic unit ratio were prepared prior to the electrospinning process. The solvent system was composed of dichloromethane (DCM) (D/1850/17, Fisher) or a mixture of DCM and dimethylformaldehyde (DMF) (227056, Sigma) accordingly. Weight/weight (w/w) solutions were prepared by dissolving 1 g of polymer with their solvent system as specified in each experimental chapter. Table 7 shows the polymer solutions prepared for the electrospinning process. Solutions were covered in parafilm and left in a see-saw rocker (SSL4, StuartTM) for 24 hours at room temperature (RT) to homogenize the polymer solution.

Table 7. Polymer solutions without bioactive compounds were coded with an "A" followed by a numerical value.

Code	Polymer	w/w Polymer concentration	Solvent 1	Solvent 2	Solvent proportion (Solvent 1: Solvent 2)
A1	PLGA 50:50	15%	DCM	N/A	N/A
A2		20%	DCM	DMF	4:1
A3		20%	DCM	DMF	3:1
A4	PLGA 75:25	15%	DCM	DMF	3:1
A5		20%			1:1
A6		20%			3:1
A7	PCL	8%	DCM	DMF	3:1
A8		12%	DCM	N/A	N/A
A9		12%	DCM	DMF	3:1

2.2.2. *Preparation of polymer solutions with bioactive compounds*

Polymer solutions of PCL and PLGA with a 50:50 and 75:25 glycolic:lactic unit ratio were prepared prior to the electrospinning process. The solvent system was composed of a mixture of DCM and DMF (unless otherwise specified). The bioactive compounds tested were 2dDr (121649, Sigma), E2 (E8875, Sigma), and lyophilized AV (*Aloe Barbadensis)* powder (MI0301, Makers Ingredients).

With the exception of AV, weight/weight (w/w) solutions were prepared by dissolving the bioactive compound (by itself or in combination), on the polar fraction of the solvent system (DMF) by shaking the solution for 10 min. For AV, dimethyl sulfoxide (DMSO) (10103483, Fisher) was used as a primary solvent at a concentration of 200 mg/mL and mixed properly for 5 min using a micropipette before adding the DMF. The amount of bioactive compound was added in terms of percentage weight (% wt.) in relation to the amount of polymer. Once dissolved, DCM was added in the right proportion to complete the solvent system. w/w polymer solutions were prepared by dissolving 1 g of polymer (PLGA or PCL) with their respective solvent system. Table 8 shows the polymer solutions prepared for the electrospinning process. Solutions were left in a see-saw rocker (SSL4, StuartTM) for 24 hours at RT to homogenize the polymer solution.

Table 8. Polymer solutions with bioactive compounds. Each polymer solution was coded with a "B" followed by a numerical value.

Code	Polymer	w/w Polymer concentration	Solvent system	Bioactive compound	Bioactive compound % wt.
B1	PLGA 50:50	20%	DCM:DMF (3:1)	2dDr	5%
B2					8%
B3					10%
B4					15%
B5				E2	5%
B6					10%
B7	PLGA 75:25	20%	DCM:DMF (3:1)	2dDr	1%
B8					10%

B9		8%	DCM:DMF (3:1)	2dDr	8%
B10					8%
B11				2dDr	10%
B12			DCM:DMF 3:1		15%
B13	PCL			E2	8%
B14		12%			10%
B15			DCM:DMF + DMSO (3:1) + 500 µL	AV	5%
B16					10%
B17				AV + 2dDr	10% + 8%

2.3. Electrospinning of fibrous scaffolds

Fibrous scaffolds were fabricated using electrospinning. The polymer solutions mentioned on section 2.2 were electrospun under the same environmental RT conditions (18 - 22 °C). The differences between the fabrication of RES and TCES are shown in the following sections.

2.3.1. Electrospinning of RES

A vertical electrospinning set-up was used to fabricate both RES and TCES (Figure 13). To fabricate RES, 1 mL syringes with 20 gauge 1" syringe tips (8001213, Fisnar) were loaded with ~1.1 mL of the polymer solution. The syringe was loaded into a syringe pump (Harvard apparatus PHD 22/2000) and the syringe cap was connected to a voltage supply. The static collector was covered with silicon-coated paper and placed at a distance of 12 cm from the needle tip. Process

parameters (flow rate and voltage) are detailed for every solution using their code as a reference in Table 9. Electrospun membranes were stored at 4ºC in sealable bags.
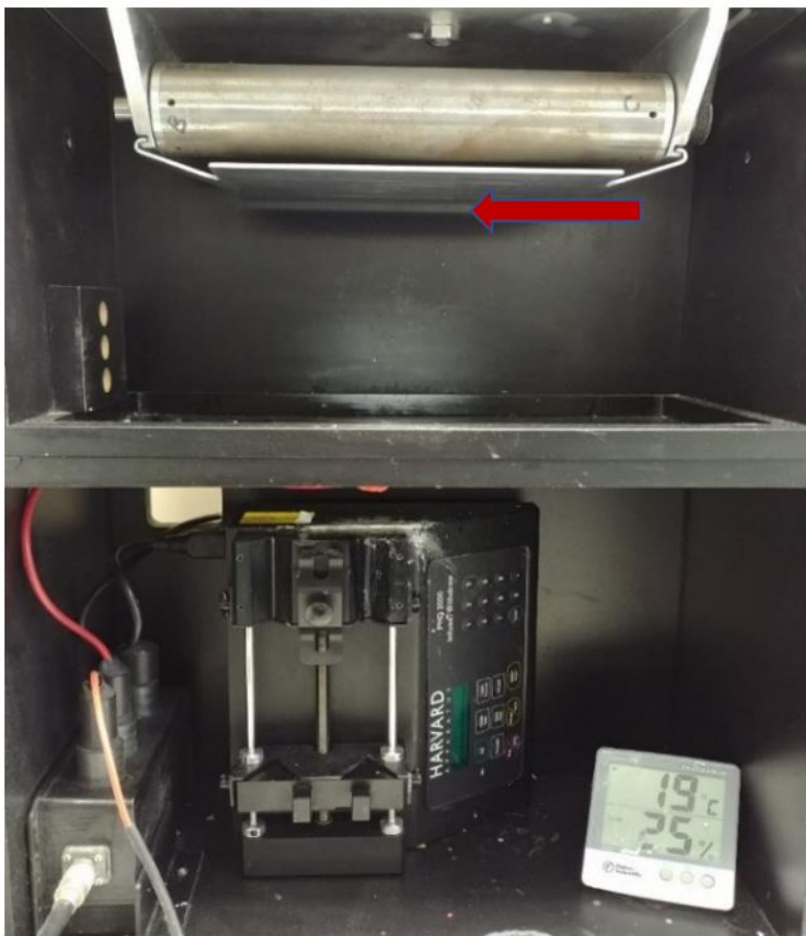
Figure 13. Custom-made horizontal electrospinning set up. The electrospun mats were collected using the plain static collector shown in the image (red arrow). Temperature and humidity were monitored during the electrospinning process.

Table 9. Electrospun process parameters for electrospun solutions with and without bioactive compounds.

Code	Voltage	Flow rate	Code	Voltage	Flow rate
A1	10 – 20 kV	1 – 3 mL/h	B1	21 – 22 kV	1 – 2 mL/h
A2	17 – 18 kV	0.5 – 2 mL/h	B2		
A3	18 – 20 kV	0.5 – 2 mL/h	B3	22 – 24 kv	1 – 1.5 mL/h
A4	18 – 20 kV	0.3 – 1 mL/h	B4		
A5	15 – 18 kV	0.3 – 2 mL/h	B5	19 – 21 kV	1 – 2 mL/h
A6	20 – 22 kV	0.3 – 0.5 mL/h	B6		
A7	18 – 20 kV	1 – 4 mL/h	B7	21 – 23 kV	0.3 – 0.5 mL/h
A8	18 – 22 kV	1 – 4 mL/h	B8	22 – 24 kV	0.3 – 0.4 mL/h
A9			B9	19 – 20 kV	1 – 4 mL/h
			B10	20-22 kV	
			B11		
			B12		
			B13	19-21 kV	
			B14		
			B15	21 – 23 kV	
			B16		
			B17	18 – 19 kV	3 – 4 mL/h

2.3.2. Electrospinning of TCES

Patterned collectors and electrospinning were combined as described by Ortega et al. [269], [271] to manufacture the TCES. Figure 14 shows a schematic of the manufacturing method. First, our patterned collectors were placed on top of the grounded metal collector coated with silicon-coated paper. Conductive carbon adhesive discs (AGG3347N, agar scientific) were used to hold the patterned collectors in place.
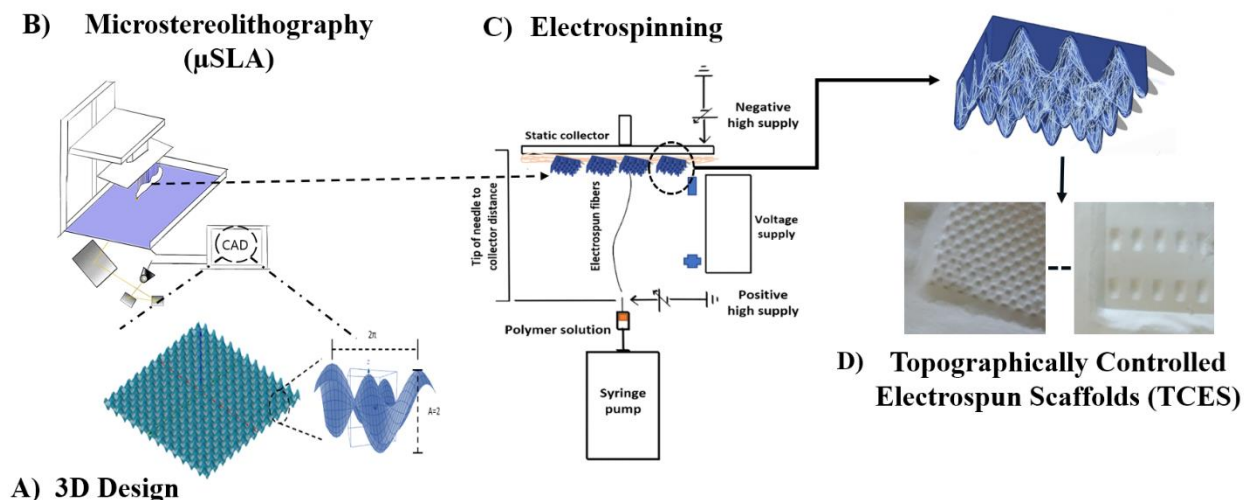
Figure 14. Schematic for fabrication of TCES. The micropatterned collectors were fabricated using μSLA and placed into a vertical electrospinning set up to generate the topographically controlled scaffolds.

Collectors were set at a distance between 12 and 13 cm from the syringe tip. The polymer solutions used to create TCES were all made using the DCM:DMF solvent system (except for the AV solution which requires 500μL of DMSO). For each batch of four patterned collectors, 1 mL of the polymer solution was loaded and electrospun using the appropriate flow rate and voltage. Due

to the presence of the collectors, the electrospinning process parameters were different from those of the plain electrospun membranes with the same polymer solution.

Table 10 shows the parameters used for each solution. Approximately 200 µL of polymer solution were electrospun on top for every collector. The resulting TCESs were cut before being peeled from the patterned collector to avoid structural damage to the scaffold.

Table 10. Polymer solutions and electrospinning process parameters used to fabricate TCES (See Table 7 and Table 8 for the full description of each solution).

Code	Polymer	w/w Polymer concentration	Bioactive compound and % wt	Voltage	Flow rate
A3	PLGA 50:50	20%	N/A	19 kV	0.5 – 2 mL/h
B3			10% 2dDr	21 – 23 kV	
A7	PCL	8%	N/A	18 kV	3 – 5 mL/h
B9			10% 2dDr	19 kV	
A9		12%	N/A	19 kV	
B10			8% 2dDr	20 – 21 kV	
B11			10% 2dDr		
B14			10% E2	19 kV	
B16			10% AV	21 – 22 kV	

2.4. Plasma deposition

Air plasma (AP) deposition was used to increase hydrophilicity of the PCL scaffolds for cell culture. Both TCES and RES were placed in a Zepto plasma cleaner (Diener electronic) using a glass petri dish. The chamber was set with low-power parameters of 10 W (radio frequency of 40 KHz). Air was used for the plasma deposition. Exposure times of 2 and 5 minutes were tested. Right after plasma treatment, scaffolds were placed inside sealable bags and stored at 4 °C. Silica gel sachets (103804, Merck) were placed inside the sealable bags to remove any moist that may affect the electrospun membranes.

2.5. Characterization of fiber morphology and diameter

RES and TCES samples of 5 x 5 mm were coated with a 10 nm gold layer (SC 500A, Emscope) and mounted on aluminum pin stubs (AGG301, agar scientific) with carbon tabs (AGG3347N, agar scientific). Scaffolds were analyzed under a HITACHI SEM (FE SEM, JSM-6500F, JEOL; and FE/VP SEM, TM3030Plus, HITACHI). Spot size and voltage were set up at 3.5 nm and 10 kV respectively for all samples. ImageJ software v. 1.48 from NIH (National Institutes of Health, USA) [292], was used to measure fiber diameter on the SEM micrographs. Three independent tests were performed by duplicate for each topography (N = 3, n = 2) (for TCES only), and three independent tests with 15 fibers measured for each micrograph to evaluate fiber diameter (N = 3, n = 15) for (RES and TCES). Additionally, the performance of the patterned collectors to create topographical cues on the TCES was evaluated using the following Equation (2):

Reproducibility factor = Size of feature (scaffold) / Size of feature (collector)   (2)

Equation 2. The reproducibility of the TCES was evaluated by calculating the ratio between the size of the feature on the scaffold and the size of the feature on the collector. To approximate the

73

height of the topographical cues a trigonometrical approach has used. A schematic of the method used is shown in Figure 15.
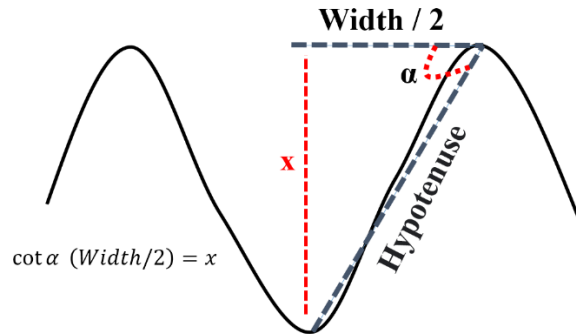
Figure 15. Trigonometric method used to calculate the height of the topographical cues (x). The α angle and the hypothenuse length values were taken from the original CAD designs, whereas the width was measured from the SEM micrographs.

2.6. Characterization of mechanical properties – uniaxial tensile testing

Mechanical testing on RES was performed using a motorized force tester MultiTest-dV (Mecmesin, UK). A 25 N load cell (ELS 25 N, Mecmesin, UK) was used to perform a uniaxial tensile test. Vector Pro software (version 6.2.0, Mecmesin, UK) was used to control the force tester and for data analysis. Samples were cut as square pieces of 8 mm width by 22 mm length to use 5 mm of each side to grip the samples and allowed 12 mm gap between the grips (as shown in Figure 16. The test speed was set up as 6 mm / min and the thickness of the samples was measured to normalize the data. Data for the percentage of maximum elongation and maximum stress versus strain were recorded for each scaffold. Two independent tests were performed by triplicate for each material (N = 2, n = 3)
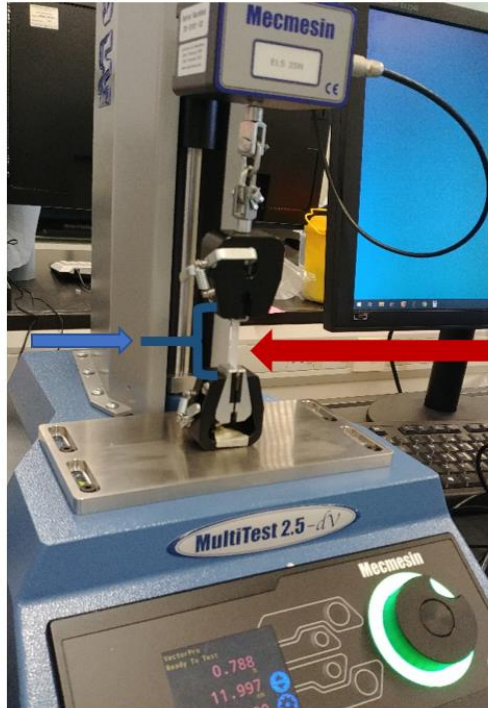
Figure 16. MultiTest mechanical testing machine loaded with a plain electrospun scaffold (red arrow). The distance between the grips (12 cm) is highlighted (blue arrow).

2.7. Morphological changes of RES

A study of the shrinkage ratio of RES in an aqueous environment was performed using PBS at human body temperature. Samples were cut as squares of 1.5 x 1.5 cm using a scalpel and each sample was placed inside a bijou containing 5 mL of PBS and incubated at 37.5°C. Samples were photographed and measured using a digital camera and ImageJ software after 6, 24, and 48 h of incubation. The shrinkage of the scaffold was calculated as a change in surface area in relation to the original 2.25 cm^2 area. Samples were not reused for different time points. Two independent tests were performed by triplicate for each material (N = 2, n = 3).

2.8.   Surface properties of scaffolds by water contact angle

A drop shape analyzer DSA100E (KRÜSS, Germany) was used to calculate the water contact angle (Θ) as shown in Figure 17. To evaluate this contact angle, RES samples were cut as 8 by 8 mm squared pieces and a 5 µL droplet of distilled water was placed on top. A digital camera and KRÜSS advance software were used to capture and process the data from the droplet respectively. Two independent tests were performed by triplicate for each material (N = 2, n = 3).
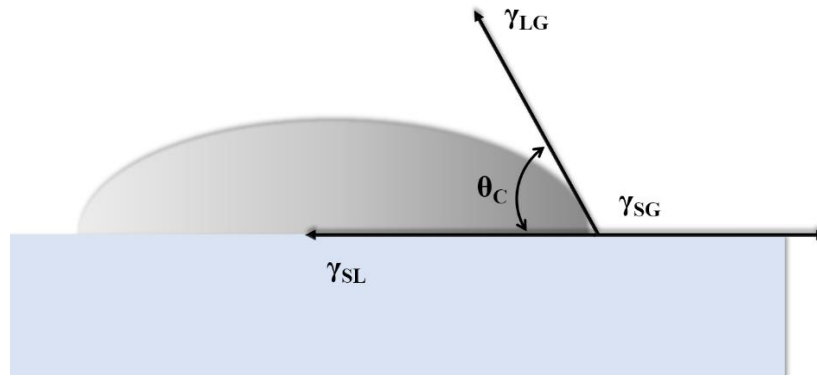
Figure 17. Schematic of how water contact angle (Θ) is calculated from the interactions between the solid-liquid (γ_{SL}), liquid-gas (γ_{LG}), and solid-gas (γ_{SG}) interfacial energies.

2.9.   Thermal properties using differential scanning calorimetry

The thermal performance of the scaffolds was evaluated by differential scanning calorimetry (DSC). Thermograms of RES (N=2, n=3) were obtained using a PerkinElmer DSC 4000 (PerkinElmer, UK). Nitrogen gas flow was of 20 mL/min and a scanning rate of 10 °C from 30 °C to 100 °C (holding 30 °C for 1 min). The weight of all the samples was recorded prior to the DSC analysis.

2.10. Release profile of bioactive compounds from electrospun scaffolds

In order to characterize the releasing profile of bioactive compounds from the RES, a non-accumulative study was performed for every bioactive compound, in which each time point is represented by a sample compared to an accumulative study where a sample is used for several time points. For all membranes loaded with bioactive compounds, squared pieces were cut and weighted. Using individual bijou containers, 7 ± 0.5 mg of the electrospun membrane were placed in for every time point, with a total of 5 samples per time point and 3 experimental repeats (N = 3, n = 5). At time zero, 5 mL (for 2dDr) or 3 mL (for E2 and AV) of PBS were added to each sample and then incubated at 37.5 °C. The difference in volume is due to the sensitivity of the quantification method. PBS samples were collected in duplicate for each time point and stored at 4°C for the compound to be quantified at the end of the experiment.

Known concentrations of every bioactive compound were prepared in PBS to be quantified using their respective assays to create a standard calibration curve. The concentrations for the calibration curve and were selected based on maximum concentrations reported by Dikici et al. and Shafaat et al [159], [166]. For all experiments, two independent tests and 5 samples for each time point were measured (N = 2, n = 5). The different quantification methods performed for each bioactive compound are described in the following sections.

2.10.1. Release of 2dDr from RES using Bials's orcinol

To quantify 2dDr, a pentose sugar assay known as Bial's Orcinol was performed [293]. First, working solutions of 0.05% w/v FeCl3•6H2O (F2877, Sigma) in 6M hydrochloric acid (HCL) (Fisher Scientific, UK) (solution [A]), and a 422 mM orcinol monohydrate (O1875, Sigma) in 95% ethanol (Fisher Scientific, UK) (solution [B]) were prepared prior to the assay. The final working

solution [C] was prepared on the day of the experiment mixing both solutions at a 15:1 A:B ratio. 500 µL of the sugar solution were mixed inside an Eppendorf tube with 500 µL of solution [C]. The sugar + solution [C] samples were incubated for 20 minutes at 100°C using boiling water. Small incisions were made on top of the Eppendorf tubes to avoid pressure to burst the container. After incubation, samples were left 10 minutes to cool at RT. 200 µL of each sample were transferred in triplicate to a non-tissue culture 96-well plate (Thermo Scientific, UK). Absorbance values at a 600 nm wavelength were obtained using a Bio-Tek ELx800 spectrophotometer and KC4 software (version 3.3, Bio-Tek Inc.).

2.10.2. Release of E2 from RES using a spectrophotometric method

The release of E2 was quantified by transferring the 1 mL of the unknown solution to a quartz cuvette and measuring absorbance at 272 nm [159], using a UV spectrophotometer (6305, Jenway^{TM}).

2.10.3. Release of AV from RES using a UV spectrophotometric method

The release of AV from the RES was quantified using a UV spectrophotometric method. The amount of AV was quantified by measuring optical absorbance of 200 µL of the AV unknown sample at 292 nm using a Varioskan Lux UV spectrophotometer (Thermo Fisher).

2.11. Statistical analysis

GraphPad Prism software (version 9.1) was used to perform statistical analyses using one-way and two-way analysis of variance (ANOVA) as applicable, followed by Tukey's multiple comparisons tests. In all cases, p values <0.05 were considered statistically significant. Differences in sample

size are due to the nature of each experimental procedure. For example, a bigger sample size (N=3, n=15) was selected to better represent the distribution of fiber diameter.

3. Results

3.1. Electrospinability of RES with and without bioactive compounds

The polymer solutions were studied for their capacity to generate a continuous electrospinning jet to generate a fibrous mat. Table 11 shows the results of all the polymer solutions tested and a brief description of their feasibility to produce RES without bioactive compounds. Table 12 shows the electrospinning results for RES loaded with bioactive compounds.

Table 11. Results of electrospinability for RES without bioactive compounds. The – sign represents a failed electrospun solution while the + represents a successful electrospun solution. Please refer to Table 7 for the full description of every solution.

Code	Polymer	Result	Comments
A1		—	Unstable polymer jet. Solution eventually blocks the syringe.
A2	PLGA 50:50	—	Polymer solution is possible to electrospun for the first 10 – 15 min. Unstable jet even at high voltages and low flow r
A3		+	Polymer jet stable for long electrospinning sessions. Worked across different flow rates and voltages
A4		—	Unstable polymer jet. Solution eventually blocks the syringe.
A5	PLGA 75:25	—	
A6		+	Polymer jet stable for long electrospinning sessions. Only worked at low flow rates.

Code	Polymer	Result	Comments
A7		+	
A8	PCL	+	Polymer jet stable for long electrospinning sessions. Worked across different flow rates and voltages
A9		+	

Table 12. Results of electrospinability for RES with bioactive compounds. The – sign represents a failed electrospun solution while the + represents a successful electrospun solution. Please refer to Table 8 for the full description of every solution.

Code	Polymer	Bioactive compound	Result	Comments
B1			+	Polymer jet stable for longer electrospinning sessions. Works across different flow rates and voltages.
B2		2dDr	+	
B3	PLGA 50:50		▬	Polymer jet unstable for longer electrospinning sessions. Only works at high voltages.
B5		E2	+	Polymer jet stable for long electrospinning sessions. Works across different flow rates and voltages.
B6			+	
B7	PLGA 75:25	2dDr	+	Polymer jet stable but only at high voltages and flow rates below 0.3 mL/h.
B8			▬	Polymer jet unstable. Not possible to electrospun.
B9	PCL	2dDr	+	Polymer jet stable for long electrospinning sessions. Works across different flow rates and voltages.
B10			+	

B11			+	
B12			+	Polymer jet stable but fibrous scaffolds have aggregates of polymer due to uneven process
B13		E2	+	Polymer jet stable but fibrous scaffolds have aggregates of polymer due to uneven electrospinning.
B14			+	
B15		AV	+	Polymer jet stable but fibrous scaffolds have aggregates of polymer due to uneven electrospinning. Polymer jet became unstable after ~ 800 µL.
B16			+	
B17		AV + 2dDR	+	Polymer jet stable but fibrous scaffolds have aggregates of polymer due to uneven electrospinning.

These results showed that electrospinning solutions of DCM:DMF were more versatile when using PCL than PLGA 50:50 or PLGA 75:25. This behavior was evident for PLGA 75:25 which required periods of up to 4 hours to electrospun 1 mL of the solution even without the introduction of 2dDr, which made the electrospinning a challenging process due to the formation of beads and polymer droplets. Because of this behavior, it was decided not to continue with the use of PLGA 75:25 for the fabrication of RES loaded with other bioactive compounds or for the fabrication of the TCES. PLGA 50:50 solution A1 was selected as the most stable for the fabrication of PLGA RES, with B1, B2, B5, and B6 showing behavior that encouraged further testing.

However, PLGA 50:50 as a material for the fabrication of RES and TCES was limited. This limitation is further explored in section 3.3 with a shrinkage study. Furthermore, 12% polymer concentration PCL solutions (A8 and A9) proved to be more stable than 8% PCL (A7) across several electrospinning sessions, making the 12% solutions more attractive candidates for further

studies. Following experiments with PCL RES and TCES were fabricated using this polymer concentration.

3.1.1. *Characterization of fiber morphology and diameter*

SEM was performed to observe the morphology of PLGA 50:50 RES when loaded with E2 and 2dDr. Table 17 shows a collection of micrographs of PLGA 50:50 RES, where a change in diameter is visible. Moreover, some of the fibers, within the same electrospinning parameters, showed larger fiber diameters (Figure 18.C, Figure 18.D, and Figure 18.F) compared to the pure PLGA 50:50 control.
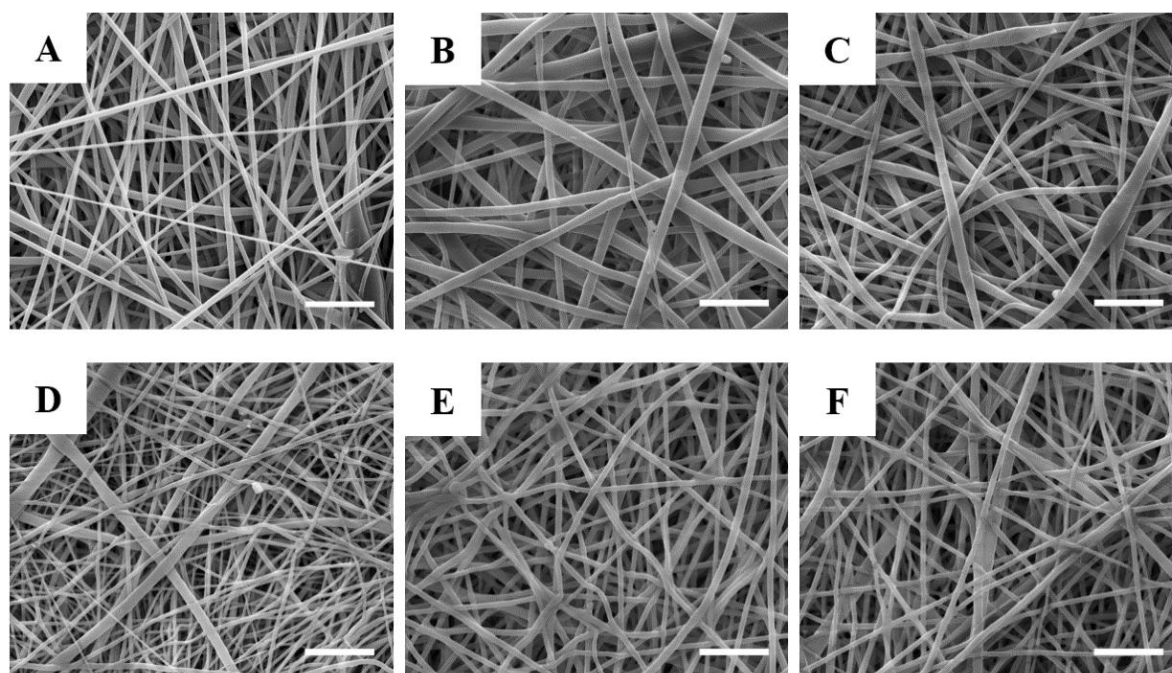
Figure 18. Micrographs of PLGA 50:50 RES with and without bioactive compounds. A) Control, B) 5% E2, C) 10% E2, D) 5% 2dDr, E) 10% 2dDr and F) 15% 2dDr. Scale bar = 10 µm.

As observed in Figure 19, fiber diameter of PLGA 50:50 RES changed depending on if E2 or 2dDr was loaded. Furthermore, fiber diameter of PLGA 50:50 RES loaded with 2dDr was significantly

different according to wt. % of 2dDr used. Fiber diameter of PLGA 50:50 RES control was significantly lower when compared to PLGA 50:50 RES 5% E2 and 10% E2.

Additionally, fiber diameter PLGA 50:50 RES control was also lower when compared to PLGA 50:50 RES 10 % 2dDr and PLGA 50:50 RES 15 % 2dDr, but not with PLGA 50:50 RES 5% 2dDr. Moreover, fiber diameter of PLGA 50:50 RES 5% 2dDr was significantly lower when compared to PLGA 50:50 RES 10 % 2dDr and PLGA 50:50 RES 15 % 2dDr. These results suggest that, when a bioactive compound is loaded into the electrospinning solution, fiber diameter changes. Furthermore, the mean fiber diameter among groups ranged between 0.5 – 1 µm.
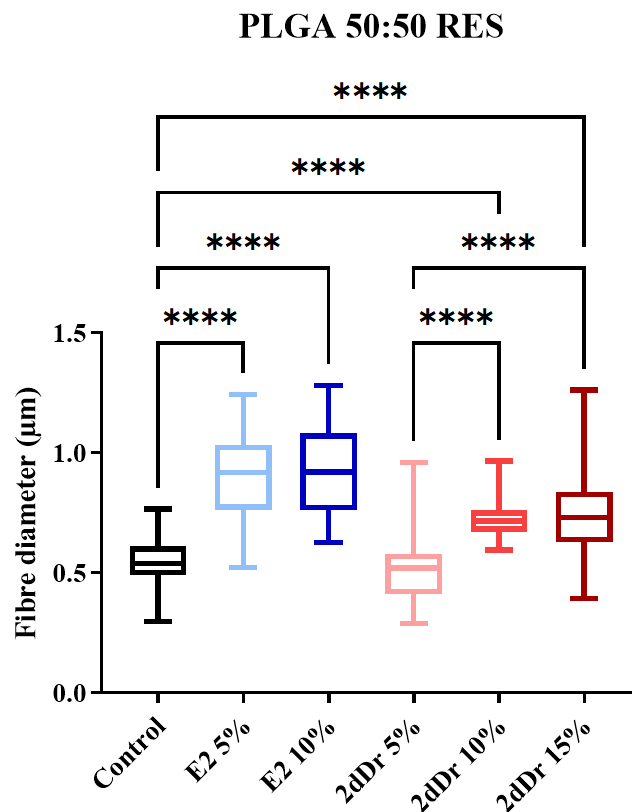
Figure 19. Box plot showing diameter of PLGA 50:50 RES loaded with 5 % and 10 % E2, and 5 %, 10 % and 15 % 2dDr. One-way ANOVA statistical analysis with Tukey comparison test. **** $p < 0.0001$. Results are shown mean $\pm$ SD. N=3, n=15.

Figure 20 shows a collection of PCL RES loaded with E2, 2dDr, and AV where different wt % concentrations were used. From Figure 20. E and Figure 20.F is visible that fiber density was different, as more space among fibers was observed. Furthermore, PCL RES loaded with aloe vera had a cotton-like texture, whereas PCL RES with either E2 or 2dDr had a paper-like texture.
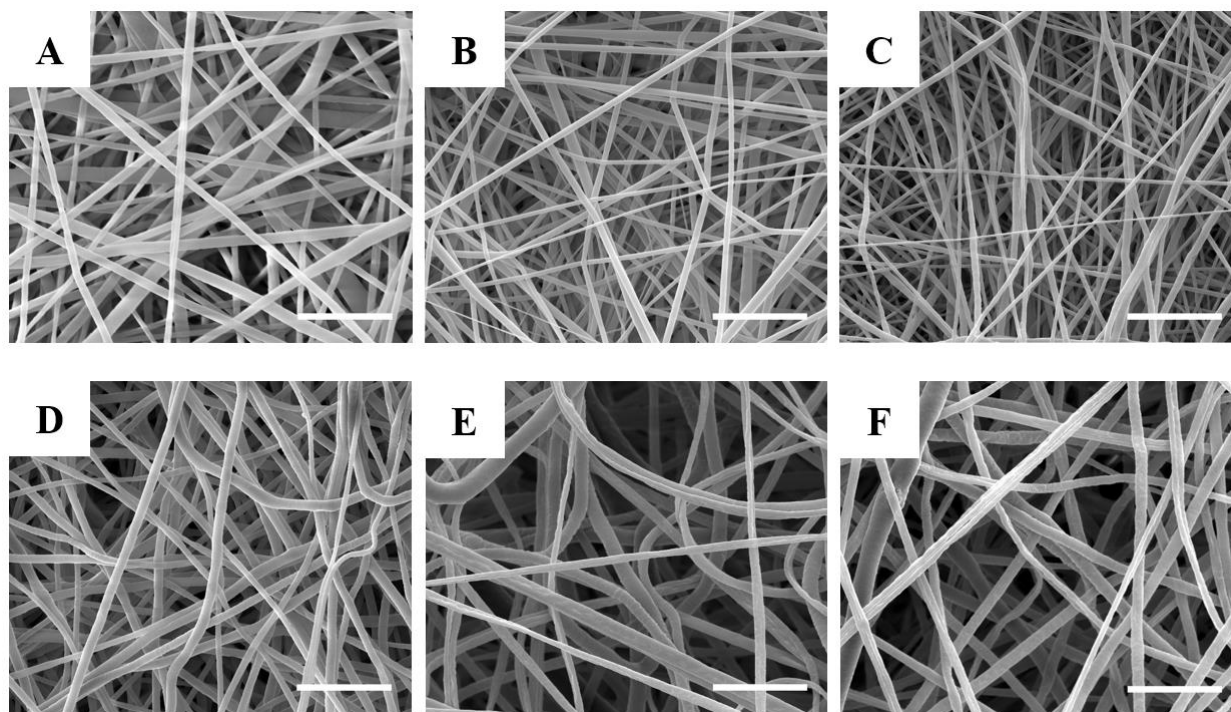
Figure 20. Micrographs of PCL RES with and without bioactive compounds. A) Control, B) 10% E2, C) 8% 2dDr, D) 15% 2dDr, E) 10% AV and F) 10% AV + 8% 2dDr. Scale bar = 10 µm.

Fiber diameter of PCL RES was different when bioactive compounds were loaded into the electrospinning solution, as shown in Figure 21. Fiber diameter of PCL RES loaded with 10 % E2 was significantly higher compared to PCL RES control. Also, the fiber diameter of PCL RES loaded with 10 % AV and PCL RES loaded with 10 % AV + 8 % 2dDr was higher compared to PCL RES control. Nevertheless, the fiber diameter of PCL RES loaded with 8% 2dDr and fiber diameter of PCL RES loaded with 15% 2dDr was not significantly different when compared to

84

PCL RES control, even though fiber diameter of PCL RES 8% 2dDr and PCL RES 15% 2dDr were significantly different between them.
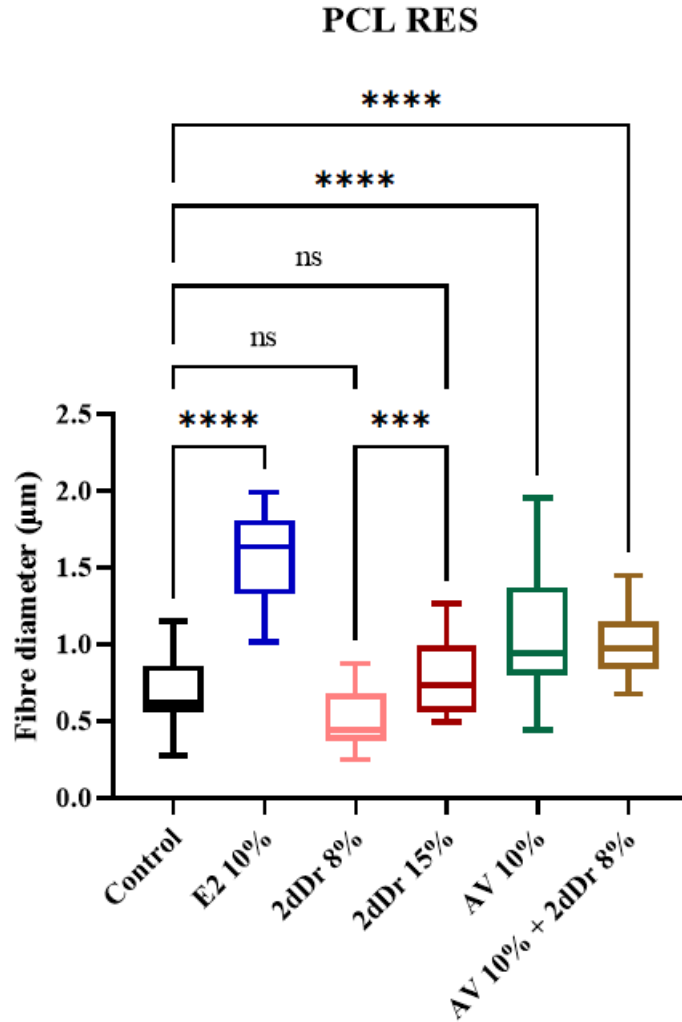
Figure 21. Box plot showing diameter of PLGA 50:50 RES loaded with 5 % and 10 % E2, and 5 %, 10 % and 15 % 2dDr. One-way ANOVA statistical analysis with Tukey comparison test. **** $p < 0.0001$, *** $p < 0.001$, ns $p \geq 0.05$. Results are shown as mean $\pm$ SD. N=3, n=15

Because of the hydrophobicity of PCL, an air plasma (AP) treatment was performed to improve cell adhesion. Figure 22 shows the difference in fiber diameter between non treated and AP treated PCL RES. Interestingly, the increase in fiber diameter after AP observed in the control PCL RES

was significantly higher than the changes found in PCL RES loaded with 2dDr, E2, or AV after AP treatment.
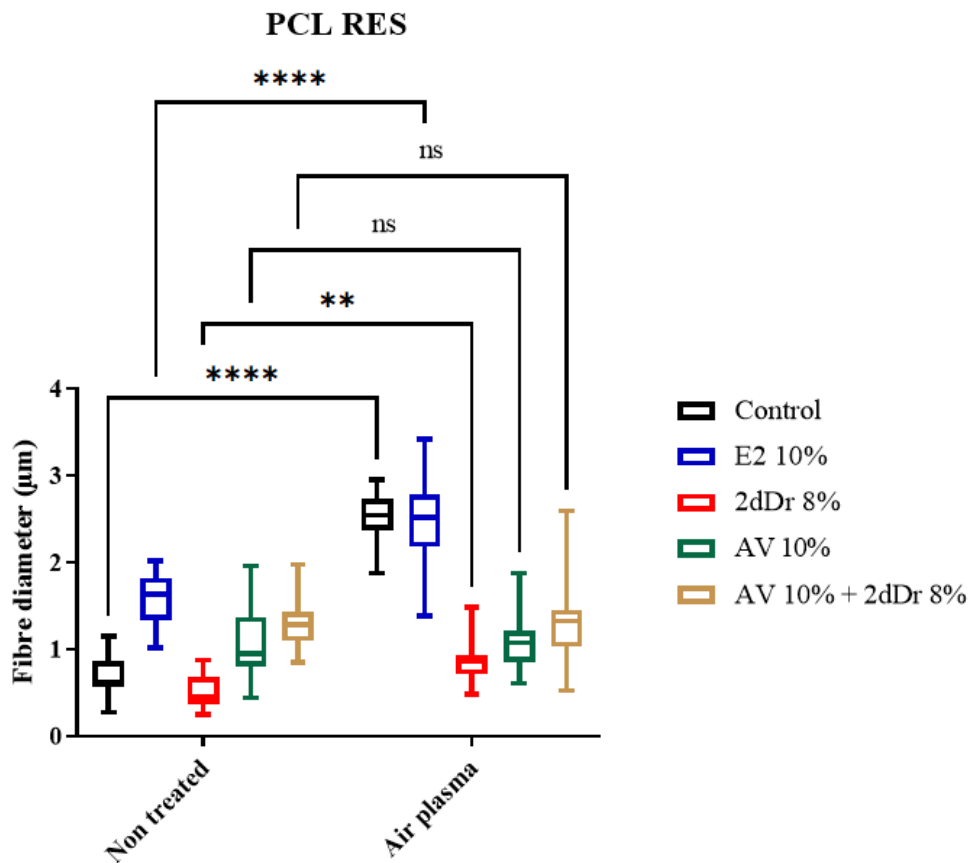
Figure 22. Box plot showing the diameter of PCL RES after and before air plasma treatment. PCL RES loaded with 8% 2dDr, 10% E2, and 10% AV were also measured to evaluate changes in fiber diameter. Two-way ANOVA statistical analysis with Tukey comparison test. **** $p < 0.0001$, *** $p < 0.001$, ns $p \geq 0.05$. Results are shown as mean $\pm$ SD. N=3, n=15

3.2. Characterization of RES chemical properties

The analysis of the DSC diagrams (Figure 23) showed similar T_m for all PCL groups, suggesting a minimal change due to the inclusion of the bioactive compounds within the fibers. The most

significant change was observed for the RES loaded with 10% AV that showed an average T_m of 3° C lower than the control. The low PCL Tg value of -60°C is not shown on the DSC diagrams due to is low clinical relevance when used as wound dressings.
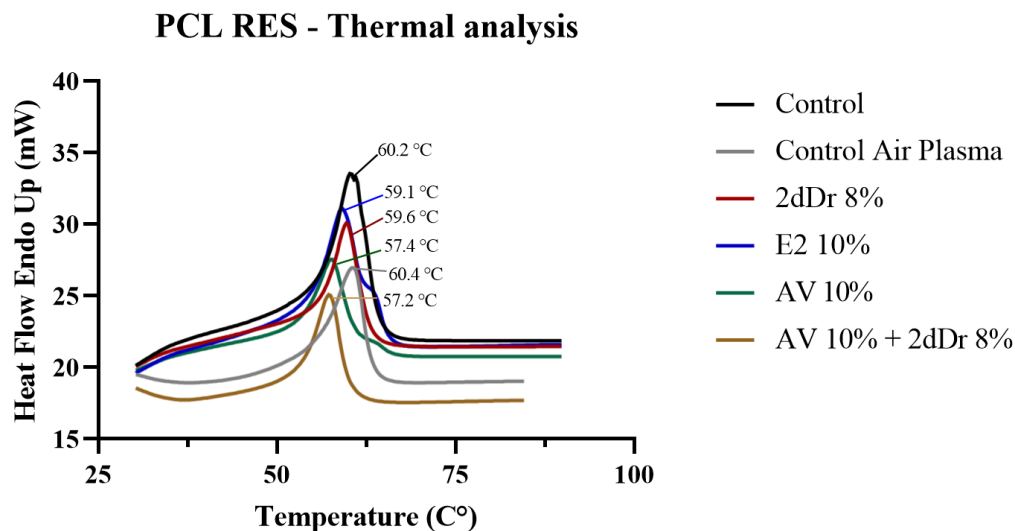
Figure 23. DSC diagrams for PCL RES loaded with 2dDr, E2, AV, or AV + 2dDr. T_m values are shown for each group. N=2, n=3.

3.3. Characterization of RES physical properties

The contact angle was measured to evaluate how hydrophilicity was modified due to air plasma treatment and by the introduction of bioactive compounds. The contact angle of non-treated PLGA 50:50 was 132° ± 8°, which was more hydrophobic in comparison to its counterpart AP treated PLGA 50:50 (119 ° ± 10 °). Moreover, contact angle non-treated PLGA 75:25 was significantly more hydrophobic than AP treated PLGA 75:25 (132° ± 5° and 45° ± 4° respectively), as seen in Figure 24. PLGA 50:50 loaded with 10 % 2dDr was more hydrophilic after air plasma treatment. Moreover, among the air plasma treated scaffolds, PLGA 75: 25 and PLGA 50:50 loaded with 10 % 2dDr were significantly more hydrophilic than PLGA 50:50. These results suggested that air

87

plasma treatment of PLGA scaffolds made the scaffolds more hydrophilic, and hence, cell adhesion would be improved. Quantification of contact angle for plasma treated samples (stored at 4°C) was carried out withing 24 h of the treatment to avoid hydrophobic recovery.
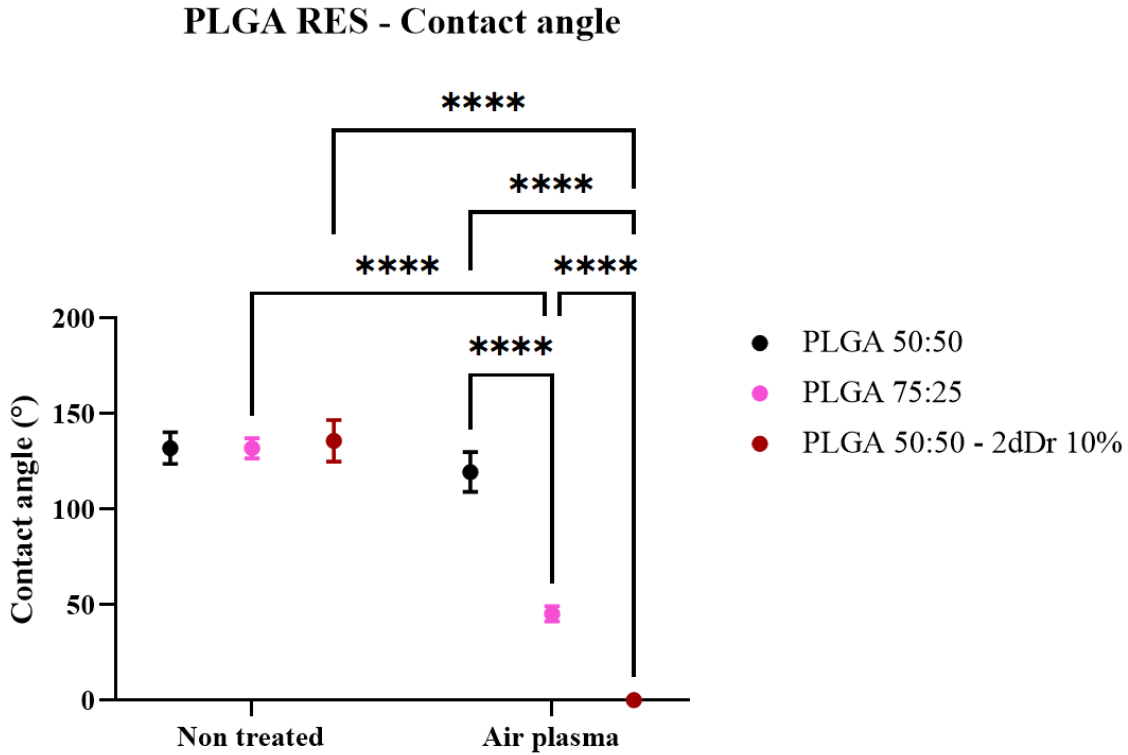
Figure 24. Plot graph showing contact angle changes in PLGA scaffolds with and without air plasma treatment. Results are shown as mean ± SD. Two-way ANOVA was used to analyze statistical differences **** $p < 0.0001$. N=2 n=3.

In contrast, PCL RES showed significant changes in contact angle when bioactive compounds were added (Figure 25). Additionally, to evaluate any effects of traces of the solvent system, a PCL RES fabricated only with DCM as a solvent was compared against the conventional DCM:DMF solvent used to fabricate both RES and TCES. Compared to the DCM:DMF control (109.5° ± 8°) the DCM control showed a higher contact angle of 132.1° ± 4°. Furthermore, RES

loaded with 15% 2dDr (128° ± 8°), 10% AV (141° ± 10°), and 10% AV – 8% 2dDr (143.8° ± 10°) showed an increase in water contact angle when compared to the DCM:DMF control. Only the 10% E2 (119.8° ± 5°) and 8% 2dDr (84° ± 9°) groups had no significant difference and a lower contact angle respectively against the DCM:DMF control. After air plasma treatment, the contact angle was 0 ° for all PCL scaffolds.
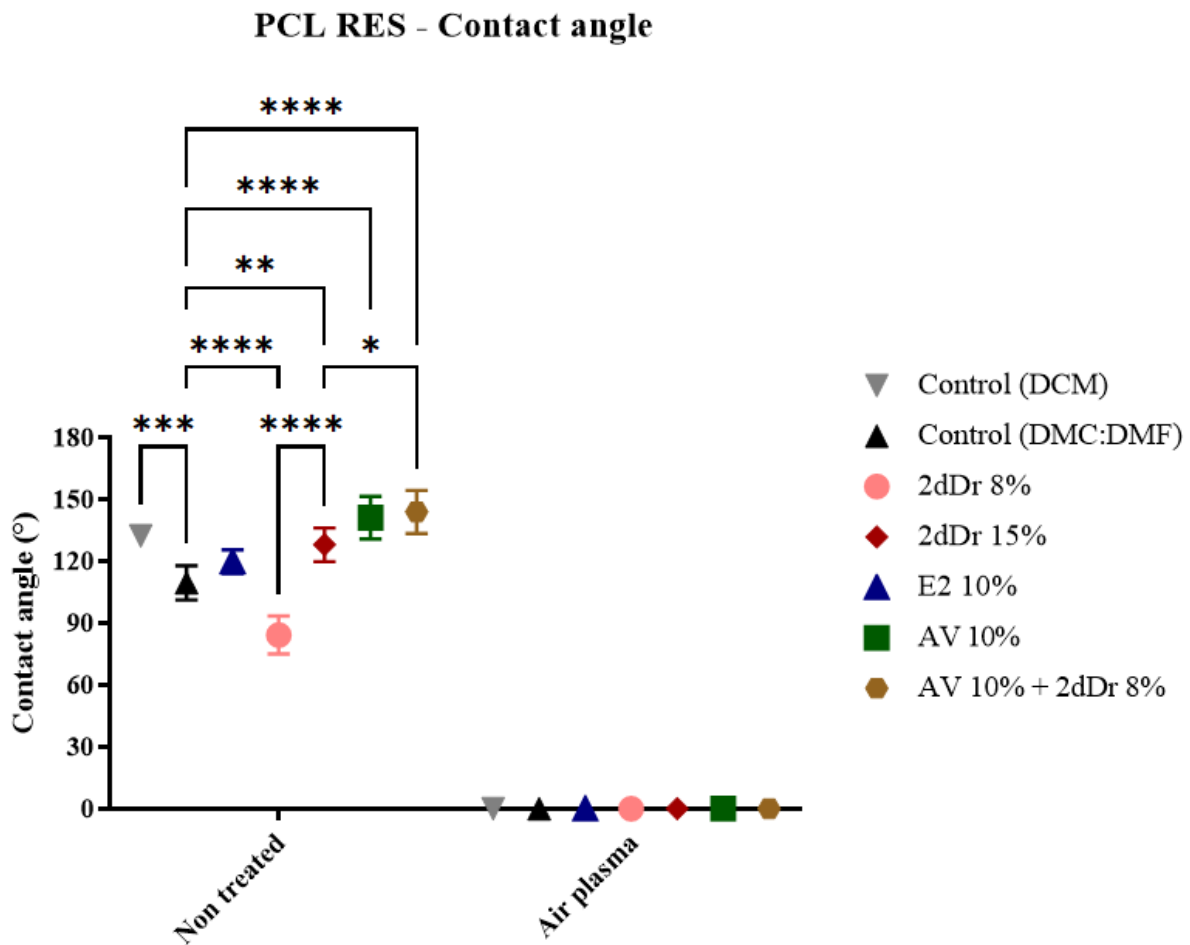
Figure 25. Plot graph showing contact angle changes in PCL scaffolds with and without air plasma treatment. Results are shown as mean ± SD. Two-way ANOVA was used to analyse statistical differences **** $p < 0.0001$, *** $p < 0.001$, ** $p < 0.01$, * $p < 0.05$. N=2 n=3.

The capacity of the PCL and PLGA to preserve the architecture of the scaffold at body temperature was evaluated by measuring the shrinkage of the RES. Figure 26 shows how PLGA and PCL scaffolds shrank when incubated in PBS at 37 °C for 6 hours, 24 hours, and 48 hours. PLGA 50:50 scaffolds, PLGA 50:50 loaded with 10 % 2dDr and AP treated PLGA 50:50 scaffold shrank 71 %, 71 %, and 72 %, respectively, during the first 6 hours. In contrast, PCL scaffolds, PCL scaffolds loaded with 8 % 2dDr and air plasma treated PCL scaffold had no shrinkage during the first 6 hours. Within 24 hours and 48 hours, PLGA scaffolds shrank 10 % more than in 6 hours. PCL scaffolds shrank up to 5 % within 24 hours and 48 hours. These results suggest that PLGA scaffolds would not be suitable for preserving microtopographical cues for *in vitro* cell culture.
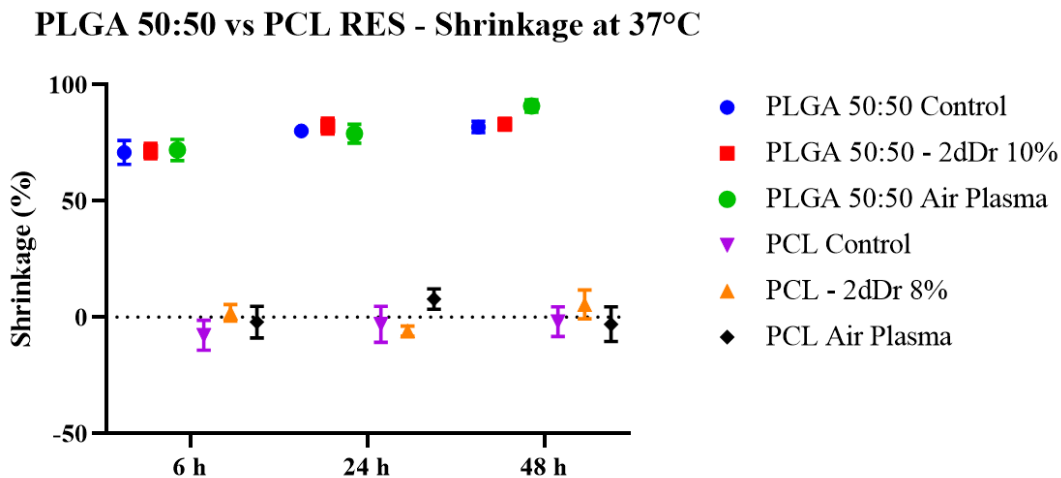
Figure 26. Plot graph showing the shrinkage of PLGA and PCL scaffold at 37 °C at 6 hours, 24 hours, and 48 hours. Results are shown as mean ± SD. N=2 n=3.

Figure 27 shows PLGA 50:50 RES and PCL RES, pure AP treated, and loaded with 8% 2dDr (AP treated and non AP treated) before incubating them in PBS at 37 °C and 5 % CO_2 (called dry sample). Then, after 6 hours PLGA 50:50 RES were reduced in size. In comparison, PCL did not

shrink after 6 hours in PBS at 37 °C and 5 % CO_2. This change in size due to temperature and not humidity was observed when PLGA 50:50 RES shrank after being incubated at 37 °C and 5 % CO_2 without the PBS while PCL RES did not undergo any morphological changes. Figure 28 shows how PCL RES original dimensions (1.5 cm x 1.5 cm) were maintained whereas the dimensions of PLGA 50:50 RES were reduced after 6 hours. However, there is no data to determine if the scaffolds swell after the incubation period.
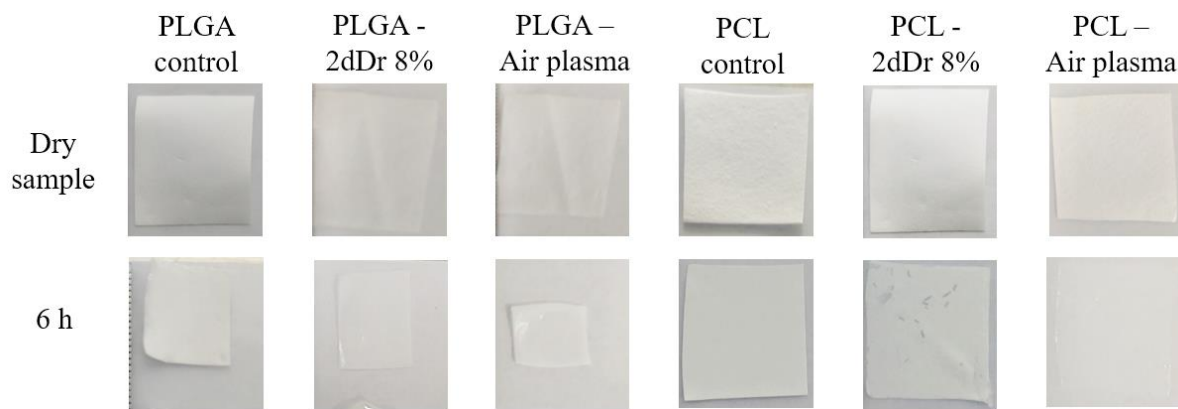
Figure 27. Images of PLGA 50:50 and PCL RES, showing that after 6 hours of being incubated in PBS at 37 °C, 5 % CO_2, PLGA RES were shrunk whereas PCL RES did not shrink.

PCL Control   PLGA Control
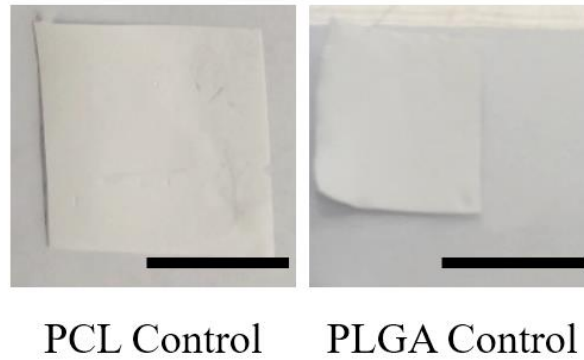
Figure 28. Images of PCL RES and PLGA RES after being incubated for 6 hours at 37 °C, 5 % CO_2. PCL RES original dimensions were maintained (1.5 cm x 1.5 cm) whereas PLGA RES dimensions decreased. Scale bar = 1 cm.

Interestingly, the opacity of AP treated PCL RES changed after being incubated in PBS at 37 °C and 5 % CO_2 for 6 hours in comparison to PCL RES with no treatment, as seen in Figure 29. AP treated PCL RES (left in Figure 29) was more transparent than non-treated PCL RES.

Figure 29. Opacity changes of PCL RES with air plasma treatment (left) and with no plasma treatment (right) after 6 hours of being incubated in PBS at 37 °C, 5 % CO_2.

Regarding mechanical strength, there was no significant difference found between the tensile strength of PLGA 50:50 RES with and without the addition of 2dDr (Figure 30).

PLGA 50:50 RES - Max stress vs Strain
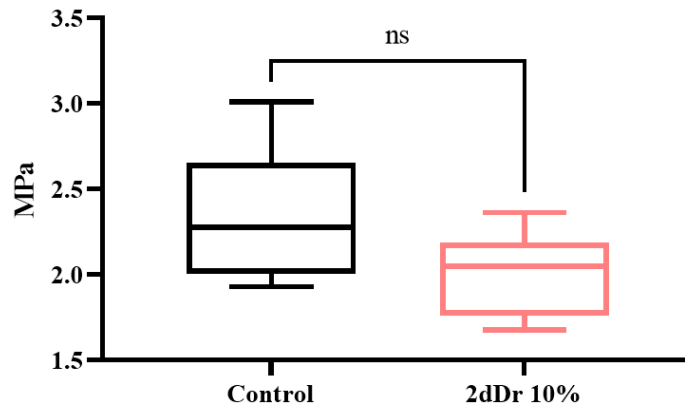
Figure 30. Box plot of tensile strength of PLGA 50:50 RES and PLGA 50:50 with 10 % 2dDr RES. One-way ANOVA was performed for statistical analysis. Results are shown as mean ± SD. ns p ≥ 0.05. N=2 n=3

Furthermore, tensile strength was also tested on the PCL RES scaffold. PCL air plasma control was significantly higher in comparison to other groups, regardless of which bioactive compound was added or if the PCL RES was prepared with DCM only or DCM: DMF only. Nevertheless, PCL control (DCM:DMF) showed no significant difference among PCL DCM, 10 % E2, 8 % 2dDr, 15 % 2dDr and 10 % AV (Figure 31). Therefore, tensile strength was not different among groups except for air plasma treated PCL RES.

PCL RES - Max stress vs Strain
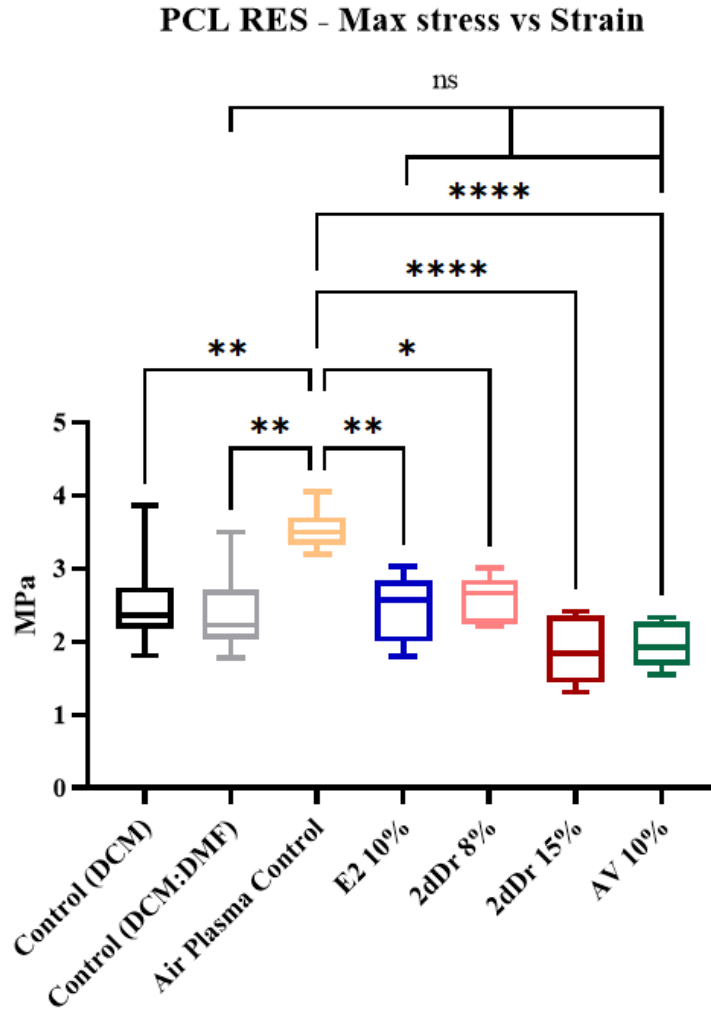
Figure 31. Tensile strength graph of PCL RES, showing the difference in tensile strength depending on the modification of the PCL RES. One-way ANOVA with Tukeys comparison post-test. Results are shown as mean $\pm$ SD **** $p < 0.0001$, *** $p < 0.001$, ** $p < 0.01$, * $p < 0.05$, ns $p \geq 0.05$. N=2 n=3.

On the contrary of what was observed regarding tensile strength, maximum elongation evaluation revealed that air plasma treated PCL RES showed significantly lower maximum elongation percentage in comparison to other PCL RES groups. Nevertheless, all non-treated PCL RES

elongate more than what was expected for our application. Table 13 shows the average thickness

of the RES used for mechanical testing.
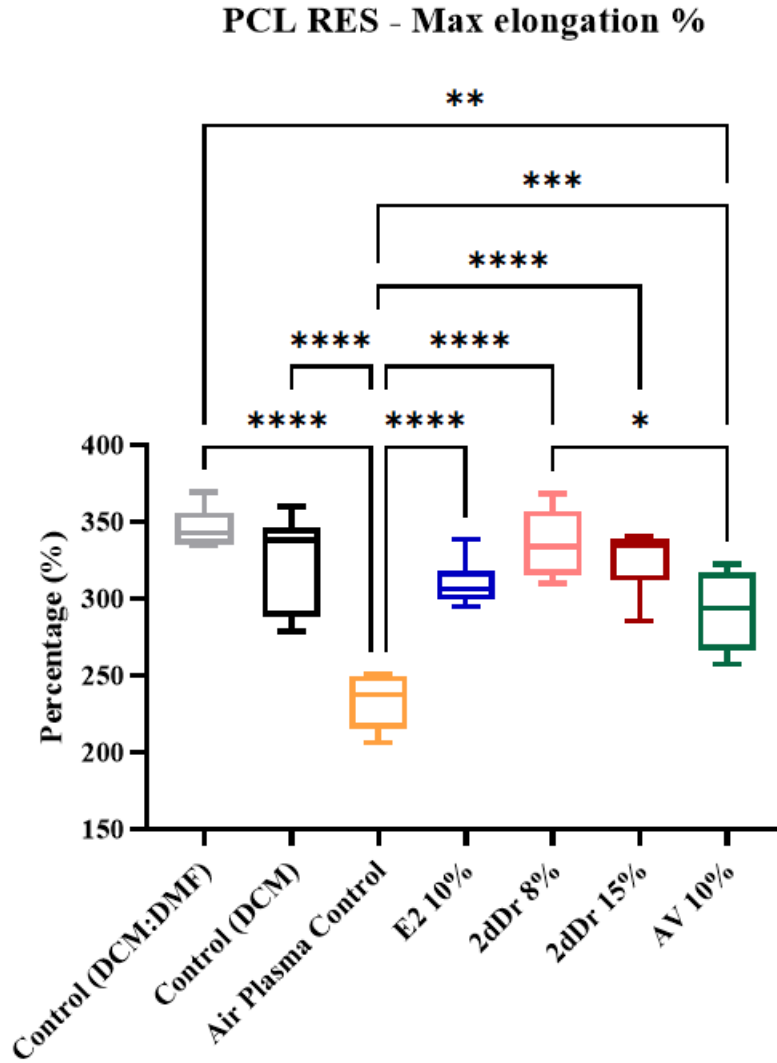
Figure 32. Maximum elongation % graph of PCL RES loaded with different bioactive compounds.

One-way ANOVA with Tukeys comparison post-test. Results are shown as mean ± SD. **** p <

0.0001, *** p < 0.001, ** p < 0.01, * p < 0.05. N=2 n=3.

Table 13. Average thickness of PLGA 50:50 and PCL RES (N=2, n=3).

RES	Average thickness (µm)	RES	Average thickness (µm)
PLGA	68 ± 7	PCL (DCM:DMF)	58 ± 7
PLGA 10% 2dDr	62 ± 5	PCL (DCM)	125 ± 14
PCL 8% 2dDr	147 ± 8	PCL – AP treated	157 ± 23
PCL 15% 2dDr	113 ± 15	PCL 10% E2	101 ± 19
		PCL 10% AV	114 ± 22

3.4.   Release of bioactive compounds from RES

Release of 2dDr from PCL RES, PLGA 50:50 RES, and PLGA 75:25 RES was tested using Bial's orcinol assay. A calibration curve was calculated of concentration (µM) against absorbance (Figure 33). Then, this calibration curve was used to quantify the release of 2dDr from PCL RES, PLGA 50:50 RES, and PLGA 75:25 RES at 1, 6, 24, 48, 168, and 240 hours.

2dDr calibration curve

$Y = 0.0003040X + 0.04915$

$R^2=0.9905$
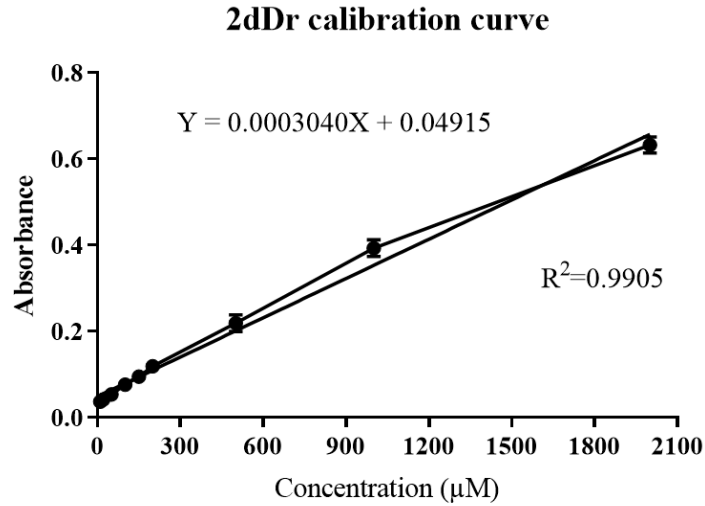
Figure 33. Calibration curve of 2dDr concentration (µM) against absorbance using Bial's orcinol assay. Results are shown as mean ± SD. N=2 n=5.

PCL RES (non-treated), PLGA 50:50 RES, and PLGA 75:25 RES loaded with 10% 2dDr were incubated in PBS at 37 °C and 5 % CO_2 for a total time of 240 hours. Release of 2dDr was measured at each time point, using a different sample each time. The results showed that most of the 2dDr was released immediately within 1 hour. However, 2dDr in solution was detectable and therefore did not degrade after 240 hours, as observed in Figure 34.

2dDr (10% wt.) released from RES
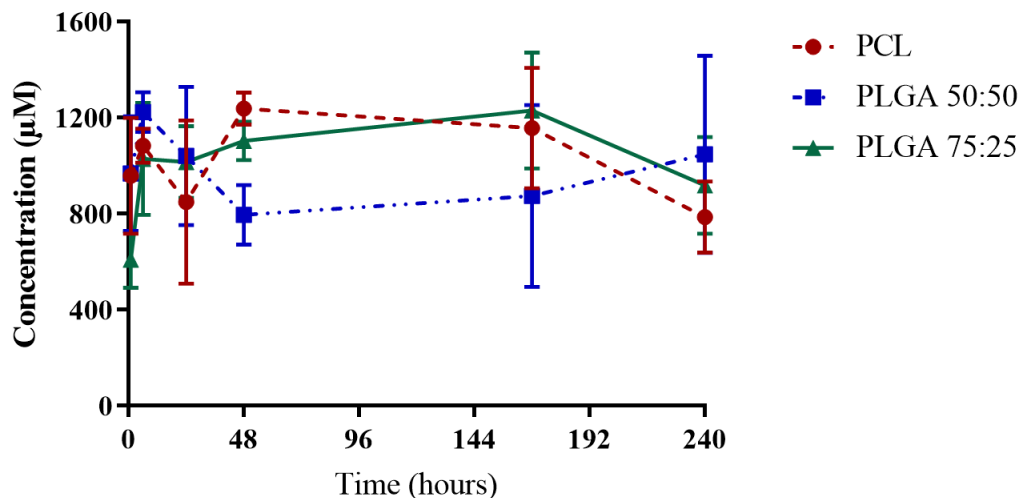
Figure 34. Non-accumulative release of 2dDr from PCL RES, PLGA 50:50 RES, and PLGA 75:25 RES for 1 hour, 6 hours, 24 hours, 48 hours, 168 hours, and 240 hours at 37.5 °C. Results are shown as mean ± SD. N=3 n=5.

Figure 35 shows a close-up of the release of 2dDr graph in Figure 34 displaying the 1 hour, 6 hours, 24 hours, and 48 hours time points and with the addition of a PCL-AP treated group. Given the 7 ± 0.5 mg weight of the scaffolds, the maximum concentration in 5 mL PBS should be 1050 ± 70 µM. A release of 2dDr between 500 µM and 850 µM is observed in the 1 hour time point. Then, a slight increase is seen at 6 hours. At 24 hours, a decrease in the release of 2dDr is observed, whereas, at 48 hours, the release of 2dDr increased for all groups except for PLGA 50:50 RES. These results highlight that 2dDr was released within 48 hours. Additionally, to evaluate any loss of 2dDr before and after the electrospinning process, the amount of sugar present in an entire PCL RES with 2dDr was measured. Our results showed that from the theoretical 8.8 mg of sugar-loaded on the PCL electrospun solution, 8.01 ± 0.01 mg were released in total from the PCL RES suggesting a yield of 91% (n=3).

2dDr (10% wt.) released from RES
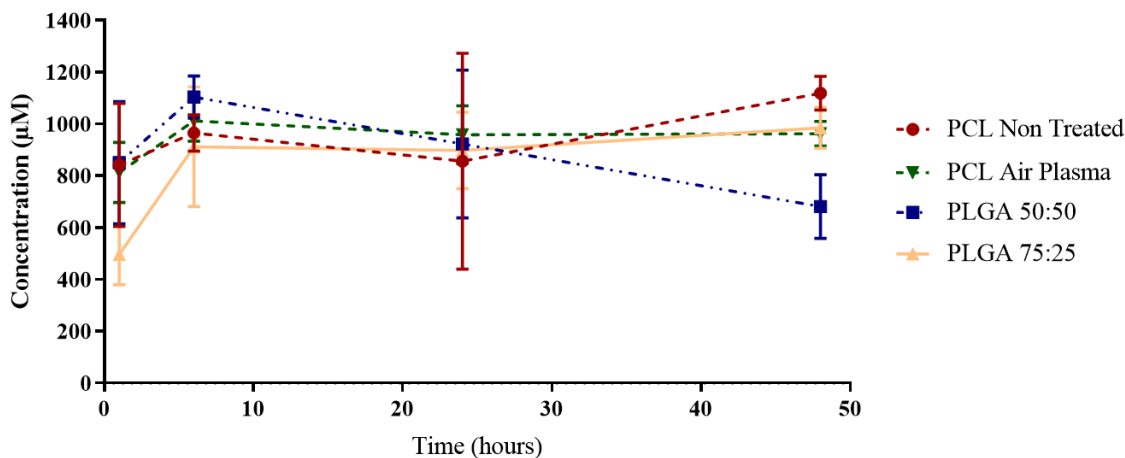
Figure 35. Non-accumulative release of 2dDr from PCL RES, PCL air plasma RES, PLGA 50:50 RES, and PLGA 75:25 RES for 1 hour, 6 hours, 24 hours, and 48 hours at 37.5 °C. Results are shown as mean ± SD. N=3 n=5.

The calibration curve of E2 had a low R^2 coefficient value as shown in Figure 36. Furthermore, in contrast with the fast burst release of 2dDr, the release of E2 from PCL RES showed that after 72 hours the average E2 concentration of $225 \pm 21.8\,\mu M$ (Figure 37). Given the weight of the scaffolds and the PBS volume used, the total amount of E2 released at 72 hours was about $183\,\mu g$ of the total average of $700\,\mu g$ (maximum concentration of $860\,\mu M$). Therefore, only 25% of the E2 was released after 72 hours. No E2 was detected during the first hour of incubation.

E2 calibration curve

$$Y = 0.0002762*X + 0.2312$$

$$R^2 = 0.8230$$

Absorbance vs Concentration (µM)
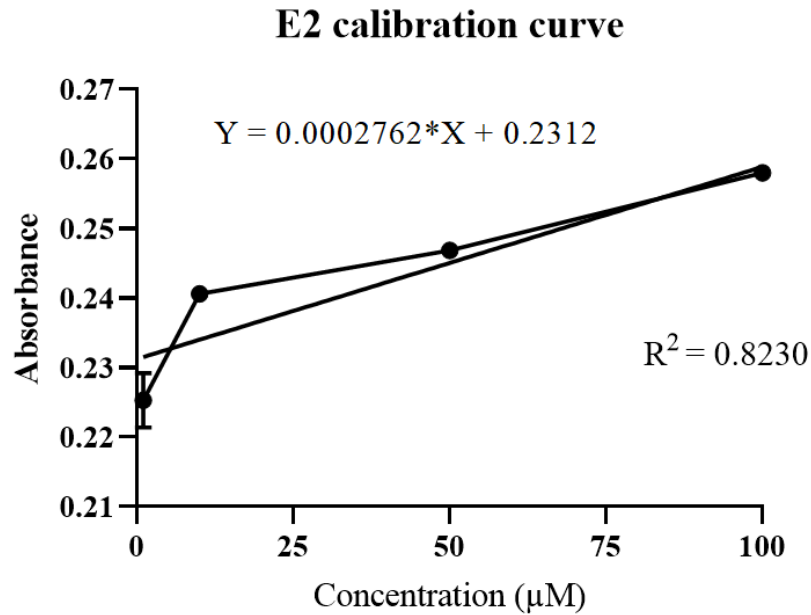
Figure 36. Calibration curve of E2 concentration (µM) against absorbance using UV spectroscopy at 272 nm. Results are shown as mean ± SD. N=2 n=5.

E2 (10% wt.) released from RES

PCL Air Plasma

Concentration (µM) vs Time (hours)
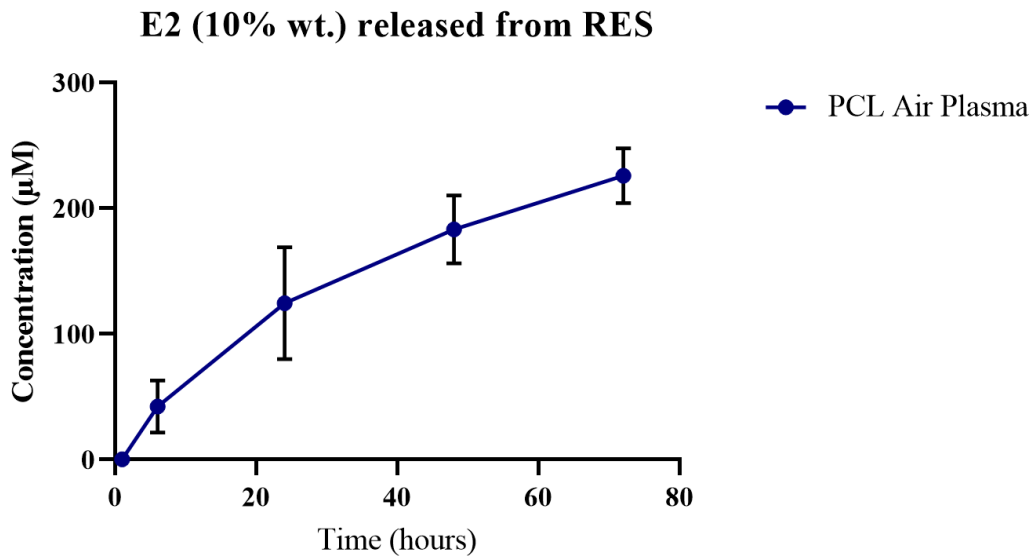
Figure 37. Non-accumulative release of E2 from AP treated PCL RES for 1 hour, 6 hours, 24 hours, 48 hours, and 72 hours at 37.5 °C. Results are shown as mean ± SD. N=3 n=5.

The calibration curve of AV proved to be linear at low concentrations from 0.001 mg/mL to 0.1

mg/mL (Figure 38). However, at higher concentrations, the absorbance does not follow a linear

trend (Figure 39) and thus the low concentration curve was used to quantify the release of AV.

AV calibration curve

$$Y = 0.3641*X + 0.02541$$

$$R^2 = 0.9414$$
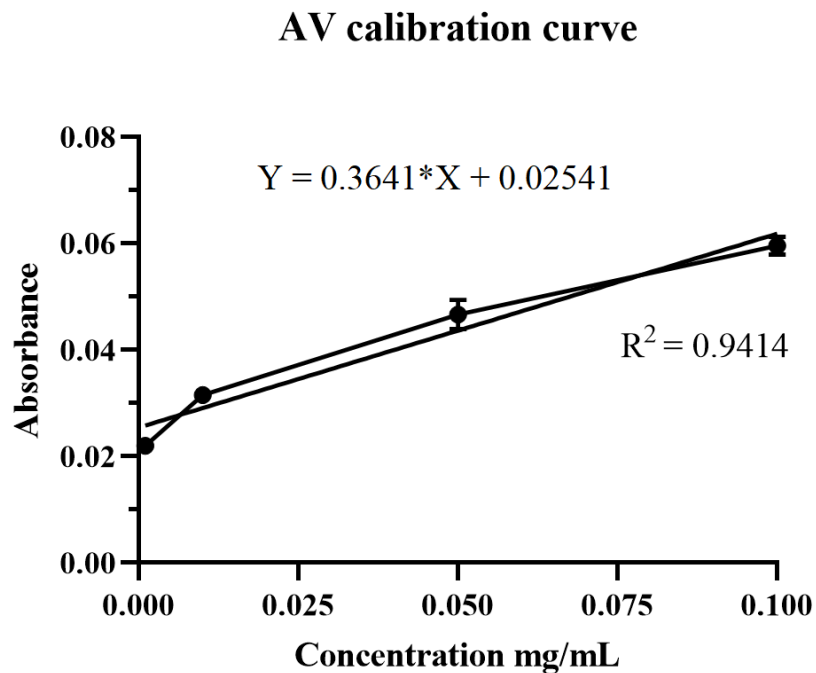
Figure 38. Calibration curve of AV concentrations from 0.01 – 0.1 mg/mL against absorbance

using UV spectroscopy at 292 nm. Results are shown as mean ± SD. N=2 n=5.

AV calibration curve

$$Y = 0.07069 * X + 0.03518$$

$$R^2 = 0.6275$$
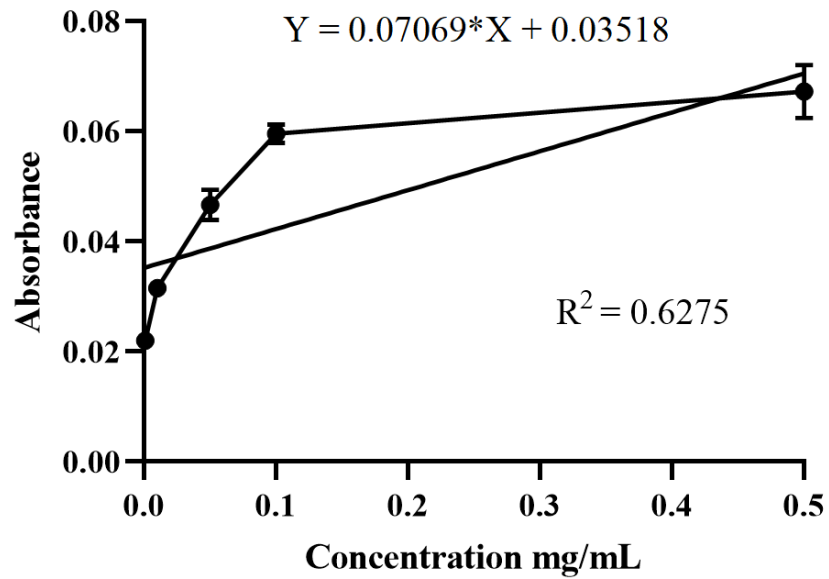
Figure 39.Calibration curve of AV concentrations from 0.01 – 0.5 mg/mL against absorbance using UV spectroscopy at 292 nm. Results are shown as mean ± SD. N=2 n=5.

The release of AV from PCL RES was slightly faster than the release of E2 but slower than 2dDr. Given the maximum AV concentration of 0.233 mg/mL, only 29.18% (0.068 mg/mL) of the total AV was released after 72 hours (Figure 40). Approximately 25% of the AV loaded into the RES was released within the first 24 hours.

AV (10% wt.) released from RES
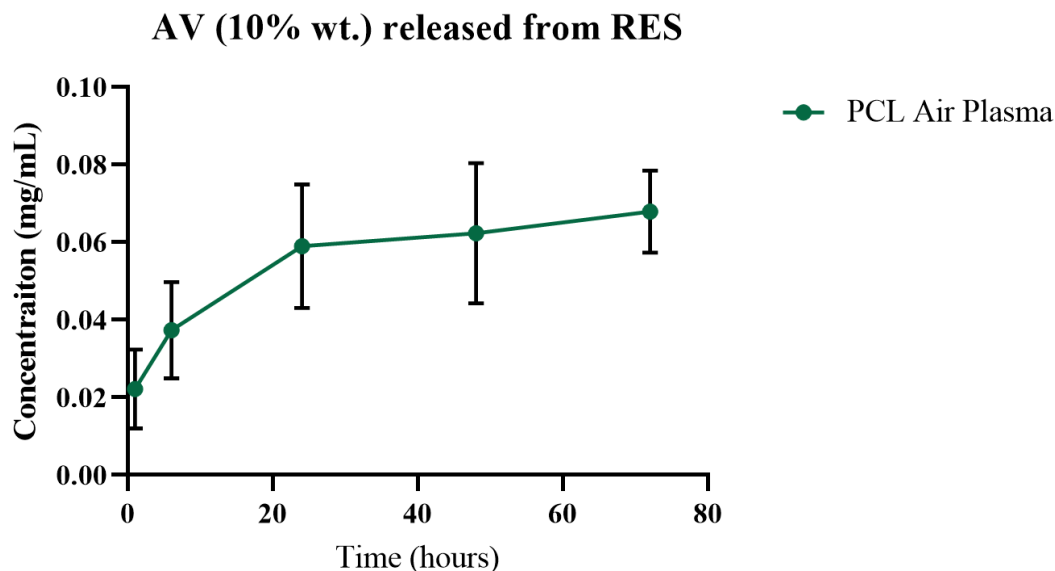
Figure 40. Non-accumulative release of AV from AP treated PCL RES for 1 hour, 6 hours, 24 hours, 48 hours, and 72 hours at 37.5 °C. Results are shown as mean ± SD. N=3 n=5.

3.5.   Characterization of 3D printed collectors

SEM of patterned collectors C1, C2, C3, C4, C5, and C6 (refer to Table 6) are shown in Figure 41. In all collectors, some microtextures were observed. This microtexture present in the collectors was attributed to post-fabrication steps such as solvent washing, air drying, or UV curing. Collectors C2, C6, and C4 are observed in Figure 42.A, Figure 42.B, and Figure 42. C, respectively. The dimensions of each patterned collector were not different between the model in CAD and the final fabricated collector. Collectors C1, C3, and C5 are not shown in Figure 42, as these were no longer used. The reason for this is explained further in section 3.6 (electrospinability of the TCES). To facilitate the nomenclature, patterned collector C2 was renamed as collector A, C6 as collector B, and C4 as collector C.
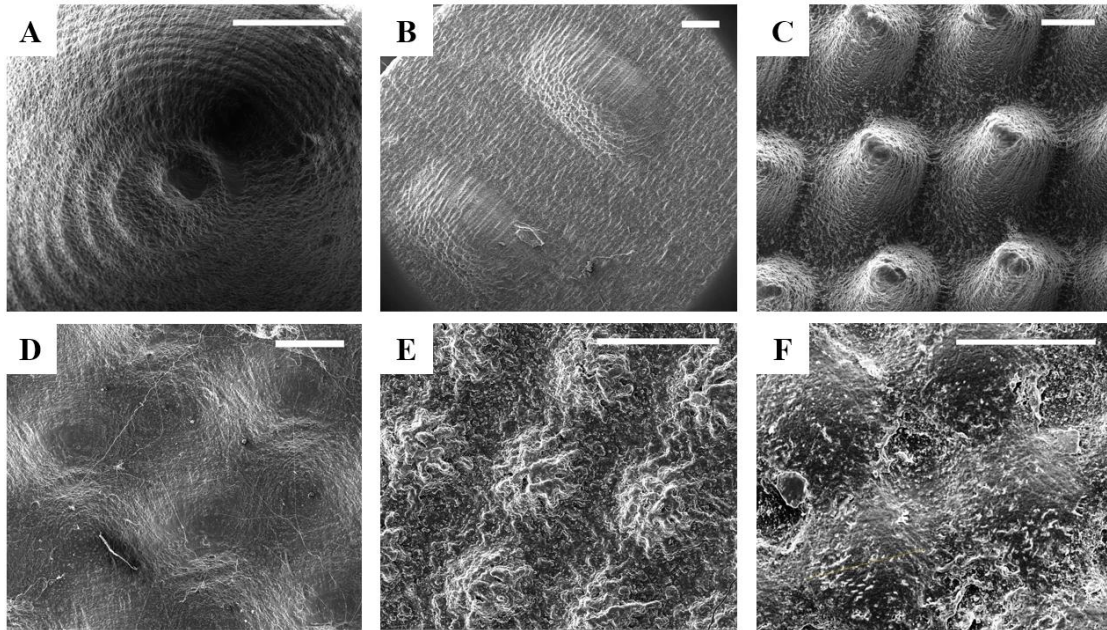
Figure 41. Micrographs of patterned collectors. A) C1, B) C2, C) C3, D) C4, E) C5, F) C6. Scale bar = 500 µm.
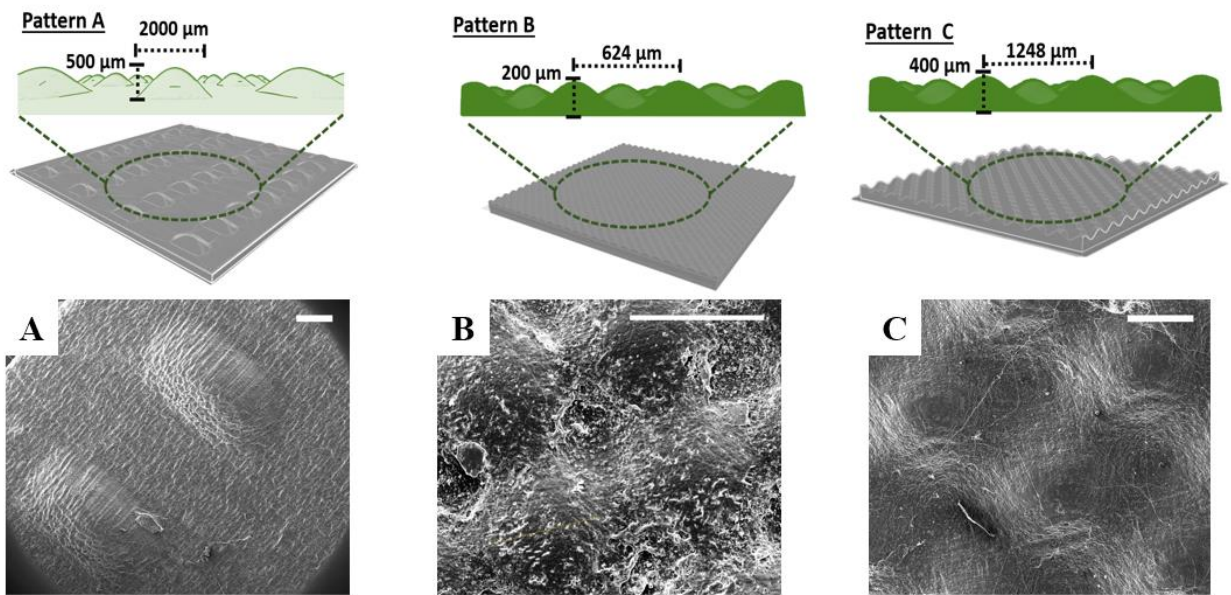
Figure 42. Micrographs of patterned collectors used to successfully fabricate TCES. A) C2, B) C6, C) C4. Scale bar = 500 µm.

3.6.   Electrospinability of TCES with and without bioactive compounds

Several electrospinning solutions of PLGA 50:50 and PCL were tested for their feasibility to fabricate TCES using different patterned collectors. As mentioned in section 3.5, just 3 patterned collectors were further tested. The selection criteria were based on the electrospinability of the collectors and how close they resemble the native morphology of the niches. Table 14 shows the results of all the polymer solutions tested and how feasible it was to produce TCES.

Table 14. Results of electrospinability for TCES with and without bioactive compounds. The – sign represents a failed electrospun solution while the + represents a successful electrospun solution. Please refer to Table 10 for the full description of every solution.

Code	Polymer	Result	Comments
A3	PLGA 50:50	—	Fibers rather avoided the surface of the collector. Even at higher voltages or flow rates. The best result was with lower flow rates, but fibers do not resemble the microtopography.
B3		—	
A7	PCL	—	Fibers rather avoided the surface of the collector. Higher voltages and flow rates made a small improvement on this behavior, but the electrospinning jet was not stable. Best results were achieved at lower flow rates. However, fibers did not resemble the microtopography.
B9		—	
A9		+	Electrospun fibers were directed towards the collector with no further issues with electrospinability or fiber infiltration in the microfeatures regarding the collector used.
B10		+	Fibers were deposited on the collectors and TCES were able to preserve some topographical cues.
B11		—	Electrospun jet was not stable, blockage on the capillary occurred.

B14		+	No difference in electrospinability was noticed between this solution and A9 (PCL only). TCES successfully fabricated.
B16		+	Fibers were deposited on the collectors and TCES were able to preserve some topographical cues.

Preliminary attempts with PLGA 50:50 showed that the polymer with its solvent system was not suitable to successfully recreate the microtopography of the patterned collectors, even without the inclusion of bioactive compounds. Figure 43 shows SEM micrographs of PLGA 50:50 TCES fabricated with patterned collector C5 (Figure 43.A, Figure 43.B, Figure 43.C) and patterned collector C3 (Figure 43.D). High fabrication variability was observed (Figure 43.A, Figure 43.B, Figure 43.C) because, even though the same patterned collector was used, the PLGA 50:50 TCES obtained were different every time that was fabricated. For all tested collectors, it was observed that fibers were not incorporated into the microfeature of the collector, with only some fibers being deposited on the top surface. This behavior created niches that only resemble the size of the tip of the microfeature.
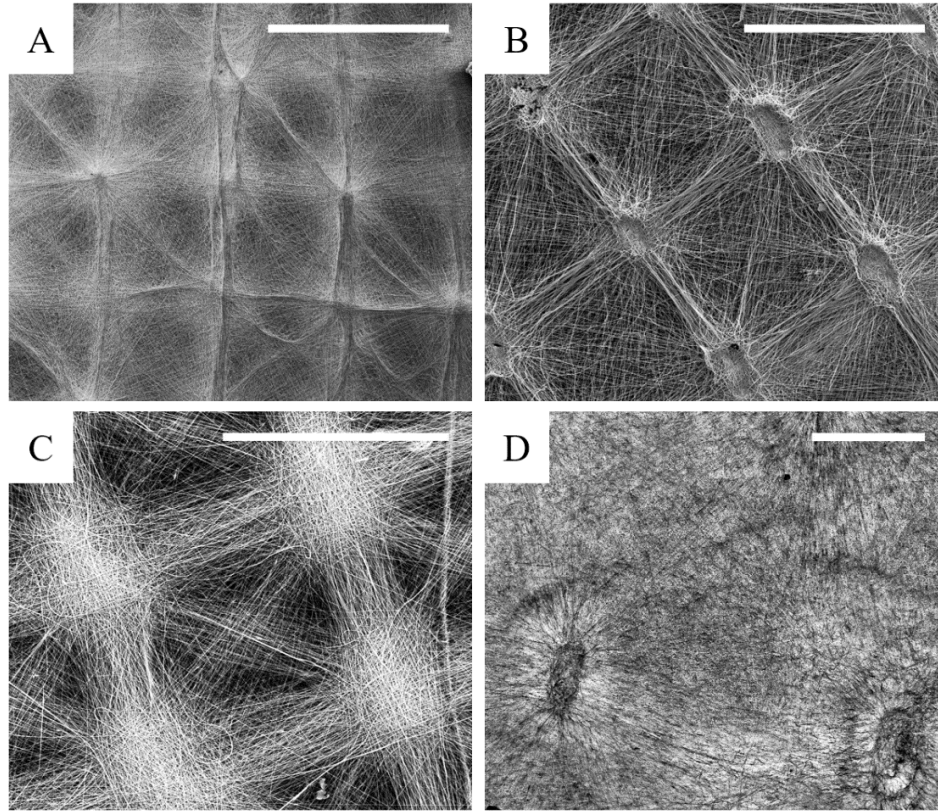
Figure 43. PLGA 50:50 TCES fabricated using patterned collector C5 (A, B, and C) and patterned collector C3 (D). Scale bar = 500 µm.

However, it is important to highlight that with optimal electrospinning solution (A9) and process parameters, it was possible to fabricate TCES using any of the collectors presented in this work. The following section shows the results of PCL TCES fabricated using the three selected pattern collectors (Figure *42*) with the electrospinning solution A9 (PCL 12% DCM:DMF) and solutions B10, B14, B16 (loaded with 8% 2dDr, 10% E2, and 10% AV respectively).

3.6.1. *Scaffold morphology and fiber diameter*

PCL was electrospun on the collectors, and TCES were fabricated, using collector A (Figure 44.A), collector B (Figure 44. B), and collector C (Figure 44.C). Microfeatures were successfully

fabricated using electrospun fibers. Furthermore, micrographs of AP treated TCES showed slight changes in the microfeature size (Figure 44.D).
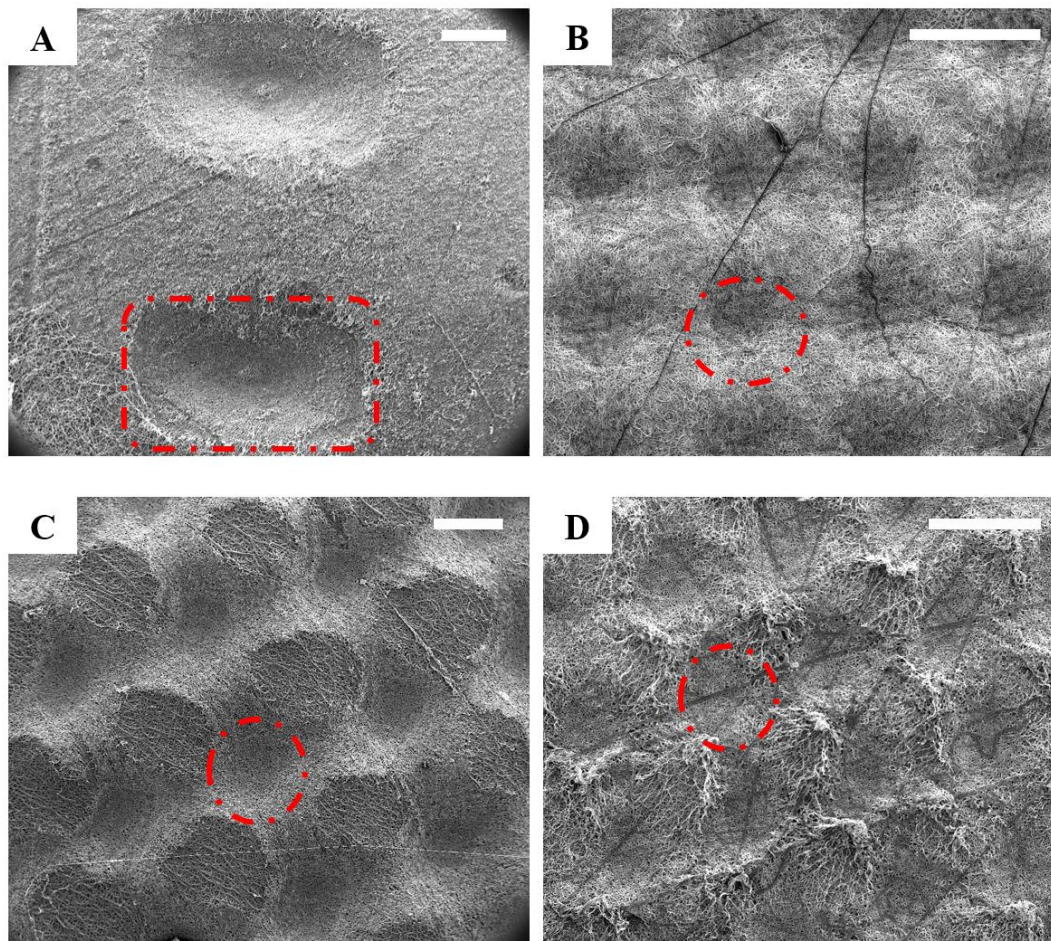
Figure 44. TCES fabricated on A) patterned collector A, B) patterned collector B, C) patterned collector C, and D) patterned collector B with AP treatment. Microfeature is highlighted with a red dashed circle. Scale bar = 500 µm.

SEM micrographs of cross-sections of PCL RES and PCL TCES were obtained (Figure 45). It can be observed that PCL TCES (right) preserved the morphology of the patterned collector. This further proves the feasibility of using PCL fibers to fabricate microfeatures.
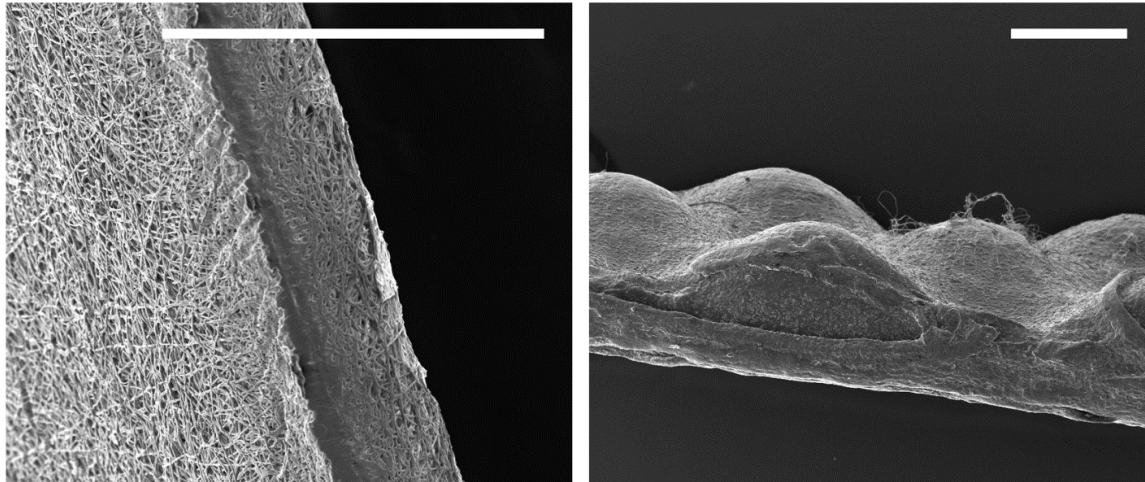
Figure 45. SEM micrographs of cross-sections of PCL RES (left) and PCL TCES (right) fabricated using patterned collector B. Scale bar = 500 µm.

In comparison with RES, preserving micro and macrostructure of the scaffolds is critical for the fabrication of TCES. When PCL RES were exposed to AP treatment for 2 minutes at 50 W, instead of the standard 10 W used for all PCL scaffolds, the morphology of the scaffold changed (Figure 46, A). During the air plasma treatment process, it was noticeable by eye that, when PCL RES were exposed to 50 W, the morphology of the scaffold changed, making it smaller and losing its original morphology. PCL RES exposed at 10 W did not show any morphological changes (Figure 46, B). Thus, 10 W was kept as the power parameter for AP treatment of TCES to avoid any significant change in morphology. Figure 47. A shows the fiber morphology of PCL TCES with no plasma treatment and Figure 47.B shows PCL TCES with AP treatment. It was visible that fiber diameter was different between PCL TCES with no AP treatment and PCL RES with AP treatment.
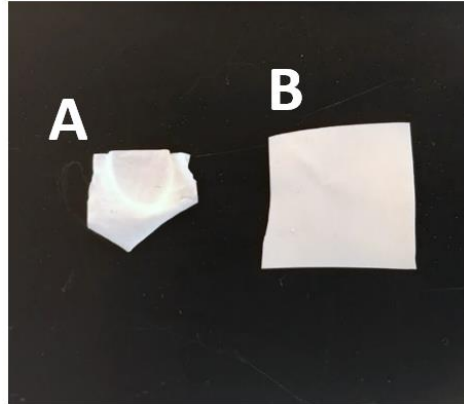
Figure 46. PCL scaffold after air plasma treatment where A) was exposed to higher plasma settings, 50 W, than in B) 10 W.
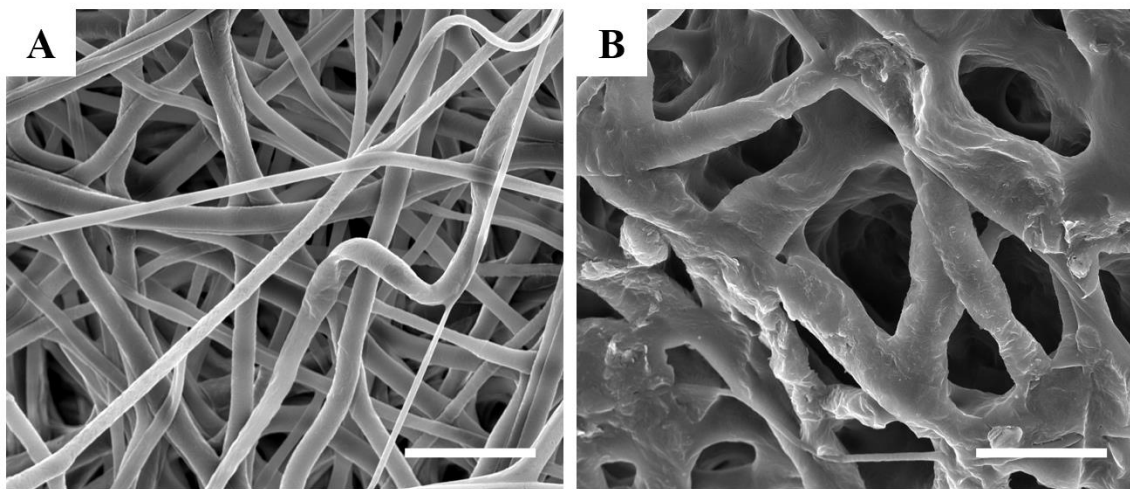
Figure 47. Micrographs of PCL TCES with A) no AP treatment, and B) AP treated. Scale bar = 10 µm.

TCES fiber diameter (no AP treatment) is shown in Figure 48. The fiber diameter of TCES fabricated with pattern A was 2.2 ± 0.3 µm, which was significantly higher in comparison to TCES fabricated with pattern B (1.2 ± 0.3 µm). Additionally, fiber diameter of TCES fabricated with pattern C was higher (1.9 ± 0.3 µm) compared to TCES fabricated with pattern B. Nevertheless,

no significant difference was found between fiber diameter of TCES fabricated with pattern A and TCES fabricated with pattern C. The average size of the microfeatures in the TCES is shown in Figure 49. The data shows that there was a low variation in the size of the microfeatures present on the TCES.
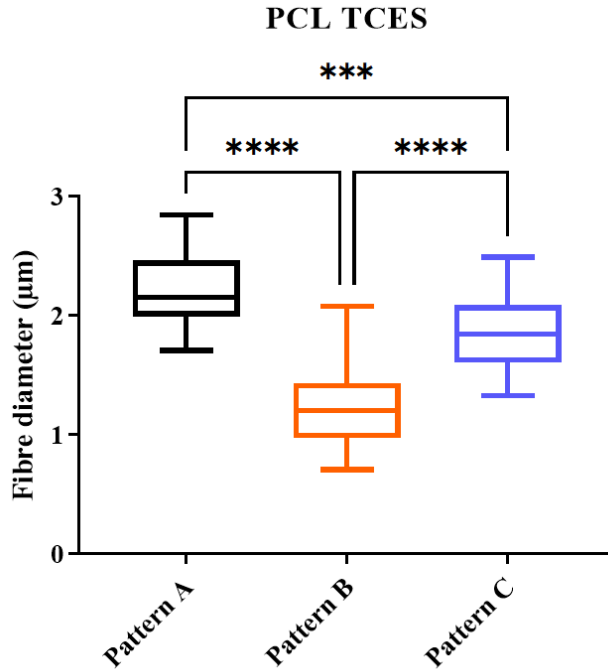
Figure 48. Box plot showing TCES fiber diameter using pattern A, pattern B, and pattern C. Results were analyzed with One-way ANOVA. **** $p < 0.0001$. Results are shown as mean $\pm$ SD. N=3 n=15.
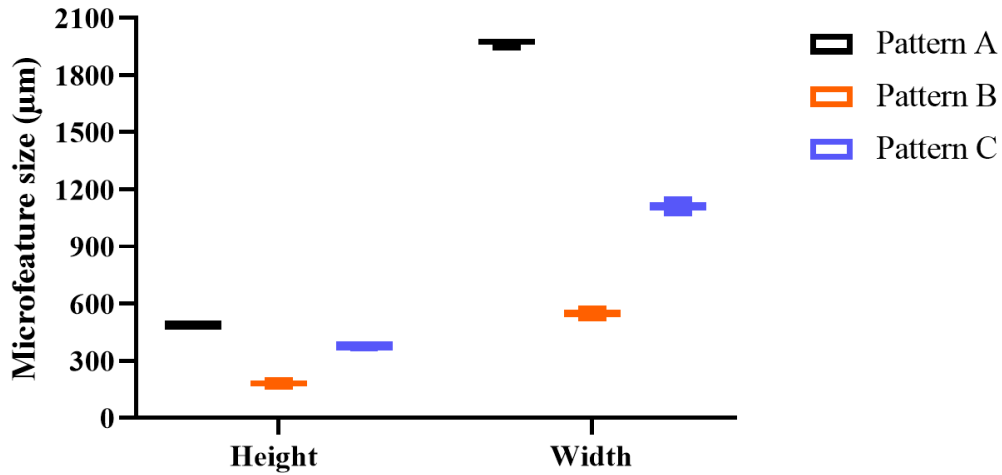
Figure 49. Box blot of microfeature size of TCES made with patterned collectors A, B, and C. Results are shown as mean ± SD. N=3 n=3.

Fabrication of TCES with patterned collectors is of major importance for this project. However, reproducibility is also important, as it would guarantee that the TCES will always have the same dimensions for further biological evaluation. From Figure 50, it was observed that the most reproducible pattern was pattern A. Nevertheless, even when both patterns B and C were also reproducible, pattern B was the most difficult to fabricate because of its smaller width and height (that closely resemble native rete ridges) as it was more difficult to get the electrospun fiber further inside a small space. However, all 3 patterns were reproducible.
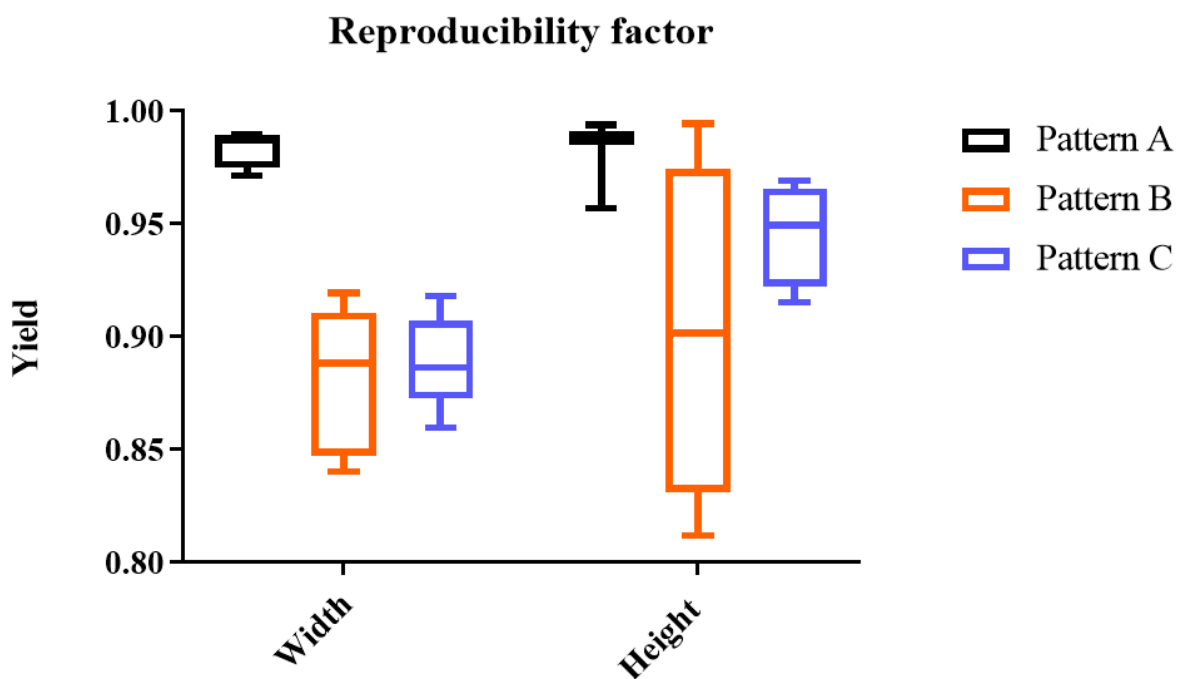
Figure 50. Reproducibility factor for the fabrication of TCES using pattern A, pattern B, and pattern C, for both width and height. Results are shown as mean ± SD. N=3 n=3.

TCES were fabricated using pattern C, where 8 % 2dDr (Figure 51.B), 10 % E2 (Figure 51.C) or 10 % AV (Figure 51.D) were loaded. From the micrographs in Figure 51, it can be seen that the morphology of the microfeatures was different according to the bioactive compound that was loaded. Microfeatures on TCES loaded with 2dDr or with AV were smoother compared to microfeatures on TCES loaded with E2 or with no bioactive compound. Furthermore, TCES loaded with aloe vera showed no fibrous structure, in comparison to TCES loaded with 2dDr.
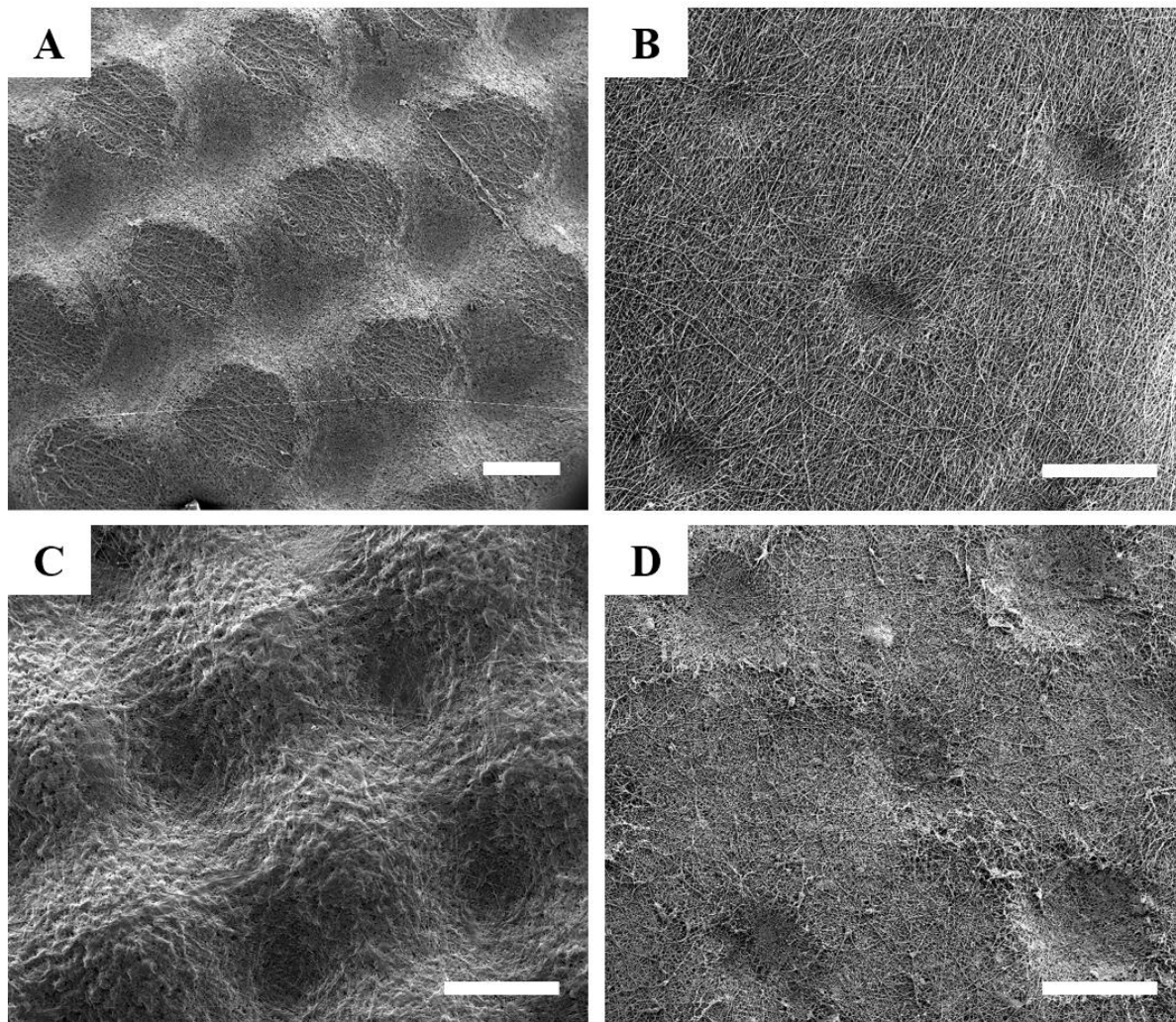
Figure 51. TCES fabricated using pattern C with A) no bioactive compound (control), B) 8 % 2dDr, C) 10 % E2, and D) 10 % aloe vera. Scale bar = 500 µm.

Figure 52 and Figure 53 show the fiber diameter and size of the microfeature respectively of TCES fabricated with patterned collector C and loaded with bioactive compounds. For fiber diameter, only the scaffolds loaded with E2 showed an increase when compared with the control. Furthermore, analysis of the microfeature average size showed that the inclusion of AV and 2dDr produced smaller features when compared with the control. TCES loaded with E2 showed a slight decrease in height but no significant difference in width when compared with the pure PCL control.

Table 15 shows a summary of the microfeature size for all PCL TCES fabricated with and without bioactive compounds.

TCES fibre diameter
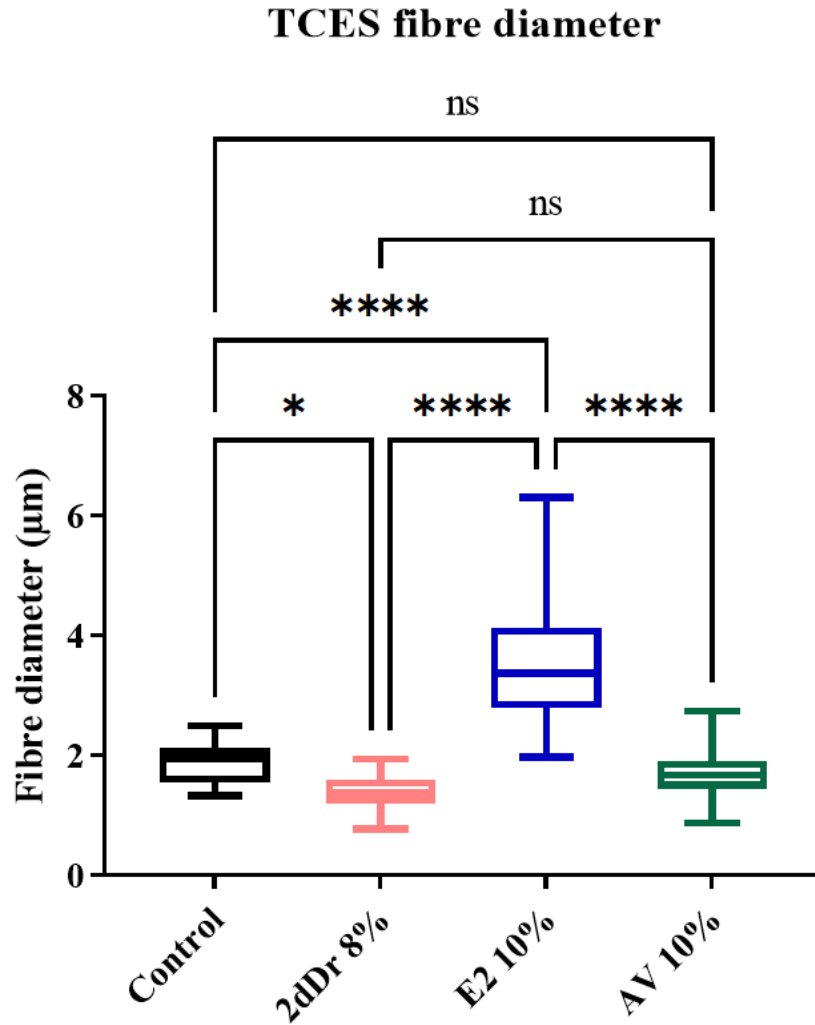
Figure 52. Box plot showing diameter of TCES made with patterned collector C and loaded with bioactive compounds. Results were analyzed with One-way ANOVA. **** $p < 0.0001$, * $p < 0.05$, ns $p \geq 0.05$. Results are shown as mean ± SD. N=3 n=15.
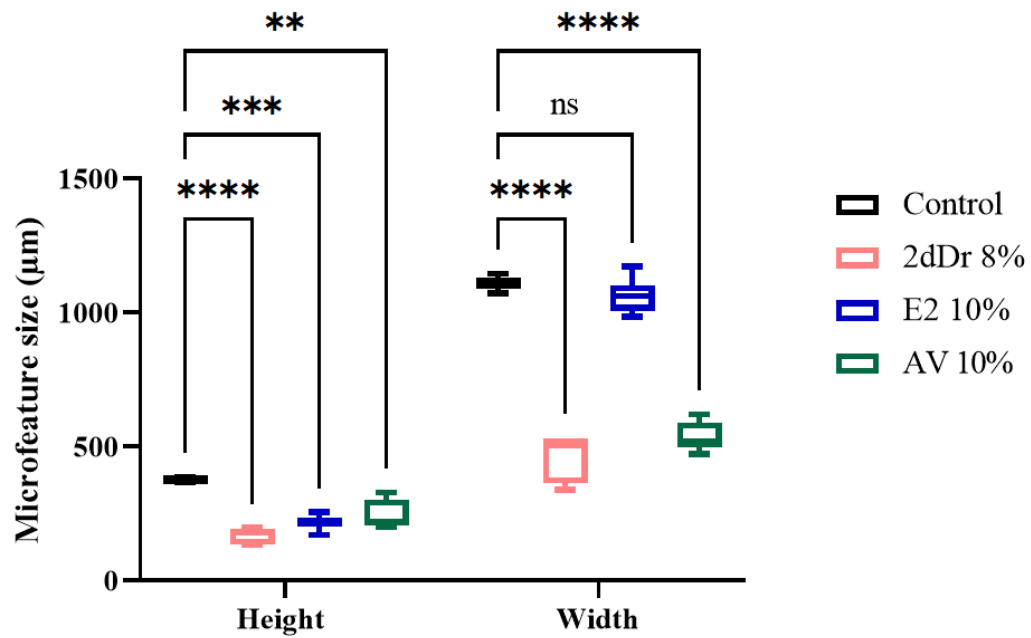
Figure 53. Box blot of microfeature size of TCES made with patterned collector C and loaded with bioactive compounds. Results were analyzed with One-way ANOVA. **** $p < 0.0001$. *** $p < 0.001$, ** $p < 0.01$, ns $p \geq 0.05$. Results are shown as mean ± SD. N=3 n=15.

Table 15. Summarize data of microfeature size for all PCL TCES with and without bioactive compounds. Results are shown as mean ± SD. N=3 n=3

Patterned collector	Bioactive compound	Height (µm)	Width (µm)
A	N/A	489 ± 55	1967 ± 17
B	N/A	180 ± 15	547 ± 20
C	N/A	376 ± 8.45	1108 ± 25
	2dDr	158 ± 30	498 ± 94
	E2	226 ± 18	1063 ± 67
	AV	246 ± 54	537 ± 55

4. Discussion

The electrospinning process is a versatile fabrication technique that has been used for a wide range of tissue engineering applications and the delivery of relevant biomolecules. Our results showed that introducing bioactive compounds within the electrospinning solution is less of a challenge when the polymer to electrospin is less complex in its chemical structure. The electrospinning process of PLGA has been reported with different solvents but most authors agree that low flow rates are needed to maintain a stable jet [263]. Nonetheless, optimization can be achieved by changing to solvents such as 1,1,1,3,3,3-hexafluoro-2-propanol, chloroform, or pure DCM as well as increasing the concentration of the polymer [294].

The instability of the PLGA electrospun jet is related to the fluid elasticity of the electrospinning solution and the co-polymeric structure of PLGA in which two different subunits (glycolic and lactic acid) are reacting with the solvent and the chain entangle within the polymer jet is more

117

complex than linear polymers. Regarding the ratio of the lactic and glycolic acid, several authors have studied the electrospinability of different blends and ratios of PLGA, showing that the PLGA electrospinning process is more susceptible to changes in the dielectric constant of the polymer solution [250], [263], [295]. Using our current DCM:DMF solvent system, the PLGA electrospinning process is more complex and prone to instability when working out of the standardized parameters.

PCL is a linear polymer that can be easily electrospun to produce different alignments and fiber diameters and that has been used to fabricate implants for soft tissue regeneration and collagen stimulation [296]. In comparison with PLGA, PCL can be electrospun under a variety of different conditions and the parameters in which the fibers are produced are so broad that they can be changed during the electrospinning process to produce scaffolds with different fiber diameters. From a fabrication point of view, the use of PCL makes a more stable and reproducible electrospinning process, and thus PLC is a better candidate to reliably introduce 3D microtopographies within electrospun fibers.

The two components selected for the solvent system, DCM and DMF, were versatile enough to dissolve the three polymers tested in this thesis (PLGA 50:50 and 75:25, and PCL) as well as to solubilize the bioactive compounds (2dDr, E2, and AV). The rationale behind the use of these solvents is due to their high volatility and their ability to interact with different chemical substances. Another attractive property of the DCM:DMF solvent system is their high tolerance within their clinical use which is 600 ppm (parts per million) for DCM and 880 ppm for DMF according to the EMA (European medicines agency) [297]–[299]. Research within our group (Villanueva et al., publication under preparation) has proved that electrospun scaffolds fabricated using the DCM:DMF solvent system showed significantly lower values than those presented by

118

the clinical use thresholds [300]. DCM is a non-polar solvent that can dissolve most common synthetic polymers such as PCL and PLGA, however, polar compounds such as 2dDr are only soluble in polar solvents such as DMF. Therefore, by combining these two solvents it was possible to introduce different molecules within the solution. Additionally, it was theorized that the use of DMF also aids in the electrospinning process as it can interact with the humidity that some polymer pellets bring to the polymer solution as environmental contamination.

Regarding the inclusion of bioactive compounds, the work presented here shows that it is possible to produce scaffolds loaded with bioactive compounds up to 15% of their polymer weight. Loading these compounds, however, severely limits the electrospinability of the polymer solutions. In the case of PLGA 50:50 for example, the introduction of 15% 2dDr made the electrospinning process unstable and thus this represents the highest concentration possible. For PLGA 50:50 + E2 RES, the inclusion of the hormone had a significant impact on the electrospinability even when the concentration was lower than 10% wt. This behavior is due to the interaction not only of the biomolecule within the polymer solution but also with the process parameters, as it has been shown that compounds that change conductivity, dielectric constant of the solvent, surface tension, and viscosity alter the electrospinability of the solution [250], [301].

Although possible to electrospin, PLGA 75:25 scaffolds were significantly more challenging to fabricate due to the low flow rate that required about 4 hours to spin 1 mL of polymer. This behavior became more evident with the inclusion of 2dDr in which even at flow rates lower than 0.3 mL/hr the electrospun jet was unstable and impossible to electrospun after 30 - 40 min. To overcome the slow flow rate and low stability of the electrospinning jet, higher polymer concentrations or other solvent systems could be tested as reported by several authors [230], [302]–[304]. Because the stability of the electrospinning jet is crucial to fabricate the TCES, PLGA 75:25

was discarded as a suitable polymer for this application, and therefore no *in vitro* or *ex ovo* results are shown in future experimental chapters.

When loading bioactive compounds on PCL solutions, the versatility of the polymer allowed the fabrication of highly concentrated 2dDr and E2 fibrous membranes. Moreover, only PCL solutions were loaded with AV because the instability caused by the change from blend electrospinning used to load 2dDr and E2, to emulsion electrospinning was only overcome on PCL polymer solutions. The high solubility of AV on DMSO proved to be enough to create highly concentrated solutions that can introduce up to 10% of the polymer weight. Furthermore, the stability of PCL solutions allowed us to successfully combine both 2dDr and AV into a single RES. Recently Yao et al. showed the benefits of using aloe vera/polaxamer hydrogels to deliver E2 [305], thus our work here explores for the first time the feasibility of using PLC fibrous scaffolds to deliver 10% wt. AV and 8% wt. 2dDr. Similar to the PLGA 50:50, the concentrations reported here are the maximum limit that could be electrospun using the PCL DCM:DMF solvent system. Figure 54 shows the chemical structure and properties of DCM, DMF, and DMSO.

DCM
Dielectric constant = 8.93
Dipole moment = 1.67 D

DMF
Dielectric constant = 36.71
Dipole moment = 3.86 D

DMSO
Dielectric constant = 46.68
Dipole moment = 3.96 D
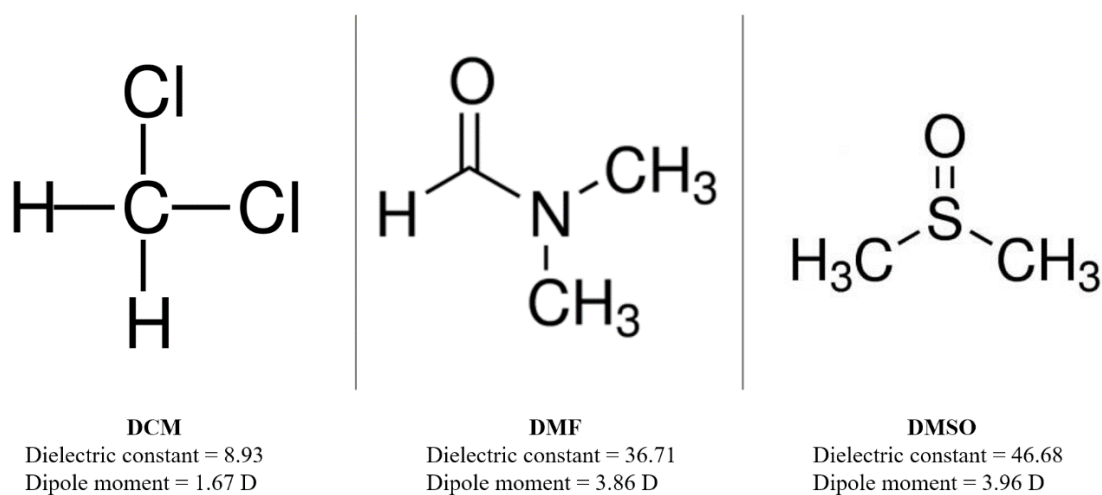
Figure 54. Chemical structure and properties of DCM, DMF and DMSO.

Fiber diameter across PCL and PLGA RES showed that with the selected electrospinning parameters it is possible to produce fibers within the 0.6 to 1.8 µm size. The addition of bioactive compounds on PLC solutions had a slight change in fiber diameter. The inclusion of E2 and AV specifically, increases the fiber diameter (E2) and the size standard deviation (AV). For tissue engineering applications, it has been reported that fiber diameter not only controls cell infiltration but also can induce differentiation in the case of stem cells. Liu et al. showed that HDF seeded on scaffolds with fiber diameters lower than 0.97 µm interact with the surface as if they were culture on 2D films [306]. Furthermore, Sun et al. showed HaCat migration is also controlled by fiber diameter and that thick 10µm fibers are capable of inducing attachment for both HaCat and HDF cell lines [307]. Therefore, the ideal fibrous scaffold has a homogenous population of fibers within the micron range to allow cell infiltration.

Higher concentrations of up to 30% wt. of AV had been reported for PCL electrospun scaffolds [308] with other studies showing lower or the similar 10 – 15% wt. concentrations showed in this work [309]–[312]. Other studies increased the concentration of AV by modifying the physical properties of AV and mixing it with PVA, however, this approach requires the use of higher temperatures that could compromise the bioactivity of the AV [313]. The key factor on the maximum amount of AV loaded into electrospun scaffolds is the use of more volatile solvents. Nevertheless, both of these studies required the use of emulsion electrospinning or the combination of two solvents as the complex mixture of the several components of the AV (polysaccharides, proteins, vitamins, and minerals) are not completely dissolved by most of the common polymer solvents [185], [188].

In comparison, introducing E2 and 2dDr into electrospun scaffolds is a straightforward procedure performed by blend electrospinning. Several studies have reported concentrations of E2 lower than

those presented here ranging from 0.1% wt. to 5% wt. [159], [166], [314], [315]. It is unclear if the maximum concentrations used in those studies were limited by the electrospinning process or are related to the low concentrations of E2 needed to induce an angiogenic response [316]. Regarding 2dDr, Dikici et al. had reported the inclusion of up to 50% wt. of 2dDr on PHBV electrospun scaffolds, such a high concentration of 2dDr could be possible due to the use of methanol over DMF or due to the higher hydrophilicity compared to PCL of the polymer PHBV used to deliver 2dDr [166]. To the best of our knowledge, no other studies have attempted the introduction of 2dDr on PCL or PLGA electrospun scaffolds.

Plasma treatment of PCL fibers was necessary to achieve rapid cell attachment due to the hydrophobic nature of the polymer [317]. Although not as significant as the plasma treatment, the addition of bioactive compounds on the PCL fibers also influences wettability with fibers loaded with 2dDr and AV showing lower contact angle values than those of the pure PCL. Several research groups have reported the activation of PCL fibers to enhance biocompatibility or to create delivery platforms for the delivery of complex biomolecules [318]. Because plasma treatment is a waste-free surface modification method that is also beneficial as a partial sterilization technique [319], its use for the activation of TCES is a promising approach to preserve the morphology of the scaffold.

The standard Bial's orcinol method for pentose sugars probed to be sensible enough to detect low micromolar concentrations of 2dDr and produced a linear calibration curve with a high R^2 coefficient (0.99). However, the E2 calibration curve showed a nonlinear behavior and low R^2 coefficient (0.82) uncharacteristic of other studies that have quantified the release of E2 [159], [166]. Because E2 is not soluble in water, our work here used a highly concentrated solution of E2 in DMSO to prepare the µM solutions used for the calibration curve. Although we also

122

implemented the use of other solvents such as methanol or ethanol to dissolve E2, the data showed that more work needs to be done to fully characterize a more reliable quantification method for E2.

In contrast with scaffolds loaded with 2dDr and E2, there are a limited number of studies that have reported the release of AV from polymeric scaffolds due to its complex nature. The two most popular approaches are the use of the Lugol's iodine staining solution [320] or by UV spectroscopy [312], [321]. Because the origin of the AV (gel or fillet) and its manufacturing process are highly related to the chemical composition of the AV, it is important to select the most accurate quantification method based on the AV source. In the present work, the UV spectroscopy method was preferred due to the low concentration of AV expected to be released from the scaffold (μg/mL) and that about 55% of the AV composition is polysaccharides [322].

Zeng et al. studied how the similarities in the chemical properties of the solvent and polymer to electrospun have an effect on the drug release. The principle is that a sustained release from electrospun fibers is mainly controlled by the similarities in polarity between the drug and the polymer and the complete solubility of the drug in the solvent. This explains the burst release from scaffolds loaded with the polar 2dDr and the sustained release from scaffolds loaded with E2 [323]. In the case of AV, a release faster than E2 and slower than 2dDr was expected because of its complex mixture of polar (sugars and proteins) and non-polar (polysaccharides and phenolic compounds) fractions [185], [188]. The other factor related to the release profile for blend electrospun scaffolds is the proportion of polymer/compound on the electrospinning solution [288]. Therefore, future work could explore the effects of a higher PCL concentration to alter the burst release of 2dDr.

The initial release experiment was set up for 240 hours to evaluate the long-term release of the scaffolds. The information from this initial experiment revealed that in comparison with other studies, the burst release of the 2dDr from both PCL and PLGA scaffolds occurred within the first 6 hours with approximately 80% of the 2dDr being released. In comparison, Dikici et al. reported a sustained release of 2dDr from PHVB electrospun scaffolds with ~ 32 mM around day 5 which is about 70% of the total 2dDr loaded [166]. However, a similar burst release (>90% of 2dDr release within 24 hours) was observed by Andleeb et al. when loading 2dDr on cotton wound dressings [168]. Moreover, Azam et al. loaded 2dDr on alginate dressings with a 50% being released within the first 24 hours [170], highlighting the importance and effects that the polymer matrix and how 2dDr is loaded have on controlling its release.

The slow release of E2 from electrospun scaffolds has been reported before by several authors with Mangir et al. and Shafaat et al. showing a release of E2 at 133 and 90 days, respectively [158], [159]. For our work with PCL RES, a longer release experiment should be necessary to determine the amount of time necessary to release more than 90% of the E2 content as only 25% was released within 72 hours. Similar to E2, the release profile of AV showed a burst release of 25% of its total content followed by a steady release on the following 2 days. However, to the best of our knowledge, only one study has characterized the release of Aloe vera from electrospun scaffolds as having a release above 75% within the first 24 hours [312].

The effects of a sustained or burst release of proangiogenic agents as well as a full rationale of reducing the release time period for all the materials and compounds to 72 hours is fully explained in chapter III as it is related to the *ex ovo* CAM assay. Future work should explore and characterize the effects in the release profile of introducing more than one bioactive compound at different

concentrations into the electrospun fibers. Additionally, the effects of fiber porosity on release profile should be addressed to better understand the burst-release observed for all the compounds.

The analysis of the chemical and physical properties of the RES revealed that the inclusion of the bioactive molecules had minimal impact on the melting point. Regarding tensile strength, scaffolds loaded with high concentrations of 2dDr (15% wt.) showed the lowest values of tensile strength. For skin tissue engineering applications, the use of an elastic material is preferable due to the native elasticity of the skin (tensile strength between 2 – 16 MPa) as it will allow patient movement when implanted [324], [325]. The RES fabricated here have all tensile strength values between 1.8 and 3.6 MPa making them suitable candidates to be used for skin tissue regeneration. The main difference in tensile strength and max elongation% was observed when comparing non-treated and AP treated PCL scaffolds. This change could be related to an increase in surface area due to plasma etching [326] as observed on the SEM micrographs.

Regarding melting point, the 3°C decrease on the PCL melting point (60°C) when loaded with AV + 2DdR would be relevant mainly for sterilization or long-term storage [327]. Because of the low glass transition temperature of the PCL (-60°C) [296], it was decided not to study any possible changes caused by the inclusion of the bioactive compounds on the RES. Therefore, all our DSC diagrams only cover temperatures from 30°C to 100°C. Moreover, the changes in contact angle upon adding the bioactive compounds are interesting for future tissue engineering applications, as they can alter the wettability of the scaffold while enhancing its bioactivity without the need for any surface treatment (Figure 55). Therefore, introducing the hydrophilic 2dDr or AV, or the hydrophobic E2 is a promising strategy to activate the PCL scaffolds and modifying cell attachment for tissue engineering applications. This change in wettability and its effects on cell behavior are further explored in chapter III.
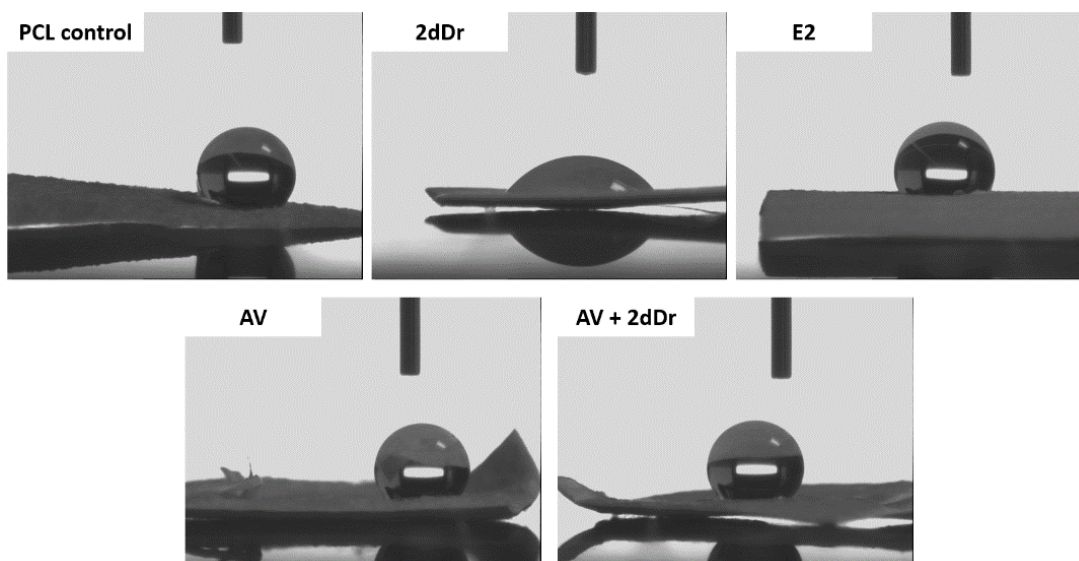
Figure 55. Images of average water contact angle for PCL RES loaded with bioactive compounds.

Several studies have reported the shrinkage of PLGA scaffolds as well as strategies to overcome this behavior [328], [329]. However, because of the nature of this work, preserving the entire micro and macro structure of the scaffold was critical to select the most appropriate material. Our study with PLGA and PCL scaffolds showed that after 6 h in PBS at 37.5°C the PLGA scaffolds suffered an average decrease in size of 70% of their original size regarding the plasma treatment or the addition of 2dDr. In comparison, PCL constructs preserve their morphology even after 48 h under the same conditions. Based on these results, it was decided to explore the manufacture of PLGA TCES but not to use these scaffolds for cell culture or any other *in vitro* experiments. A comprehensive rationale of this decision is shown in chapter III when discussing cell culture on both TCES and RES.

The change in opacity of PCL upon plasma treatment has been reported before by Sharma et al. and it is related to the capacity of non-treated PCL to entrap air between the fibers due to its high hydrophobicity when compared with the AP treated scaffolds that allow for water penetration and thus change the optical properties for the scaffold [330]. This change in opacity, although more

relevant for ophthalmic applications [330], [331], can be useful for monitoring *in vitro* or *in vivo* wound development.

The porosity of the electrospun fibers was not evaluated on this work. However, this topographical cue is critical for protein deposition and cell attachment. Moreover, because of the bioactive compounds loaded into the fibers, it is expected that the porosity would change for each group depending on the compound loaded and its concentration. Future work could explore the effects of porosity on tissue integration, scaffold degradation, and cell migration through the scaffold after implantation.

Fabrication of microtopographical cues was possible for both PLGA and PCL electrospun solutions. Nonetheless, PLGA 20% solutions were only able to replicate the top surface of the collectors. Fibers do not reach the lower features of the collector and most of the electrospun solution formed aggregates around the collector. Changes to the concentration of PLGA or to the electrospinning parameters (voltage, flow rate, and distance from the collector) failed to produce any difference regarding the fabrication of TCES, and in some cases completely disrupted the electrospinning process. The use of PLGA for the fabrication of TCES has been explored before by Ortega et al. using collectors with micropockets to mimic the palisades of Vogt [269]. The microfeatures on the collector used by Ortega et al. were separated from one another and thus allowed for a more homogeneous fiber deposition.

Paterson et al. reported the use of PCL electrospun fibers to fabricate TCES on metallic collectors with bigger microfeatures than the ones presented here. The results from Paterson et al. were similar to the data shown in this work in that it is easier to replicate the width of the microfeatures rather than the height [270]. The PCL polymer concentration used by Paterson et al. was lower

(10%) than the one used in this work (12%), our findings suggest that an increase in viscosity aids in the control of the electrospinning jet and allows for direct fiber deposition on the surface of the collector. This could explain why the patterned collectors with microfeatures similar to the ones shown here (1158 µm and 1287 µm) produced scaffolds with less defined features. Moreover, our data showed that the fabrication of TCES is also highly susceptible to changes in the electrospinning parameters as a decrease in flow rate hinders the collection of fibers on the top surface of the collector (Figure 56).
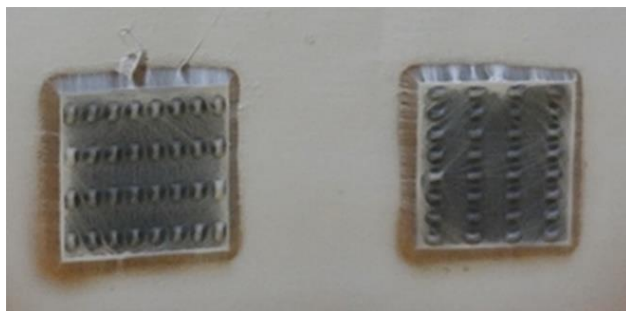
Figure 56. Effects on fiber deposition upon lowering the electrospinning flow rate from the standard 4 mL/hr to 2 mL/hr. Fibers are deposited on the plain collector and avoid the surface of the patterned collector.

Our work here shows that it is possible to mimic microfeatures of 624 µm in width and 200 µm in-depth present on patterned collector B. To the best of our knowledge, this is the first time that such small features have been successfully mimicked using biocompatible and biodegradable fibrous constructs and that produce microfeatures with an average size margin of error of 10%.

The introduction of the bioactive compounds on the electrospinning solution altered the production of the scaffold according to the nature of the compound. This change in electrospinability was critical when fabricating TCES as a stable polymer jet is crucial to direct the electrospun fibers

towards the patterned collector. Using the most effective patterned collector (pattern C) we evaluated the performance of fabricating 2dDr, E2 or AV loaded TCES. Our results showed that electrospinning solutions loaded with E2 were significantly better to replicate the microfeatures than the 2dDr and AV solutions. It was hypothesized that the non-polar nature of E2 improves its solubility on the DCM:DMF solvent system and allows for an electrospinning process highly similar to the PCL control. This behavior would explain why the solutions loaded with the highly polar 2dDr produced the less defined microfeature even at lower concentrations (8% wt.) than those of E2 (10% wt.).

Regarding fiber structure of the TCES loaded with bioactive compounds, the only difference in fibers diameter across the PCL control, 2dDr, E2, and AV groups was observed for TCES loaded with E2 that showed an increase in fiber diameter. Although 2dDr and AV loaded TCES showed less defined microfeatures, their morphology could induce an effect on cell behavior as other researchers have shown that microfeatures with similar dimensions have an effect on cell metabolic activity [271]. To the best of our knowledge, this is the first time that fibrous microtopographical scaffolds have been used to replicate the stem cell microenvironment while delivering bioactive compounds to enhance tissue regeneration.

In comparison to the PLGA scaffolds, there were no changes on microstructure on PCL scaffolds incubated at 37 °C on PBS. Moreover, no changes in fiber morphology were observed under the SEM for non-plasma treated PCL scaffolds. However, further experimental data is required to evaluate the effects of temperature and time on hydrophobic recovery for PCL RES and TCES treated with air plasma. The loss of the hydrophilic coating created by the plasma treatment has been studied before by Campeu et al. reporting hydrophobic recovery within the first 7 days for samples left at room temperature [332]. Future work would also bee needed to improve on the

degradability of the scaffolds. Due to the hydrophobic nature of PCL, its degradation rate is slower than that of PLGA and several authors have tried to overcome this challenge, while retaining the mechanical properties of PCL constructs. One of the most common approaches is the use of PCL blends with natural polymers, such as gelatin.

Although other authors have produced bioactive artificial stem cell microenvironments, these approaches usually required more complex techniques such as covalent immobilization, microfluidics, and biomolecular patterning are often used only on *in vitro* models [69], [333]– [336]. Therefore, our strategy has the potential to produce a wound dressing that can recreate the rete ridges while improving skin regeneration by delivering bioactive compounds.

5.   Conclusion

In this chapter, we focused on the development, characterization, and optimization of PCL RES and TCES as well as exploring the inclusion of bioactive/angiogenic compounds within the electrospun fibers. The presented methodology allowed for the fabrication of different biodegradable artificial 3D structures that resemble the rete ridges by combining electrospinning with micropatterned collectors. Moreover, we have explored both PCL and PLGA as fabrication materials for TCES but due to the PLGA's high shrinkage at cell culture conditions and its lower stability when electrospinning, PCL was selected as the most reliable material to preserve the microtopography of the patterned collectors.

The inclusion of 2dDr, E2, and AV into the scaffolds was possible at different concentrations but had a negative effect on the electrospinability of RES above 10% wt. for E2, 15% wt. of 2dDr, and 10% wt. of AV. The release of E2 and AV from the scaffolds was characterized by an initial burst release within the first 24 hours followed by a steady and slow release in which less than 30% of

the total compound was released after 72 hours. In comparison, scaffolds loaded with 2dDr showed a release of up to 90% within the first 24 hours. The difference in the release is due to the chemical interaction of the compound within the electrospinning solution and can have different biological effects that would be tested in further chapters.

In the case of fabricating TCES, introducing AV or 2dDr resulted in changes in the microstructure of TCES, whereas the inclusion of E2 showed no changes in the microstructure of the TCES. For the fabrication of TCES, the maximum work concentrations used were 8% wt. 2dDr, 10% wt. E2, and 10% wt. AV. Although optimization of the electrospinning process was required, our methodology shows that it is possible to produce scaffolds with well-defined fibrous microenvironments loaded with relevant bioactive compounds.

Furthermore, there were no changes in tensile strength or melting point upon the introduction of these components. However, the introduction of the bioactive compounds influenced water contact angle increasing or decreasing the hydrophilicity of the scaffolds. Additionally, AP treatment proved to be an effective surface modification method to increase hydrophilicity without compromising the microstructure of the TCES.

The methodology shown in this chapter is a promising approach to fabricate fibrous matrices that introduced synthetic rete ridge-like structures that can deliver bioactive compounds to enhance skin regeneration. Further optimization could enhance the ability of the scaffolds to mimic certain microfeatures that have deep and narrow topographical cues as well as exploring lower concentrations of 2dDr and E2 to further preserve the microfeatures on the scaffold. This chapter builds the basis on the fabrication of TCES and RES that would be tested for their biological effects *in vitro*, *ex ovo*, and on tissue engineered skin models in chapters III and IV.

Chapter IV. *In vitro* effects of bioactive compounds on skin primary cells and the chick chorioallantoic membrane assay

1. Introduction

The use of proangiogenic agents to improve skin regeneration has been established before as a strategy to overcome the slow ingrowth of blood vessels that hinders the function and viability of most tissue constructs. However, even the gold standard agent used for promoting vascularization, VEGF, presents drawbacks and limitations that need to be addressed on a case-to-case basis. In the case of skin, these challenges include but are not limited to: prolonged inflammatory response [337], cellular and molecular conditions that resemble the condition of human psoriasis [337], [338], and skin carcinogenesis by disrupting the proliferation, survival, or stemness of the keratinocyte population and cancer cells [339]–[342]. Therefore, characterizing and understanding the effects of novel alternatives to VEGF has become critical for tissue engineering applications.

In order to study an angiogenic agent, it is important to understand its mechanism. In general, most angiogenic agents fall into the classical category of inducing physiological angiogenesis by binding to a specific transmembrane receptor. Examples of classical angiogenic factors include VEGF, FGF, PDGF, insulin-like growth factors (IGFs), interleukin-6 (IL-6), and tumor necrosis factor (TNF). The main pathways activated by these proangiogenic agents have been studied before for their role in endothelial cell migration and proliferation [115], [129], [343]. However, the activation of most angiogenic signaling pathways promotes the production of transcription factors and genes that are primarily expressed under specific physiological conditions such as wound healing. Therefore, for skin tissue engineering it is important to study the effects on cell

behavior not only for endothelial cells but for other cell types related to wound healing such as dermal fibroblasts and epidermal keratinocytes.

In this chapter, the *in vitro* use of 2dDr, E2, and AV in solution was explored to observe changes in cell proliferation and viability for dermal fibroblasts, epidermal keratinocytes, and adipose-derived stem cells. The importance of fibroblasts and keratinocytes on skin cell development has been well documented, however, the use of adipose derived stem cells and their potential clinical applications have become of special interest since the early 21st century. Their ability to undergo self-renewal, multilineage differentiation and their role in the expression of cytokine and growth factors make adipose derived stem cells an accessible and promising cell type to be used for tissue engineering applications [344].

Although our research group has explored the use of 2dDr and E2 to improve pelvic floor repair [158], [159] and manufacture complex skin wound dressings [168], [170], their effects *in vitro*, especially for 2dDr, are yet to be fully characterized for key skin cell types. Nonetheless, the effects of E2 on fibroblasts and keratinocyte proliferation have been studied before but using concentrations below the minimum concentration loaded into the electrospun scaffolds described in chapter II [180], [345]–[347]. In the case of AV, most of its medical relevance is related to its anti-inflammatory and anti-microbial capabilities [188], with only a few studies showing the effects of the entire AV fraction on skin cells [348], [349]. Therefore, it is important to have *in vitro* cell data that shows the effects of 2dDr, E2, or AV in solution on a range of concentrations that includes the potential dosage to be delivered by the RES or TCES fabricated in the previous chapter.

Furthermore, the chick chorioallantoic membrane (CAM) assay was used to evaluate the proangiogenic effect of each compound when loaded into PCL or PLGA RES. The CAM assay is an extraembryonic quantitative or semi-quantitative method based on the growth of primitive vessels on the chorioallantois to evaluate the formation of new vessels or their inhibition when exposed to soluble factors, cells, or tissues [350]. The simplicity of the assay compared to other alternatives such as the corneal micropocket assay or the mesentery assay, its reliability, and low economical cost makes the CAM assay an attractive model that allows the visualization of sprouting angiogenesis [351], [352].

Characterizing the angiogenic potential of the compounds as well as their effects on skin cell proliferation and viability is a key step for defining the right dosage to be delivered on a more complex model using RES or TCES. Understanding how these factors of angiogenesis and skin cell behavior are related is key to improve tissue regeneration and vascularization of the construct.

1.1. Aim and objectives

The aim of this experimental chapter was to study the effects of 2dDr, E2, and AV in solution on *in vitro* cell culture and to determine the optimal range for these bioactive compounds to be delivered. Furthermore, to evaluate the angiogenic potential of 2dDr, E2, or AV when used in solution or loaded into RES. In order to achieve this aim; the following objectives for this experimental chapter were established.

- Isolate and expand primary skin cells from tissue obtained from patients undergoing elective breast reductions and abdominoplasties (research ethics number 15/YH/0177 under the Human Tissue Authority 12179).

- Investigate the effects of solubilized 2dDr, E2, or AV on metabolic activity and cell proliferation for human dermal fibroblasts.

- Investigate the effects of solubilized 2dDr, E2, or AV on metabolic activity and cell proliferation for human epidermal keratinocytes.

- Investigate the effects of solubilized 2dDr on metabolic activity and cell proliferation for adipose-derived stem cells.

- Observe the changes in cell migration for adipose-derived stem cells when exposed to solubilized 2dDr.

- Assess the angiogenic potential of PLGA RES loaded with 2dDr when implanted on the chick chorioallantoic membrane assay.

- Assess the angiogenic potential of PCL RES loaded with 2dDr, E2, AV, and AV +2dDr when implanted on the chick chorioallantoic membrane assay.

2. Materials and Methods

2.1. Cell culture protocol

Skin human primary cells were used to study the effects *in vitro* of 2dDr, E2, and AV in solution on metabolic activity and cell proliferation. These cells were also used to fabricate skin tissue engineering models (as described on chapter IV), to test the effects of the microtopographies of the TCES to mimic the rete ridges.

2.1.1. Preparation of cell culture medium

Green's medium, MesenPRO RS™ medium (12746012, Thermo Fisher), and supplemented Dulbecco′s Modified Eagle′s medium (referred only as DMEM) were prepared using the following supplement list (Table 16). Reagents were purchased from Sigma (UK) unless specified.

Table 16. Supplement list that shows the concentrations and reagents used to prepare each cell medium.

Supplement	Green's medium	DMEM	MesenPRO RS™
MesenPRO RS™ Growth Supplement	N/A	N/A	10 mL
Basal liquid medium (MesenPRO RS™ Basal Medium)			500 mL
Foetal calf serum (Biowest Biosera)	10% v/v		N/A
Penicillin- streptomycin	100 IU/mL - 100 mg/mL		

Amphotericin B	0.625 µg/mL		
Ham's F12 (N4888)	3:1 v/v	N/A	
DMEM AQ media (D0819)	DMEM AQ : Ham's F12	N/A	
L-glutamine	N/A	2 mM	
Bovine insulin	5 µg/mL		
Adenine	6.25 µg/mL		
3,3′,5-Triiodo-L-thyronine/ Apo-Transferrin	0.2 µM / 5 µg/mL	N/A	
Hydrocortisone	0.4 µg/mL		
EGF	10 ng/mL		
Cholera toxin	8.5 ng/mL		

2.1.2. Isolation of primary cells and preparing decellular de-epidermized dermis

The human skin was used to isolate dermal fibroblasts, dermal keratinocytes, and adipose derived stem cells. The skin was obtained from patients undergoing elective breast reductions and abdominoplasties who gave informed consent for use of their excised skin for research purposes through the Sheffield hospital directorate of Plastic, Reconstructive Hand and Burns surgery research ethics number 15/YH/0177 under the Human Tissue Authority 12179.

First, on the day of arrival tissue details were recorded and a batch number was created. This batch number was recorded for all experiments for traceability purposes. The skin graft was processed by Dr. Victoria Workman and Mrs. Vanessa Singleton to separate adipose tissue and the dermal

component. This skin harvest process as well as the isolation of primary cells were carried on inside a class II biosafety cabinet using sterile instruments.

For the skin harvest, a styrofoam board previously covered with sterile plastic was used to secure one end of the skin biopsy using several 21G hypodermic needles. After manually stretching the other side of the biopsy, a number 22 sterile blade was used to create a 2 mm thickness biopsy. This resulting split thickness skin biopsy was stored at 4 ℃ in PBS + 1% Penicillin- streptomycin + 0.625 µg/mL amphotericin B for no more than 7 days.

Isolation and culture of primary human epidermal keratinocytes and primary human dermal fibroblasts were performed using the method described by Gosh et al. [353]. The skin biopsy that was not used for cell isolation was treated to create decellular de-epidermized dermis (DED).

DED was prepared by incubating the skin biopsy with a 1 M NaCl solution at 37℃ for 8 to 12 h. After incubation, the skin biopsy was transferred to a petri dish and the epidermal component was removed using sterile forceps. The DED was transferred to a 180 mL container with fresh Greens medium and stored in a human tissue fridge.

2.1.3. Isolation and culture of primary human epidermal keratinocytes

Primary human epidermal keratinocytes (HDK) were isolated by transferring the skin biopsy to a sterile petri dish containing PBS where it was cut into small square pieces about 5 – 6 mm using a scalpel. The skin pieces were transferred to a universal tube containing 10 mL of Difco-Trypsin and incubated at 4 ℃ for 18 h. After incubation, skin pieces were transferred to a petri dish containing 10 mL of Green's medium, and the epidermis was peeled off by holding down the dermis with forceps and using a scalpel to gently scrape the epidermal layer. After removing the

epidermis, the top part of the dermis was scraped with a scalpel to remove basal keratinocytes (this process was repeated for all skin pieces). The remains of the dermis were transferred to a universal tube containing Green's medium. After removing the epidermis for all pieces, the medium from the petri dish was centrifuged at 1000 rpm for 5 min and the pellet was resuspended with 4 mL of Green's medium. This cell suspension was seeded on T-75 flasks by transferring 1 mL per flask containing 12 mL of Green's medium. Cells were incubated at 37°C in a 5% CO_2 humidified atmosphere.

Immediately after HDK seeding, irradiated 3T3 cells (i3T3) were seeded into each flask as a feeder layer for the culture [354]. These i3T3s were cultured and cryopreserved by Mrs Vanessa Singleton (cell density for each vial was approximately of $1x10^6$ cells) and irradiated with gamma rays (60 greys). To seed the i3T3s, each vial was retrieved from the liquid nitrogen to be defrosted and resuspended with 10 mL of Green's medium and then centrifuged at 1000 rpm for 5 min. For each flask of HDK, one vial of i3T3s was added.

Cell medium was changed every two days until confluence was reached, if a low-density feeder layer was noticed, another vial of i3T3s was added as described before. Cell passaging was performed by removing the cell medium and then washing with 5 mL of PBS, followed by a 5 min incubation with ethylenediaminetetraacetic acid (EDTA) solution (E8008, Sigma) to remove the feeder layer. Once the i3T3s were detached, EDTA was removed, and cells were incubated with 5 Trypisin-EDTA (T3924, Sigma) for 10 min. After incubation, cells were washed with 10 mL of Green's medium and transferred to a universal tube to be centrifuged at 1000 rpm for 5 min. The supernatant was removed using a stripette without disturbing the pellet and cells were reseeded at a ratio of 1:4 into T75 flasks with 12 mL of Greens media each. For every new flask of HDK, a

new vial of i3T3s was added as described before. HDK were used no further than passage 4 for all experiments.

2.1.4. Isolation and culture of primary human dermal fibroblasts

Human dermal fibroblasts (HDF) were isolated after removing the epidermal component of the skin biopsy (as described in methods section 2.1.3). The dermal component was placed in a petri dish (about 3 x 3 cm) and minced into pieces of 1 mm^2 using a sterile scalpel. The minced dermis was incubated in 10 mL of collagenase A for 18 h at 37ºC. Right after incubation, the digested dermis was washed with 10 mL of DMEM and transferred to a new universal tube to be centrifuged at 2000 rpm for 10 min. The supernatant was removed without disturbing the pellet using a stripette. The pellet was resuspended in 7 mL of DMEM and transferred to a T-25 flask. Cell medium was changed every 3 days until confluence was reached and cells needed to be passaged to a T-75 flask. Cell passage was performed by washing the flask with 5 mL of PBS and adding 3 mL of Trypsin-EDTA for a T-25 flask or 5 mL for a T-75 flask. After 5 min incubation with Trypsin-EDTA, 10 mL of DMEM were used to wash the cells, and then the cell suspension was transferred to a universal tube to be centrifuged at 1000 rpm for 5 min. The supernatant was removed without disrupting the pellet using a stripette and cells were reseeded at a ratio of 1:3 into new T-75 flasks with 10 mL of DMEM. HDF were used between passages 4 to 9 for all experiments. Cells were incubated at 37°C in a 5% CO_2 humidified atmosphere.

2.1.5. Isolation of adipose derived stem cells

Adipose tissue was placed in a petri dish with 10 mL of PBS + 10% Penicillin- streptomycin. The sample was manually minced until it reached an almost liquid composition using a scalpel. The samples were collected in a universal tube and washed with 10 mL of PBS + 1% Penicillin-

streptomycin. The samples were centrifuged at 1300 rpm for 5 min and the tissue was transferred to a new centrifuge tube using a Pasteur pipette. A saline solution (HANK solution) containing 0.1% collagenase type A, 0.1% albumin bovine fetal serum, and 1% Penicillin- streptomycin was added at a 1:2 ratio in relation to the sample volume. This solution was incubated for 40 min at 37°C and shaken every 10 min to aid chemical disaggregation. After incubation, the digested solution was centrifuged at 1300 rpm for 8 min. The floating fractions consisting of adipose cells were discarded and the stromal vascular fraction (SVF) was resuspended in DMEM medium. The SVF was washed with cell medium and centrifuged at 1300 rpm for 8 min with 15 mL of DMEM. Finally, the resulting pellet was resuspended with 5 mL of MesenPRO RS™ medium and transferred to a T25 flask. Cells were incubated at 37°C in a 5% CO2 humidified atmosphere.

After 24 h incubation, the cell medium was discarded, and the flask was washed with PBS to remove non-adherent cells. Cell medium was changed every 2 days until confluence was reached and cells needed to be passaged to a T-75 flask. Cell passage was performed by washing the flask with 5 mL of PBS and adding 3 mL of Trypsin-EDTA (T3924, Sigma) for a T-25 flask or 5 mL for a T-75 flask. After 5 min incubation, 10 mL of DMEM were used to wash the cells, and then the cell suspension was transferred to a universal tube to be centrifuged at 1000 rpm for 5 min. The supernatant was removed without disrupting the pellet using a stripette and cells were reseeded at a ratio of 1:3 into new T-75 flasks with 10 mL of MesenPRO RS™ medium. AdSCs were used between passages 2 to 8 for all experiments. Cells were incubated at 37°C in a 5% CO_2 humidified atmosphere.

2.1.6. Cryopreservation of skin primary cells

Once 80% cell confluency was reached, the cell medium was discarded, and flasks were washed with PBS twice. 5 mL of Trypsin-EDTA were added to each flask and incubated for 5 to 7 min at 37°C in a 5% CO_2 humidified atmosphere. After the incubation, cells were gently tapped to encourage detachment from the flask. Once detached, 10 mL of the corresponding cell medium were added to the flask and the solution was transferred to a universal tube and centrifuged at 1000 rpm for 5 minutes. Immediately after centrifugation, the supernatant was discarded, and the cells were resuspended with 1 mL of cell medium. Cells were then counted using a hematocytometer. Freezing media (FBS + 10% DMSO) was added accordingly to the cell suspension to reach a cell density of approximately 1 x 10 ^{6} cells/mL. Labeled cryovials were used to hold 1 mL of the freezing media + cells suspension. These cryovials were transferred to the -80°C. If needed for long-term storage, cells were transferred into liquid nitrogen.

2.2.   *In vitro* cell culture to evaluate bioactive compounds

The effects in cell viability and cell proliferation *in vitro* of 2dDr, E2, and AV in solution were assessed using the metabolic activity resazurin reduction assay and the DNA quantification Picogreen^{TM} assay, respectively. Additionally, the effects of 2dDr on AdSC cell migration were studied using a simple scratch migration assay. Three independent tests were performed by triplicate for each experiment (N = 3, n = 3).

2.2.1. Seeding skin primary cells for in vitro testing

One day before the experiment, bioactive compound solutions were prepared by creating a stock solution with a concentration two times higher than the maximum concentration tested *in vitro* for

that cell type. To create this stock solution, the selected compound was weighed, and the corresponding cell medium was added inside a class II safety cabinet. In the case of E2 solutions, 500 µL of DMSO were added to solubilize the molecule before mixing with the cell medium. As a result, a 1% DMSO on cell medium was introduced as a control for E2 experiments. The stock solutions were then filter-sterilized with a 0.2 µm syringe filter (Filtropur S Sarstedt AG & Co, 83.1826.001, Germany) and kept at 4°C for no more than 10 days. The concentrations tested were selected based on the maximum possible concentration to be released from an average 1.5 x 1.5 electrospun scaffold.

On the day of the experiment, the stock solution was diluted with the corresponding cell medium as necessary to create different concentrations. Tested concentrations of bioactive compounds are shown in Table 17. Cells were cultivated in 48-well plates as described in methods sections 2.1.3 (HDK), 2.1.4 (HDF), and 2.1.5 (AdSC). In the case of HDK, i3T3s were replaced by HDF. Cell densities used for each cell type are shown in Table 17. Different well plates were used for each time point due to the destructive nature of the Picogreen^{TM} assay.

The concentrations of bioactive compounds used for in vitro testing were lower than the maximum amount of compound loaded into the scaffolds. The rationale for this is that the release profile of the scaffolds varies and that the amount of media use would also alter the final concentration between experiments (for example when implanted on skin models). Therefore, it was decided to use lower concentrations of compounds that could easily be delivered by the scaffolds as all of these are below the maximum concentration threshold before the electrospinning solution is impossible to electrospun.

Table 17. Concentrations and cell densities tested to study the *in vitro* effects of 2dDr, E2, and AV on different cell types.

Cell type (s)	Bioactive compound	Cell density	Concentrations
HDF	2dDr	3200 cells/cm2	10, 50, 100, 500, 1000 µM
	E2		10, 50, 100, 200 µM
	AV		1, 5, 10, 20, 50 mg/mL
HDF + HDK	2dDr	HDK = 2400 cells/cm2 HDF = 800 cells/cm2	50, 100, 500, 1000, 1500 µM
	E2		10, 50, 100, 200 µM
	AV		1, 5, 10, 20, 50 mg/mL
AdSC	2dDr	3200 cells/cm2	50, 100, 500, 1000, 1500 µM

2.3.   Assessment of *in vitro* cell metabolic activity

A resazurin salt stock solution (R7017, Sigma) was prepared prior to the experiment. The necessary amount of resazurin was weighted to prepare 100 mL of a 1mM concentration. The resazurin powder was then transferred to a sterile universal tube and 10 mL of sterile PBS were added and then filter-sterilized with a 0.2 µm syringe filter (Filtropur S Sarstedt AG & Co, 83.1826.001, Germany). To complete the final volume, the sterilized resazurin solution was placed in a 180 mL container and 90 mL of sterile PBS were added. This stock solution was covered from light using aluminum and stored at 4°C for no more than 6 months. On the day of the experiment, a 10% v/v resazurin + cell medium working solution was prepared using the resazurin stock

solution. The cell medium of each well was discarded and replaced with 800 µL of the resazurin working solution. Samples were incubated 37°C in a 5% CO_2 humidified atmosphere.

After an incubation period of 4 h, 200 µl of each well were collected by triplicate and transferred to a 96-well plate. The fluorescence signal of the samples was read using a spectrophotometer (FLx800, Bio-Tek Instruments Inc.) and KC4 software (version 3.3, Bio-Tek Inc.) set for an λex = 540 nm and λem = 630 nm. The resazurin assay was performed on days 1, 4, and 6.

2.4. Assessment of *in vitro* cell proliferation

As preparation for the assay, a 1x Tris-EDTA (TE) buffer was prepared from the 20x 200 mM Tris-HCl - 20 mM EDTA (pH 7.5) buffer included on the Invitrogen™ Quant-iT™ PicoGreen™ dsDNA assay kit (P758, Fisher). This 1x TE buffer (refer from now on only as TE) was used to prepare the Picogreen™ working solution by diluting the 200-fold 100 µL aliquot with 19.9 mL of TE buffer. The Picogreen™ working solution was covered from light using aluminum foil and was kept at 4°C for no more than 1 month.

Immediately after evaluating cell metabolic activity, the remaining resazurin solution was discarded and samples were washed with PBS before adding 250 µL of the TE buffer on each well. Next, the plate was covered with parafilm paper on the edges and placed inside a -80°C freezer for 15 min to induce cell lysis using the freeze–thaw method. Samples were retrieved and defrosted using a water bath. Once completely defrosted, 250 µL of the Picogreen™ working solution were added and incubated for 5 min at RT. After incubation, 150 µL were taken by triplicate per sample and transferred to a 96-well plate.

Sample fluorescence was read at λex = 480 nm and λem = 520 nm using a spectrophotometer plate reader (FLx800, Bio-Tek Instruments Inc.) and KC4 software (version 3.3, Bio-Tek Inc.). The Picogreen^{TM} assay was always performed using the same samples used for the metabolic activity assay.

2.5. Assessment of *in vitro* cell migration

AdSC cell migration was assessed using the scratch assay. First, 50,000 cells were seeded into 6-well plates (5200 cells/cm^2) as described in methods section 2.1.5. The cells were left to incubate for 24 h before starting the scratch assay. On the day of the experiment, a scratch was made using a 1 mL pipette tip. Finally, medium was changed to DMEM supplemented with 2dDr at 50, 100, 500, and 1000 µM concentrations, with pure DMEM used as a control. Photographs of the scratch were taken using an optical Motic microscope with a 10x magnification lens and a digital camera at 0, 1, 3, 6, 20, 24, and 30 hours. Two independent tests were performed by triplicate for each experiment (N = 3, n = 3). ImageJ software v. 1.48 from NIH (National Institutes of Health, USA) [292], was used to measure the size of the scratch at the different time points. Images were analyzed by creating a black and white composite using ImageJ IsoData threshold function.

2.6. *In vitro* cell imaging

Changes in cell morphology *in vitro*, when exposed to different bioactive compounds, were studied using fluorescence microscopy. Following the procedure described in methods section 2.2, cells were seeded at the appropriate cell density and exposed to different concentrations of 2dDr, E2, and AV on the same day when the metabolic and proliferation assays (sections 2.3 and 2.4 respectively) were performed.

146

2.6.1. *Fixation and staining*

Right after completing both metabolic and proliferation assays, cells were fixed at RT by washing the samples with PBS and adding 1 mL of 3.7% paraformaldehyde per sample for 45 minutes. After fixation, formaldehyde was discarded, and samples were washed with PBS. To permeabilize the cell membrane, PBS was removed and 1 mL of 0.1% Triton-X100 was added to each well and incubated for 30 minutes at RT. To stain the samples, the triton solution was removed and samples were washed with PBS twice and 1 mL of a 1µg/mL (stock solution 300mM, dilution 1:1000) DAPI (4',6-diamidino-2-phenylindole) and phalloidin-TRITC (Tetramethylrhodamine isothiocyanate) solution was incubated for 1 h at RT covered from light using aluminum foil. After incubation, the staining solution was discarded, and samples were washed with PBS twice and stored at 4°C. (nuclei and F actin)

2.6.2. *Epifluorescence microscopy and image analysis*

The samples were imaged using an Inverted Olympus IX73 (Olympus, UK) with a 10x objective. Excitation wavelengths of 358 nm for DAPI and 540 nm for phalloidin-TRITC were used with exposure times ranged from 70-150 ms for DAPI and 800-900 ms for phalloidin TRITC. Three images were taken from the sample at different positions of the well. ImageJ software v. 1.48 from NIH (National Institutes of Health, USA) [292], was used to combine both DAPI and phalloidin-TRITC channels.

2.7. Chick chorioallantoic membrane assay

The performance of RES as carriers of 2dDr, E2, and AV was studied using the *ex ovo* chick chorioallantoic membrane (CAM) assay as described by Mangir et al. [167]. Pathogen-free

fertilized white leghorn chicken eggs (*Gallus gallus domesticus*) obtained from Henry Stewart Co. Ltd (UK) were incubated and handled under the guidelines of the Home Office, UK ((in compliance with UK Home Office Animals [ScientificProcedures] Act 1986 and definition of chicken as a Protected Animal from development day 14). The temperature of the eggs was recorded every day and damaged specimens were disposed of accordingly. The eggs were stored at 10°C for no more than 10 days until the experiment started. Figure 57 shows the schematic representation of the CAM methodology used to evaluate angiogenic activity.
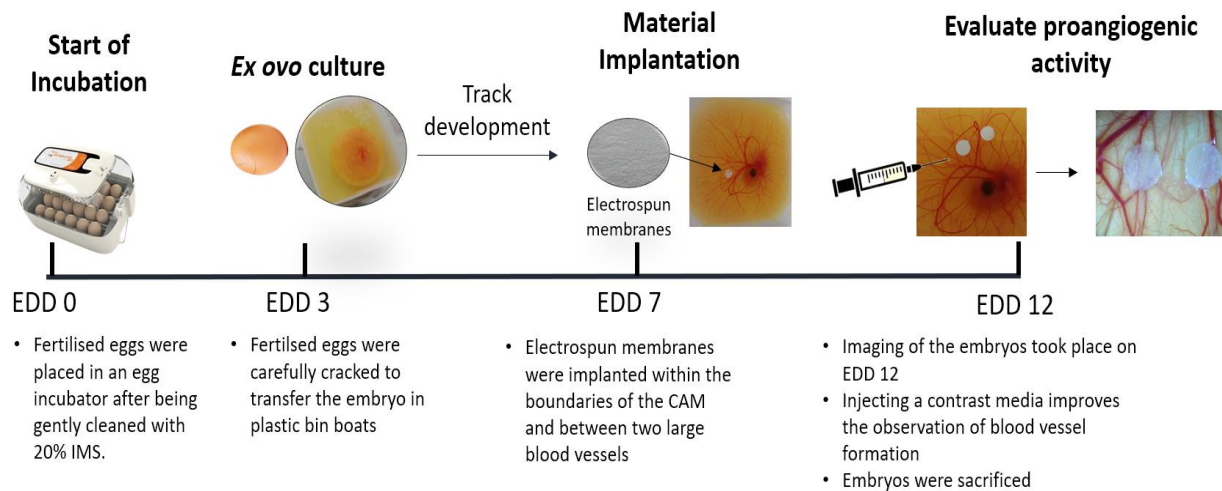
Figure 57. Schematic representation of the CAM methodology used to evaluate proangiogenic activity.

2.7.1. *Chick embryo incubation*

On embryonic development day (EDD) 0, eggs were gently cleaned with a 20% industrial methylated spirit (IMS) solution (Fisher Scientific, UK), and incubated in a humidified hatching incubator (Rcom King Suro Max-20, P&T Poultry) at 38°C. These incubators were previously cleaned using 70% IMS and left to air-dry inside a class II biosafety cabinet for 24h. A 120 mL

pot was put inside each incubator to hold 50 of dH$_2$0 to maintain a humidified environment throughout the incubation period. Two independent tests were performed with 5 samples per experiment (N = 2, n = 5).

2.7.2. *Ex-ovo culture*

Cracking of the eggshells was executed on EDD 3. Before the cracking, the edges of 100 mL square weigh boats (Starlabs, UK) were cut, and the boats were cleaned with 70% IMS followed by a wash with PBS. The weighting boats were placed inside sterile petri dishes and filled with 3 mL of PBS + 1% penicillin- streptomycin solution (100 IU/mL - 100 mg/Ml). On the day of cracking, the incubator was stopped, and the eggs were marked with a pen on the top side of the egg to signal where the embryo would be during the cracking. After stopping the incubator, the eggs were left for 10 min before doing the cracking. The eggs were cracked inside the weighting boats and placed immediately after inside a humidified incubator (Binder, Tuttlingen) at 38°C.

The embryos were left inside the incubator for the rest of the experiment (from EDD 3 to EDD 12). Embryos were checked daily for any malformation or infection. Damaged embryos were disposed of accordingly.

2.7.3. *Implantation of scaffolds and application of bioactive compound*

The RES used for this experiment were fabricated as described in chapter II section 2.3.1. Table 18 shows the concentrations of bioactive compounds and materials tested. Electrospun scaffolds were implanted on EDD 7 using 8 mm disks cut from the electrospun mats and implanted within the boundaries of the CAM. Additionally, for the control groups 8 mm ID silicone rings were used

to hold VEGF, 2dDr, E2, and AV solutions. These rings were sterilized with 70% IMS and washed with PBS before being implanted on the CAM.

Table 18. Materials and concentrations of bioactive compounds used to fabricate RES and test their angiogenic potential on the CAM assay.

Polymer	Bioactive compound	Concentration
N/A	2dDr	250 µM
		1000 µM
	E2	500 µM
	AV	20 mg/mL
	VEGF	60 ng/day
PLGA 50:50	N/A	N/A
	2dDr	10% wt.
		15% wt.
PCL	N/A	N/A
	2dDr	10% wt.
		15% wt.
	E2	10% wt.
	AV	10% wt.
	AV + 2dDR	10% + 8% wt.

2.7.4. *Imaging and analysis of angiogenesis*

On EDD 12, images were captured using a digital camera and MicroCapture software (version 2.0). To increase the contrast between the blood vessels and the sample, a white hydrating body cream (Neutrogena, UK) was injected into the surrounding area of the sample (Figure 58). This media contrast was not injected directly into the surrounding area but rather carefully injected from a corner area to avoid any damage to the blood vessels surrounding the sample.
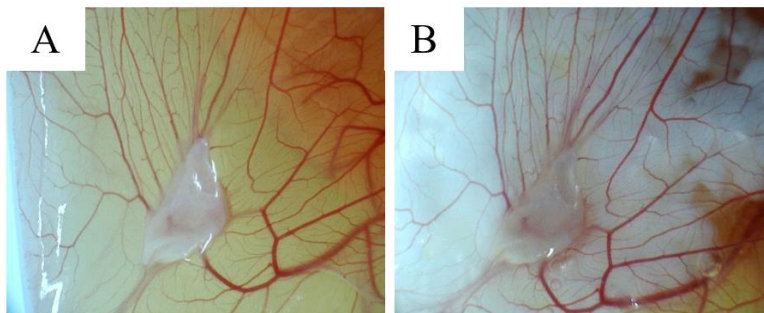
Figure 58. Comparison of vessel visibility between an electrospun scaffold implanted on CAM without media contrast (A) and the use of media contrast (B).

After imaging, embryos were sacrificed by either decapitation or bleeding. ImageJ software v. 1.52 [292] was used to process and analyze blood vessel formation. The image was split in into its RBG components, preserving the green channel for "Mexican Hat" filtering, contrast-enhancing, and unmask filtering. The resulting image was then transformed to binary and processed using the vessel analysis tool [355] to quantify vascular density. Figure 59 shows an overview of the image processing used to analyze the CAM data.
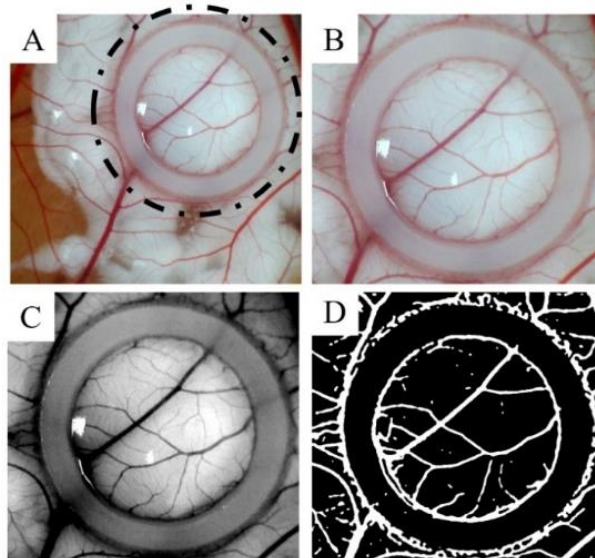
Figure 59. Image processing used to analyze the CAM data. First, the image was cut (A-B) followed by enhancing the contrast (C) to create a black and white image that was used to quantify the vessels (D).

2.8. Statistical analysis

GraphPad Prism software (version 9.1) was used to perform statistical analyses using one-way and two-way analysis of variance (ANOVA) as applicable, followed by Tukey's multiple comparisons tests. In all cases, p values <0.05 were considered statistically significant.

3. Results

3.1. HDF viability and proliferation when exposed to bioactive compounds

The effects in metabolic activity and cell proliferation for skin cell types HDF, HDK, and AdSC, when exposed to solubilized 2dDr, E2, and AV, were successfully assessed using the resazurin assay, the Picogreen^{TM} quantification assay, and fluorescence imaging. The results in this thesis showed that cell response was dosage-dependent for all three bioactive compounds.

152

In the case of HDF, fluorescence microscopy images showed that concentrations of all the 2dDr concentrations tested have a positive effect on cell proliferation and do not affect cell morphology (Figure 60). The resazurin assay showed that concentrations of 2dDr below 500 µM have a positive effect on metabolic activity when compared with the control group across all the time points measured (Figure 61). However, a 1000 µM concentration did not show any significant differences in metabolic activity at day 6 when compared against the control group. The proliferation assay confirmed that all 2dDr concentrations tested have a positive effect on HDF proliferation at days 4 and 6 (Figure 60). Interestingly, the 1000 µM 2dDr concentration showed the highest cell proliferation, whereas the lowest 10 µM concentration showed the highest increase in metabolic activity and a slight increase in cell proliferation when compared to the control group.
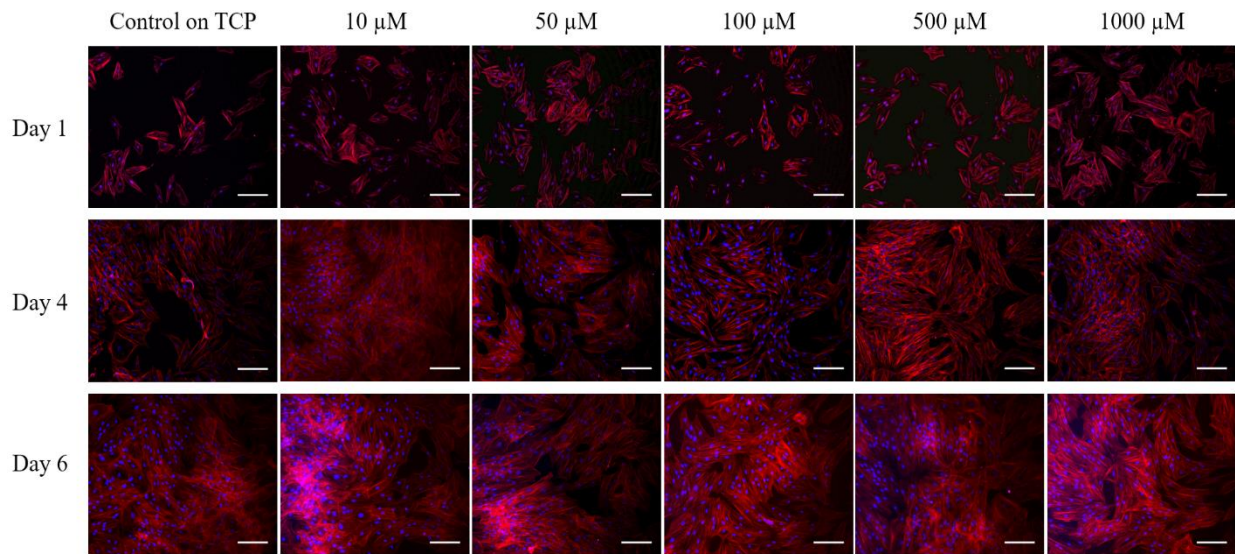
Figure 60. Images of HDF when cultured with different concentrations of solubilized 2dDr for 1, 4, and 6 days. Cells were stained for F-actin filaments (phalloidin-TRITC - red) and cell nuclei (DAPI - blue). Scale bar = 200 µm.
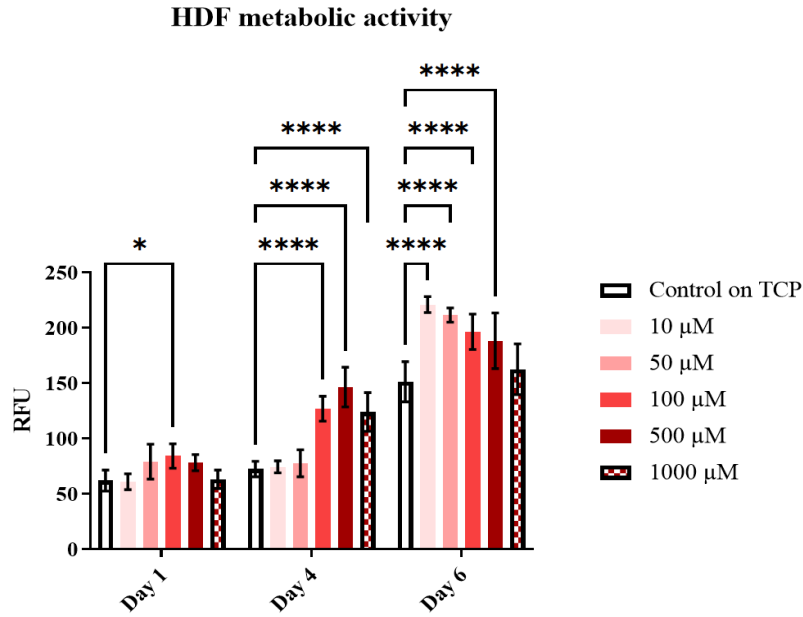
Figure 61. Metabolic activity of HDF seeded with different concentrations of 2dDr for 6 days. Results are shown as mean ± SD. Two-way ANOVA statistical analysis with Tukey comparison test. **** $p < 0.0001$, * $p < 0.05$. N=3, n=3.
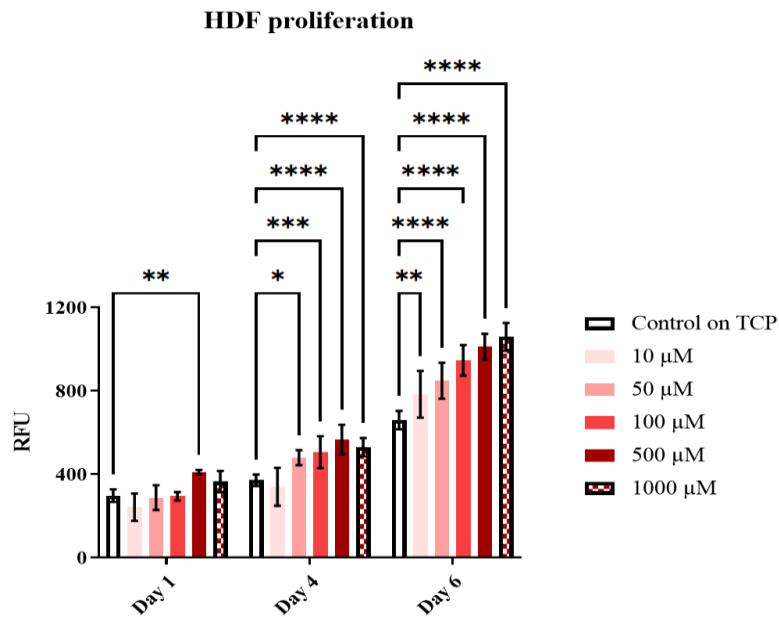
Figure 62. Cell proliferation of HDF seeded with different concentrations of 2dDr for 6 days. Results are shown as mean ± SD. Two-way ANOVA statistical analysis with Tukey comparison test. **** $p < 0.0001$, ** $p < 0.01$, * $p < 0.05$. N=3, n=3.

Regarding HDF exposed to solubilized E2, our results showed that concentrations above 50 µM have a significant negative effect on cell metabolic activity and proliferation. This behavior was observed on the fluorescence images (Figure 63), and metabolic (Figure 64), and proliferation (Figure 65) assays. For the 100 µM and 200 µM concentrations of E2, the final DMSO concentration was about 0.4% and 0.8% respectively. Therefore, the inclusion of a 1% DMSO control confirmed that the decrease in metabolic activity and proliferation of HDF at concentrations higher than 50 µM was not related to the presence of DMSO but rather the high concentration of E2. The metabolic and proliferation assays showed that the 10 µM concentration of E2 had no significant effect on cell behavior when compared to the control group across days 1, 4, and 6, and therefore was considered non-cytotoxic.
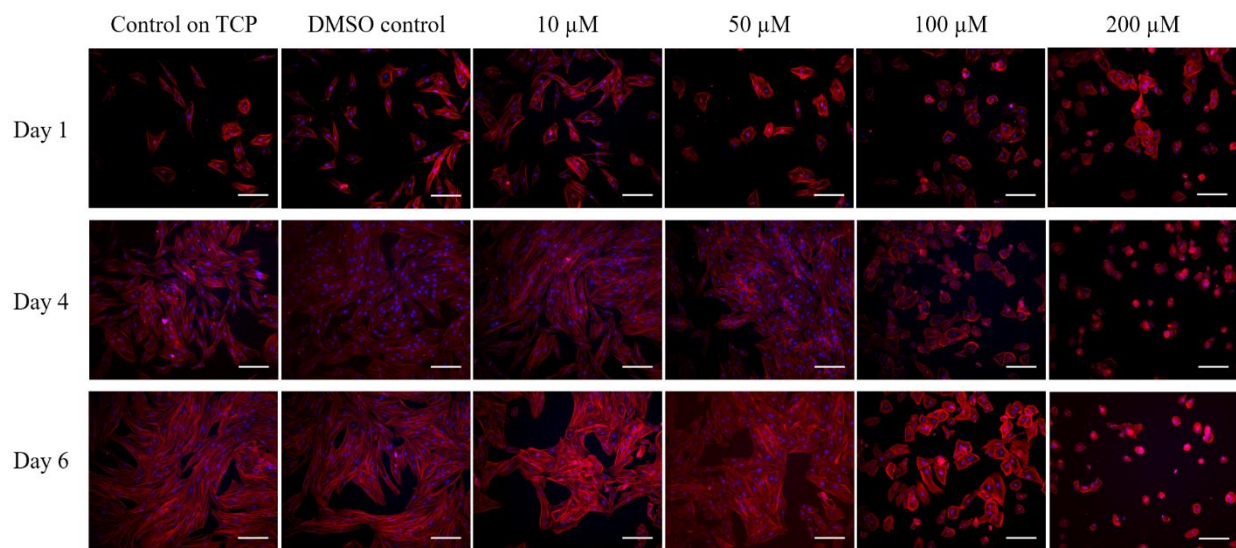
Figure 63. Images of HDF when cultured with different concentrations of solubilized E2 for 1, 4, and 6 days. Cells were stained for F-actin filaments (phalloidin-TRITC - red) and cell nuclei (DAPI - blue). Scale bar = 200 µm.
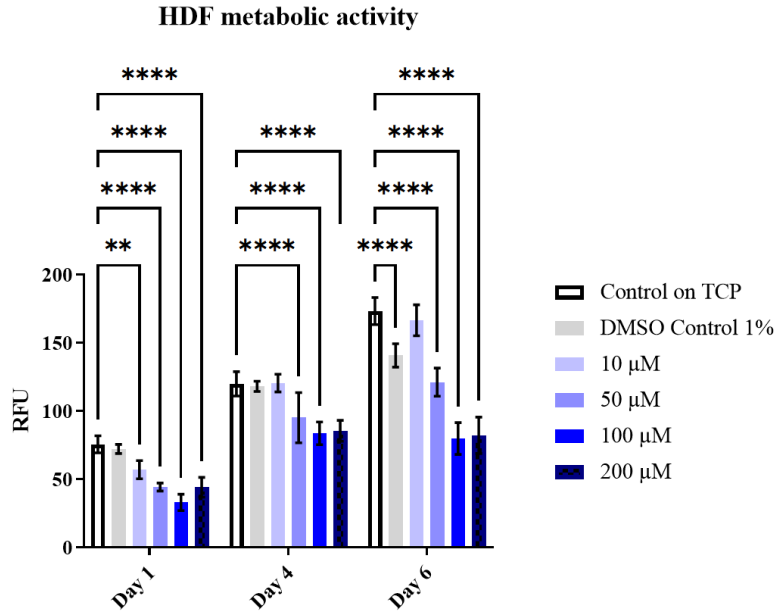
Figure 64. Metabolic activity of HDF seeded with different concentrations of E2 for 6 days. Results are shown as mean ± SD. Two-way ANOVA statistical analysis with Tukey comparison test. **** p < 0.0001, ** p < 0.01. N=3, n=3.
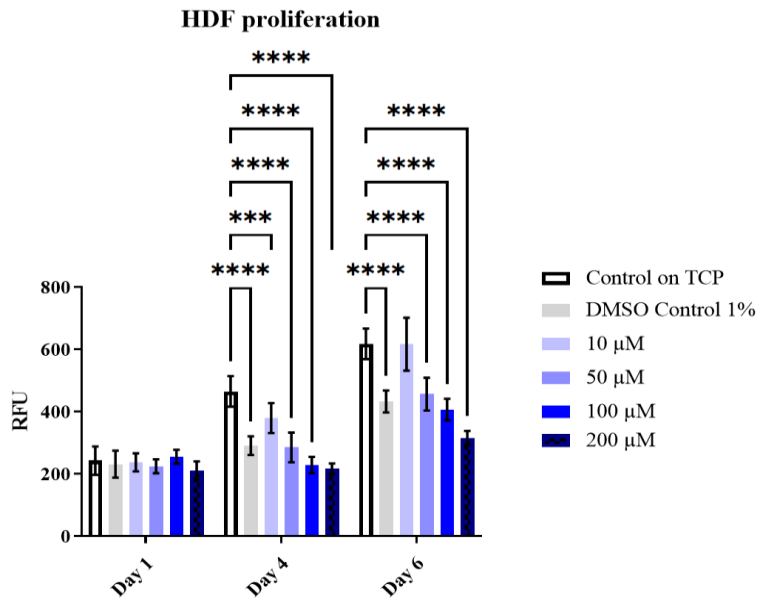
Figure 65. Cell proliferation of HDF seeded with different concentrations of E2 for 6 days. Results are shown as mean ± SD. Two-way ANOVA statistical analysis with Tukey comparison test. **** p < 0.0001, *** p < 0.001. N=3, n=3.

The presence of AV into the HDF culture proved to increase the metabolic activity and for concentrations below 5 mg/mL. Fluorescence images (Figure 66) showed a clear increase in the number of cells for the 1 mg/mL concentration when compared to the control and showed that the 10, 20, and 50 mg/mL concentrations hindered cell proliferation. Additionally, fluorescence images showed a slight change in cell morphology for HDF exposed to concentrations higher than 5 mg/mL. These results were also observed on the metabolic (Figure 67) and proliferation (Figure 68) graphs where the 20 and 50 mg/mL showed values near to zero and thus were considered cytotoxic for HDF across all time points. However, a concentration of 1 mg/mL of AV almost doubled the cell proliferation at day 6 when compared to the control, further proving its dosage-dependent response.
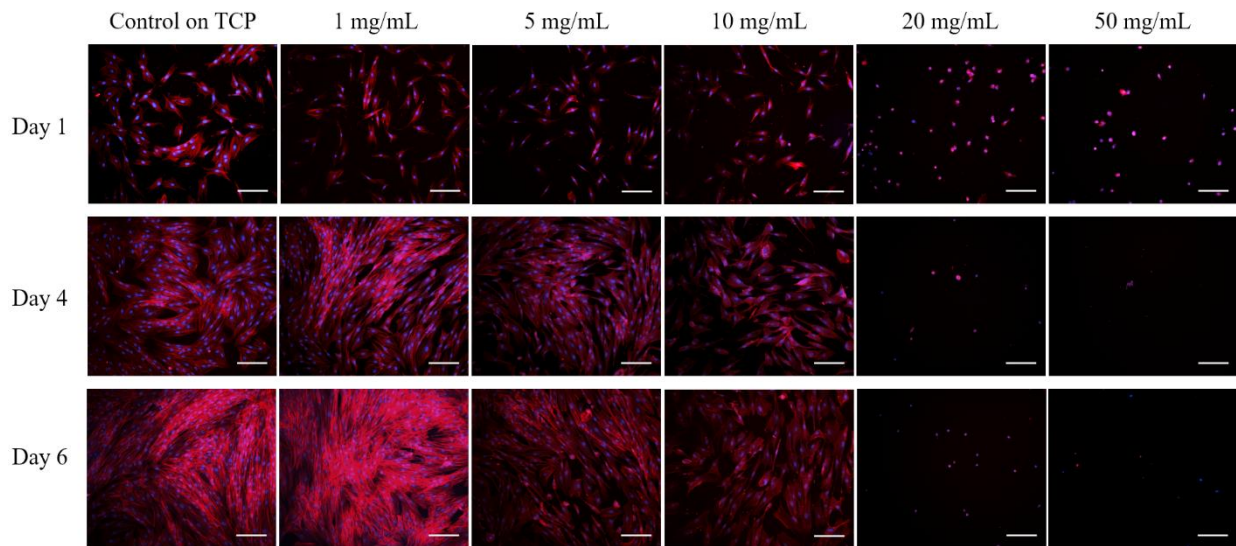
Figure 66. Images of HDF when cultured with different concentrations of solubilized AV for 1, 4, and 6 days. Cells were stained for F-actin filaments (phalloidin-TRITC - red) and cell nuclei (DAPI - blue). Scale bar = 200 µm.
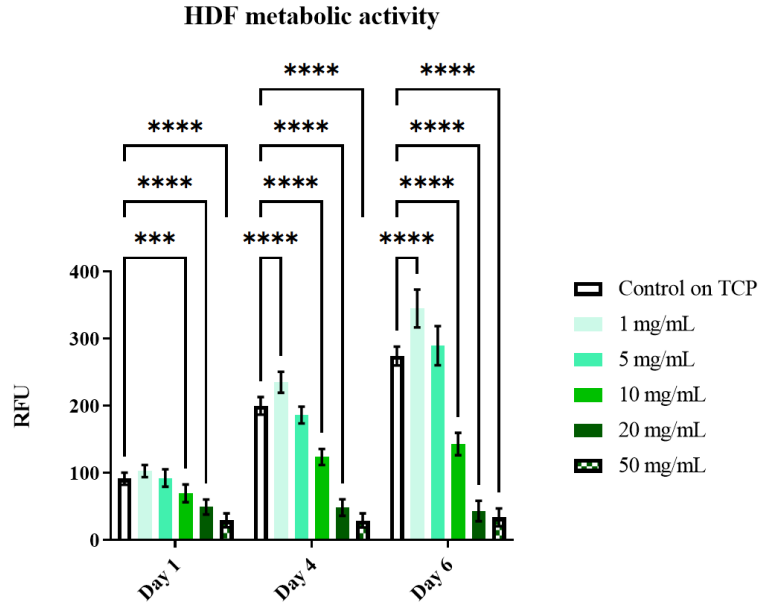
Figure 67. Metabolic activity of HDF seeded with different concentrations of AV for 6 days. Results are shown as mean ± SD. Two-way ANOVA statistical analysis with Tukey comparison test. **** $p < 0.0001$, *** $p < 0.001$. N=3, n=3.

Figure 68. Cell proliferation of HDF seeded with different concentrations of AV for 6 days. Results are shown as mean ± SD. Two-way ANOVA statistical analysis with Tukey comparison test. **** $p < 0.0001$, ** $p < 0.01$. N=3, n=3.

3.2. HDK + HDF viability and proliferation when exposed to bioactive compounds

In contrast with the monoculture of HDF, the culture of HDK + HDF with different concentrations of 2dDr showed that none of the concentrations tested have a positive effect on metabolic activity or cell proliferation. Fluorescence images (Figure 69) do not indicate any increase or decrease in cell proliferation at any time point. Nonetheless, both metabolic (Figure 70) and proliferation (Figure 71) assays showed that the cell behavior of HDK + HDF is affected when exposed to concentrations above 500 µM, with 1500 µM showing a significant decrease in cell activity when compared to the control group.
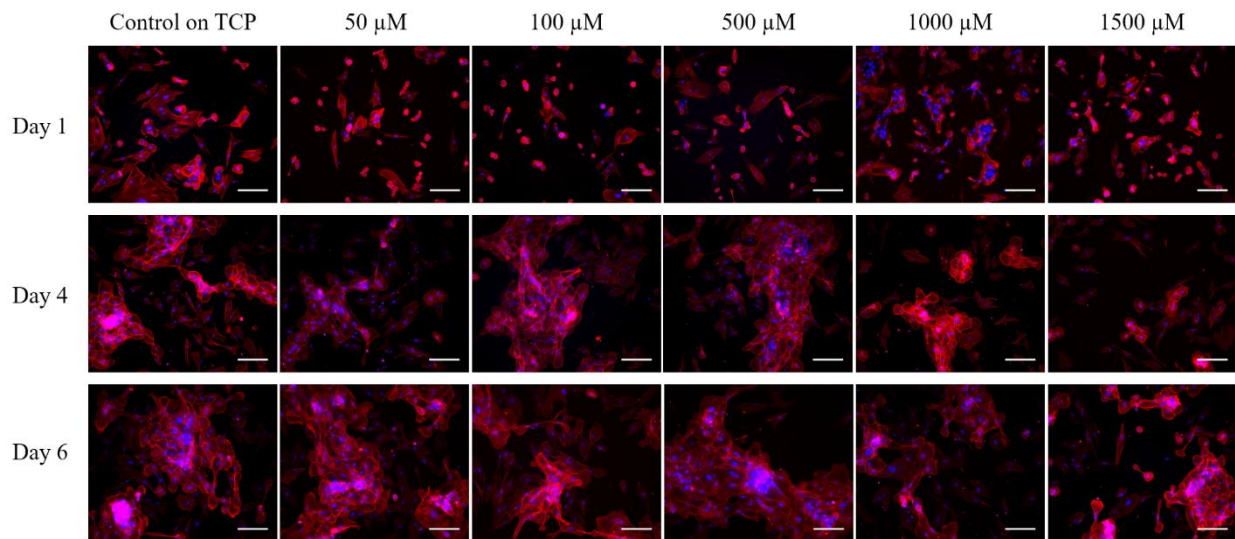
Figure 69. Images of HDK + HDF when cultured with different concentrations of solubilized 2dDr for 1, 4, and 6 days. Cells were stained for F-actin filaments (phalloidin-TRITC - red) and cell nuclei (DAPI - blue). Scale bar = 200 µm.

HDK + HDF metabolic activity
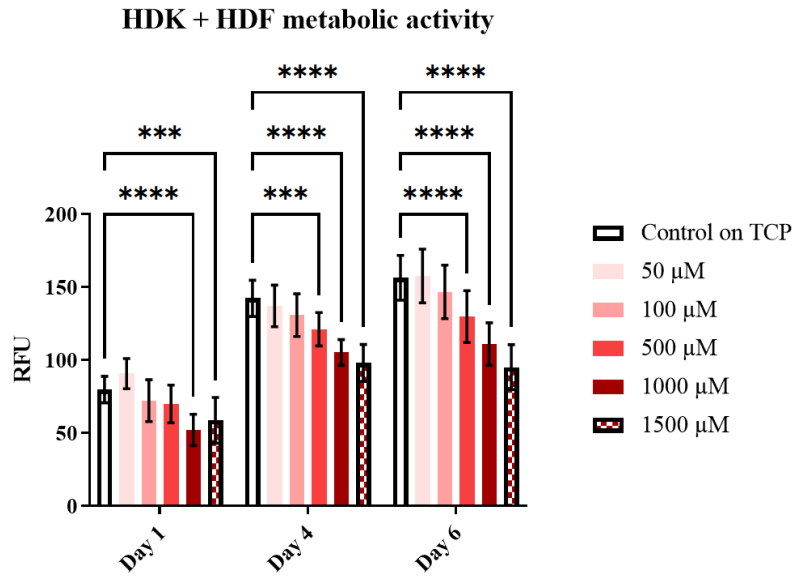
Figure 70. Metabolic activity of HDK + HDF seeded with different concentrations of 2dDr for 6 days. Results are shown as mean ± SD. Two-way ANOVA statistical analysis with Tukey comparison test **** $p < 0.0001$, *** $p < 0.001$. N=3, n=3.

HDK + HDF proliferation
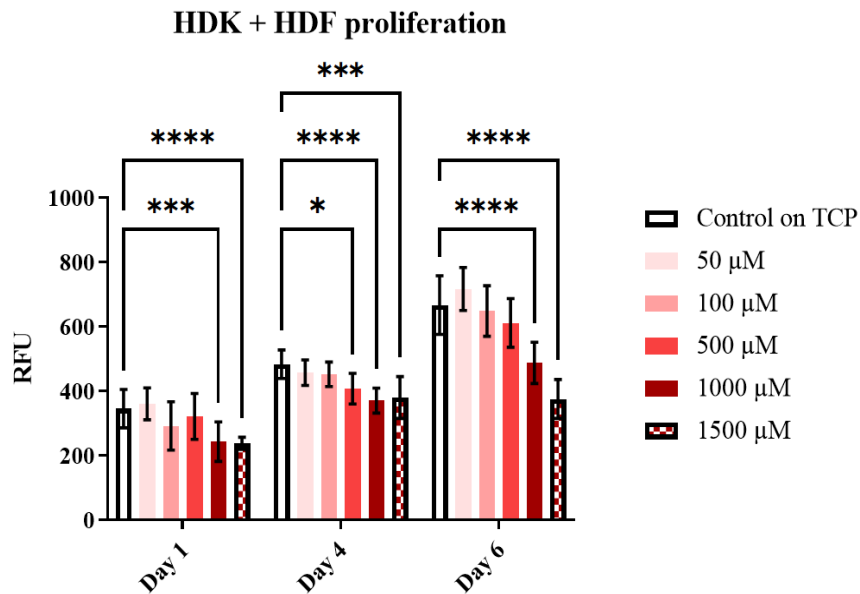
Figure 71. Cell proliferation of HDK + HDF seeded with different concentrations of 2dDr for 6 days. Results are shown as mean ± SD. Two-way ANOVA statistical analysis with Tukey comparison test **** $p < 0.0001$, *** $p < 0.001$, * $p < 0.05$. N=3, n=3.

Similar to HDK + HDF culture when exposed to solubilized 2dDr, the addition of E2 hindered both cell proliferation and cell metabolic activity. Fluorescence images showed that concentrations above 10 µM severely hindered cell proliferation and suggested that HDF were the most affected as their number seems to be lower on 50, 100, and 200 µM concentrations of E2. Figure 73 and Figure 74 showed all concentrations generate lower values of cell metabolic activity and proliferation when compared to the control group regarding the time of exposure to E2. The 1% DMSO showed similar values to the lower concentration of 10 µM suggesting that the cytotoxic effects of the E2 concentrations above 50 µM are not related to the use of DMSO to solubilize the bioactive compound.
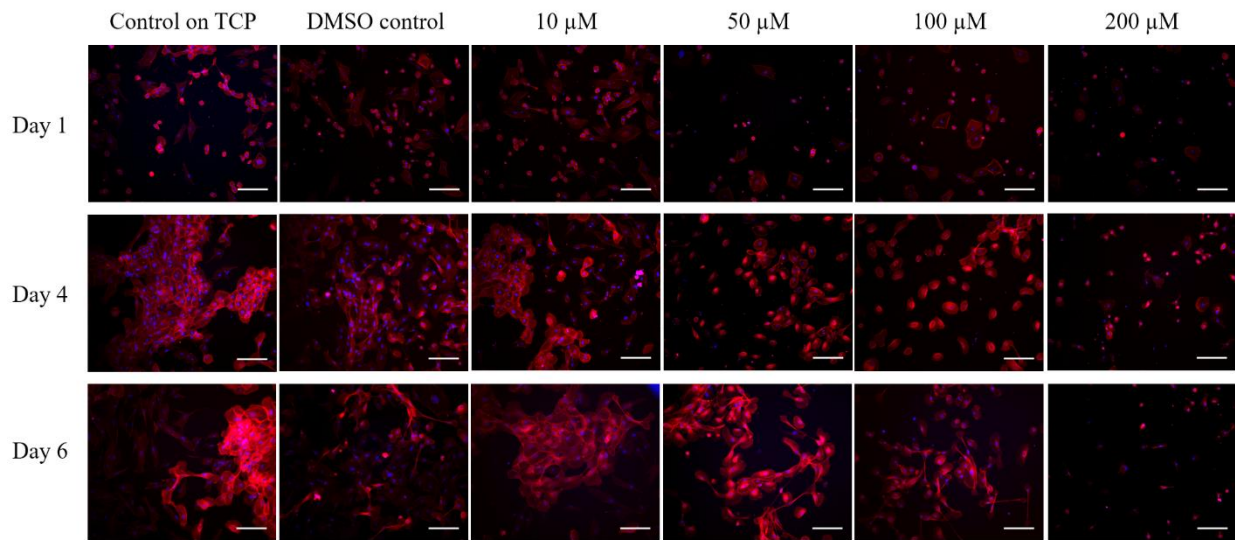
Figure 72. Images of HDK + HDF when cultured with different concentrations of solubilized E2 for 1, 4, and 6 days. Cells were stained for F-actin filaments (phalloidin-TRITC - red) and cell nuclei (DAPI - blue). Scale bar = 200 µm.
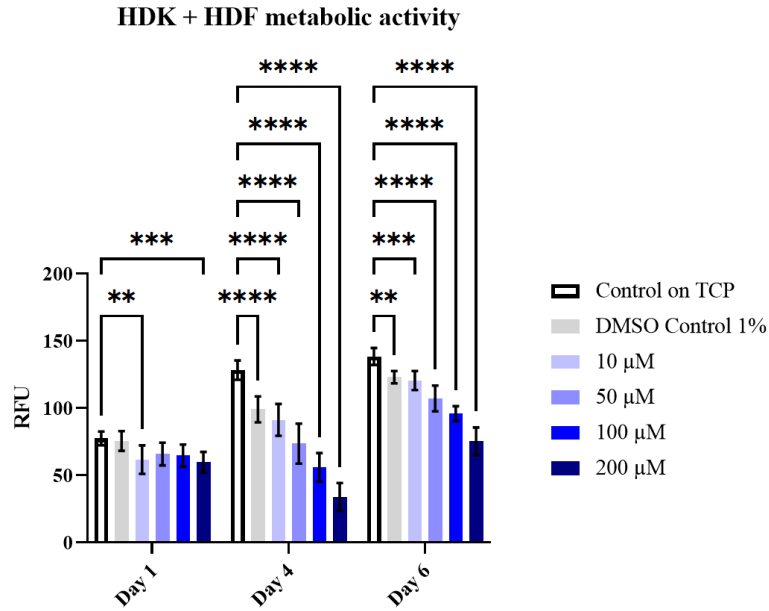
Figure 73. Metabolic activity of HDK + HDF seeded with different concentrations of E2 for 6 days. Results are shown as mean ± SD. Two-way ANOVA statistical analysis with Tukey comparison test. **** $p < 0.0001$, *** $p < 0.001$, ** $p < 0.01$. N=3, n=3.
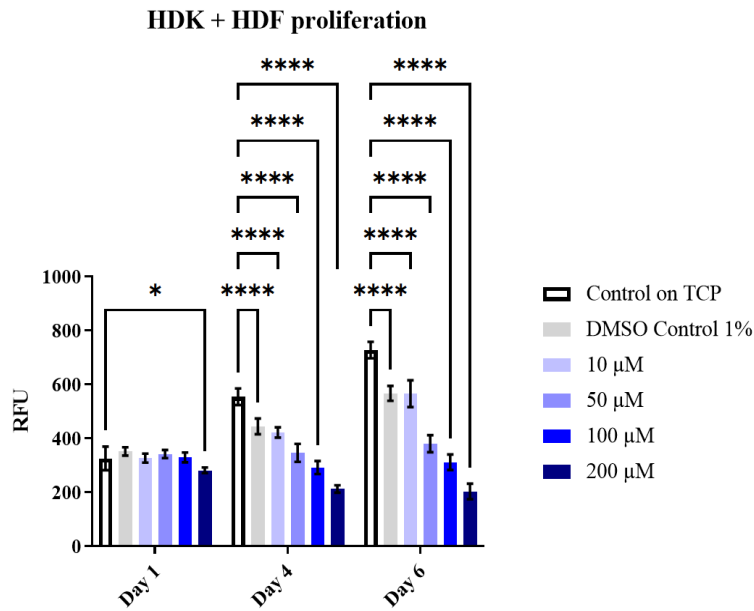
Figure 74. Cell proliferation of HDK + HDF seeded with different concentrations of E2 for 6 days. Results are shown as mean ± SD. Two-way ANOVA statistical analysis with Tukey comparison test **** $p < 0.0001$, * $p < 0.05$. N=3, n=3.

The introduction of AV into the HDK + HDF culture produced similar results as with the use of E2. Fluorescence microscopy images (Figure 75) showed lower cell density for concentrations above 1 mg/mL with a distinct change in cell morphology for cells cultured with 20 and 50 mg/mL of AV. None of the concentrations tested had a positive effect on metabolic activity (Figure 76) or cell proliferation (Figure 77). However, concentrations of 1 mg/mL showed the lowest cytotoxicity for all time points when compared to the control. Our results showed that HDK + HDF are more sensitive to the inclusion of AV in solution than the HDF monoculture and that concentrations above 10 mg/mL had a significant negative on cell behavior.
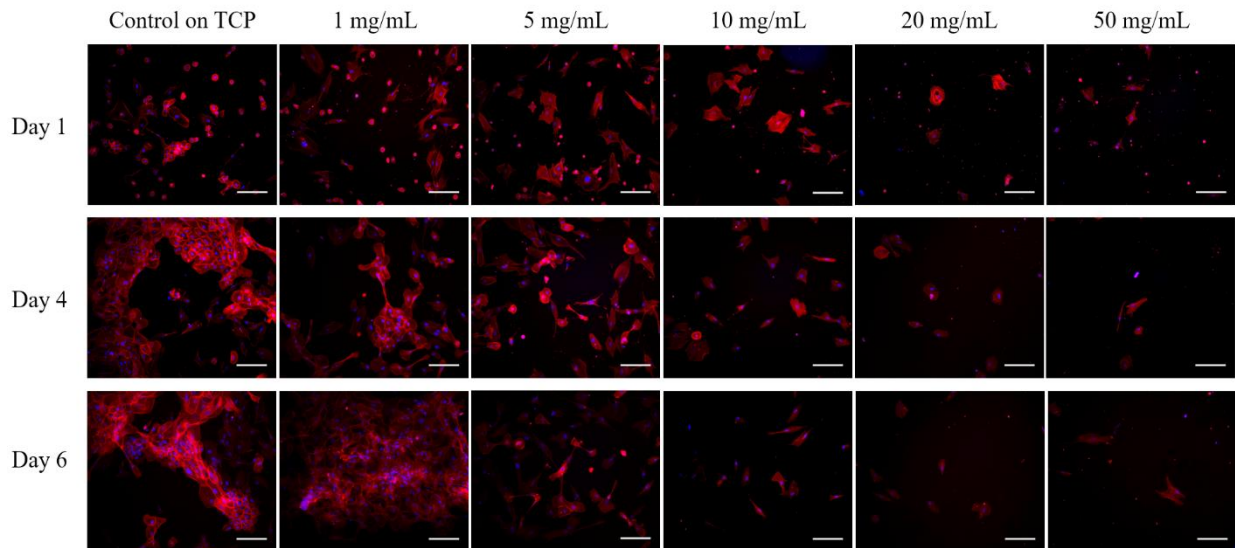
Figure 75. Images of HDK + HDF when cultured with different concentrations of solubilized AV for 1, 4, and 6 days. Cells were stained for F-actin filaments (phalloidin-TRITC - red) and cell nuclei (DAPI - blue). Scale bar = 200 µm.

HDK + HDF metabolic activity
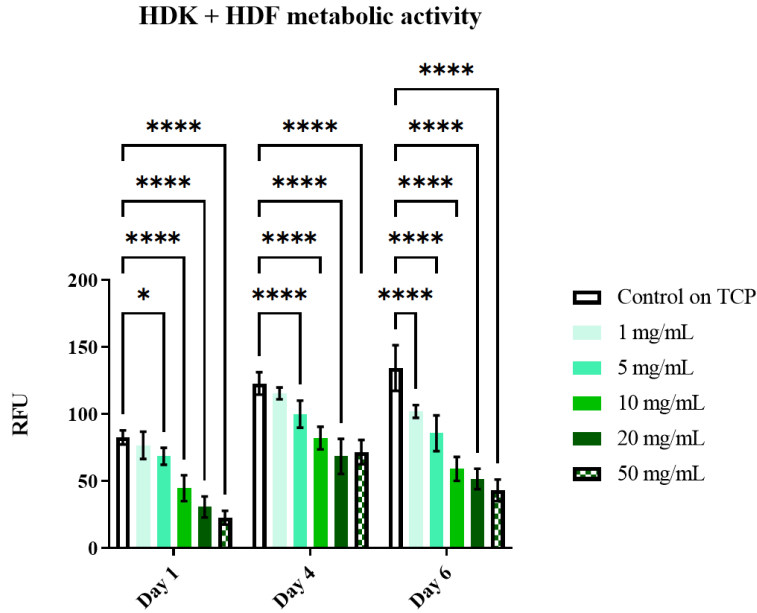
Figure 76. Metabolic activity of HDK + HDF seeded with different concentrations of AV for 6 days. Results are shown as mean ± SD. Two-way ANOVA statistical analysis with Tukey comparison test **** $p < 0.0001$, * $p < 0.05$. N=3, n=3.

HDK + HDF proliferation
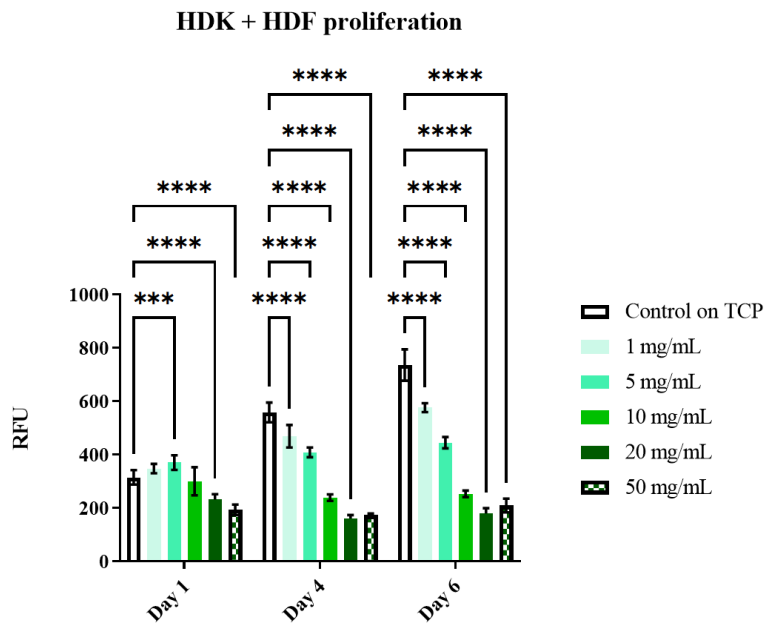
Figure 77. Cell proliferation of HDK + HDF seeded with different concentrations of AV for 6 days. Results are shown as mean ± SD. Two-way ANOVA statistical analysis with Tukey comparison test. **** $p < 0.0001$, *** $p < 0.001$. N=3, n=3.

3.3. AdSC viability, proliferation, and migration when exposed to 2dDr

Exposing the AdSCs to concentrations of 2dDr higher than 100 µM induced the formation of well-defined areas in which cells did not proliferate as can be observed on the fluorescence images shown in Figure 78. The resazurin assay showed that all concentrations decrease the metabolic activity when compared against the control group but only at day 6. For days 1 and 4, there was no significant difference among the 2dDr concentrations or against the control group. In comparison with HDF or HDK + HDF, AdSCs were more sensitive to lower concentrations of 2dDr (50 µM) as the metabolic activity (Figure 79) and cell proliferation (Figure 80) values were lower at day 6 when compared to the control group. The proliferative assay supports the idea of 2dDr having a negative effect on cell behavior as all concentrations tested showed lower than the control group from day 4 onwards, with 1500 µM having the most significant effect.
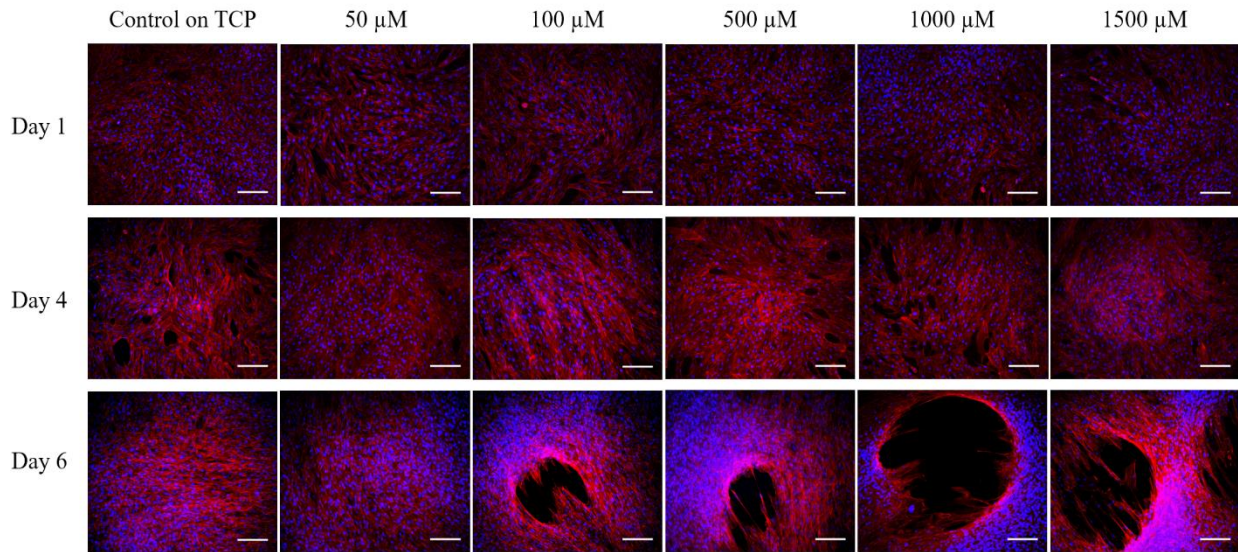
Figure 78. Images of AdSC when cultured with different concentrations of solubilized 2dDr for 1, 4, and 6 days. Cells were stained for F-actin filaments (phalloidin-TRITC - red) and cell nuclei (DAPI - blue). Scale bar = 200 µm.
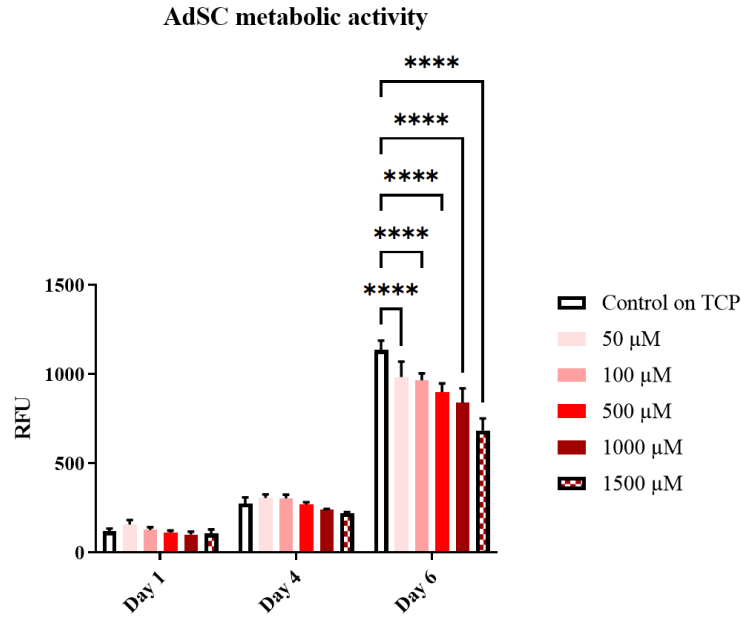
Figure 79. Metabolic activity of AdSC seeded with different concentrations of 2dDr for 6 days. Results are shown as mean ± SD. Two-way ANOVA statistical analysis with Tukey comparison test. **** p < 0.0001, * p < 0.05. N=3, n=3.
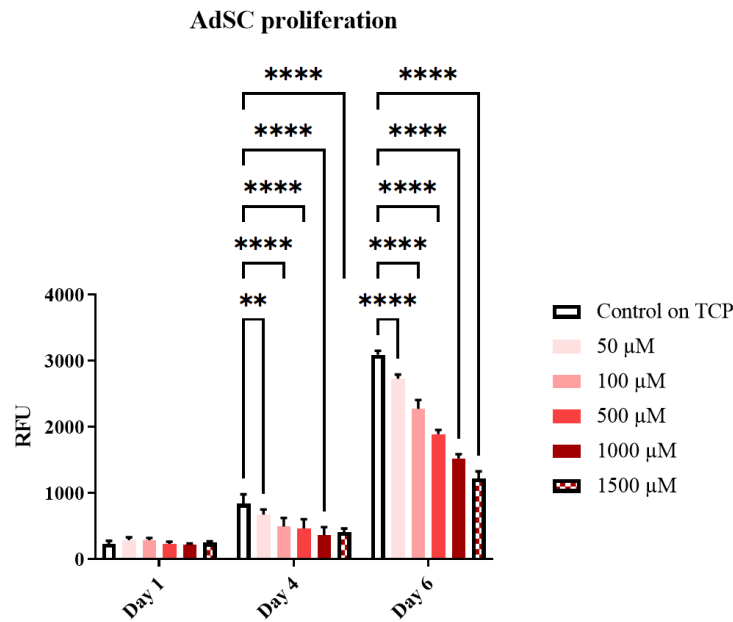
Figure 80. Cell proliferation of AdSC seeded with different concentrations of 2dDr for 6 days. Results are shown as mean ± SD. Two-way ANOVA statistical analysis with Tukey comparison test. **** p < 0.0001, * p < 0.05. N=3, n=3.

The scratch migration assay showed that low 2dDr concentrations of 50 and 100 µM accelerate cell proliferation and aid to the closure to the scratch as seen in Figure 81. Moreover, Figure 82 shows the difference in the closure percentage of the scratch across 2dDr concentrations. Similar to AdSC metabolic activity and cell proliferation, the scratch assay reveals that 500 and 1000 µM showed a lower percentage than the control group, suggesting a negative effect on cell behavior.
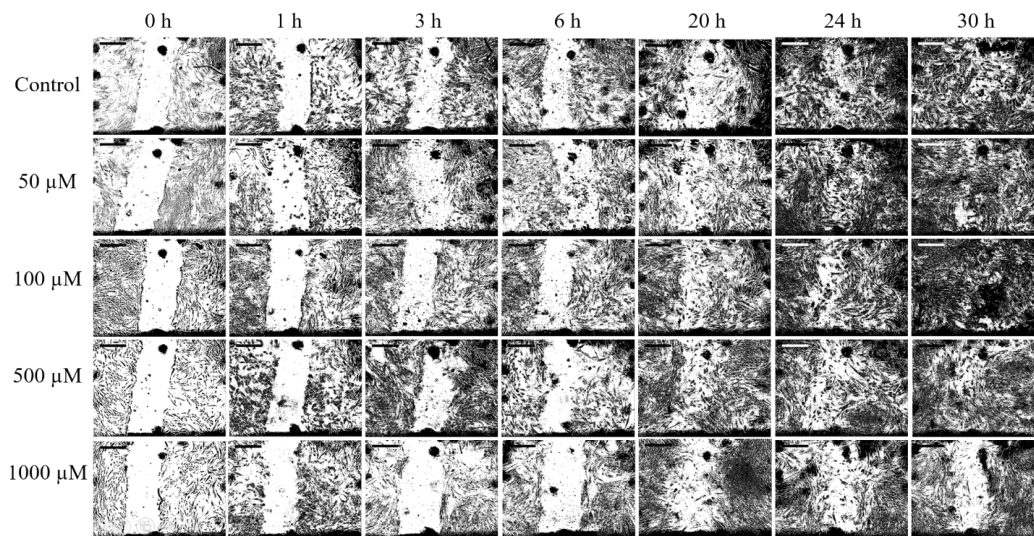
Figure 81. Images of AdSC migration scratch assay when cultured with different concentrations of solubilized 2dDr for 0, 1, 3, 6, 20, 24, and 30 hours.
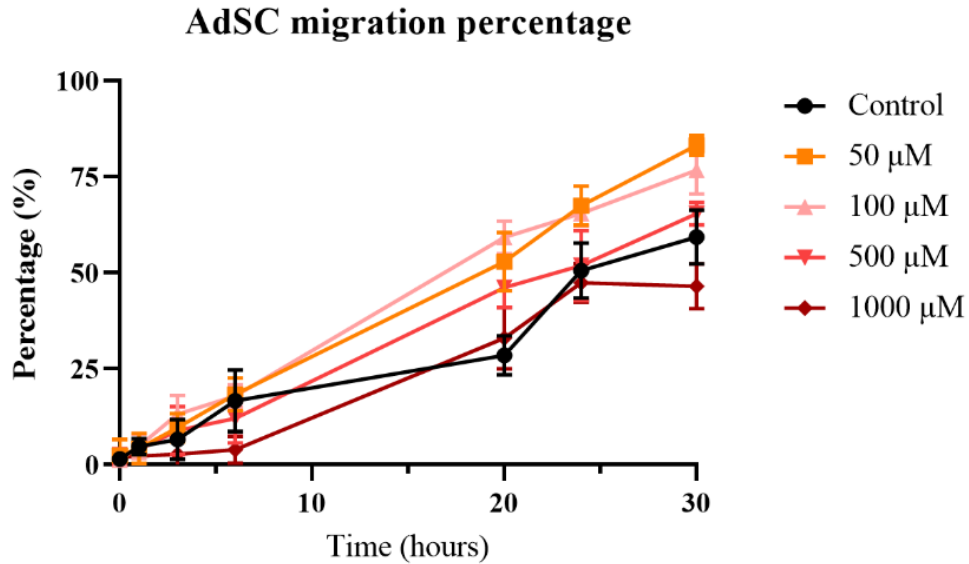
Figure 82. Percentage of migration for AdSC migration scratch assay when cultured with different concentrations of solubilized 2dDr for 0, 1, 3, 6, 20, 24, and 30 hours. Results are shown as mean ± SD. N=2, n=3.

3.4. Angiogenic potential of PLGA RES loaded with 2dDr

Implanting PLGA 50:50 RES loaded with 2dDr on the CAM assay revealed the angiogenic potential of the scaffolds compared against a VEGF control and to 2dDr in solution at different concentrations. Figure 83 shows a comparison of composite images from the CAM assay when exposed to PLGA 50:50 RES loaded with 10% wt. and 15% wt. 2dDr against a 250 µM, 1000 µM

2dDr control solutions and VEGF (80 ng/day) control. Furthermore, Figure 83 also exemplifies the shrinking behavior of PLGA scaffolds studied in the chapter II.
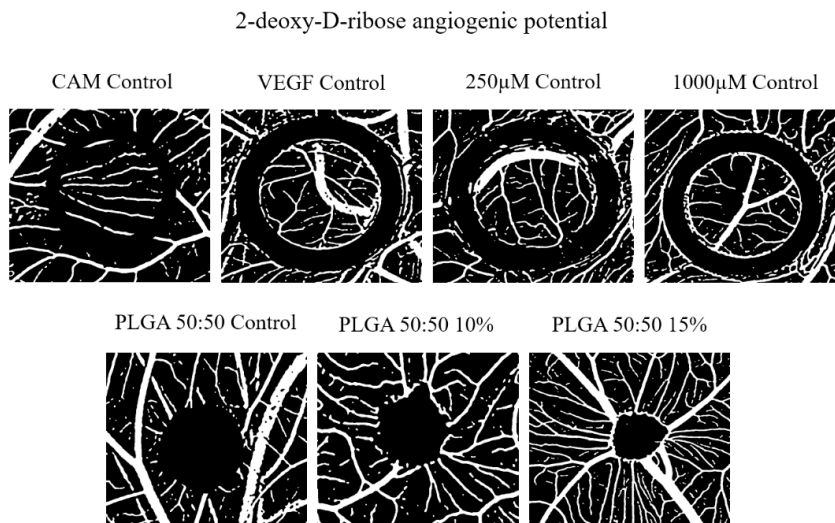
Figure 83. Composite images of CAM assay when cultured with 2dDr both in solution and loaded into PLGA 50:50 RES.

The analysis of the vascular density of the area around the scaffolds is shown in Figure 84 revealed that 1000 µM 2dDr solution and the 15% wt. 2dDr PLGA scaffold generated the highest amount of vascularization with values of 16.38% ± 3.3 and 18.4% ± 2.9 respectively, whereas the PLGA control showed the lowest value of 12.8% ± 1.7. However, none of these values were higher than the VEGF control with 19.9% ± 1.4. Moreover, decreasing the 2Ddr concentration to 10% wt. on PLGA scaffolds and 250 µM in solution generated a lower average angiogenic response of 16.5% ± 2 and 16% ± 2.3, respectively.
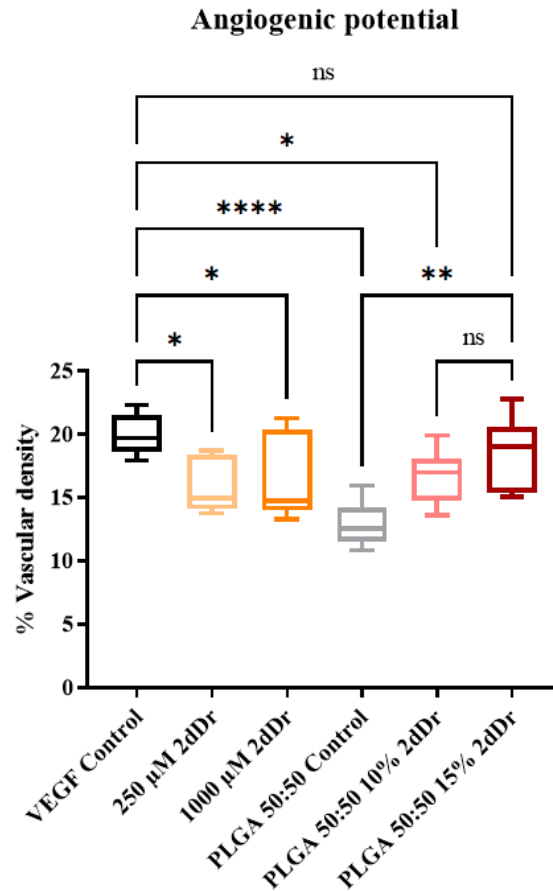
Figure 84. Vascular density of CAM assay when cultured with 2dDr both in solution and loaded into PLGA 50:50 RES. Results are shown as mean ± SD. One-way ANOVA statistical analysis with Tukey comparison test. **** $p < 0.0001$, ** $p < 0.01$, * $p < 0.05$, ns $p \geq 0.05$. N=2, n=5.

3.5. Angiogenic potential of PCL RES loaded with 2dDr

The implantation of PCL RES loaded with 2dDr on the CAM assay showed similar dosage-dependent behavior. Figure 85 shows the comparison of the composite images from the CAM assay when PCL RES were loaded. In contrast with the PLGA RES loaded with 2dDr, only the PCL RES with the highest concentration of 15% wt. 2dDr shrunk under the conditions of the CAM assay whereas the control and the 10% wt. scaffolds preserved their original dimensions.

PCL RES vascular density showed similar values to the PLGA samples loaded with 2dDr. For the 10% wt. and 15% wt. 2dDr PCL RES, the average values of 16.4% $\pm$ 1.8 and 18.26% $\pm$ 2.7 respectively, were higher than those found for the PCL control (12.46% $\pm$ 0.9) and the 250 μM (16.05% $\pm$ 2.3) and 1000 μM (16.38 $\pm$ 3.3) solutions. However, as with the PLGA RES, there was no statistical significance between the 10% wt. and 15% wt. 2dDr.
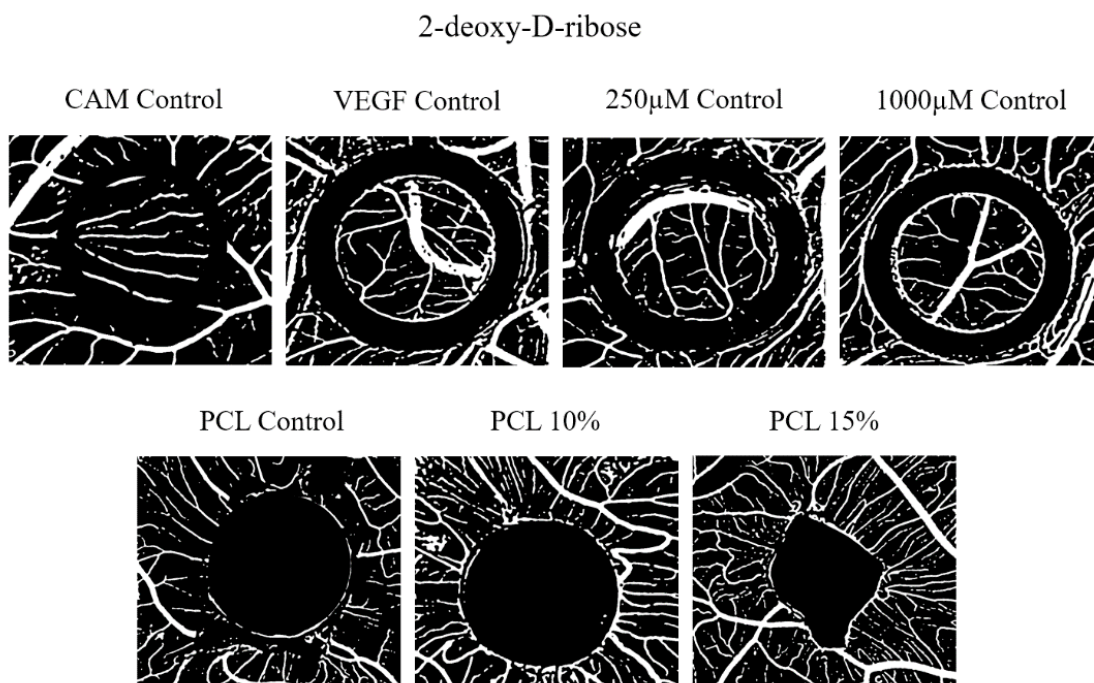
Figure 85. Composite images of CAM assay when cultured with 2dDr both in solution and loaded into PCL RES.
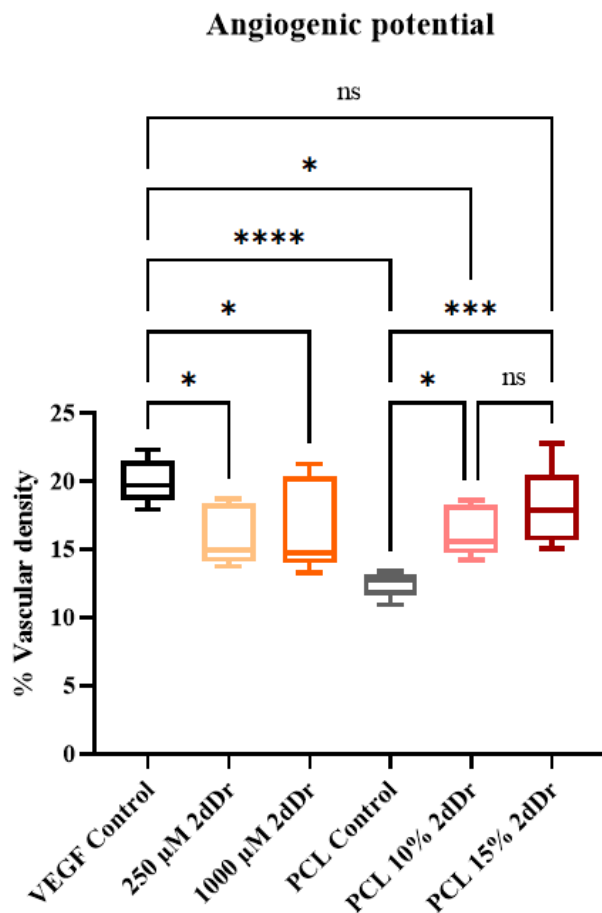
Figure 86. Vascular density of CAM assay when cultured with 2dDr both in solution and loaded into PCL RES. Results are shown as mean ± SD. One-way ANOVA statistical analysis with Tukey comparison test. **** p < 0.0001 , * p < 0.05, ns p ≥ 0.05. N=2, n=5.

3.6.   Angiogenic potential of PCL RES loaded with E2

The angiogenic potential of PCL RES loaded with E2 can be observed in Figure 87when comparing the composite images of the VEGF control against a 500 µM solution and a PCL control. Moreover, the 10% wt. E2 PCL RES showed a higher vessel density when compared to the control

and 500µM groups. As with the PCL RES loaded with 2dDr, no shrinkage was detected for the E2 loaded scaffolds under the conditions of the CAM assay.

17β-oestradiol angiogenic potential
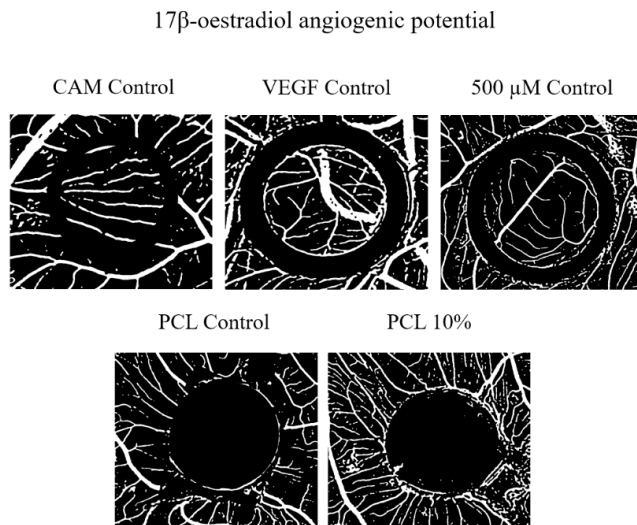
Figure 87. Composite images of CAM assay when cultured with E2 both in solution and loaded into PCL RES.

The vascular density analysis (Figure 88) showed that both the E2 500µM solution (15.29% ± 0.7) and the 10% wt. RES (16.39% ± 1.1) produced a higher number of blood vessels on CAM when compared to the PCL control (12.46% ± 0.9). However, the VEGF control remained as the strongest angiogenic agent (19.96% ± 1.4). Regarding the higher average vascular density of the 10% wt. compared to the 500 µM solution there was no statistical significance between both groups.
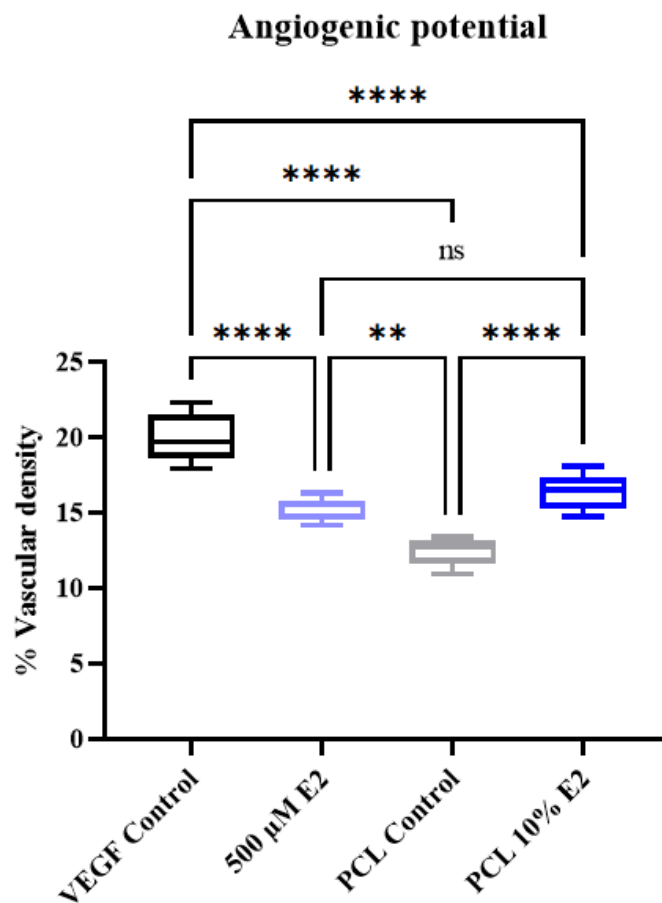
Figure 88. Vascular density of CAM assay when cultured with E2 both in solution and loaded into PCL RES. Results are shown as mean ± SD. One-way ANOVA statistical analysis with Tukey comparison test. **** $p < 0.0001$, ** $p < 0.01$, ns $p \geq 0.05$. N=2, n=5.

3.7. Angiogenic potential of PCL RES loaded with AV

The last bioactive compound tested on CAM was AV. The comparison of the composite images from CAM (Figure 89) revealed the strong angiogenic potential of AV solutions and AV-loaded RES. The presence of AV into the scaffolds had a similar effect on the size of the RES as observed when loaded with 2dDr.In this case, both 10% wt. AV and 10% wt. AV + 8% wt. 2dDr showed

shrinkage under the conditions of the CAM assay. Figure 90 shows the angiogenic potential of AV in solution and the RES scaffolds loaded with AV or AV + 2dDr. Our results indicate that the 20 mg/mL AV solution had the highest angiogenic response of 19.15% ± 1.5 compared to the 10% wt. AV scaffold with 18.8% ± 2.6. Moreover, introducing both AV and 2dDr into the PCL RES showed no increase in vascular density (16.72% ± 1.7). Interestingly, the vascular density of the 20 mg/mL AV solution was the highest among all tested bioactive compounds in solution, PLGA RES or PCL RES.
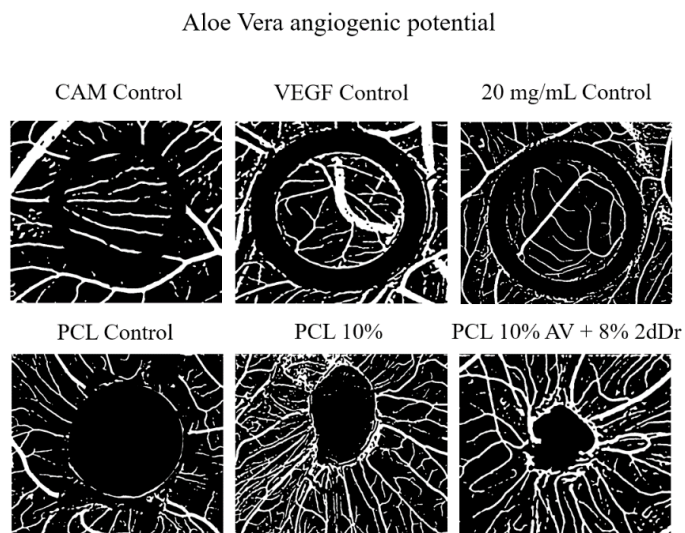
Figure 89. Composite images of CAM assay when cultured with AV both in solution and loaded into PCL RES.
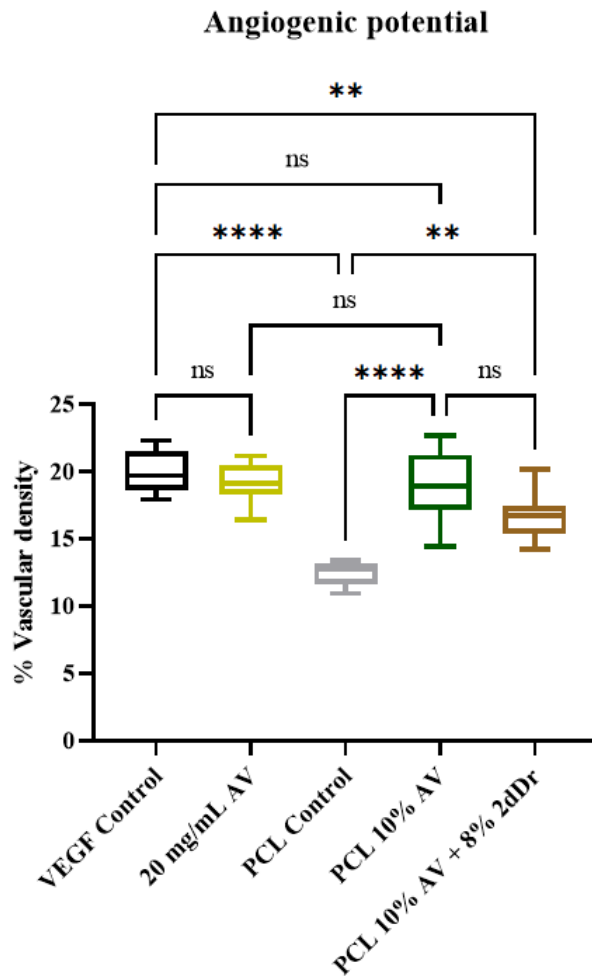
Figure 90. Vascular density of CAM assay when cultured with AV both in solution and loaded into PCL RES. Results are shown as mean ± SD. One-way ANOVA statistical analysis with Tukey comparison test. **** $p < 0.0001$, ** $p < 0.01$, ns $p \geq 0.05$. N=2, n=5.

3.8. Comparison of the angiogenic potential of 2dDr, E2, and AV

Comparing the composite images of all PCL RES loaded with bioactive compounds revealed that the inclusion of AV and AV + 2dDr had a significant impact on the morphology of the scaffolds. Furthermore, the vascular density analysis of the PCL RES (Figure 92) showed that although the average response of the 10% wt. AV has the highest among all bioactive compounds and its

combination (AV + 2dDr), there was no statistical significance between groups. However, all RES

loaded with bioactive compounds produced a higher angiogenic response than the control group.
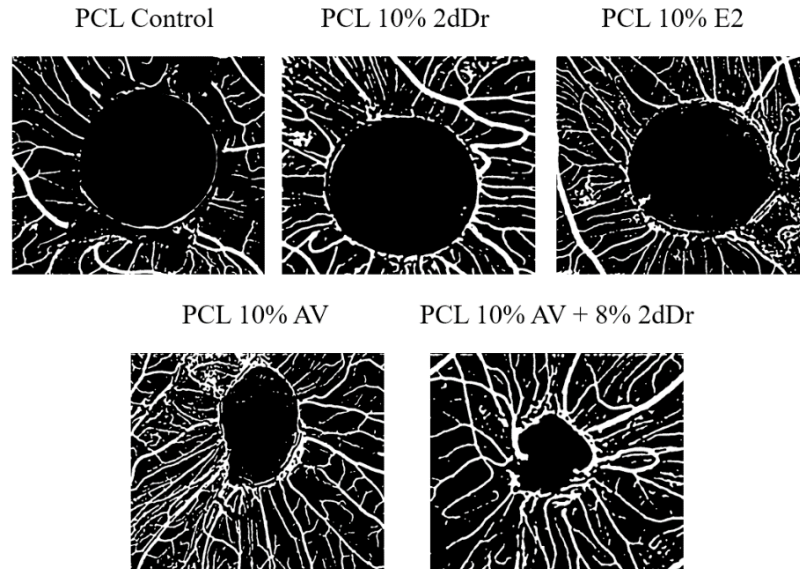
Figure 91. Comparison of composite images of CAM assay when cultured with 2dDr, E2, AV, or

AV + 2dDr loaded into PCL RES.
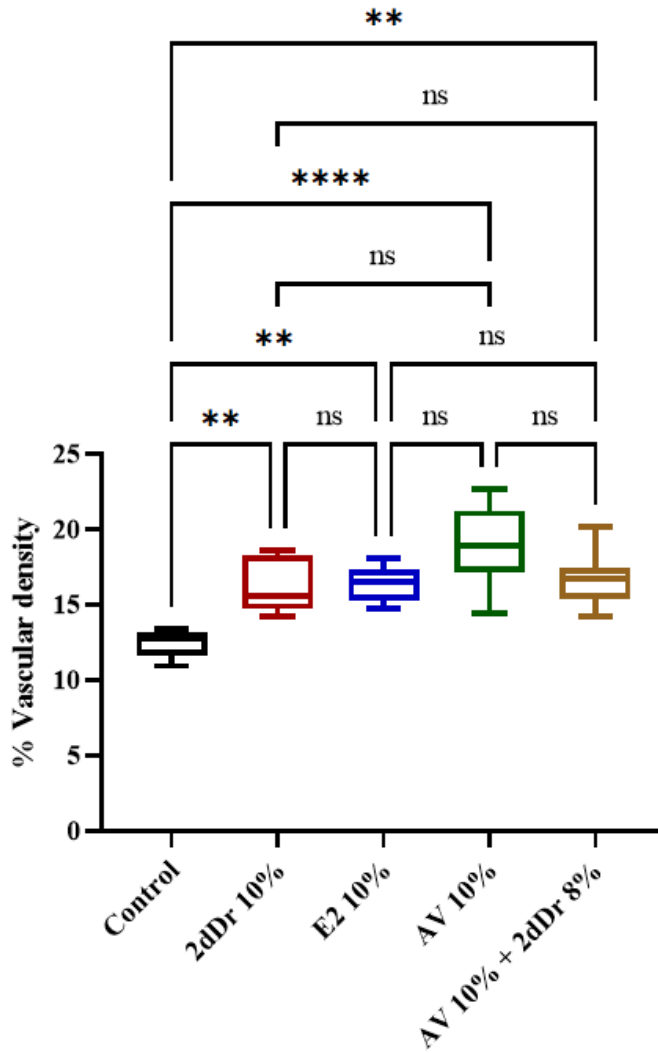
Figure 92. Vascular density of CAM assay when cultured with 2dDr, E2, AV or AV + 2dDr loaded into PCL RES. Results are shown as mean ± SD. One-way ANOVA statistical analysis with Tukey comparison test. **** $p < 0.0001$, ** $p < 0.01$, ns $p \geq 0.05$. N=2, n=5.

4. Discussion

The cell viability and cell proliferation of HDF, HDF + HDK, and AdSC exposed to different concentrations of 2dDr, E2, or AV showed the dose-dependent mechanism of each compound for each cell type. Moreover, fluorescence images of the cell culture aid in observing any changes in cell morphology and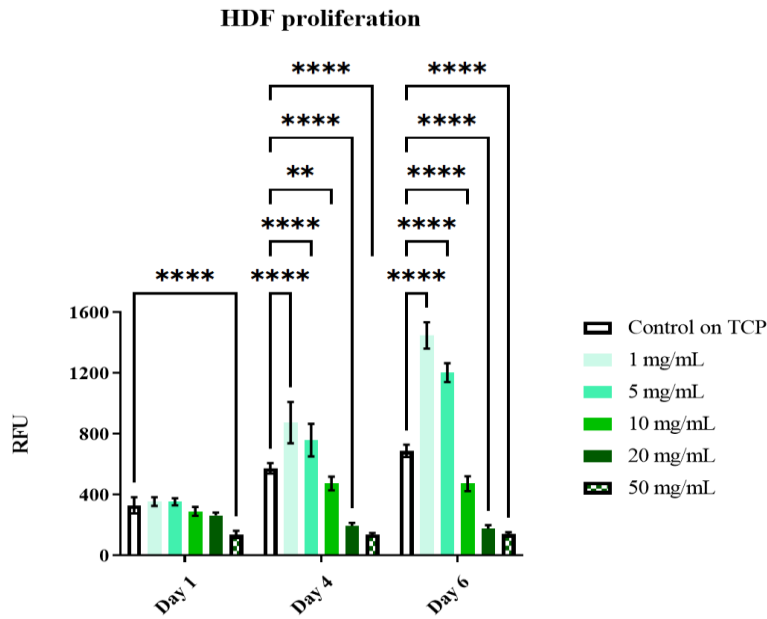 differences in cell proliferation. The results from these studies showed us the individual behavior of each cell type and contributed to defining an effective concentration that can be loaded into RES or TCES that does not hinder cell behavior.

Dermal fibroblasts play an active role and regulate several steps of skin regeneration such as producing new ECM, contracting the wound, breaking the fibrin clot, and collagen production [356]. When exposed to 2dDr, HDF showed an increase in metabolic activity for concentrations above 500 µM from day 1 with the 10 µM concentration showing the highest metabolic activity value after 6 days in culture. Moreover, cell proliferation also increased for all concentrations from day 4, with the 1000 µM concentration showing the highest values of cell proliferation. Such increase in metabolic activity and cell proliferation has been reported for aortic endothelial cells by Dikici et al [169] but not for dermal fibroblasts. A hypothesis for this behavior comes from the work of Dikici et al. and Yar et al.in which the introduction of 2dDr stimulates the production of VEGF on endothelial cells via two possible routes: 1) by the promotion of oxidative stress due to production of 2dDr and enzymatic degradation of thymidine, or 2) by the activation of NOX2 that triggers NF-κB that upregulates VEGFR2 [157], [161], [169].

Although HDF are not characterized for their proliferation and migration in presence of VEGF, Bondarenko et al. studied the effects of VEGF *in vitro* on HDF and reported an increase in cell proliferation and migration [357]. Moreover, although HDF produces VEGF *in vivo*, this growth

factor is mainly expressed by HDK, with certain conditions such as psoriasis increasing the production of VEGF for both HDF and HDK [358]. Our results showed that concentrations between 50 µM and 100 µM did not change the proliferation or metabolic activity of HDF + HDK, with higher concentrations showing a decrease in proliferation and viability. Because of the increase in proliferation for the monoculture of HDF, an increase in the seeding ratio of HDK+HDF was expected. However, the analysis of the fluorescence microscopy images revealed a homogeneous distribution as with the control group.

To the best of our knowledge, this is the first time that the effects of 2dDr are studied for a co-culture of HDF + HDK. However, studies by Brown & Bicknell and Hammerberg et al. have reported the effects of TP (responsible for the catalysis of production of 2dDr from thymidine) on the increased proliferation of keratinocytes [123], [359], where its overexpression has been related to an increase in vascular density for psoriatic skin and tumor growth [164], [360]. As described before, high levels of 2dDr could induce the production of TP and initiate an angiogenic response, as high elevated levels of TP are common in physiological and pathological angiogenesis [123], [172]. Although there was no significant increase in cell proliferation or metabolic activity for the HDF + HDK experiment shown in this thesis, future experiments should aim to quantify the differences in the expression of VEGF at different concentrations of 2dDr to fully characterize the angiogenic potential *in vitro*.

Another relevant skin cell type are the highly proliferative and versatile AdSC. The use of AdSC to improve skin wound healing has been explored before by several authors which agree on their capacity to secrete cytokines and growth factors, their effect on HDK proliferation, and their synergistic role with HDF on VEGF production, protection from UV radiation, and aging [361]–

[363]. Therefore, studying the effects of 2dDr on AdSC could help us to understand its effect on their paracrine functions in human skin.

Nonetheless, similar to HDK, this is the first time that the effects of 2dDr on AdSC are studied. The metabolic and proliferative studies in this thesis showed a decrease compared to the TCP control regarding the concentration of 2dDr. However, the fluorescence microscopy images showed the over confluent cell populations for all the concentrations with some high concentrations showing circular formations at the center of the well. Due to the high proliferative nature of AdSC, one hypothesis is that the experiment would require a lower cell density to better observe any effects on proliferation when exposed to 2dDr. Although it has not been fully characterized, there are reports that suggest that VEGF is a key regulator of AdSC [364], [365], which would indicate a higher response when delivering 2dDr *in vivo*.

The scratch assay showed that 50μM and 100μM concentrations of 2dDr can increase cell migration compared to the TCP control whereas concentrations higher of 500μM and 1000μM showed lower values. However, there is not enough data to support that 2dDr could induce proliferation and migration *in vitro* as other compounds (such as VEGF, TGFβ1, TNF-α, and PDGF-D), that have been tested to study their effects on AdSC migration have shown more conclusive results on a shorter or similar time frame [364], [366], [367].

The prescence of areas with low AdSC density on the well plate should be further studied to understand if this was due to the high cell density by the end of the experiment or due to the interactions of AdSC and 2dDr. Therefore, additional experimental data is required to further conclude the effects of 2dDr on AdSC cell behavior. Such experiments could include but are not limited to: observing the expression of stem cell markers, co-culture of HDF + AdSC, and using a

3D *in vitro* model. Nonetheless, the results shown in this thesis are a starting point to understand the effects of 2dDr on AdSC.

In comparison with 2Ddr, the effects of E2 on HDF cell behavior have been characterized before [346], [347], [368], [369] due to the major role of estrogens on skin homeostasis and regeneration. Data from our metabolic and proliferative assays showed that 10 µM concentrations had no negative effects compared to the control group. Furthermore, fluorescence microscopy images showed no changes in cell morphology for HDF exposed to a low concentration of E2. In contrast, all concentrations above this threshold decreased cell proliferation or viability. Therefore, the ideal concentration of E2 to be delivered should not be higher than 10 µM.

Stevenson et al. and Ascroft et al. had studied the effects of E2 on the expression of TGF-β1 and collagen deposition for HDF [346], [370]. Their results suggested that E2 has an active role on skin aging and that low levels could lead to impaired healing and that nM concentrations of E2 can regulate the expression of TGF-β1 which is key for HDF proliferation, matrix deposition and remodeling, angiogenesis, and fibroblast differentiation into myofibroblasts [371], [372]. Moreover, Makrantonaki et al proposed that there is an interplay between E2 and IGF-I for HDF and human sebocytes (responsible for lipid maintenance on the skin surface) as E2 induced the production of IGF-I and increased lipid synthesis on HDF [347]. Additionally, E2 was found to increase HDF expression of estrogen receptors (ER) mRNA and IGF-I receptor [368]. All these studies further demonstrate the positive effects of E2 on skin regeneration when delivered at low nM concentrations.

Interestingly, a study from Trompezinski et al. showed that the membrane-derived lipid prostaglandin E_2 (PGE_2) increases the production of VEGF on HDF, with PGE_2 being secreted

during the inflammation phase of wound healing to reduce inflammation and promote healing [373], [374]. Although the relation between E2 and PGE_2 is not completely clear, the combination of these two factors has also been reported to induce the production of prolactin on dermal fibroblasts [375]. Prolactin is known to stimulate HDK proliferation and production of VEGF [376]. Therefore, a fibrous membrane that delivers E2 into the wound site could potentially improve vascularization by activating more than one angiogenic pathway in different cell types *in vivo*.

E2 is known to stimulate the proliferation of HDK and suppress oxidative stress apoptosis via the expression of cyclin D2 and anti-apoptotic protein Bcl-2, respectively [377]. However, our data did not show an increase in proliferation or cell viability even at the lowest 10µM concentration, suggesting that lower nM - ρM concentrations, such as the ones used by Kanda & Watanabe, Verdier-Sevrain et al., and Urano et al. are needed to increase HDK RNA synthesis, ER-α expression, and cell proliferation or metabolic activity [345], [377], [378]. The activation of ER receptors is especially critical as has been related to keratinocyte differentiation during wound healing [379]. However, as with 2dDr, a higher dosage of E2 could potentially contribute to chronic inflammatory conditions such as psoriasis that is characterized by over the proliferation of keratinocytes and abnormal angiogenesis [376], [380].

AV is a complex compound that incorporates several bioactive molecules into the *in vitro* culture, and thus understanding its effect on cell viability and proliferation is key for future applications either on 3D models or *in vivo*. The culture of dermal cells with AV or its individual components has proved to increase the production of TGFβ1 and bFGF, both key factors in the wound healing process that mediate collagen deposition, HDF proliferation, and angiogenesis [348], [381], [382]. However, even though AV is one of the most well-known active compounds for skin regeneration

183

its *in vitro* mechanism is still not fully understood. The results from this thesis showed that AV concentrations lower than 5 mg/mL had a significant increase in both metabolic activity and proliferation for HDF, with concentrations above 5 mg/mL having a negative effect on cell behavior. Fluorescence images showed a significant increase in cell density for HDF exposed to 1 mg/mL of AV, with only concentrations higher than 5 mg/mL causing disruptive effects on the characteristic spindle-shaped morphology of HDF.

The effects of AV improving cell response at low concentrations had been reported by Hormozi et al. and Zandit et al. in which µg/mL concentrations of AV showed to increase cell metabolic activity of embryonic mouse fibroblasts and ovine fibroblasts respectively [348], [349]. Another study by Shafaie et al. showed that AV induces a higher proliferation, migration, and angiogenic response on HDF than in endothelial cells, which would indicate a higher expression of VEGF or TGFβ1 [383]. Additionally, a major polysaccharide of AV (acemannan) has been found to stimulate the expression of VEGF and keratinocyte growth factor-1 (KGF-1), both key components of the wound healing process [381]. KGF specifically is of high importance to mediate the formation of the rete ridges by increasing the proliferation of HDK or remodeling of the papillary projections by metalloproteases [384].

Moreover, µM concentrations of some AV components have been identified as inhibitors of HDK proliferation [385], while other studies have shown that AV accelerates migration and proliferation of HDK [386]–[388], highlighting the synergistic interaction of the AV compounds [190]. Furthermore, AV has been used to treat psoriasis, which among other pathological conditions is characterized by the elongation of the rete ridges by inhibiting the abnormal proliferation of HDK [389]. However, the results from the metabolic activity and proliferation experiments shown in this thesis did not support these findings. None of the concentrations tested showed an increase in

184

HDK proliferation or viability. Interestingly, the fluorescence microscopy images indicate a higher cell density for HDK seeded with 1 mg/mL of AV. A possible explanation for this is that the lowest concentration used in this study is above the range in which HDK could increase proliferation. This is further supported when looking at the AV source used in other studies that have similar concentrations but a higher water content, thus the bioactive fraction introduced into the cell culture is lower when compared to the lyophilized powder used in this thesis.

Nonetheless, characterization of the expression of relevant biomolecules by skin cell types in the presence 2dDr, E2, or AV is needed to better understand their role in angiogenesis and skin wound healing. The data shown in this thesis focused on the effects on proliferation and metabolic activity, but future experiments could quantify the expression of VEGF, IGF-I, bFGF, or other relevant proteins by the western blot technique. Moreover, a more complex 3D model is needed to better understand the physiological effects of delivering these bioactive compounds on the wound site. The use of such models is further explored in chapter IV.

Regarding the angiogenic potential of the bioactive compounds loaded into RES, the data from the CAM assay showed similar results to those reported before for 2dDr, E2, and some compounds present on AV [159], [166], [168], [198]. Unfortunately, a direct comparison of the CAM data among studies is not always possible as the angiogenic response is usually quantified using different methods such as image analysis, histology, or a using a qualitative grading scale.

Although there was no statistical significance among the bioactive compounds, all of them showed a higher vascular density around the scaffold compared to their pure RES control. Moreover, there was no statistical difference between loading 2dDr on PLGA (16.59% ± 2) than in PCL (16.41% ± 1.8) RES. However, the pure PLGA RES had a slightly higher average angiogenic response

(12.8% ± 1.7) than its PCL counterpart (12.46% ± 0.9). Because the degradation by-products of PLGA have been reported as angiogenic, a higher response was expected for the PLGA sample [223]. The rationale for this behavior could be related to the degradation rate of PLGA that usually happens after the first week, meaning that CAM was never exposed to the angiogenic lactate [220], [223], [390].

In the case of 2dDr, Dikici et al. has shown that concentrations as high as 50% wt. can induce a mild angiogenic response. Our data further demonstrated the dosage-dependent nature of 2dDr, as our lower 10% wt. concentration induced a higher angiogenic response than the 50% wt. concentration [166]. Another study by Andleeb et al. showed that 5% 2dDr loaded into wax-coated cotton fibers is enough to induce a strong angiogenic response [168]. Nevertheless, the angiogenic response of 2dDr did not reach the values shown by the VEGF control on the CAM assay shown in this thesis. Furthermore, Dikici et al. also reported on the higher angiogenic response of VEGF in comparison to higher concentrations of 2dDr [166]. These studies support the dose-dependent behavior of 2dDr and its potential to promote the expression of VEGF for tissue engineering applications.

It is important to highlight that previous studies showed a slower release of 2dDr compared to the data showed for the release of 2dDr from the RES fabricated on this thesis (as described on chapter II), meaning that the 2dDr concentrations used in this experiment were delivered to the CAM within the first hour. In comparison, both Dikici et al. had released about 80% of the total 2dDr amount by day 7 and Andleeb et al. showed a release of 90% by day 5[166], [168]. The release profile of each construct is critical to induce an angiogenic response, in the case of the concentrations used in this thesis, because of the high release rate, even if higher concentrations

were to be loaded into the RES, the rapid release into the CAM assay had the potential to inhibit endothelial cell proliferation, migration, and cause other undesired side effects.

In contrast, lower 5% wt. concentrations of E2 have proved to be enough to induce blood vessel formation on CAM with concentrations above that threshold generating a lower angiogenic response [159], [166]. However, as with 2dDr, the release of E2 from the RES is key to establish its angiogenic potential on the CAM. In chapter II, the release of E2 from PCL RES was found to be 25% of the total amount by day 3, which is higher than the values reported by Dikici et al. with 1.6% of E2 released by day 7 but similar to those reported by Shafaat et al. with ~30% and by day 5 [159], [166].

Moreover, to the best of our knowledge, this is the first time that the lyophilized AV compound is loaded into electrospun scaffolds and studied under the CAM assay, as other studies have focused on the effects of individual compounds or the entire AV gel [198]. The data from this thesis showed the potential of AV-loaded scaffolds to induce blood vessel formation using a 10% wt. AV concentration. This concentration generated blood vessel formation when tested on CAM and produced the highest vascular density values among the bioactive compounds tested, being only below those recorded for the VEGF control. Additionally, the effect of combining 2dDr and AV was tested on CAM where vascular density was lower than the values reported for each compound when loaded individually. Nonetheless, further combinations of lower concentrations of 2dDr and AV could be explored to better understand its effects, as it has been reported before that AV combined with E2 can significantly improve endometrial regeneration [305].

Nevertheless, understanding the angiogenic potential of 2dDr, E2, and AV requires future experiments using endothelial cells and animal models that can provide more information about

its dose-dependent mechanism and their effects in wound healing either in solution or when delivered by RES.

5. Conclusion

The results of this thesis aimed to characterize both the *in vitro* behavior and the performance on CAM of 2dDr, E2, and AV to define a non-cytotoxic range of concentrations that could improve skin regeneration. In the case of 2Ddr, concentrations above 500 µM can potentially hinder cell proliferation or viability, although higher concentrations loaded into RES (10% wt. and 15% wt.) can still induce blood vessel formation on CAM. However, E2 is only effective on nM concentrations, therefore the lowest concentration tested on this thesis, 10 µM, is still above the maximum concentration where cell behavior is not hindered. Nonetheless, due to the slow release of E2 from the RES, the 10% wt. concentration proved to generate an angiogenic response on CAM. Finally, AV showed an increase in cell proliferation and viability when used at a concentration of 1 mg/mL, and the highest average vascular density recorded on this thesis among the bioactive compounds tested (18.82%).

Furthermore, handling of PLGA scaffolds was challenging due to the shrinkage and its low wettability compared to AP treated PCL. Because preserving the microfeatures and inducing rapid cell attachment are key aspects of the desired final construct, the data from this chapter supported the decision of not using PLGA (either 50:50 or 75:25) on future experiments.

Using AdSCs is a promising approach with potential for tissue engineering constructs and clinical applications. However, their low availability over the realization of this thesis limited the number of experiments that could have been designed to observe their behavior in presence of E2 and AV. However, the work on this thesis showed that it is possible to have viable AdSC proliferating under

lower concentrations of 2dDr that are known to be angiogenic and therefore inducing the production of VEGF.

The data from this chapter has defined working concentrations of 2dDr, E2, and AV that can induce angiogenic activity on CAM and that in some cases increase cell viability and proliferation. This data in conjunction with the release data from chapter II are important milestones towards testing the effects of such concentrations on more complex skin 3D models using RES or TCES.

Chapter V. Effects of topographically controlled electrospun scaffolds on skin tissue engineered models

1. Introduction

2D cell culture techniques have been used to test and evaluate new drugs and materials since the beginning of the 20th century. However, cell behavior is highly controlled by spatial interactions and the use of 3D models and scaffolds is considered a more accurate way for mimicking and understanding cell behavior [391], [392]. Aspects of cell behavior that are controlled by spatial interactions including cell proliferation, metabolic activity, response to mechanical stimulation, drug metabolism, differentiation, morphology, and protein synthesis [393].

As with any other tissue, the 3D structure of human skin is responsible for regulating cell interactions of specialized cells on a nano and micro scale. During the past 2 decades, several skin 3D models have been used to study wound healing, immune response, and drug delivery *in vitro* [394]. Primarily, these models aim to replicate the collagenous nature of the dermal component while allowing for keratinocyte maturation of the epidermal layer. The formation of a fully stratified epidermis is one of the main advantages of a 3D culture of keratinocytes, as traditional 2D techniques grow cells into a flat submerging surface which can alter gene expression and cell function [395], [396].

The most basic techniques of 3D cell culture tend to use synthetic networks made with biodegradable polymers to replicate the ECM structure and support cell adhesion and proliferation. This approach allows cells to produce their own ECM and remodel the scaffold as it is slowly degraded [397]. However, some alternative approaches used non-degradable materials such as

PDMS as the dermal component of the skin model [398], [399]. In contrast, most 3D complex models introduce collagen I or collagen-GAG-chitosan matrices in which cells can infiltrate and proliferate while providing a barrier layer for keratinocytes [201], [397]. This last approach generates tissue engineered skin faster than the synthetic scaffold approach but requires a higher quality control of the collagenous material and increases the cost significantly [400].

The use of collagen matrices to culture keratinocytes on an air-liquid interface was crucial to develop the de-epidermized dermis model. Some of the advantages of using de-epidermized dermis as a dermal substrate include that the basement membrane proteins aids in the formation of a multilayer differentiated epidermis, and that has a positive influence on fibroblast proliferation [401]. Originally, these models were developed using a co-culture of dermal fibroblasts and epidermal keratinocytes, however, these models have been further developed to introduce T cells, melanocytes, and to study specific cell interactions without the need of an animal model [395], [402], [403]. Nonetheless, the tissue specific microenvironments present inside the hair follicles and at the DEJ (referred to as rete ridges) are usually omitted from the 3D skin models [38].

In recent years mimicking the stem cell microenvironment provided by the rete ridges has been studied for its effects on preserving the homeostatic regulation of epidermal renewal. These microenvironments guard a population of keratinocyte stem cells that are key to maintain the quality of the tissue and ensure its self-renewal throughout the host life span [82]. Many studies have focused on replicating the microscale structural cues of the rete ridges using lithographic fabrication techniques and collagen hydrogels [1], [40], [278], [404]. Moreover, these studies aim to create complex *in vitro* 3D models to study the relation between the rete ridges and cell behavior and the effects on skin regeneration. However, there are only a few studies that attempt to create potential clinical devices to re-introduced lost rete ridges after injury [405].

191

The work on this thesis is based on the work of Ortega et al. of combining additive manufacturing and electrospinning for the creation of fibrous microfabricated constructs that recreate to a degree the topographical cues present on the DEJ [269], [271]. In this experimental chapter, the TCES and RES are tested to observe their effects on cell proliferation and viability when using dermal cell lines (with or without the addition of bioactive compounds). Additionally, TCES and RES were placed on skin models to study the ability of the scaffolds to induce the formation of rete ridge-like structures on a healthy or damaged 3D skin model.

It is important to study the effects in cell proliferation and epidermal stratification of introducing the proangiogenic 2dDr or the adult stem cells AdSC into a skin model as this could have positive effects on skin regeneration. Both 2dDr and the AdSC have been studied *in vitro* on a 2D culture model, where the AdSC population has been co-cultured to observe the effects of their paracrine activity on dermal keratinocytes [166], [363], [406]. However, there are no studies about the effects of 2Ddr or AdSCs on a more complex skin tissue engineered model.

This experimental chapter combines the fabrication of bioactive micropatterned fibrous scaffolds and tissue engineered skin models to study their effects on cell proliferation and epidermal stratification when implanted on 3D skin tissue engineered models. The data from the study will aid to evaluate the potential of using such topographically controlled membranes to enable the design of a biomimetic and cost-effective medical device for the treatment of skin injuries or pathologies that compromise the structure of the rete ridges.

1.1. Aim and objectives

The aim of this experimental chapter was to i) study the effects of culturing HDF or HDK on RES or TCES loaded with bioactive compounds 2dDr, E2, or AV and to ii) observe the effects on epidermal stratification and rete ridge formation when skin tissue engineered models were implanted with TCES and when cultured with 2dDr or AdSC. In order to achieve this aim; the following objectives were established.

- Develop tissue engineered skin models from tissue obtained from patients undergoing elective breast reductions and abdominoplasties (research ethics number 15/YH/0177 under the Human Tissue Authority 12179).

- Investigate the effects of HDF cell proliferation for different microtopographies of TCES.

- Investigate the effects of HDK + HDF cell proliferation for different microtopographies of TCES.

- Evaluate the metabolic activity of HDF cultured on PCL RES loaded with bioactive compounds 2dDr, E2, or AV.

- Evaluate the metabolic activity of HDF + HDK cultured on TCES loaded with bioactive compounds 2dDr, E2, or AV.

- Observe the effects on skin architecture for TCES implanted on tissue engineered skin models.

- Assess the effects on epidermal stratification for skin tissue engineered models cultivated with AdSC or 2dDr.

- Assess the effects on cell metabolic activity for burned skin tissue engineered models when implanted with TCES or RES.

2. Materials and Methods

2.1. Preparation of PCL RES and TCES

RES and TCES were fabricated as described in chapter II methods section 2.3.1 and 2.3.2. The PCL scaffolds were prepared days before the experiment and were plasma treated as described in the methods section. The micropatterned TCES and plain RES with or without the addition of bioactive compounds were tested for *in vitro* cell culture and the fabrication of skin tissue engineered models. RES and TCES were stored inside sealable bags at 4°C until the day of the experiment.

2.2. *In vitro* cell culture on RES and TCES

Human dermal fibroblasts (HDF) and human epidermal keratinocytes (HDK) were isolated and cultured as described in chapter III methods section 2.1. Two separate experiments were carried out to observe the effects of monocultured HDF (cell densities 100,000 HDF per scaffold), and HDK + HDF co-culture (cell density of 300,000 HDK - 100,000 HDF per scaffold) on different electrospun scaffolds. Cells were isolated as described in chapter II.

A day before the experiment, scaffolds were cut into 15×15 mm square pieces. On the day of the experiment, scaffolds were placed on 6-well plates and a metal ring (ID 10 mm) was placed on top to hold the cell suspension and to maintain the scaffold in place. Cells were then cultured on the center of the ring by seeding 500 µL of the cell suspension, and 1 ml of cell media outside the metal ring. Samples were cultured at 37°C in a 5% CO_2 humidified atmosphere. After 24 h, the metal ring was removed, and the scaffolds were transferred to a new 6-well plate. Table 19 shows

the scaffolds used for these experiments. Two independent tests were performed by triplicate per experiment (N = 2, n = 3).

Table 19. Electrospun scaffolds (RES and TCES) tested for *in vitro* cell culture.

Type of scaffold	Pattern used	Bioactive compound	Concentration (% w/w)	Cell lines tested
TCES	A	N/A	N/A	HDF, HDK + HDF
	B	N/A	N/A	HDF, HDK + HDF
		2dDr	8%	HDF, HDK + HDF
		E2	8%	HDF, HDK + HDF
		AV	10%	HDF, HDK + HDF
	C	N/A	N/A	HDF, HDK + HDF
RES	N/A	N/A	N/A	HDF, HDK + HDF
		2dDr	8%	HDF
			10%	
		E2	8%	
			10%	
		AV	10%	
		AV + 2dDr	10% - 8%	

2.3. Assessment of metabolic activity for cells seeded on TCES and RES

Cell metabolic activity was measured as described in chapter II methods section 8.2. Using a 1mM resazurin stock solution a 10% v/v resazurin + cell medium working solution was prepared. On the day of the experiment, the cell medium of each well was discarded and replaced with 2 mL of the resazurin working solution. Samples were covered from light and incubated for 3 h at RT.

After an incubation period of 3 h, 200 µl of each well were collected by triplicate and transferred to a 96-well plate. The fluorescence signal of the samples was read using a spectrophotometer (FLx800, Bio-Tek Instruments Inc.) set for an λex = 540 nm and λem = 630 nm. Scaffolds were washed with PBS and fresh media was added. The resazurin assay was performed on days 1, 4, and 6. Following the resazurin assay, scaffolds were fixed with a 3.7% formaldehyde solution for 1 h at RT. The samples were stored at 4°C to be imaged using SEM and lightsheet microscopy.

2.4. SEM imaging of cell cultured RES and TCES

RES and TCES cultured with cells were prepared for SEM following a standard hexamethyldisilazane dehydration process. After fixation, samples were dehydrated using increasing concentrations of ethanol (35% - 100%) for 15 min each. To complete the dehydration process, a hexamethyldisilazane (HMDS) (440191, Sigma) was used in 1:1 proportion with ethanol for 1 h followed by a 5 min incubation in pure HDMS. Samples were allowed to dry at RT inside a fume cupboard for 20 min.

After dehydration, samples were coated with a 10 nm gold layer (SC 500A, Emscope) and mounted on aluminum pin stubs (AGG301, agar scientific) with carbon tabs (AGG3347N, agar scientific) and analyzed under a HITACHI SEM (FE SEM, JSM-6500F, JEOL; and FE/VP SEM,

TM3030Plus, HITACHI). Spot size and voltage were set up at 10 kV and 3.5 nm respectively for all samples. ImageJ software v. 1.48 from NIH (National Institutes of Health, USA) [292], was used to measure the size of the microfeature on the SEM micrographs.

2.5. Creating tissue engineered skin models and burned skin models

Skin models were made as reported by Harrison et al. [407] and Chakrabarty et al. [408]. First, the DED previously prepared as described in chapter III section 2.1.2 was cut into 15×15 mm squares using a sterile blade and placed in 6-well plates with the dermal side facing down. The dermal side was identified by its distinctive clearer tone and because the DED folds towards the dermal component. Once inside the well plate, a metal ring was placed on top of the DED to hold the cell suspension in the center of the models.

On development day (DD) -2, Cells were cultured as described in chapter III section 2.1.3 and 2.1.4 (i3T3s were not used for the fabrication of skin models). Cells were cultured at densities of 300,000 HDK, and 100,000 HDF per model and seeded inside the metal ring with 500 µL of Green's media. These skin models were used as a control and to study tissue regeneration on our burned skin model experiment. For evaluating the effects of TCES and RES on skin model epidermal stratification, the TCES membrane was placed on top of the DED followed by the addition of the metal ring. Same cell densities were used for both groups. For models seeded with AdSC, cells were cultivated on the dermal side one day before the experiment (DD -3) to be used 24 h after to fabricate conventional skin models as described before. Skin models were cultured at 37°C in a 5% CO_2 humidified atmosphere. Table 20 shows the conditions and scaffolds tested on the skin tissue engineered models.

Table 20. Electrospun scaffolds (RES and TCES) and conditions tested on skin tissue engineered models.

Scaffold/Condition Tested	Pattern used	Bioactive compound	Concentration
TCES	A	N/A	N/A
	B		
		2dDr	8% wt.
	C	N/A	N/A
RES	N/A	N/A	N/A
		2dDr	8% wt.
2dDr in solution	N/A	2dDr	100 µM
AdSC	N/A	N/A	50,000 cells/model

After an incubation period of 24 h (DD -1), the metal rings were removed from the skin models and 2 mL of Green's media were added to each sample. The next day (DD 0), sterile metal grids were placed inside a new 6-well plate and the skin models were transferred on top of the grids using sterile forceps. To create an air-liquid interface for each skin model, the adequate volume of Green's medium was added to each well so the surface of the grids would be barely covered in media. This volume usually ranged between 4.2 and 6 mL of cell medium. Figure 93 shows an image of the metal grids and rings used for this experiment. Cell medium was changed every 2 days and the skin models were maintained at 37°C in a 5% CO_2 humidified environment. The skin

models on DD 0 were cultivated until DD 10 followed by a 2 h fixation step with 3.7% formaldehyde at RT.
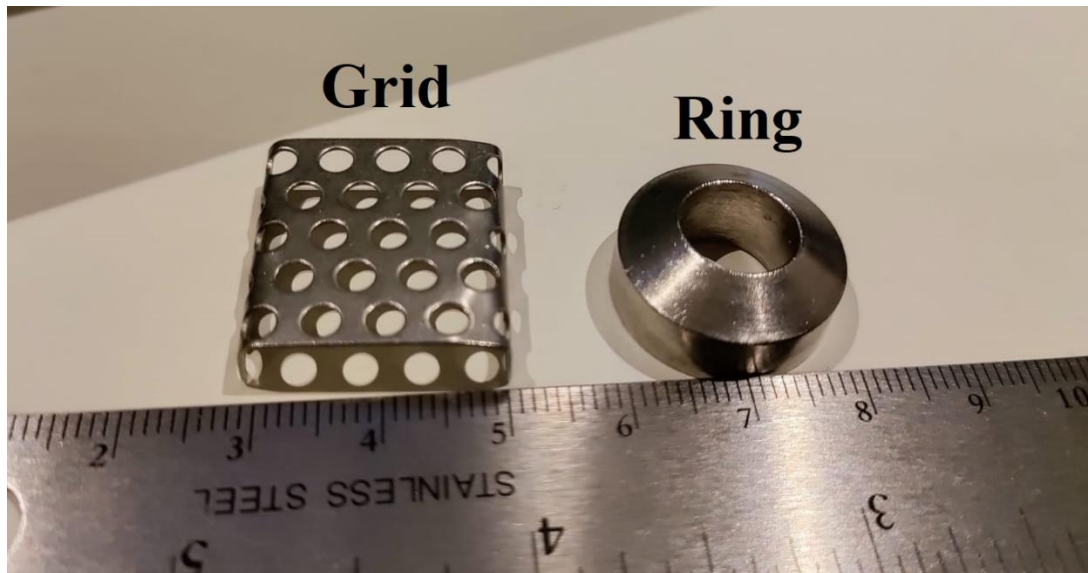
Figure 93. Stainless steel ring (right) and grid (left) used to hold the cell suspension and maintain the skin model on an air-liquid interface.

To create burned skin models, control skin models were burned on DD7 by placing a platinum small vessel cauterizer (DBE1003, SLS) for 3 seconds, to damage the superficial epidermal layer. TCES and RES were then implanted on top of the damaged area. Cell medium was changed, and the models were left to incubate up to DD 12. Burned models were fixed as described previously by incubating the models for 2 h at RT with a 3.7% formaldehyde solution. Models were washed with PBS and stored at 4°C. Figure 94 shows a schematic representation of the methodology used to fabricate the skin models.
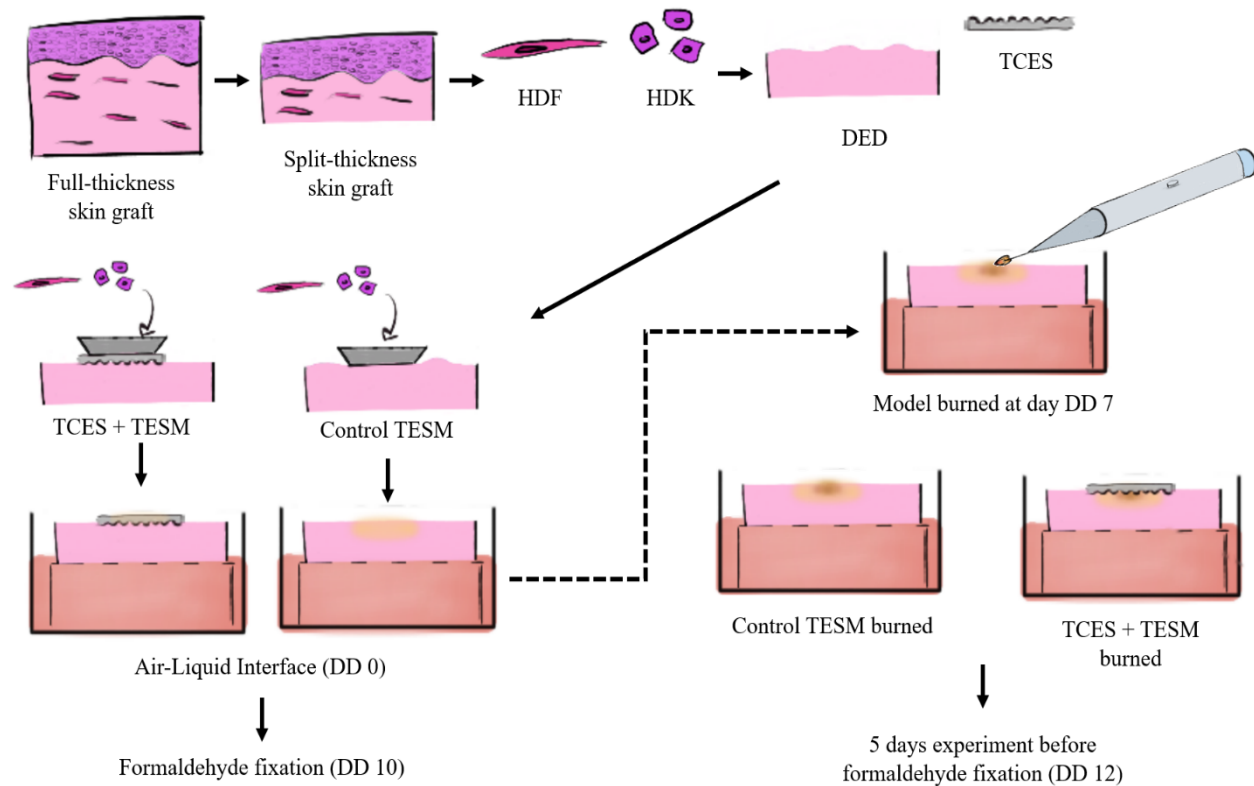
Figure 94. Schematic representation of the methodology used to fabricate tissue engineered skin models (TESM) and burned skin models.

2.6. Assessment of metabolic activity on skin models

A resazurin reduction assay was performed to evaluate the effects on metabolic activity for healthy and burned skin models with and without RES and TCES. On DD 7, before damaging the models with a cauterizer, all control skin models were transferred to a new 6-well plate containing 2 mL of 10% resazurin working solution in Green's medium. The resazurin working solution was prepared as described before by making a filter-sterilized 1 mM solution of resazurin salt in PBS (see methods section 8.2). Samples were covered from light and incubated for 3 h at 37°C in a 5% CO_2 humidified atmosphere.

After incubating the samples with the resazurin, 200 µL of each well by duplicate were transferred to a 96-well plate. The fluorescence signal of the samples was read using a spectrophotometer (FLx800, Bio-Tek Instruments Inc.) and KC4 software (version 3.3, Bio-Tek Inc.) set for an λex = 540 nm and λem = 630 nm. Models were then placed back on the original 6-well plate with the metal grids and the epidermal layer was damaged using a cauterizer as described in methods section 2.5. Models were then implanted with RES, TCES, or RES loaded with 2dDr. At DD12, the resazurin assay was performed again as described before to measure any differences in metabolic activity.

After completing the resazurin assay, skin models were incubated for 2h at RT with a 3.7% formaldehyde solution. Samples were washed with PBS and stored at 4°C. One independent test was performed by triplicate for this experiment (n = 3).

2.7. Lightsheet microscopy of RES, TCES, and tissue engineered skin models

Lightsheet microscopy was used to observe cell distribution and expression of relevant biomarkers across the samples from different angles. The samples used for lightsheet imaging were previously fixed after assessing metabolic activity, or in the case of tissue engineered models, after completing DD10. Figure 95 shows a schematic of the methodology used to image the samples using lightsheet microscopy.
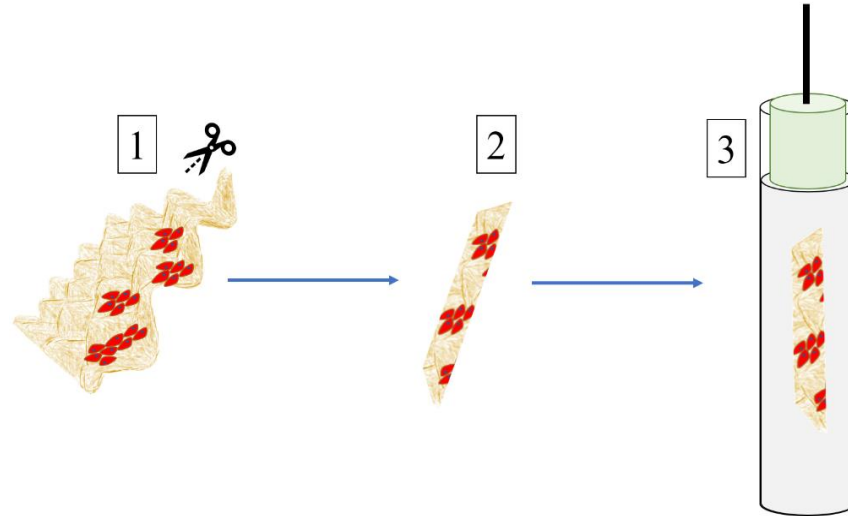
Figure 95. Schematic representation of the mounting technique used for imaging the scaffolds by lightsheet microscopy. First, a cross-section of the stained scaffold was cut to fit the diameter of the glass capillary (1-2). Then, the sample is mounted into the capillary using an agarose solution (3).

2.7.1. Sample preparation and immunostaining

Fixed samples were prepared by cutting 2×5 mm cross-sections of the center area and transferred them to a 48-well plate. Samples were then permeabilized using 500 µL of 0.1% Triton X-100 for 1 h. Samples were washed twice with PBS to remove any restudies of Triton and then incubated with 3% w/v BSA solution in PBS for 1 h to block any nonspecific proteins.

TCES and RES seeded only with HDF were stained with DAPI for cell nuclei, phalloidin-TRITC for F-actin filaments, and Alexa Fluor® 488 (ab150077, abcam) for collagen type IV (COL IV). After permeabilization, samples were incubated with 400 µL of rabbit polyclonal COL IV (ab6586, abcam) primary antibody for 24 h at 4ºC (1:400 in 1% BSA). The scaffolds were then washed with PBS and incubated with anti-rabbit Alexa Fluor® 488 (ab150077, abcam) for 4 h at RT (1:600 in

1% BSA). Samples were washed with PBS twice and incubated for 1 h at RT with 500 µL of a DAPI stock solution 300mM, dilution 1:1000 and phalloidin TRITC solution in PBS. Samples were washed with PBS and stored at 4°C until imaged.

Tissue engineered skin models, RES, and TCES seeded with HDF + HDK were stained for cell nuclei using DAPI and immunostained for COL IV and integrin β1 (Iβ1) following the protocol previously described. The incubation of primary antibodies rabbit polyclonal COLIV and mouse monoclonal Iβ1 (ab24693, abcam) was performed simultaneously. Anti-rabbit Alexa Fluor® 488 and anti-mouse Alexa Fluor® 647 (ab150115, abcam) secondary antibodies were incubated for COL IV and Iβ1 respectively at concentrations of 1:500 in 1% BSA at RT for 4h. Samples were then washed with PBS and stored at 4°C.

2.8. Lightsheet imaging and image processing

Samples were placed inside the lightsheet chamber by mounting them into a 2.15 mm glass capillary with a 1% w/v low gelling temperature agarose solution (A9414, Sigma) heated at 70°C using a block heater (Thermo Scientific, UK). A lightsheet microscope (Lightsheet Z.1, Carl Zeiss) and ZEN lite software (2012, Carl Zeiss) were used to control and capture the samples. A Zeiss W Plan-Apochromat 10×/0.5 numerical aperture (NA) lens was used for detection and a Zeiss LSFM 5×/0.1 NA lens for illumination.

The sample was located and focused before selecting the optimal slide side of the Z stack that ranged from 4 to 6 µm. At least two views of 0º and 45º views were set up for each experiment. Some experiments were set up for six views of 0º, 45º, 90º, 180º, 225º, and 270º to better appreciate the infiltration of the cells from the top of the scaffold.

Lasers 638 nm, 488 nm, and 405 nm were used for excitation of Alexa Fluor® 647, Alexa Fluor® 488, and DAPI respectively. For emission, band pass 545-590, low pass 660, and short band 550 filters were used. Software ZEN lite (2012, Carl Zeiss) was used for image acquisition and processing. Software ZEN lite (2012, Carl Zeiss) was used for image acquisition and processing. Raw files were processed by creating a maximum intensity projection. Raw images of every channel and a complete processed image were saved for later analysis using ImageJ software v. 1.52 [292].

2.9.   Histological analysis of tissue engineered skin models

Histology sections of the skin tissue engineered models were made using the paraffin wax embedded method. All samples used were previously fixated with paraformaldehyde as described in methods section 12 and 12.1.

2.9.1. *Wax embedding and sample sectioning*

Fixed skin models were cut by the center section to produce two symmetric samples. These two samples were placed inside a plastic cassette and labeled accordingly. This procedure was carried out for all the samples. The cassettes with the samples were placed inside a Leica TP1020 tissue processor (Leica Biosystems, UK) for an 18 h cycle in which the samples were dehydrated with different concentrations of ethanol and xylene and submerged on melted wax. Once the cycle was completed, samples were retrieved from the tissue processor and the cassettes were discarded. Samples were then placed inside metal molds and melted was poured inside to create a wax mold with the sample on it. Wax molds were stored at 4°C inside sealable bags.

Sectioning of the samples was performed using a microtome RM2145 (Leica, UK). Thickness was set at 10 µm and at least 12 – 15 sections were taken for every sample. The sections were collected on Polysine® glass slides (Thermo Scientific, UK) and left to dry for 24 h before staining.

2.9.2. *Hematoxylin and Eosin staining*

To stain the samples with hematoxylin and eosin (H&E), slides were placed in a hydration process. First, samples were soaked in xylene (Fisher Scientific, UK) for 5 min followed by washes of 100%, 70%, and 50% IMS for 3 min each. Then samples were placed 1 min in distilled water followed by a 2 min stain step in Harris Hematoxylin solution (HHS32, Sigma) and a 5 min stain step with Eosin Y (HT110232, Sigma). A dehydration process was followed using washes of 70% and 100% IMS, and xylene for 30 seg each. Samples left to air dry inside a fume cupboard for 1 min and then were mounted with a glass cover slide using DPX (100579, Merck). Slides were stored at RT and covered from light until imaging.

2.9.3. *Image processing and analysis*

Images of the histology sections were taken under a light microscope (Motic DM-B1) at 10x and 20x magnification using the Motive live imaging module software (Motic 2.0). Features such as the epidermal stratification and size of the artificial niches were especially of interest. At least three representative images were taken per slide with three independent tests performed by triplicate for each experiment (N = 3, n = 3). ImageJ software v. 1.48 from NIH (National Institutes of Health, USA) [292], was used to measure the size of the microfeatures formed for both the TCES and control skin models.

3. Results

3.1. Analysis of HDF behavior when seeded on TCES

Evaluating the performance of RES and TCES to induce an effect on cell behavior *in vitro* or on skin tissue engineered models is critical to estimate their potential to aid skin regeneration on *in vivo* models. The initial results showed that seeding HDF on TCES had no visible effect on the expression of COL IV when compared to a scaffold with no pattern. Figure 96 shows that HDF proliferated across the microtopographies and that there was no distinctive proliferation pattern related to the presence of the microfeatures on the TCES, regardless of high or width of such topographical cues. Moreover, the cell viability assay on the TCES confirmed that there is no statistical significance in cell metabolic activity among different patterns of TCES. Nonetheless, there is a small increase in cell metabolic activity for HDF seeded on patterns B and C when compared to the PCL control at day 6 (Figure 97).
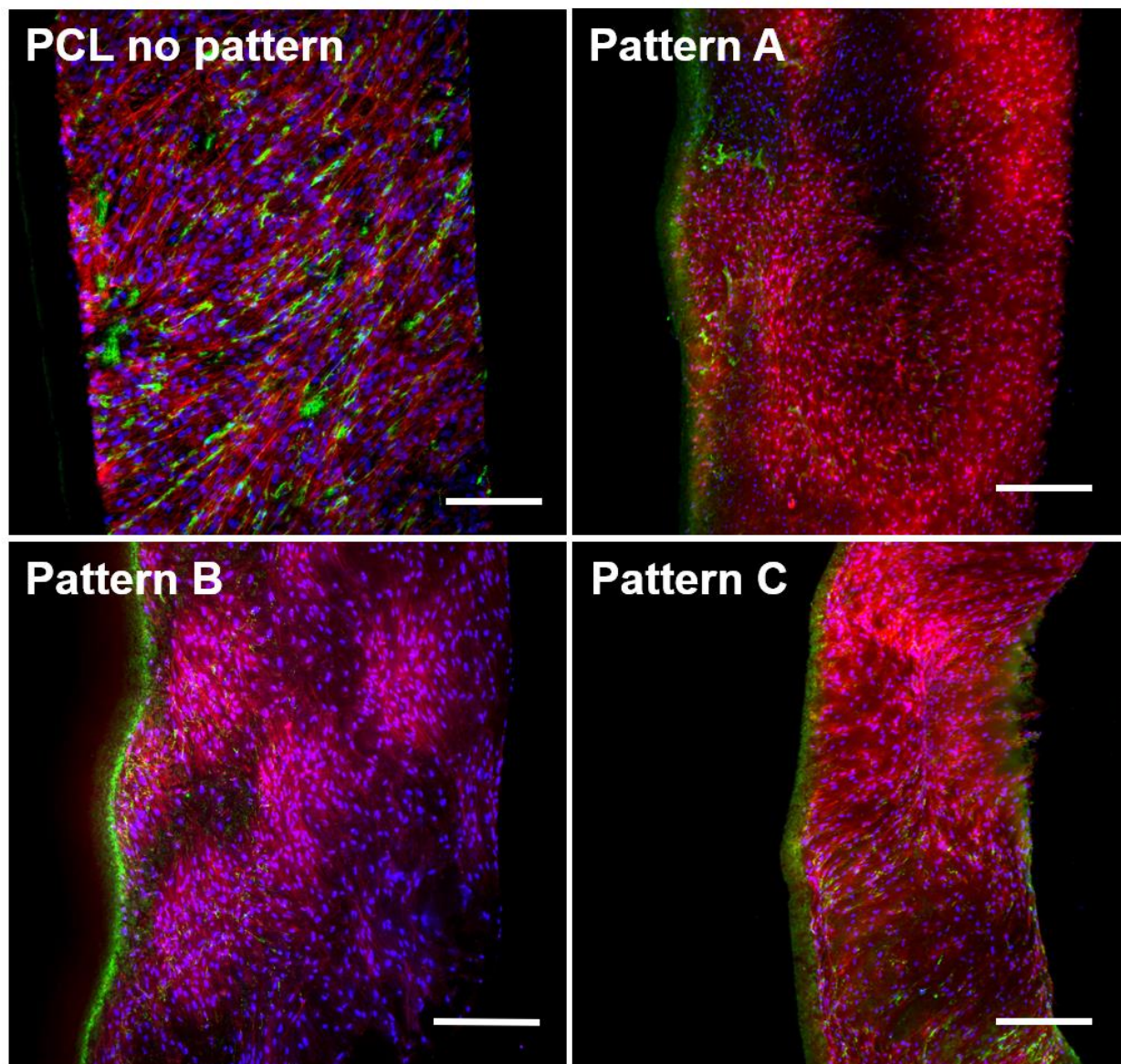
Figure 96. Immunostained lightsheet microscopy images showed TCES compared against a RES PCL control. The three patterned TCES were seeded with HDF for 6 days and stained for COL IV (green), cell nuclei (blue), and F-actin filaments (red). Scale bar = 200 µm.

TCES - HDF metabolic activity
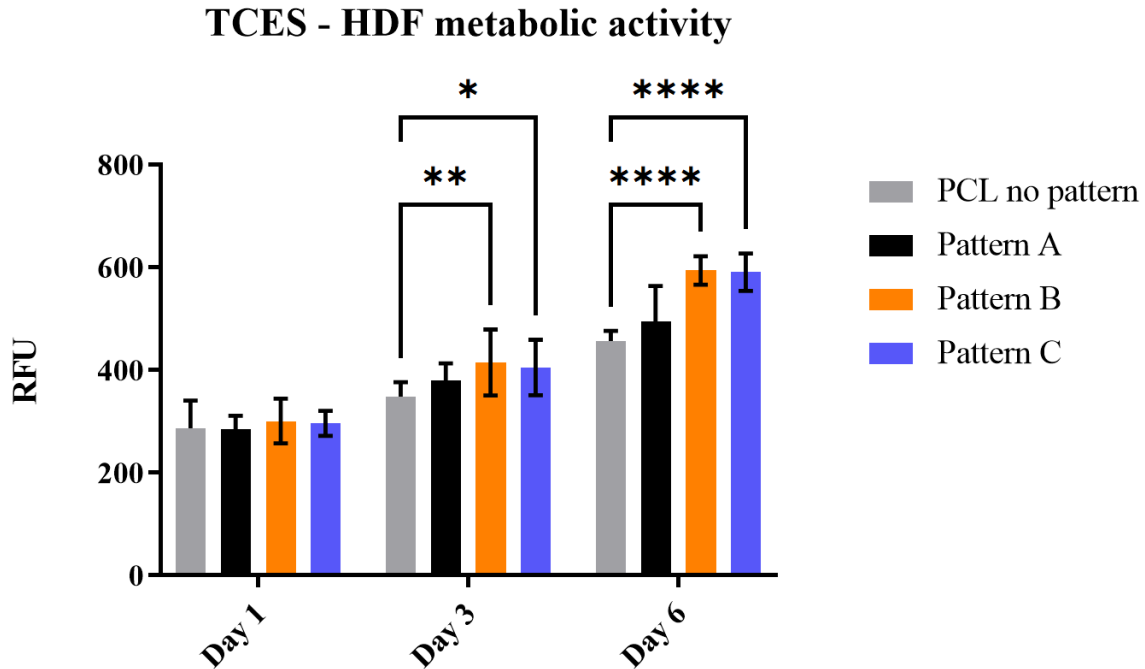
Figure 97. Metabolic activity of HDF when seeded on TCES with patterns A, B and C for 6 days compared against a RES control. Results are shown as mean ± SD. Two-way ANOVA statistical analysis with Tukey comparison test. **** $p < 0.0001$, ** $p < 0.01$, * $p < 0.05$. N = 2, n = 3.

3.2. Analysis of HDK + HDF behavior when seeded on TCES

As with the monoculture of HDF, the performance of TCES seeded with HDK + HDF was analysed by lightsheet microscopy to observe any changes in cell behaviour when compared to the plain RES control. The results on this thesis showed that depending on the microfeatures present on the TCES, cells were more likely to form colonies and these generated clusters of Iβ1 as shown in Figure *98*. TCES made with patterns A and C showed that higher contents of Iβ1 at the bottom of the microfeatures, with pattern C showing a higher expression of COLIV at the top of the microfeatures. However, TCES fabricated with pattern B showed clusters of Iβ1 at the top of the artificial ridges.
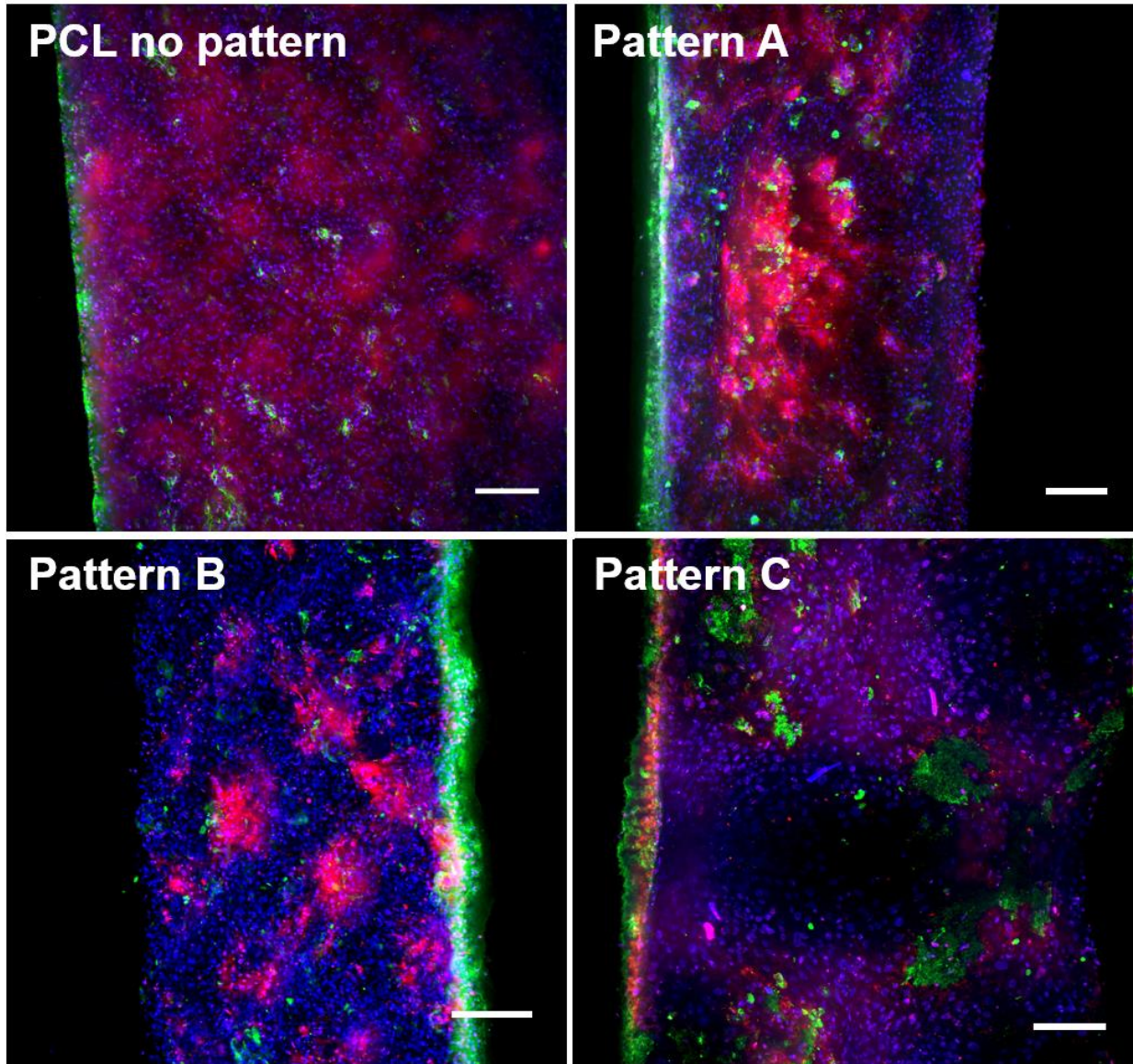
Figure 98. Immunostained lightsheet microscopy images showed TCES compared against a RES PCL control. The three patterned TCES were seeded with HDK + HDF for 6 days and stained for COL IV (green), cell nuclei (blue), and Iβ1 (red). Scale bar = 200 μm.

The formation of colonies on the microtopographies of TCES seeded with HDK + HDF was also observed under the SEM. Figure 99 highlights the cell distribution for pattern A, B, and C. In contrast with the lightsheet microscopy images, SEM images showed that cells are more likely to

proliferate at the bottom of the microfeatures rather than the top. This behavior was also observed by the amount ECM deposited at the bottom of the microfeatures. In comparison, the plain RES control showed no distinctive pattern of proliferation or ECM deposition. Figure 100 shows a cross-section of TCES pattern C seeded with HDK + HDF. The interface between the ECM deposited by the cells at the bottom of the microfeature integrates with the scaffold as it proliferates. Both SEM and lightsheet microscopy images demonstrated that the topographical cues fabricated with PCL electrospun scaffolds were preserved even after 6 days in culture conditions.
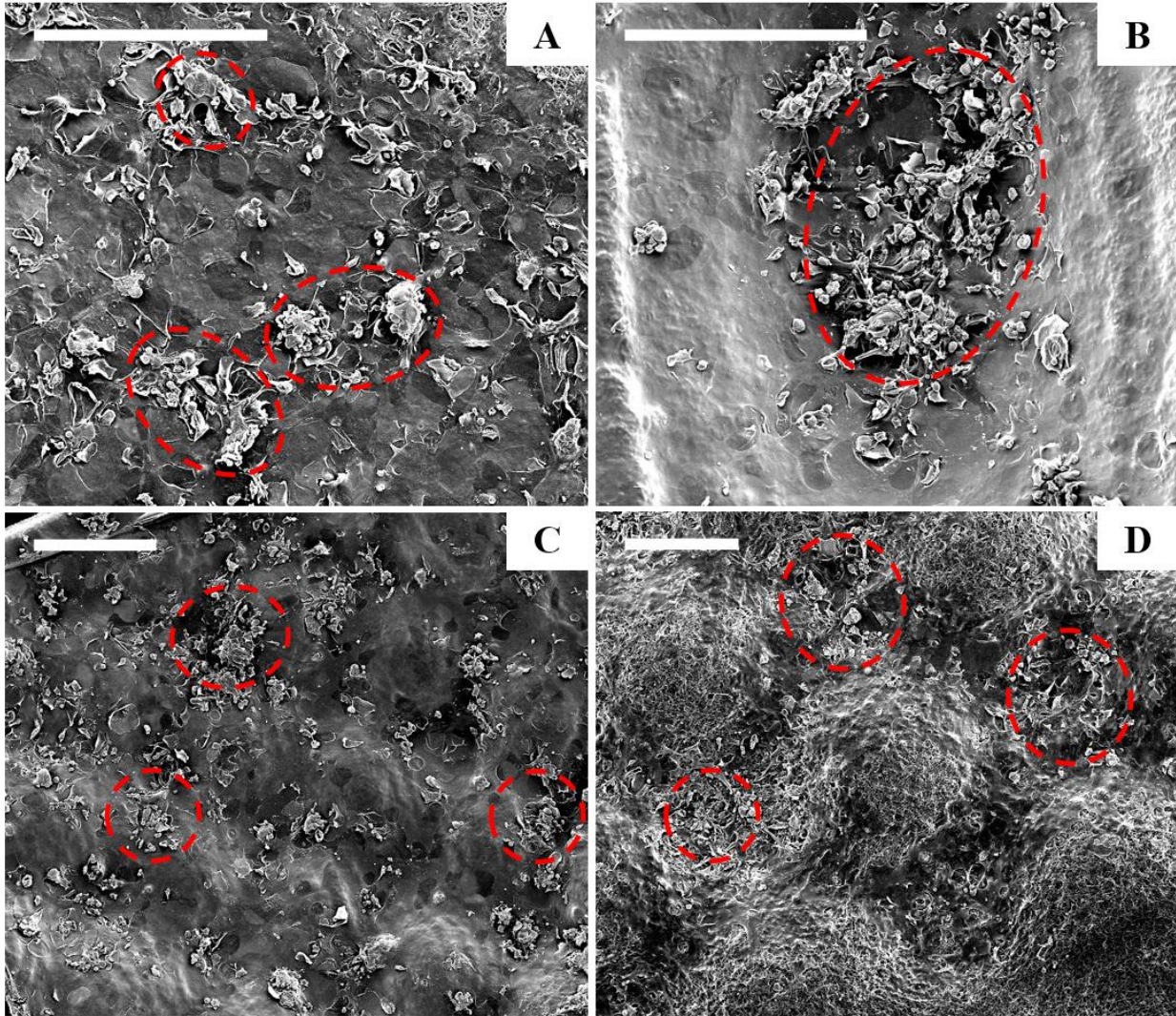
Figure 99. SEM images showing cell distribution and matrix deposition of HDK + HDF seeded on TCES and compared against a RES control. A) PCL control, B) pattern A, C) pattern B, and D) pattern C. HDK + HDF that proliferated on top of the scaffold are highlighted in red. Scale bar = 500 µm.
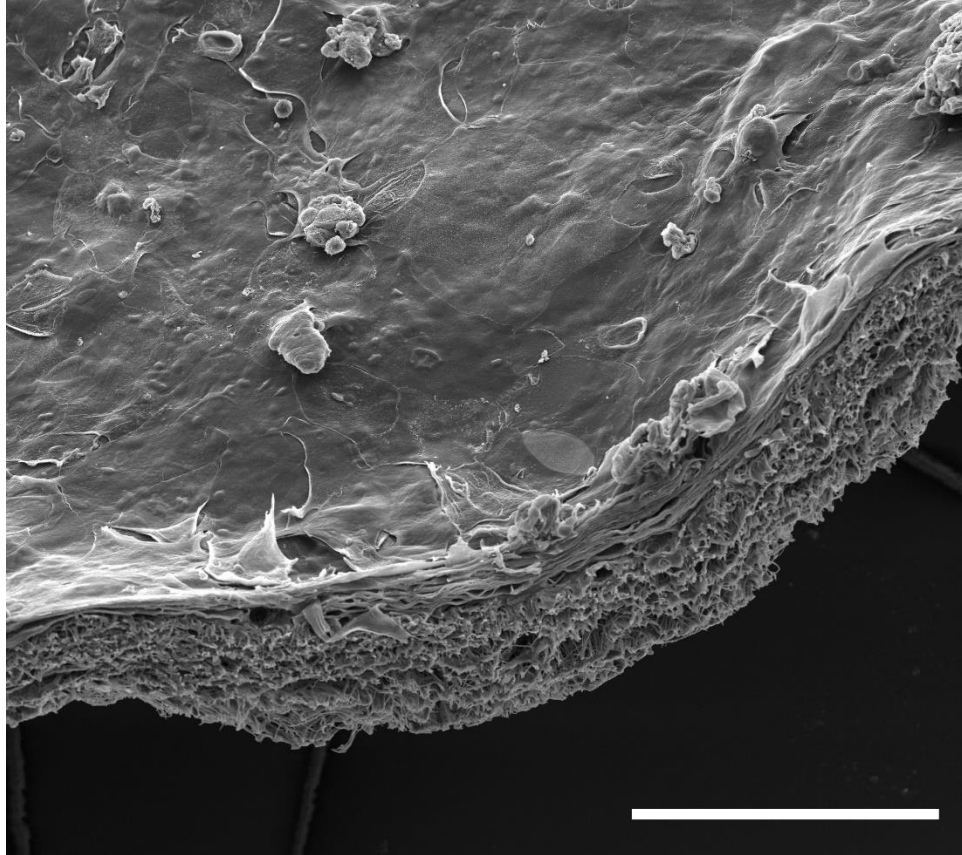
Figure 100. SEM image of TCES pattern C cross-section seeded with HDK + HDF (300,000 HDK, 100,000 HDF). The shape of the microfracture is mostly retained even after 6 days in culture. ECM deposition can be observed at the top side where the cells were cultured. Scale bar = 500 µm.

The resazurin viability assay of HDK + HDF seeded on TCES showed an increase in cell metabolic activity for the TCES groups compared to the plain RES. Figure 101 shows higher values of metabolic activity for cells seeded on TCES at day 3 and 6 compared to the RES control with no statistical differences between patterns for day 3 and 6.

TCES - HDK + HDF metabolic activity
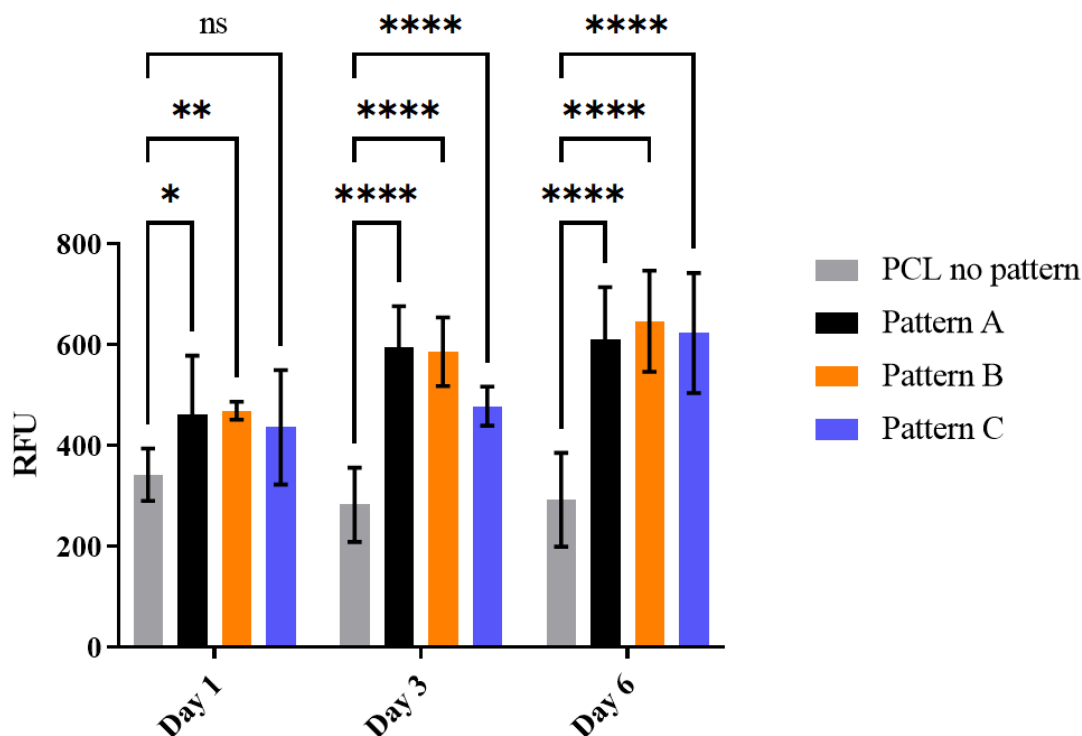
Figure 101. Metabolic activity of HDK + HDF when seeded on TCES with patterns A, B and C for 6 days compared against a RES PCL control. Results are shown as mean ± SD. Two-way ANOVA statistical analysis with Tukey comparison test. **** $p < 0.0001$, ** $p < 0.01$, * $p < 0.05$, ns $p \geq 0.05$. N = 2, n = 3.

3.3. Analysis of HDF behavior when seeded on RES loaded with bioactive compounds

The effects of adding bioactive compounds on PLC scaffolds was initially tested using HDF and RES. SEM micrographs showed the proliferation of HDF on the top surface of the scaffold for 2dDr, E2, and AV loaded RES (Figure 101). Furthermore, the analysis of metabolic activity of HDF revealed that RES loaded with 8% wt. 2dDr, or 10% wt. AV showed higher values when compared to 10% wt. E2 and 8% wt. 2dDr + 10% wt. AV (Figure 103). Nonetheless, none of the

RES loaded with bioactive compounds showed higher values than the control with only the 2dDr and AV groups showing no significant differences to the control by day 6. The lowest metabolic activity values were obtained for cells seeded on 10% wt. E2 RES at day 4 and 6.
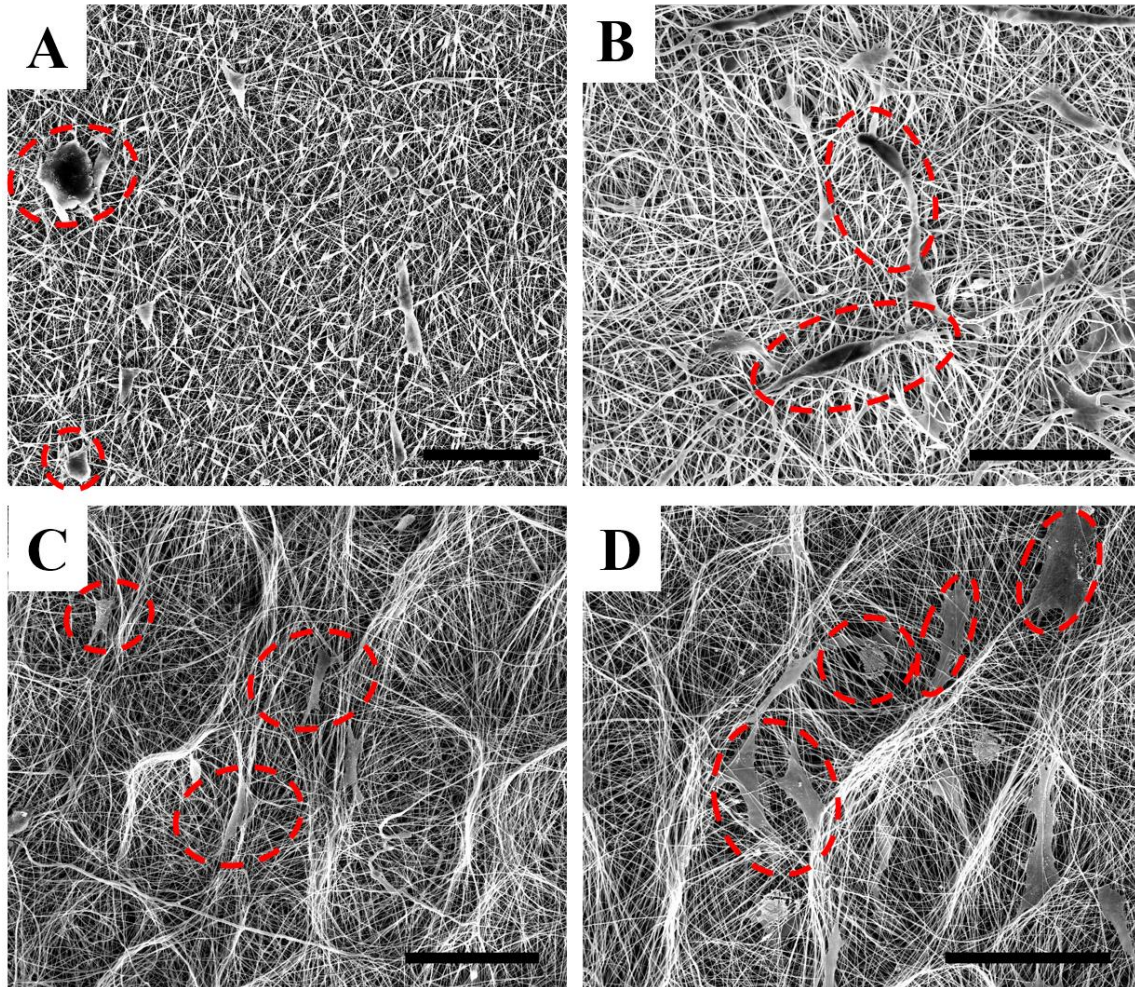
Figure 102. SEM images showing cell distribution and matrix deposition of HDF (10,000 cells) on RES at day 3. A) PCL control, B) 8% wt. 2dDr, C) 10% wt. E2, and D) 10% AV. HDF that proliferated on top of the scaffold are highlighted in red. Scale bar = 500 µm.
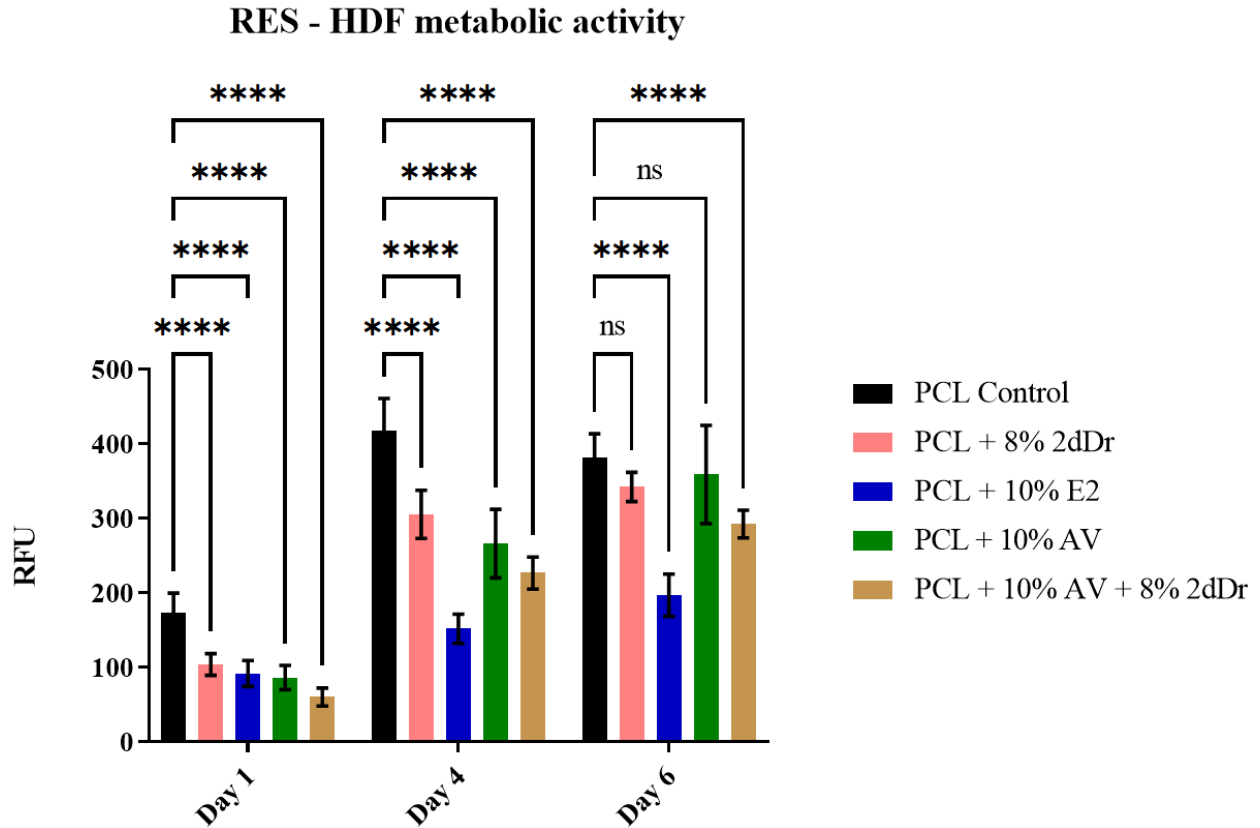
Figure 103. Cell metabolic activity of HDF seeded on PCL RES loaded with bioactive compounds 2dDr, E2, AV, or in combination. Results are shown as mean ± SD. Two-way ANOVA statistical analysis with Tukey comparison test. **** $p < 0.0001$, ns $p \geq 0.05$. N = 2, n = 3.

3.4. Analysis of HDK + HDF behavior, when seeded on TCES and RES, loaded with bioactive compounds

The proliferation of HDK + HDF seeded on RES loaded with bioactive compounds was observed under the lightsheet microscope. Figure 105 shows the expression of Iβ1 and COL IV for 2dDr, E2, and AV RES. Figure 104 shows a TCES under the lightsheet microscope with no cells as a control. However, no cell viability assay was performed to observe any changes in metabolic activity for HDK + HDF seeded on RES. Nevertheless, the assessment of HDK + HDF seeded on

TCES loaded with bioactive compounds was carried out using the most reproducible pattern C to fabricate the scaffolds. Figure 106 shows that proliferation of HDK + HDF on TCES was altered by the introduction of the bioactive compounds. Images of the TCES + 2dDr and TCES + AV indicate the high proliferation of cells, expression of Iβ, and that the topographical cues were lost during the cell culture experiment. In comparison, the TCES + E2 preserved the microfeatures of the scaffolds and showed a similar proliferation pattern as the TCES control where HDK colonies can be observed at the bottom of the microfeatures due to the presence of Iβ1 clusters.

Figure 104. TCES sample under the lightsheet microscope to use as a control. No auto-fluorescence was detected under the same lasers used to image the cell seeded samples.
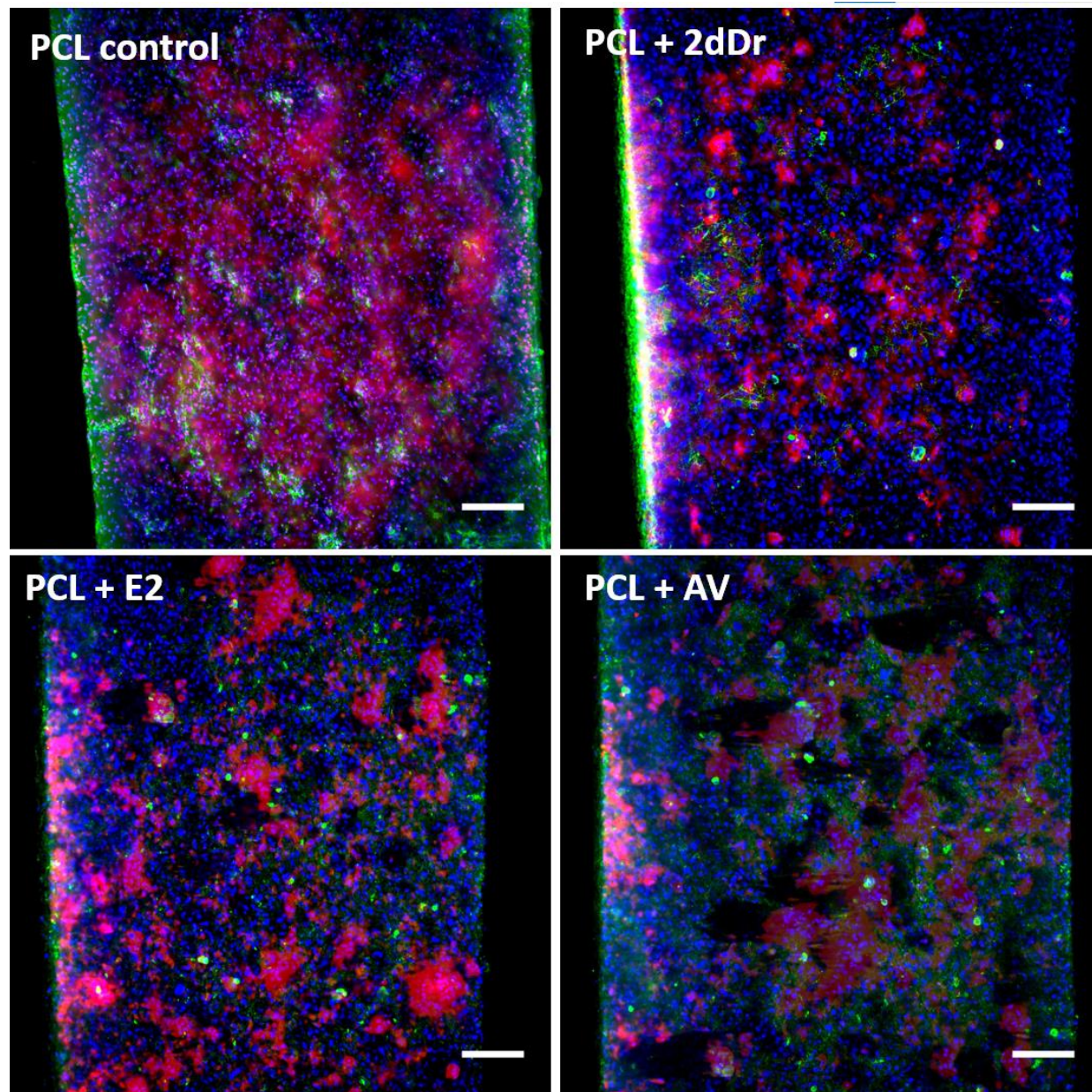
Figure 105. Immunostained lightsheet microscopy images of RES loaded with bioactive compounds 2dDr, E2, or AV compared against a RES PCL control. The RES were seeded with HDK + HDF for 6 days and stained for COL IV (green), cell nuclei (blue), and Iβ1 (red). Scale bar = 200 μm.
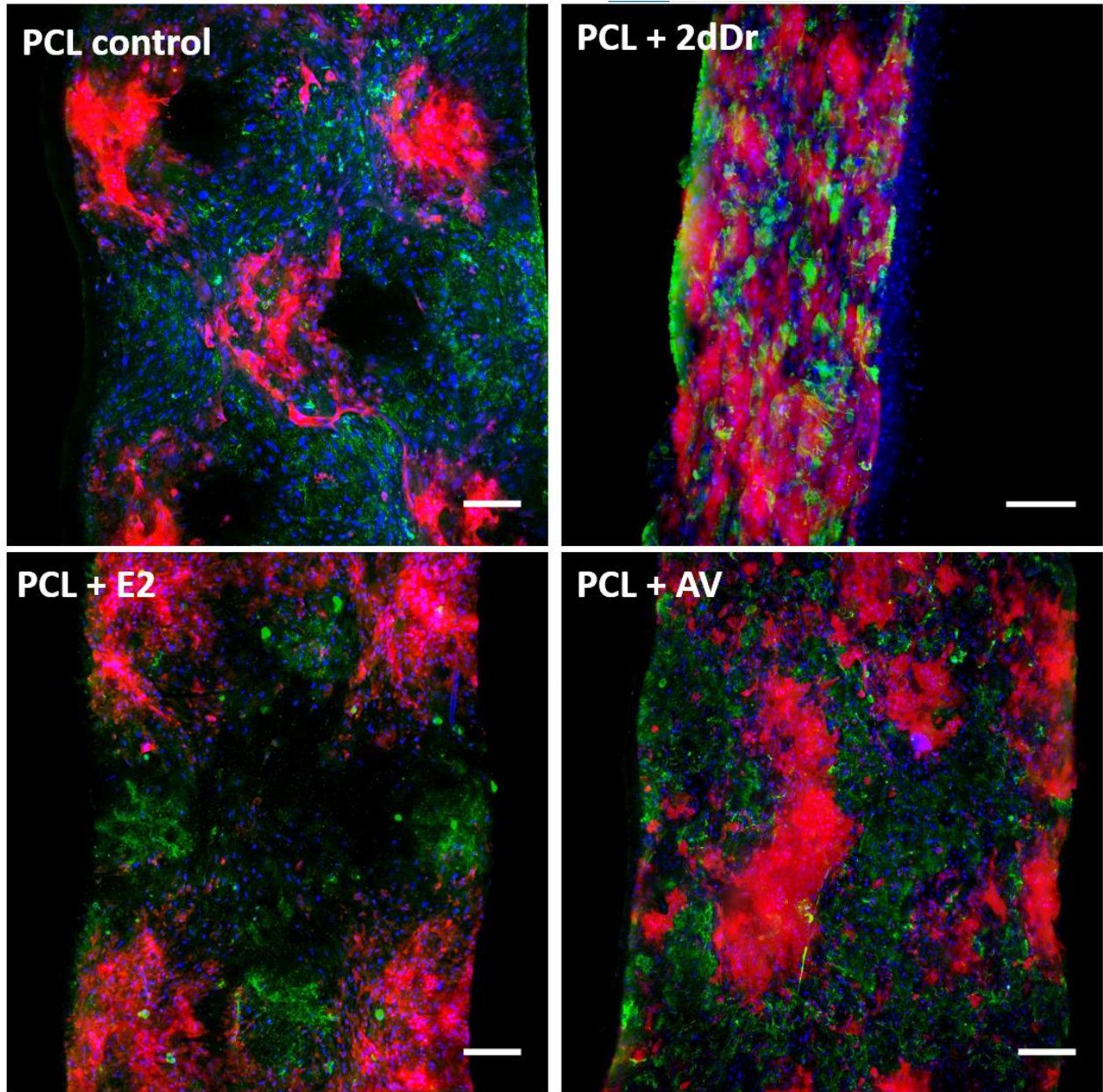
Figure 106. Immunostained lightsheet microscopy images of TCES loaded with bioactive compounds 2dDr, E2, or AV compared against a RES PCL control. The TCES were seeded with HDK + HDF for 6 days and stained for COL IV (green), cell nuclei (blue), and Iβ1 (red). Scale bar = 200 μm.

The results from the viability assay showed that HDK + HDF had higher metabolic activity when seeded on the TCES control and that the presence of bioactive compounds decrease these values (as shown in Figure 107). Moreover, loading E2 into the TCES proved to induce the higher metabolic activity values among the bioactive compounds group, followed by AV and finally 2dDr showing the lowest metabolic activity values from all the TCES tested.
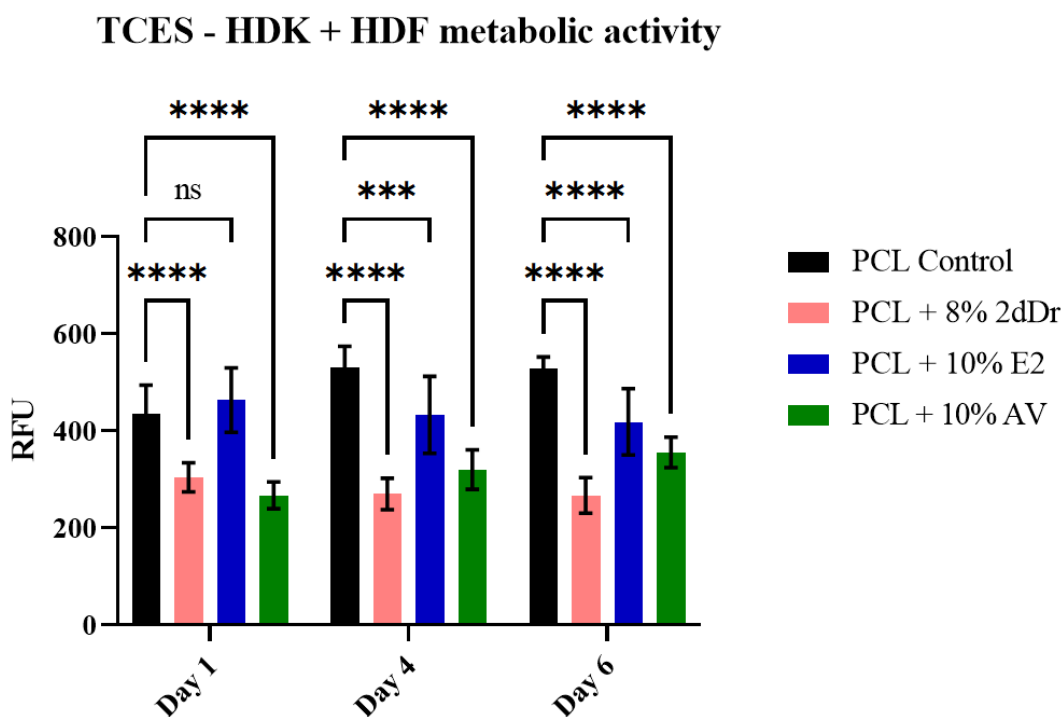
Figure 107. Cell metabolic activity of HDK + HDF seeded on PCL TCES loaded with bioactive compounds 2dDr, E2, or AV. Results are shown as mean ± SD. Two-way ANOVA statistical analysis with Tukey comparison test. **** $p < 0.0001$, ns $p \geq 0.05$. N = 2, n = 3.

3.5. Formation of rete ridge-like structures on tissue engineered skin models when implanted with TCES

Skin tissue engineered models were successfully fabricated to observe the effects of TCES on the development of rete ridge-like structures. Preliminary experiments were carried out to determine the most suitable time point to evaluate the rete ridge formation. Figure 110 shows the difference in epidermal stratification and rete ridge formation between the skin models fabricated at DD 6 and DD 10 compared to the full-thickness and split-thickness donor skin prior to the cell isolation and DED fabrication process. The results from these experiments indicate that at DD 10 skin models are more suitable to be used to evaluate TCES performance due to the presence of elongated rete ridges and keratinocyte stratification and of paramount importance on skin development.
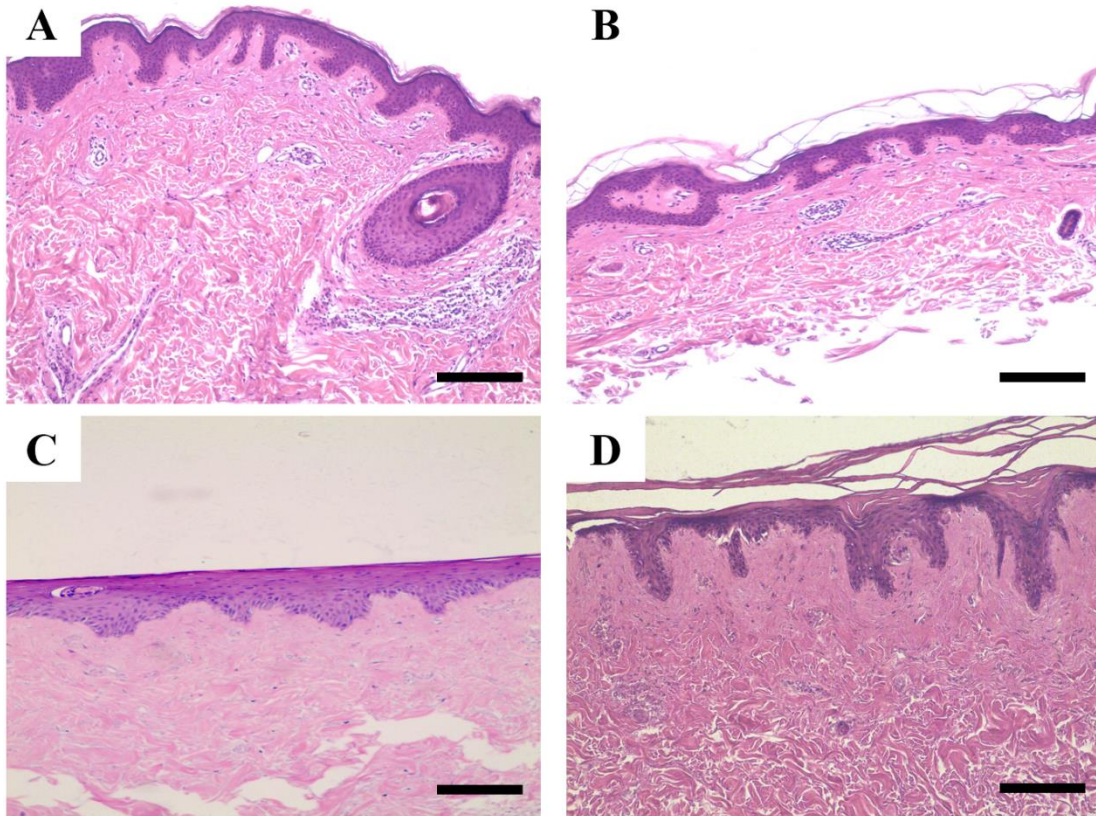
Figure 108. Comparison of epidermal development between A) full-thickness and B) split-thickness donor skin against skin tissue engineered models at C) DD6 and D) DD 10. This optimization was used to define the better time frame to study rete ridge formation. Scale bar = 200 μm.

Histological analysis of the skin models implanted with TCES showed an improvement on tissue integration when compared to the plain RES control (Figure 109). Additionally, all patterns were able to induce the formation of synthetic structures that resemble their original microfeatures. Furthermore, the highest cell proliferation and tissue integration was observed for the TCES pattern B which are the smallest and with the highest similarity to the native rete ridges. When measuring the dimensions of the structures generated by the TCES on the epidermal layer (Figure 110), it was observed that all TCES patterns produced structures with the same height as the ones

present on the skin model control (148.3 ± 21.06 µm). Nonetheless, even the smallest TCES pattern B induced the formation of features (360.06 ± 61.5 µm) twice the average width of the rete ridges present on the skin model control (113.29 ± 36.08 µm). Although, the template pattern C is wider than pattern B by 624 µm, the features produced by TCES pattern C on the skin models were barely wider (430.3 ± 62.54 µm) than those showed on pattern B. As expected, TCES pattern A produced the widest features among all TCES groups (959.4 ± 101.06 µm) due the original template dimensions (2000 µm) that double those of pattern C.
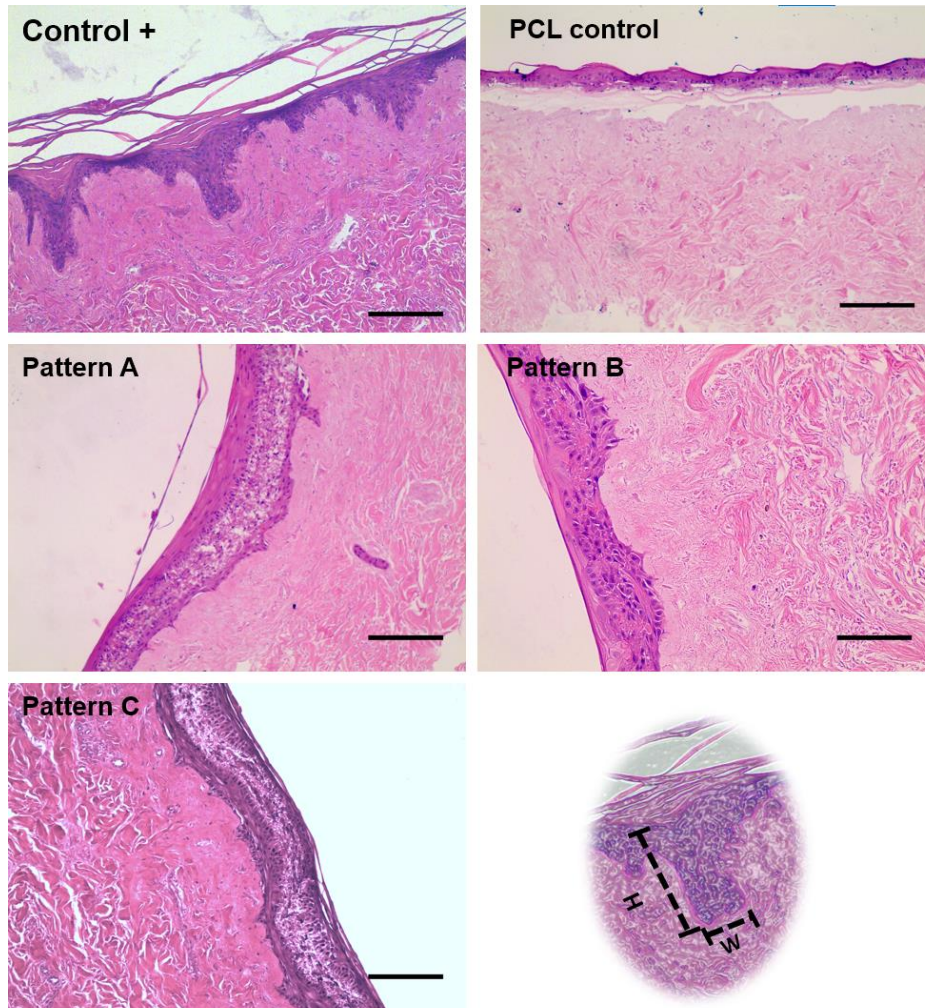
Figure 109. Comparison of the microfeatures created using TCES compared to a skin model control group and a RES control. H&E histology sections show TCES made from patterns A, B, and C showed the formation of features and cell infiltration through the scaffold whereas the plain PCL showed no features and poor tissue integration compared to the control. Scale bar = 200 µm.
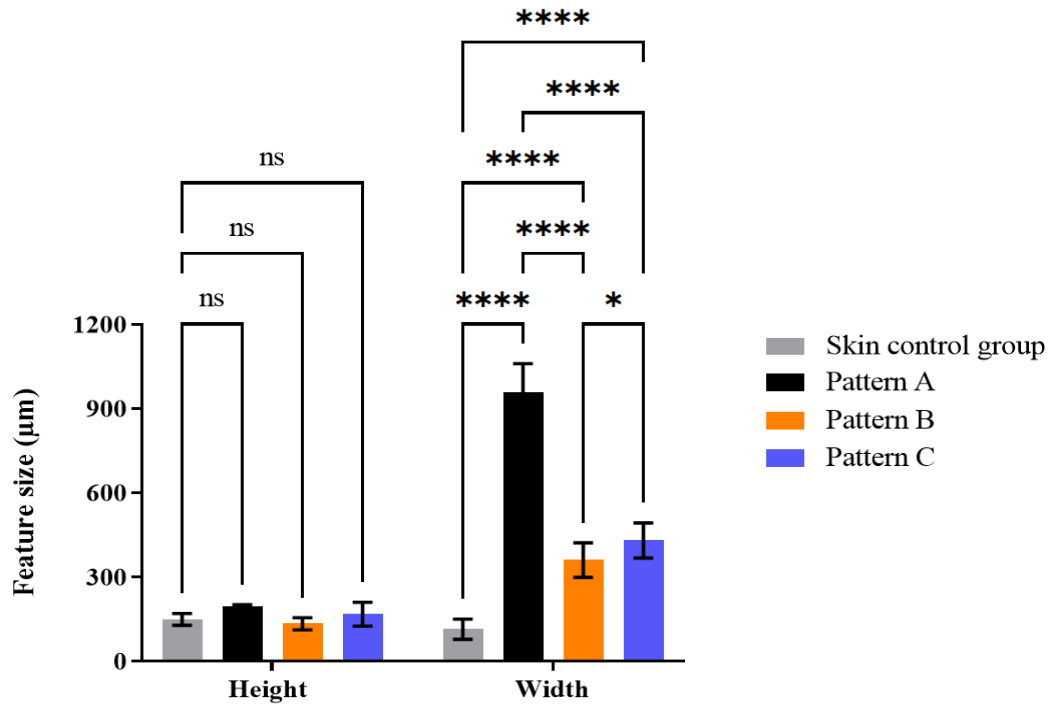
Figure 110. Comparison of the width and height of the microenvironments created using TCES compared to a skin model control group. Measurement of the features showed no significant difference between the height of the TCES and the skin model control group. In contrast, all TCES groups showed microenvironments with greater widths compared to the skin control group. Results are shown as mean $\pm$ SD. Two-way ANOVA statistical analysis with Tukey comparison test. **** $p \leq 0.0001$, ns $p \geq 0.05$. N = 3, n = 3.

The differences in tissue integration from RES to TCES can be further observed using SEM. Figure 111 shows that skin models implanted with plain RES had low to no integration with the dermal component. This behaviour is improved when pattern A TCES were implanted as cells were able to infiltrate the scaffold towards the dermal component of the model compared to a control group. However, both RES and TCES groups did not show the level of integration and tissue stratification observed for the skin model control group.
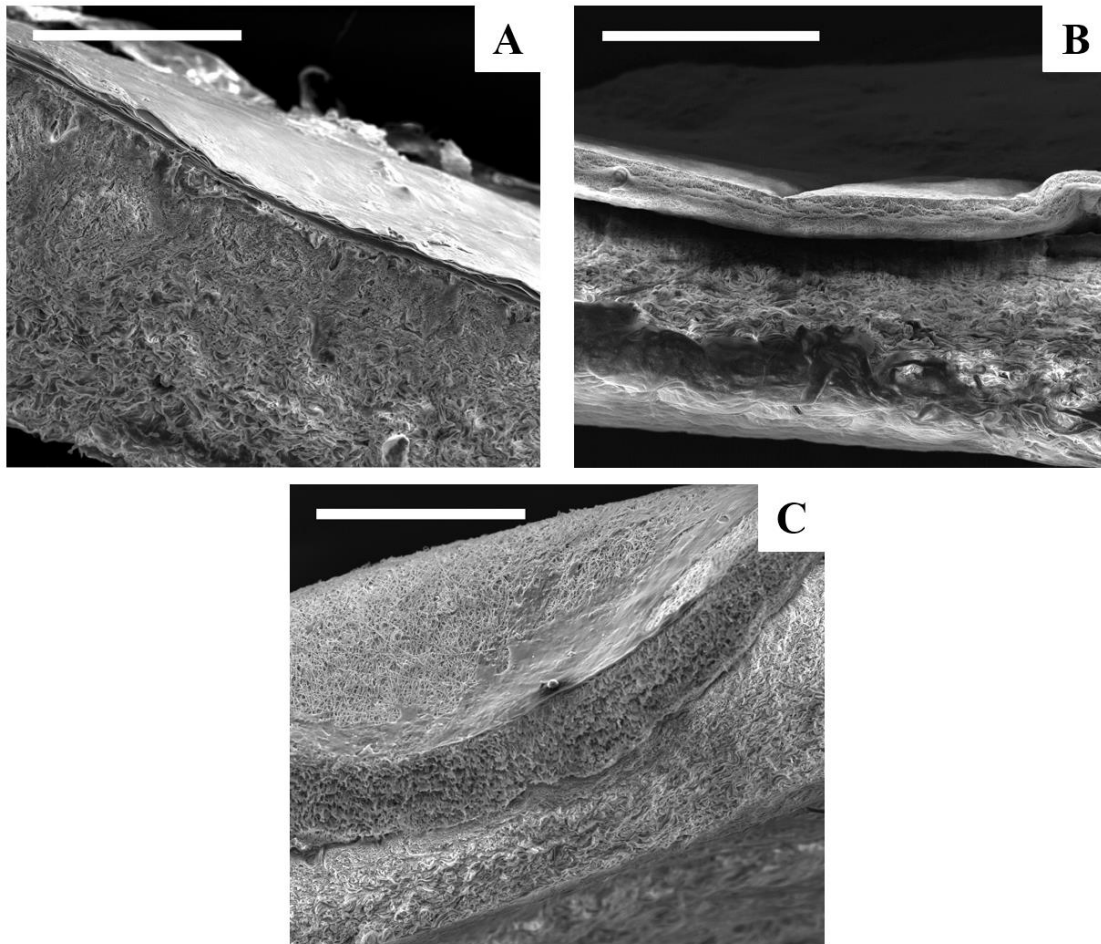
Figure 111. SEM images of skin tissue engineered models seeded with fibrous scaffolds. Images show cell infiltration between the epidermal and dermal component for A) control group, B) PCL control (RES), and C) pattern A (TCES). scale bar = 500 µm.

The characteristic expression of COL IV on the DEJ, and Iβ1 at the base of the rete ridges was observed for the skin model control group (Figure *112*). However, plain PCL membranes showed poor tissue integration and the absence of microfeatures. Furthermore, differences in cell distribution of the epidermal layer can be observed in skin models implanted with TCES patterns A and C compared to the control group. TCES pattern A showed the higher expression of COLIV when compared to the TCES groups. Skin models implanted with TCES pattern B showed an

epidermal layer with a cell distribution and expression of relevant markers similar to the skin control group. Comparing histology sections and lightsheet images revealed that although RES scaffolds showed a more similar stratification and an expression pattern to the skin group than the one seen on TCES groups (pattern A, B and C).
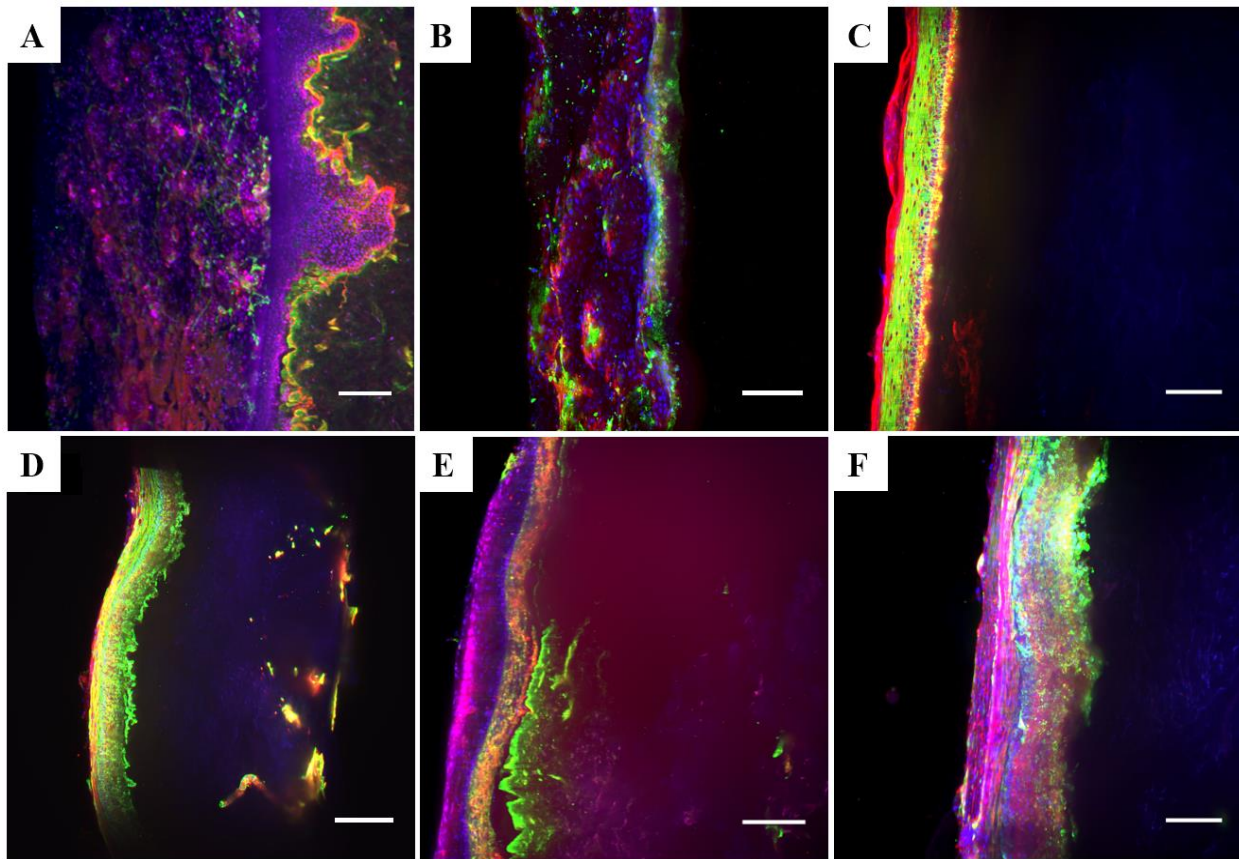
Figure 112. Lightsheet microscopy immunocytochemistry images. A) Skin model control, B) TCES pattern B + HDK and HDF, C) PCL plain RES on skin model, D) TCES pattern A on skin model, (E) TCES pattern B on skin model, and F) TCES pattern C on skin model. Samples were immunostained for Iβ1 (red), COL IV (green), and DAPI (blue). Scale bar = 200 μm.

3.6.   Introducing AdSCs into skin tissue engineered models

The effects of introducing AdSC into skin tissue engineered models were observed using histological sections of the models at day 10. Figure 113 indicates the proliferation and infiltration of AdSC from the dermal component of the skin models. Additionally, a high level of keratinocyte stratification was observed for models seeded with AdSC compared to the control model only seeded with HDK + HDF.
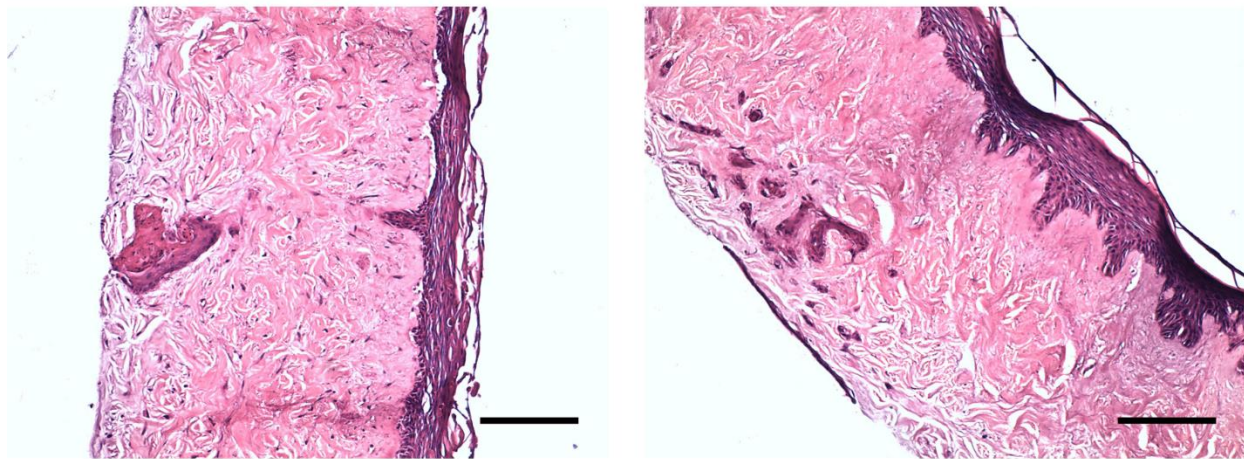
Figure 113. Development of skin tissue engineered models when seeded with AdSC. Both histology sections showed keratinization and a defined epidermal layer. Scale bar = 200 µm.

3.7.   Studying the effects of 2Ddr on skin tissue engineered models

As reported before in chapter II, exposing skin cell types to 2dDr can increase cell proliferation and metabolic activity. The effects of cultivating burned models on 100 µM 2dDr concentration in Green's media or implanting 8% wt. 2dDr scaffolds (RES or TCES) can be observed in Figure 114. Histological sections of skin models exposed to 2dDr revealed that an increase in epidermal elongations. When introduced in solution or by RES, the presence of 2dDr generated long ridge

structures that cross the entire dermal component. Furthermore, there was a significant improvement in scaffold integration for RES loaded with 2dDr when compared with the control RES. However, as described before, the TCES fabricated using PCL electrospun solutions with 2dDr have less define microfeatures than those made with pure PCL which translates to weak artificial features on the skin models.

The formation of elongated features on skin models exposed to 2dDr is further shown in Figure 115. Models exposed to Green's media with 100µM 2dDr showed epithelial extensions of 578 ± 85.2 µm (n=3), whereas skin models implanted with 8% wt. 2dDr RES also generated abnormal epithelial extensions about 652.2 ± 74.8 µm (n=3).
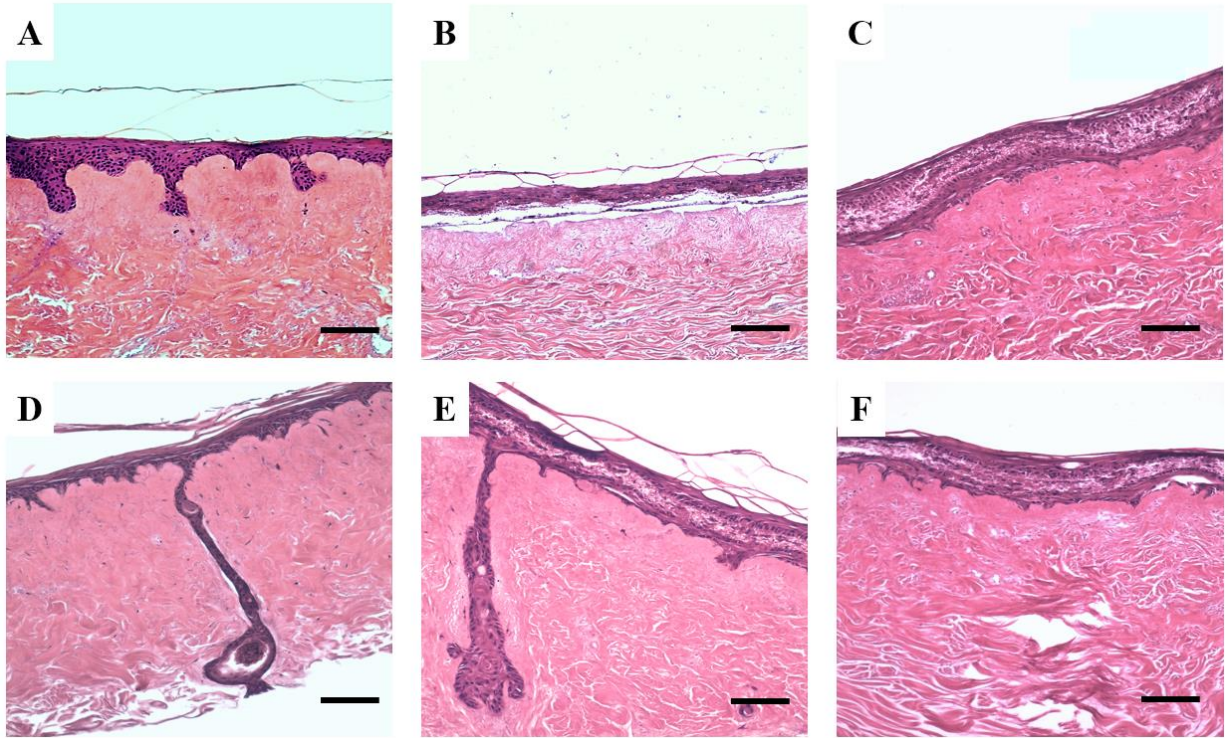
Figure 114. The effects of 2dDr on skin tissue engineered models. H&E histology sections show a comparison between: A) control skin model, B) skin model + plain RES, C) skin model + TCES pattern C, D) control skin model in culture with 100µM 2dDr Green's media, E) skin model + 8% wt. 2dDr RES, and F) skin model + 8% wt. 2dDr TCES pattern C.
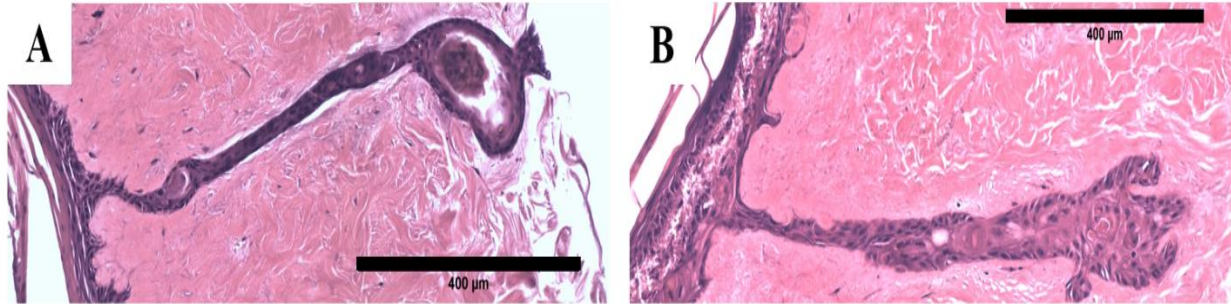
Figure 115.Comparison of H&E histology sections from skin models supplemented with 2dDr. A) Skin model cultured with 100 µM 2dDr Green's media, and B) skin model implanted with 8%wt. 2dDr RES. The formation of epidermal extensions was characteristic for the models with 2dDr.

3.8. The use of burned skin models to study the effects of TCES and 2dDr on *in vitro* wound healing

Burned skin tissue engineered models were successfully created to observe the effects of TCES and 2Ddr on *in vitro* wound healing. Histological sections of the burned skin models showed the damage caused by the burning of the epidermal layer at DD 7 (Figure 116-A) and how the skin model is not able to fully regenerate by DD12 (Figure 116-D). However, implanting a TCES or introducing 100µM 2dDr medium after burning the model had a positive effect on epidermal regeneration as observed in Figure 116-B and Figure 116-C, respectively.

The positive effects of implanting TCES on burned skin models were also observed using the resazurin metabolic assay (Figure 117). The results from this thesis showed that the higher metabolic values for the skin models implanted with TCES pattern B. Moreover, there was a significant difference between the implanting TCES with different patterns, with pattern C showing lower values than those of the TCES pattern B group. Interestingly, implanting RES

scaffolds (with or without 8% wt. 2dDr) did not show any significant increase in cell metabolic activity when compared to the burned control.
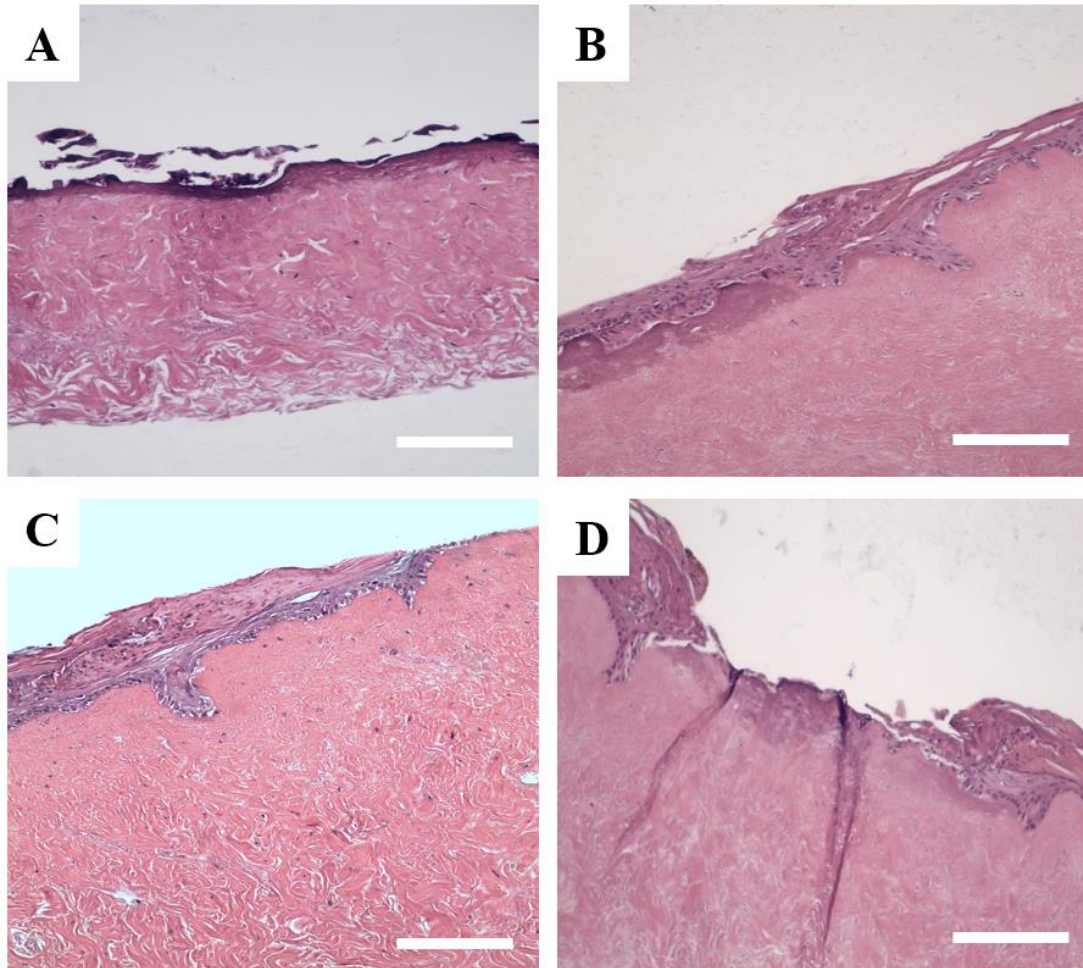
Figure 116. H&E histology sections of burned skin tissue engineered models at different time points and under different culture conditions. A) Skin model burned and fixed at DD7, B) skin model burned at DD 7 with TCES (pattern B) implanted afterward and fixed at DD 12, C) skin model burned at DD7 with cell media supplemented with 100μM 2dDr for 5 days, and D) skin model control burned at DD 7 and fixed at DD 12. Scale bar = 200 µm.
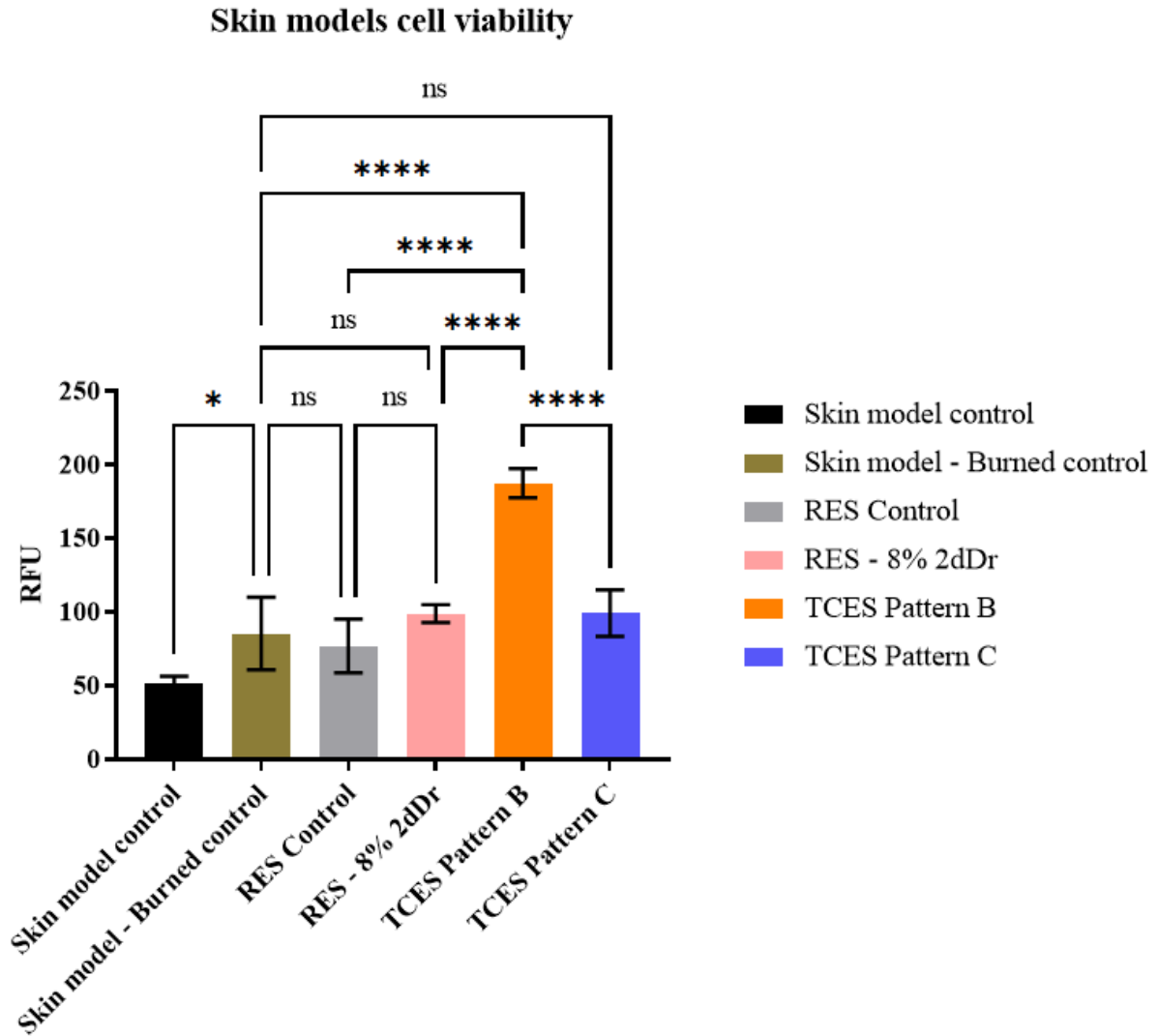
Figure 117. Comparison of cell viability at DD12 for skin tissue engineered models burned at DD7 and exposed to different conditions or scaffolds. The average value of the skin tissue engineered model at DD 7 (before burned) was subtracted for each data point. Results are shown as mean $\pm$ SD. One-way ANOVA statistical analysis with Tukey comparison test. **** $p < 0.0001$, * $p < 0.05$, ns $p \geq 0.05$. N=1, n=3.

4. Discussion

The performance of the random electrospun scaffolds (RES) and topographically controlled electrospun scaffolds (TCES) was successfully evaluated by *in vitro* cell culture and the use of skin tissue engineered models. Moreover, the effects on cell behavior for HDF and HDK + HDF when seeded on scaffolds loaded with bioactive compounds 2dDr, E2, or AV were assessed to determine their potential to improve skin regeneration. To the author's best knowledge, this is the first time that microtopographies were introduced by electrospun scaffolds on a skin tissue engineered model to induce the formation of rete ridges. Furthermore, this is the first time that the effects of 2dDr on epidermal stratification and fibroblast migration were observed on skin 3D models.

The initial experiments of this chapter explored the potential of the PCL RES and TCES as tissue engineered scaffolds. Seeding HDF on top of the RES showed that incorporating bioactive compounds on the electrospun fibers did not increase the viability of the cells compared to the pure PCL RES control. This behavior may be related to the release profile of the scaffolds for each compound. Another possibility for this cell behavior could be the high initial HDF density on the scaffolds (100,000 cells/scaffold). The high cell density could have limited the cell-material interactions leaving only cell-cell interactions to influence cell metabolic activity.

As demonstrated before in chapter II, 2dDr and AV compounds showed a fast release within the first 24 h. Because of the average weight of the scaffolds used in this experiment (~10 mg), the amount of 2dDr and AV compound released within the first 24 h was about 800 µg and 1000 µg, respectively. This would mean that for the 2 mL of media used for the experiment the concentration for each RES was 3 mM for 2dDr and 0.5 mg/mL for AV. Although the 0.5 mg/mL AV

concentration is lower than the concentrations tested in chapter II, the results in this thesis indicated that lower concentrations of AV could potentially have a positive effect on cell proliferation. Carter et al. and Suganya et al. showed that delivering low concentrations of AV had the potential of increasing metabolic activity for 3T3 and mouse fibroblasts, respectively [308], [309]. However, the 3 mM 2dDr concentration delivered by the RES was above the range tested on the TCP cell culture experiments (chapter III). Nonetheless, it is possible that the high concentration of 2dDR would limit but not completely inhibit cell proliferation of HDF, as Dikici et al. have shown that concentrations between 1 mM and 10 mM could hinder cell proliferation but no exact concentration was defined as the maximum limit for cell survival [171].

In the case of E2, the release profile of the RES characterized in chapter III showed that 14.4% of the total amount was released within the first 24 h. Therefore, the initial concentration at which HDF were exposed on the first day was about 260 µM, which is slightly above the concentrations tested in chapter III. Aside from the data shown in this thesis, no authors have reported the delivery of E2 by electrospun scaffolds at such high levels to stimulate cell behavior [159], [166], [314], [315]. This burst release of E2 would explain the low value of cell viability shown on the resazurin assay compared to the control group, 2dDR, and AV. Nonetheless, the amount of E2 loaded into the RES (10% wt.) was the highest working concentration in which the scaffolds were successfully fabricated and thus it is possible to reduce the amount of E2 loaded without significantly altering the electrospinning process.

Future work is needed to fully characterize any changes on release profile of TCES. Comparison with their RES counterparts should reveal an increase on release of bioactive compounds due to the increase of surface area by the microtopographical cues. However, because of the burst release of 2dDr observed on RES, it is possible that no changes would be detected for the TCES.

Once the effects on cell behavior of HDF seeded on RES were studied, the next step was to observe any changes in cell behavior for the HDK + HDF co-culture when seeded on TCES. The effects of HDK + HDF seeded on RES loaded with bioactive compounds were not explored in this thesis. The rationale for this decision was that seeding HDF into RES was used as a preliminary study to evaluate any possible cytotoxic effects of introducing bioactive compounds into the fibers. The main objective of this thesis was to evaluate the effects of the TCES on skin cell lines. However, future work with HDK + HDF could show the effects in marker expression and proliferation when exposed only to the bioactive compounds loaded into RES. This data could potentially be used as a comparative control and to study lower concentrations of the bioactive compounds before introducing the microtopographical cues.

The results from this thesis of HDK + HDF seeded on TCES showed that microfeatures about (180 µm height – 547 µm width) introduced by the TCES can generate an expression pattern that produces clusters of Iβ1 that are characteristic of a keratinocyte stem cell population [409]. The hypothesis for this change is that introduction of microfeatures induced the formation of HDK colonies by encouraging cell-cell interactions in a 3D environment. Differences in cell nuclei density between the bottom and top sections were observed being higher at the bottom for HDK + HDF seeded on TCES patterns A and C, but higher at the top for pattern B. When comparing TCES against a plain RES control, only pattern C showed differences in cell nuclei density for pattern C which was more likely to generate HDK colonies at the bottom of the feature but had lower nuclei density at the top. The presence of Iβ1 clusters at the bottom of the features and the expression of COL IV underneath and around the cell colonies, further support the idea of the microfeatures encouraging HDK proliferation and differentiation.

It is important to highlight that in comparison with the skin model experiments also explored in this thesis, these samples were not exposed to DED and therefore COL IV was expressed from cells seeded on top of the TCES. Nonetheless, the amount of COL IV expressed needs to be further investigated to understand the effects of TCES membranes in the expression of COL IV, Iβ1, and relevant epidermal stem cell markers such as CD34+ and CK14 [410]. Nonetheless, the presence of Iβ1 at the bottom of the microfeatures shown on the lightsheet images indicates that the artificial rete ridges could induce the formation of HDK colonies by introducing a similar micro-organization to native human skin. Furthermore, the presence of Iβ1 of the newly formed epidermal layer of the models is a marker for keratinocyte differentiation throughout the epidermal layers [97], [411], [412]. The presence of COL IV indicates the formation of the basement membrane which is key to control cell migration and differentiation of keratinocyte stem cells; it also creates biomechanical support to other components of the basement membrane [413].

Moreover, data from the resazurin assay showed that co-cultured HDK + HDF on TCES had no significant differences in cell metabolic activity among the three tested topographies. However, cells co-cultured on plain RES showed significantly lower values of metabolic activity compared to TCES groups after 1, 3, and 6 days in culture. SEM micrographs confirmed the presence of HDK and HDF at the bottom of the microfeatures and that the TCES did not lose their architecture even after 6 days in culture media, making them suitable for long-term experiments when a longer implantation time could be required.

The co-culture of HDK + HDF showed the highest metabolic activity among the bioactive compounds when seeded on TCES loaded with E2. Whereas the presence of 2dDr and AV showed a significant decrease in metabolic activity. Although the presence of E2 has proved to be beneficial for keratinocyte cell survival and proliferation [345], [377], [378], the PCL control

236

showed higher metabolic activity than the 10% wt. E2 group, suggesting that a lower dosage might be needed to further improve cell behavior. A similar hypothesis of a high dosage could explain the decrease in HDK metabolic activity when exposed to 2dDr, however, the effects of 2dDr on HDK + HDF proliferation, migration, and cell metabolic activity that had not been reported before and are yet to be fully characterized.

Although TCES loaded with AV had lower values of HDK + HDF cell viability than the pure PCL control, this was expected as µM concentrations of some AV components have been identified as inhibitors of HDK proliferation [385]. Nonetheless, other studies have shown that AV accelerates the migration and proliferation of HDK [386]–[388], highlighting the synergistic interaction of the AV compounds [190]. Therefore, it is critical to characterize the chemical composition of the AV extract used in this thesis. An interesting advantage of the use of AV compared to E2 or 2dDr is that it has been used to treat psoriasis; a dermal condition characterized by the elongation of the rete ridges. The work here shows the potential alternative to reintroduce the rete ridges dermal microenvironment while delivering a drug that inhibits the abnormal proliferation of HDK [389].

Analysis of the cell distribution revealed expression of Iβ1 localized at the tip or base of the microfeatures for the E2 and control TCES groups, respectively. This difference in cell behavior suggests that HDK proliferation and expression of relevant biomolecules were affected by the introduction of the microenvironments and bioactive compounds. In comparison, there was no distinct expression pattern of Iβ1 for cells seeded on RES regardless of the bioactive compound loaded into the scaffold. Although differences in cell proliferation was observed among RES and TCES groups.

The effects of micropatterned electrospun scaffolds on cell distribution, proliferation, and functionality have been previously reported for mouse myoblasts, NIH 3T3 cells, rat cardiomyocytes [274], [275], adipose-derived stem cells (AdSC) [414], and human keratinocytes + i3T3s [271]; however, this is the first time that the effects of different microtopographies on co-cultured HDF and HDK + HDF have been reported. The result in this thesis showed that the introduction of microfeatures within the electrospun membranes had a positive impact on HDF cell metabolic activity, as TCES groups showed high relative fluorescence values when compared to the plain RES control after 6 days in culture. However, the data from this thesis showed that HDF seeded on TCES had less significant changes in metabolic activity compared to HDK + HDF which were more susceptible to microtopographical cues present on the scaffolds and thus a better model to study the effects of the TCES loaded with bioactive compounds [291], [415].

The most common method to study the rete ridges stem cell microenvironment in a 3D model is the use of soft-lithographic methods with a PDMS mold and a synthetic or organic matrix to create a microstructure matrix [1], [40], [44]. However, recent studies by Lin et al. and Blackstone et al. have studied complex techniques to introduce rete ridges into animal and human skin models, respectively, to study wound healing and epidermal stratification [416], [417]. Furthermore, a similar technique to the one used in this thesis combined electrospun membranes and patterned collectors and was tested on an *in vivo* model by Ma et al. [274]. Their results showed an improvement in tissue integration for micro skin grafts when microtopographical cues were introduced by creating a composite scaffold.

The use of tissue engineered skin models is a powerful tool to observe cell behavior on a 3D model without the need for an animal model [408]. After 12 days in culture, H&E staining revealed that the control models developed define rete ridges and a stratified epithelium. As models are

238

fabricated using donor DED, the cultured cells can repopulate the native empty microfeatures allowing for HDK differentiation as a result of the air-liquid interface. The traditional fabrication method only introduces HDF and HDK seeded into the epidermal side of the DED. However, this thesis explored for the first time the effects of seeding AdSC to improve the development of the skin model. Preliminary data showed that these AdSC skin models appear to have a more defined stratum corneum. This improvement is related to the paracrine activity of AdSC to express VEGFA, TNF, and TGFβ1. Nevertheless, cell density, cell culture conditions, and development time are variables that need to be further explored to fully understand the effects of introducing AdSC.

The tissue engineered skin models implanted with the TCES showed expression patterns of both COL IV and Iβ1 that suggested preliminary keratinocyte stratification. Furthermore, skin control groups showed defined expression patterns of Iβ1 which is characteristic of the interfollicular dermis [45]. In the case of skin models implanted with a TCES, it can be observed that cells populated the surface of the microfeatures and then were able to migrate towards the dermal region due to the 3D fibrous nature of the scaffold. In comparison, skin models implanted with plain RES did not exhibit cell infiltration towards the dermal component suggesting that microtopographies improve cell proliferation and migration.

Pattern B TCES generated microfeatures with the closest dimensions to the control group while showing cell stratification on the epidermal layer. Patterns A and C showed a clear disruption in cell distribution across the middle section of the scaffold with mild cell infiltration to the dermal section. The height of the microfeatures generated by the TESM was not statistically different in comparison to the control group (Figure 8). Longer incubation times could reveal if cell scaffold

remodeling of the wider microfeatures could further lead to the formation of individual narrower microfeatures.

Although the use of 2dDr as an endothelial chemoattractant has been reported before by several authors [123], [163], [169], [172], this thesis showed for the first time the effects on cell migration of delivering 2dDr on skin models. H&E images of the models showed an increase in the length and number of rete ridges present on the skin models, both when delivered from RES and in solution with the cell culture media. The preliminary hypothesis for this behavior is that 2dDr could act as a chemoattractant for HDF and induce the formation of longer and defined rete ridges. Nonetheless, this hypothesis needs to be further tested by establishing the effects on cell migration *in vitro* and when seeded on dermal components that have an even surface distribution.

Our burned skin models showed that it is possible to improve healing by introducing a fibrous scaffold. However, there was no major difference between the models seeded with RES or TCES. However, the cell viability assay for the burned models indicated a significant improvement in cell metabolic activity only for the skin models burned and implanted with TCES pattern B. However, additional experiments are needed to study the healing capabilities of the TCES and their ability to reintroduce microfeatures on wounds as well as their effects when loaded with 2dDr, AV, or E2. However, the work presented here shows an improvement in regenerating the lost microfeatures of the DEJ when topographical cues are introduced on electrospun membranes.

The potential of the TCES tested in this chapter is based on their ability to be used as wound dressings. Nonetheless, based on wound type, there are ideal characteristics that should be further considered to create an ideal wound dressing. Such ideal characteristics include providing a moist environment, enhancing epidermal migration, inducing tissue synthesis, promoting angiogenesis,

and protecting against bacterial infection [418]. The current design of the TCES meets the requirements of inducing angiogenesis (via the delivery of bioactive compounds) and allowing epidermal migration, while also aiding to reconstruct the lost microstructure of the DEJ. Other critical aspects such as maintaining a moist environment on the wound would require further studies to evaluate the performance of the TCES, however, other authors have shown the benefits of using electrospun membranes to avoid wound dehydration [419], [420].

Although the aim of the TCES as a wound dressing is to reintroduce the rete ridges after any kind of injury, using these membranes would bring more benefits for patients with superficial or full-thickness burns. Because of the extensive damage of burns, and the complete loss of tissue structure and vasculature for full-thickness burns, the potential of the TCES to aid in re-epithelialization is a promising approach to improve the quality of the newly regenerated tissue [421]. Lin et al. theorized that partial-thickness burns are capable of regenerating the rete ridges by the expression of cytokeratins and alkaline phosphatase from the cells residing on the surrounding rete ridges. However, full-thickness burns showed no regeneration of the rete ridge structure, highlighting the advantages of reintroducing these structures on the wound site [416].

The work presented in this chapter demonstrates the effects of introducing micropatterned scaffolds on skin regeneration. The capacity of these scaffolds to closely reproduce the physical native environment in which stem cell populations exist *in vivo* could significantly improve the regeneration of human skin. The use of *in vitro* cell culture and tissue-engineered skin models implanted with the TCES has revealed valuable information about the expression of relevant markers that suggest the formation of a microenvironment similar to the rete ridges. Moreover, loading bioactive compounds into the TCES had an impact on cell viability that needs to be further studied to determine the effects of lower concentrations than the ones tested on this work.

241

5. Conclusion

This research demonstrates that the inclusion of microtopographies within fibrous scaffolds is a promising approach to induce the formation of a microarchitecture similar to the native rete ridges on the DEJ. These microfeatures have the potential to reintroduce stem cell microenvironments in which keratinocyte stem cells can maintain their function even after an injury. The results of this experimental chapter showed that the artificial features created by introducing TCES into skin tissue engineered models are capable of mimicking to a certain extent the shape and the spatial distribution of the skin rete ridges and increase cell viability. However, further optimization is needed to create a patterned collector with narrower features that can closely mimic the microenvironments present on the skin model controls.

The positive impact in cell metabolic activity for cells seeded on RES loaded with 2dDr and AV demonstrated the potential of these scaffolds to allow for skin cell viability while inducing a strong angiogenic response as demonstrated in chapter III. Nonetheless, the decrease in cell viability for the TCES groups loaded with bioactive compounds indicates that further experiments such as marker expression, quantification as a function of location, and DNA quantification are needed to fully characterize skin cell behavior on these scaffolds.

Furthermore, the microfeatures introduced by the TCES improved the integration between the scaffold and the dermal component of the model and improved the degree of epidermal stratification and skin-like layer formation compared to the plain RES and an improvement on wound healing when compared to the skin model control, demonstrating the potential of the microfabricated scaffolds to be used as future devices for skin tissue regeneration.

Chapter VI. General discussion, conclusion, and future work

1. Discussion

Regenerating human skin from cultured autografts has been a common treatment for split and full thickness defects. These grafts are implanted to aid regeneration and improve function, however, these approaches present challenges such as donor-skin availability, pain, scarring, and loss of function. For these reasons, tissue engineering approaches have become of importance as novel alternatives to overcome such limitations. Tissue engineered devices not only allow to control unique aspects of tissue structure in order to aid regeneration but they can also be used as delivery carriers that improve wound healing [422]. In this work, tissue engineered scaffolds were designed to reintroduce the adult stem cell microenvironments located on the rete ridges.

The role of the adult stem cells that reside within the rete ridges in the regenerative cycle of skin is still not completely understood. However, their ability to differentiate and produce a continuous cell population has made them a promising tool for tissue engineering and regenerative medicine applications. Since their discovery, *in vitro* expansion of adult stem cells using traditional 2D culture platforms has remained a challenge due to the lack of native spatial and biochemical cues, therefore, introducing complex physical cues within tissue engineered scaffolds can be a powerful approach to develop new routes for the study and control of stem cell behavior.

Previously, a study by Compton et al. showed that the formation of rete ridges can take from 6 weeks to 1 year after grafting. This delay in the formation of an appropriate proper DEJ structure has been related to impaired healing [423]. Additionally, the importance of regenerating the loss of rete ridges after an injury is related to their role as a stem cell microenvironment for keratinocyte

stem cells [78]. Furthermore, research from Lawlor & Kaur had suggested that the ridge pattern of the DEJ could also improve mechanical properties and aid in skin vascularization [81], Shen et al. studied the role of the rete ridges on wound healing with significant improvements for animal models [405], and Medalie et al. observed an extended pigmentation due to the presence of a rete ridge-like pattern [424].

The work on this thesis shows the basis of a novel alternative to regenerate the loss rete ridges by implanting topographically controlled fibrous scaffolds with similar microfeatures into the wound site. The fabrication technique used to create these scaffolds, electrospinning, allows the fabrication of dressings with different thicknesses, fiber diameters, and polymer compositions. This versatility in controlling the micro and nano structure of tissue engineered scaffolds makes it a promising approach for the fabrication of clinical devices that can be used for superficial or full-thickness burns [201], [280]. Although the combination of patterned μSLA collectors and electrospinning has been reported before to create microtopographical cues using electrospun scaffolds [269], [271], this is the first time that micropatterned fibrous membranes were tested on an *in vitro* 3D model. Furthermore, this is the first time that such complex micropatterned scaffolds were also used to deliver bioactive compounds to improve skin regeneration by stimulating key aspects of cell behavior.

Although it is mostly used to create soft aligned or random fibers, controlling fiber diameter and porosity can be achieved with simple modifications to the process or solution parameters. Its versatility to produce nano or microfibers from both natural and synthetic polymers has expanded the use of electrospinning in recent years to create 3D constructs that aim to replicate the cell fibrous environment [425]–[429]. Moreover, electrospinning is an easy to perform and scalable process that has been used in several *in vivo* and *in vitro* tissue engineering applications, but on its

own, it has limited applications for complex constructs to mimic the stem cell microenvironment. Therefore, combining electrospinning with μSLA is a promising approach to create complex tissue engineered scaffolds. Other techniques that have been successfully combined with electrospinning to introduce complexity to tissue engineered scaffolds include hydrogels [430], soft-lithography [275], and selective-laser melting collectors [270].

The selection of a biomaterial for tissue engineering applications is critical to ensure a suitable degradation rate, mechanical properties (tensile strength, elastic modulus), and overall bioactivity (surface energy). For this application, PCL was selected due to its versatility as a fabrication material, biocompatibility, capacity to be bioresorbable, and tensile strength close to human skin (21.5 ± 8.4 MPa average skin tensile strength) [296], [431]. Moreover, PCL electrospun membranes have been successfully used to create skin substitutes or wound dressings [245], making them an ideal candidate for skin tissue engineering applications.

As studied in chapter II, the mechanical properties of PLGA (another versatile biocompatible polymer) under biological conditions are not as suitable to preserve microtopographical cues due to its shrinkage. Therefore, even if PLGA presented higher bioactivity and biocompatibility without the need for further activation (plasma treatment), its use to fabricate TCES was limited. Several authors have proposed solutions to the PLGA shrinkage such as using polypropylene rings to create suspended PLGA scaffold systems (Ru et al.) or the mixture of PLGA with other polymers (such as PCL), to improve its mechanical properties (Hiep & Lee and Chou & Woodrow) [328], [432], [433]. Another advantage of using PCL that could have clinical applications is the change in optical properties found on the electrospun scaffolds after PBS incubation. The change in optical transparency could allow effective monitoring of the wound without the need of

removing the dressing. Future work could explore the use of such approaches to preserve the microstructure of TCES made of PLGA.

From the three different patterns tested on this thesis, pattern B produced the features with dimensions closest to the native skin. However, the main challenge of this fabrication technique that combines electrospinning and µSLA is to replicate narrow and long ridges, as the fibers are less able to be deposited on the surface. Nonetheless, the fibrous microenvironments fabricated were suitable for studying cell behavior under different structural conditions. The TCES fabricated allowed the observation of key parameters such as cell viability, cell proliferation, and expression of relevant markers compared to plain RES for both *in vitro* TCP culture. Moreover, the changes in cell behavior revealed changes in the structural development of the DEJ for skin tissue engineered models.

The expression of Iβ1 and COLIV was studied as indicators of the formation of basic stem cell microenvironments and the formation of a functional DEJ, respectively. The work on this thesis indicates that the microenvironments of TCES pattern B (624 µm width – 200 µm height) produced defined clusters of Iβ1 on a similar pattern to the native human skin. Furthermore, the expression of COLIV increases in areas near the cell colonies created by the introduction of the microenvironments. However, other relevant markers are key to evaluating the performance of the TCES to recreate the rete ridges. Future work could address the expression of KGF and p63 (a transcription factor), both key mediators of keratinocyte behavior [434]. KGF in particular has been studied for its relation to the formation of the rete ridges and the flattening of the DEJ [384].

The implementation of bioactive compounds to improve skin wound healing is a promising approach to some of the challenges of tissue engineering such as poor vascularization of an acute

inflammatory response. Nonetheless, in comparison with the multiple components present on the AV leaf or gel, 2dDr and E2 are small individual molecules that have biological roles related to the angiogenic activity. However, only E2 has been studied for clinical and skin tissue engineering applications using nM concentrations [159], [183], [184]. Only recently 2dDr was explored for the first time by Yar et al. as a novel proangiogenic agent with clinical applications [157]. Before the studies of Yar et al., 2dDr was mostly related to tumor growth and thus its mechanism *in vitro* and *in vivo* is still being studied [166], [168], [169], [171].

Nevertheless, the work on this thesis shows that µM concentrations of 2dDr can increase cell viability and proliferation of HDF and HDK and be beneficial for blood vessel formation. These findings of low 2dDr concentrations having positive effects on cell behavior and wound healing were also reported by Dikici et al. and Yar et al., however, this is the first time that an extensive *in vitro* study is performed for skin cell types. Furthermore, it was also the first time that a burst release of 2dDr was studied *in vitro*, as other carriers tested before showed an average sustained release for over 3 days.

In the case of scaffolds loaded with AV, it is possible to induce vascularization of the wound while reducing the risk of an extended inflammatory phase, characteristic of chronic wounds that can significantly affect the healing process and lead to continuous pain for the patient. Furthermore, systemic disorders such as atherosclerosis and cancer have been linked to severe constant inflammation and failed healing process [435].

The data on cell proliferation, cell metabolic activity, and angiogenic potential in this thesis showed that 2dDr, E2, and AV can be used at low concentrations for skin tissue engineering constructs to induce blood vessel formation after an injury without hindering cell viability.

Although the CAM data showed no difference among the bioactive compounds regarding blood vessel formation, AV was found to have the highest average vascular density. However, the overall analysis of ease of fabrication (ability to produce defined features on the TCES), cell behavior, and angiogenic potential made E2 the most attractive candidate for future studies. However, more data is needed to determine any possible side effects for the concentrations tested on this thesis using the skin tissue engineered models. Potential studies on animal models could also show the effects of E2 loaded TCES on wound healing.

Fibrous scaffolds as wound dressings also have the advantage of improving wound healing, especially in partial and full-thickness burns, by hindering the proliferation of microbial organisms in the wound bed. Once the stratum corneum of the epidermis is lost, the wound site is susceptible to environmental organisms and the formation of biofilms that impede wound healing and may lead to an aggressive infection [436]. The formation of biofilms on the wound site, although not explored in this thesis, is critical when assessing the potential clinical applications of a wound dressing. The delivery of AV into the wound site has proved to be effective to inhibit the proliferation of *Pseudomonas aeruginosa* and *Candida albicans* [437]. However, as with other deoxy-sugars, the introduction of 2dDr into wound dressings has the potential to induce the proliferation of *Pseudomonas aeruginosa* [157]. Therefore, the combination of bioactive compounds into the same construct is a promising approach to overcome some of the limitations of each compound.

In terms of fabrication, the combination of other techniques could also be beneficial to improve the performance of TCES as potential clinical devices. The most attractive option for this is the use of hydrogels as they excel at managing the exudate of the wound, relieving pain, and their non-adhesive nature makes them popular as dressings [421]. Recently, a study by Brunelle et al. showed

the fabrication of a hybrid PEG hydrogel-PCL fibrous scaffold for chondrogenic regeneration [277]. This technique allowed for the encapsulation of electrospun scaffolds using a PEG hydrogel without disruption of the fibrous nature of the scaffold. Strategies such as this one are promising approaches to generate smart and complex clinical devices to improve skin wound healing.

2. Conclusion and future work

The work developed in this thesis demonstrates the versatility of combining advanced manufacturing techniques to fabricate topographically-modified fibrous membranes that can be also used t as drug delivery carriers. The results from this thesis show how TCES membranes are a potentially powerful alternative to conventional wound dressings not only providing cells with a fibrous ECM-like environment but also providing bespoke microfeatures that resemble those found on the skin DEJ.

The data on this thesis showed that the microenvironments present on the TCES can have a positive effect on skin cells proliferation *in vitro*, tissue integration, and epidermal stratification compared to plain RES (when tested on skin tissue engineered models). These findings support the idea that the control of both nano and micro architectural features is key in tissue engineering applications. The use of TCES could significantly improve cell response compared to conventional plain electrospun scaffolds as well as preserve tissue function and quality due to the incorporation of artificial stem cell microenvironments. Nonetheless, the final dimensions of the microfeatures present on the TCES were bigger than those found in native human skin, and thus further optimization of the electrospinning process would be required.

Moreover, by loading the TCES with bioactive compounds 2dDr, E2, or AV it is possible to generate a bioactive scaffold that can induce a proangiogenic response. As shown by the CAM

and TCP *in vitro* data, 2dDr and AV have the highest potential to increase cell proliferation, viability, and blood vessel formation. However, depending on the concentration of bioactive compounds, these bioactive TCES showed morphological differences in their microfeatures compared to a pure PCL control. In this regard, E2 was the most promising compound to load into the TCES as the microfeatures were not affected by its presence. Future work could explore the use of lower concentrations to improve the fabrication of topographical cues while delivering any of the bioactive agents tested here. Additionally, exploring the antimicrobial capabilities of 2dDr, E2, and AV scaffolds would be critical to characterize their performance as potential wound dressings.

The manufactured TCES showed high potential for clinical applications due to their ease of fabrication and versatility. Additionally, combining µSLA and electrospinning could be used to recreate other cell microenvironments on several tissues as proved before by Ortega et al. [290]. Nonetheless, using the TCES as wound dressings could provide a regenerative template to promote healing and induce the formation of new rete ridges *in vivo* improving the regenerative capabilities of the new form tissue (by preserving the keratinocyte stem cell microenvironment crucial for epidermal homeostasis). The approach presented in this thesis is a versatile and easily scaled-up process that can produce complex 3D membranes to be used on wound healing applications that can also deliver bioactive agents to further aid tissue regeneration.

References

[1]   P. Viswanathan *et al.*, "Mimicking the topography of the epidermal-dermal interface with elastomer substrates," *Integr. Biol.*, vol. 8, no. 1, pp. 21–29, 2016.

[2]   M. Murphy, P. Kerr, and J. M. Grant-Kels, "The histopathologic spectrum of psoriasis," *Clin. Dermatol.*, vol. 25, no. 6, pp. 524–528, 2007.

[3]   M. Blais, R. Parentau-Bareil, S. Cadau, and F. Berthod, "Concise Review : Tissue-Engineered Skin and Nerve Regeneration in Burn Treatment," *Stem Cells Transl. Med.*, vol. 2, no. 7, pp. 545–551, 2013.

[4]   C. M. Magin *et al.*, "Evaluation of a bilayered, micropatterned hydrogel dressing for full-thickness wound healing," *Exp. Biol. Med.*, vol. 241, no. 9, pp. 986–995, 2016.

[5]   K. K. Chereddy, G. Vandermeulen, and V. Préat, "PLGA based drug delivery systems - promising carriers for wound healing activity.," *Wound Repair Regen.*, pp. 1–33, 2016.

[6]   R. G. Frykberg and J. Banks, "Challenges in the Treatment of Chronic Wounds," *Adv. Wound Care*, vol. 4, no. 9, pp. 560–582, 2015.

[7]   C. K. Sen *et al.*, "Human skin wounds: a major and snowballing threat to public health and the economy.," *Wound Repair Regen.*, vol. 17, no. 6, pp. 763–71, 2009.

[8]   J. Koehler, F. P. Brandl, and A. M. Goepferich, "Hydrogel wound dressings for bioactive treatment of acute and chronic wounds," *Eur. Polym. J.*, vol. 100, no. December 2017, pp. 1–11, 2018.

[9]   K. S. Saladin, "The Integumentary System," in *Human Anatomy*, New York: McGraw-Hill, 2014, pp. 125–126.

[10]   G. J. Summer, K. A. Puntillo, C. Miaskowski, P. G. Green, and J. D. Levine, "Burn Injury Pain: The Continuing Challenge," *J. Pain*, vol. 8, no. 7, pp. 533–548, 2007.

[11]   R. V. Shevchenko, S. L. James, and S. E. James, "A review of tissue-engineered skin bioconstructs available for skin reconstruction," *J. R. Soc. Interface*, vol. 7, no. 43, pp. 229–258, 2010.

[12] D. Wainwright, "Burns," in *Diseases and Disorders*, 1st ed., New York: Marshall Cavendish, 2007, pp. 130–133.

[13] R. X. Xu, "Clinical Evaluation on Depth of the Burns wound," in *Burns Regenerative Medicine and Therapy*, X. Sun, Ed. New York: Karger, 2004, pp. 20–22.

[14] J. A. Haagsma *et al.*, "The global burden of injury: Incidence, mortality, disability-adjusted life years and time trends from the global burden of disease study 2013," *Inj. Prev.*, vol. 22, no. 1, pp. 3–18, 2016.

[15] D. Wu *et al.*, "The Time Course Pathological Changes After Burn Injury," *Inflammation*, vol. 41, no. 5, pp. 1864–1872, 2018.

[16] J. R. Dias, P. L. Granja, and P. J. Bártolo, "Advances in electrospun skin substitutes," *Prog. Mater. Sci.*, vol. 84, no. May 2018, pp. 314–334, 2016.

[17] World Health Organization, "Burns Fact sheet," 2018. [Online]. Available: http://www.who.int/mediacentre/factsheets/fs365/en/. [Accessed: 13-Mar-2018].

[18] C. Smolle *et al.*, "Recent trends in burn epidemiology worldwide: A systematic review," *Burns*, vol. 43, no. 2. pp. 249–257, 2017.

[19] M. Peden *et al.*, "World report on child injury prevention: Burns," 2008.

[20] O. El Ezzi, M. Dolci, C. Dufour, R. Bossou, and A. de Buys Roessingh, "Surgery on burns sequelae in developing countries.," *Ann. Burns Fire Disasters*, vol. 30, no. 1, pp. 47–51, 2017.

[21] A. M. Kemp, S. Jones, Z. Lawson, and S. A. Maguire, "Patterns of burns and scalds in children," *Arch. Dis. Child.*, pp. 316–321, 2014.

[22] C. A. Harrison and S. MacNeil, "The mechanism of skin graft contraction: An update on current research and potential future therapies," *Burns*, vol. 34, no. 2. pp. 153–163, 2008.

[23] S. Bo̎ttcher-Haberzeth, T. Biedermann, and E. Reichmann, "Tissue Engineering of Skin," in *Principles of Regenerative Medicine*, vol. 36, 2011, pp. 1063–1078.

[24] S. MacNeil, "Progress and opportunities for tissue-engineered skin," *Nature*, vol. 445, no. 7130, pp. 874–880, 2007.

[25] Y. Wang *et al.*, "Burn injury: Challenges and advances in burn wound healing, infection, pain and scarring," *Adv. Drug Deliv. Rev.*, vol. 123, pp. 3–17, 2018.

[26] J. A. McGrath and J. Uitto, "Anatomy and Organization of Human Skin," in *Rook's Textbook of Dermatology: Eighth Edition*, vol. 1, T. Burns, S. Breathnach, and C. Griffiths, Eds. 2010, pp. 34–86.

[27] F. Groeber, M. Holeiter, M. Hampel, S. Hinderer, and K. Schenke-Layland, "Skin tissue engineering - In vivo and in vitro applications," *Advanced Drug Delivery Reviews*. 2011.

[28] H. Joodaki and M. B. Panzer, "Skin mechanical properties and modeling: A review," *Proc. Inst. Mech. Eng. Part H J. Eng. Med.*, vol. 232, no. 4, pp. 323–343, 2018.

[29] M. Takeo, W. Lee, and M. Ito, "Wound healing and skin regeneration," *Cold Spring Harb. Perspect. Med.*, vol. 5, no. 1, 2015.

[30] A. A. Romanovsky, "Skin temperature: Its role in thermoregulation," *Acta Physiol.*, vol. 210, no. 3, pp. 498–507, 2014.

[31] I. Angelova-Fischer, T. W. Fischer, C. Abels, and D. Zillikens, "Accelerated barrier recovery and enhancement of the barrier integrity and properties by topical application of a pH 4 vs. a pH 5·8 water-in-oil emulsion in aged skin," *Br. J. Dermatol.*, vol. 179, no. 2, pp. 471–477, 2018.

[32] C. Blanpain and E. Fuchs, "Epidermal Stem Cells of the Skin," *Annu. Rev. Cell Dev. Biol.*, 2006.

[33] H. Yousef, A. Mandy, and S. Sandeep, *Anatomy, Skin (Integument), Epidermis*. Treasure Island: StatPearls Publishing, 2017.

[34] J. R. Dias, P. L. Granja, and P. J. Bártolo, "Progress in Materials Science Advances in electrospun skin substitutes.," *Prog. Mater. Sci.*, vol. 84, pp. 314–334, 2016.

[35] A. K. Shukla, N. Dey, P. Nandi, and M. Ranjan, "Acellular Dermis as a Dermal Matrix of Tissue Engineered Skin Substitute for Burns Treatment," *Ann Public Heal. Res*, vol. 2, no. 3, p. 1023, 2015.

[36] B. Alberts *et al.*, "Stem Cells and Tissue Renewal," in *Molecular Biology of the Cell*, 6th

ed., New York, 2015, pp. 1217–1263.

[37]   S. Goletz, D. Zillikens, and E. Schmidt, "Structural proteins of the dermal-epidermal junction targeted by autoantibodies in pemphigoid diseases," *Exp. Dermatol.*, vol. 26, no. 12, pp. 1154–1162, 2017.

[38]   A. L. Clement and G. D. Pins, "Engineering the tissue-wound interface: Harnessing topography to direct wound healing," in *Wound Healing Biomaterials-Volume 1: Therapies and Regeneration*, 1st editio., M. Ågren, Ed. Massachusetts: Woodhead Publishing, 2016, pp. 253–276.

[39]   S. M. Janes, S. Lowell, and C. Hutter, "Epidermal stem cells," *J. Pathol.*, vol. 162, no. 7–9, pp. 418–24; discussion 424-6, 2002.

[40]   A. L. Clement, T. J. Moutinho, and G. D. Pins, "Micropatterned dermal-epidermal regeneration matrices create functional niches that enhance epidermal morphogenesis," *Acta Biomater.*, vol. 9, no. 12, pp. 9474–9484, 2013.

[41]   J. Xie, T. Hao, C. Li, X. Wang, X. Yu, and L. Liu, "Automatic evaluation of stratum basale and dermal papillae using ultrahigh resolution optical coherence tomography," *Biomed. Signal Process. Control*, vol. 53, p. 101527, 2019.

[42]   E. Roig-Rosello and P. Rousselle, "The human epidermal basement membrane: A shaped and cell instructive platform that aging slowly alters," *Biomolecules*, vol. 10, no. 12, p. 1607, 2020.

[43]   A. Vela-Romera *et al.*, "Characterization of the human ridged and non-ridged skin: a comprehensive histological, histochemical and immunohistochemical analysis," *Histochem. Cell Biol.*, vol. 151, no. 1, pp. 57–73, 2019.

[44]   K. A. Bush and G. D. Pins, "Development of Microfabricated Dermal Epidermal Regenerative Matrices to Evaluate the Role of Cellular Microenvironments on Epidermal Morphogenesis," *Tissue Eng. Part A*, vol. 18, no. 21–22, pp. 2343–2353, 2012.

[45]   P. H. Jones, S. Harper, and M. W. Fiona, "Stem cell patterning and fate in human epidermis," *Cell*, vol. 80, no. 1, pp. 83–93, 1995.

[46] T. Quan and G. J. Fisher, "Role of age-associated alterations of the dermal extracellular matrix microenvironment in human skin aging: A mini-review," *Gerontology*, vol. 61, no. 5, pp. 427–434, 2015.

[47] M. Ventre, F. Mollica, and P. A. Netti, "The effect of composition and microstructure on the viscoelastic properties of dermis," *J. Biomech.*, vol. 42, no. 4, pp. 430–435, 2009.

[48] F. H. Silver, J. W. Freeman, and D. Devore, "Viscoelastic properties of human skin and processed dermis," *Ski. Res. Technol.*, vol. 7, no. 1, pp. 18–23, 2001.

[49] W. Rahmani *et al.*, "Hair Follicle Dermal Stem Cells Regenerate the Dermal Sheath, Repopulate the Dermal Papilla, and Modulate Hair Type," *Dev. Cell*, vol. 31, no. 5, pp. 543–558, 2014.

[50] Y.-C. Hsu, L. Li, and E. Fuchs, "Emerging interactions between skin stem cells and their niches," *Nat. Med.*, 2014.

[51] R. K. Zwick, C. F. Guerrero-Juarez, V. Horsley, and M. V. Plikus, "Anatomical, Physiological, and Functional Diversity of Adipose Tissue," *Cell Metab.*, vol. 27, no. 1, pp. 68–83, 2018.

[52] P. Gu and A. Xu, "Interplay between adipose tissue and blood vessels in obesity and vascular dysfunction," *Rev. Endocr. Metab. Disord.*, vol. 14, no. 1, pp. 49–58, 2013.

[53] M. Brenner and V. J. Hearing, "The protective role of melanin against UV damage in human skin," *Photochem. Photobiol.*, vol. 84, no. 3, pp. 539–549, 2008.

[54] L. H. Gu and P. A. Coulombe, "Keratin function in skin epithelia: a broadening palette with surprising shades," *Curr. Opin. Cell Biol.*, vol. 19, no. 1, pp. 13–23, 2007.

[55] R. Moll, M. Divo, and L. Langbein, "The human keratins: Biology and pathology," *Histochem. Cell Biol.*, vol. 129, no. 6, pp. 705–733, 2008.

[56] D. Gutowska-Owsiak, E. I. Podobas, C. Eggeling, G. S. Ogg, and J. Bernardino de la Serna, "Addressing Differentiation in Live Human Keratinocytes by Assessment of Membrane Packing Order," *Front. Cell Dev. Biol.*, vol. 8, no. October, pp. 1–11, 2020.

[57] F. Wang, A. Zieman, and P. A. Coulombe, "Skin Keratins," *Methods Enzym.*, vol. 586,

no. 3, pp. 303–350, 2016.

[58] H. Zhou *et al.*, "The progress and challenges for dermal regeneration in tissue engineering," *J. Biomed. Mater. Res. - Part A*, vol. 105, no. 4, pp. 1208–1218, 2017.

[59] S. Ricard-Blum, "The Collagen Family Sylvie," *Cold Spring Harb Perspect Biol*, vol. 3:a004978, pp. 1–19, 2011.

[60] J. D. Harvey Lodish, Arnold Berk, S Lawrence Zipursky, Paul Matsudaira, David Baltimore, "Collagen: The Fibrous Proteins of the Matrix," in *Molecular Cell Biology*, 4th ed., New York: W. H. Freeman, 2000.

[61] Z. Ruszczak, "Effect of collagen matrices on dermal wound healing," *Adv. Drug Deliv. Rev.*, vol. 55, no. 12, pp. 1595–1611, 2003.

[62] J. Khoshnoodi, V. Pedchenko, and B. G. Hudson, "Mammalian collagen IV," *Microsc. Res. Tech.*, vol. 71, no. 5, pp. 357–370, 2008.

[63] A. M. A. Velez and M. S. Howard, "Collagen IV in normal skin and in pathological processes," *N. Am. J. Med. Sci.*, vol. 4, no. 1, pp. 1–8, 2012.

[64] W. Tsuji, J. P. Rubin, and K. G. Marra, "Adipose-derived stem cells: Implications in tissue regeneration," *World J. Stem Cells*, vol. 6, no. 3, p. 312, 2014.

[65] U. Lindner, J. Kramer, J. Rohwedel, and P. Schlenke, "Mesenchymal stem or stromal cells: Toward a better understanding of their biology?," *Transfus. Med. Hemotherapy*, vol. 37, no. 2, pp. 75–83, 2010.

[66] L. Li and T. Xie, "Stem Cell Niche: Structure and Function," *Annu. Rev. Cell Dev. Biol*, vol. 21, pp. 605–31, 2005.

[67] M. Loeffler and I. Roeder, "Tissue Stem Cells : Definition , Plasticity , Heterogeneity , Self-Organization and Models – A Conceptual Approach," *Cells Tissues Organs*, vol. 171, no. 1, pp. 8–26, 2002.

[68] V. W. Wong, B. Levi, J. Rajadas, M. T. Longaker, and G. C. Gurtner, "Stem cell niches for skin regeneration," *Int. J. Biomater.*, vol. 2012, 2012.

[69] M. P. Lutolf and H. M. Blau, "Artificial stem cell niches," *Adv. Mater.*, vol. 21, no. 32–

33, pp. 3255–3268, 2009.

[70]   J. Jiang and E. T. Papoutsakis, "Stem-Cell Niche Based Comparative Analysis of Chemical and Nano-mechanical Material Properties Impacting Ex Vivo Expansion and Differentiation of Hematopoietic and Mesenchymal Stem Cells," *Adv. Healthc. Mater.*, vol. 2, no. 1, pp. 25–42, 2013.

[71]   A. Rezza, R. Sennett, and M. Rendl, "Adult Stem Cell Niches: Cellular and Molecular Components.," *Curr. Top. Dev. Biol.*, vol. 107, pp. 333–372, 2014.

[72]   V. Greco and S. Guo, "Compartmentalized organization: A common and required feature of stem cell niches?," *Development*, vol. 137, no. 10, pp. 1586–1594, 2010.

[73]   D. L. Jones and A. J. Wagers, "No place like home: Anatomy and function of the stem cell niche," *Nat. Rev. Mol. Cell Biol.*, vol. 9, no. 1, pp. 11–21, 2008.

[74]   I. M. Conboy, M. J. Conboy, A. J. Wagers, E. R. Girma, I. L. Weismann, and T. A. Rando, "Rejuvenation of aged progenitor cells by exposure to a young systemic environment," *Nature*, vol. 433, no. 7027, pp. 760–764, 2005.

[75]   R. Buom-Yong, K. E. Orwig, J. M. Oatley, M. R. Avarbock, and R. L. Brinster, "Effects of Aging and Niche Microenvironment on Spermatogonial Stem Cell Self Renewal," *Stem Cells*, vol. 24, no. 6, pp. 1505–1511, 2006.

[76]   G. M. Crane, E. Jeffery, and S. J. Morrison, "Adult haematopoietic stem cell niches," *Nat. Rev. Immunol.*, vol. 17, no. 9, pp. 573–590, 2017.

[77]   N. Li and H. Clevers, "Coexistence of quiescent and active adult stem cells in mammals," *Science*, vol. 327, no. 5965. pp. 542–545, 2010.

[78]   R. M. Lavker and T. T. Sun, "Epidermal stem cells: Properties, markers, and location," *Proc. Natl. Acad. Sci. U. S. A.*, vol. 97, no. 25, pp. 13473–13475, 2000.

[79]   D. H. Ramos-rodriguez, S. Macneil, F. Claeyssens, and I. Ortega Asencio, "The Use of Microfabrication Techniques for the Design and Manufacture of Artificial Stem Cell Microenvironments for Tissue Regeneration," *Bioengineering*, vol. 8, no. 50, 2021.

[80]   C. Pincelli and A. Marconi, "Keratinocyte stem cells: Friends and foes," *J. Cell. Physiol.*,

vol. 225, no. 2, pp. 310–315, 2010.

[81] K. T. Lawlor and P. Kaur, "Dermal Contributions to Human Interfollicular Epidermal Architecture and Self-Renewal," *Int. J. Mol. Sci.*, vol. 16, no. 12, pp. 28098–28107, 2015.

[82] A. Webb, A. Li, and P. Kaur, "Location and phenotype of human adult keratinocyte stem cells of the skin," *Differentiation*, vol. 72, no. 8, pp. 387–395, 2004.

[83] S. J. Morrison and D. T. Scadden, "The bone marrow niche for haematopoietic stem cells," *Nature*, vol. 505, no. 7483, pp. 327–334, 2014.

[84] A. Ehninger and A. Trumpp, "The bone marrow stem cell niche grows up: Mesenchymal stem cells and macrophages move in," *J. Exp. Med.*, vol. 208, no. 3, pp. 421–428, 2011.

[85] A. J. M. Santos, Y. Lo, A. T. Mah, and C. J. Kuo, "The Intestinal Stem Cell Niche : Homeostasis and Adaptations," *Trends Cell Biol.*, vol. 28, no. 12, pp. 1062–1078, 2018.

[86] A. Leri, M. Rota, T. Hosoda, P. Goichberg, and P. Anversa, "Cardiac stem cell niches," *Stem Cell Res.*, vol. 13, no. 3, pp. 631–646, 2014.

[87] C. T. Jayasuriya, Y. Chen, W. Liu, and Q. Chen, "The influence of tissue microenvironment on stem cell–based cartilage repair," *Ann. N. Y. Acad. Sci.*, vol. 1383, no. 1, pp. 21–33, 2016.

[88] A. J. Shortt, G. A. Secker, P. M. Munro, P. T. Khaw, S. J. Tuft, and J. T. Daniels, "Characterization of the Limbal Epithelial Stem Cell Niche: Novel Imaging Techniques Permit In Vivo Observation and Targeted Biopsy of Limbal Epithelial Stem Cells," *Stem Cells*, vol. 25, no. 6, pp. 1402–1409, 2007.

[89] L.-C. Cheng, E. Pastrana, M. Tavazoie, and F. Doetsch, "miR-124 regulates adult neurogenesis in the SVZ stem cell niche," *Nat. Neurosci.*, vol. 12, no. 4, pp. 399–408, 2009.

[90] F. Doetsch, "A niche for adult neural stem cells," *Curr. Opin. Genet. Dev.*, vol. 13, no. 5, pp. 543–550, 2003.

[91] J. M. Parent, "Adult neurogenesis in the intact and epileptic dentate gyrus," *Prog. Brain Res.*, vol. 163, no. 529–817, 2007.

[92] T. Volckaert and S. De Langhe, "Lung epithelial stem cells and their niches: Fgf10 takes center stage," *Fibrogenes. Tissue Repair*, vol. 7, no. 8, pp. 1–15, 2014.

[93] D. W. Borthwick, M. Shahbazian, Q. T. Krantz, J. R. Dorin, and S. H. Randell, "Evidence for stem-cell niches in the tracheal epithelium," *Am. J. Respir. Cell Mol. Biol.*, vol. 24, no. 6, pp. 662–670, 2001.

[94] R. D'Aquino, G. Papaccio, G. Laino, and A. Graziano, "Dental pulp stem cells: A promising tool for bone regeneration," *Stem Cell Rev.*, vol. 4, no. 1, pp. 21–26, 2008.

[95] T. A. Mitsiadis, A. Feki, G. Papaccio, and J. Catón, "Dental pulp stem cells, niches, and notch signaling in tooth injury.," *Adv. Dent. Res.*, vol. 23, no. 3, pp. 275–279, 2011.

[96] K. M. Braun and D. M. Prowse, "Distinct epidermal stem cell compartments are maintained by independent niche microenvironments," *Stem Cell Rev.*, vol. 2, no. 3, pp. 221–231, 2006.

[97] U. B. Jensen, S. Lowell, and F. M. Watt, "The spatial relationship between stem cells and their progeny in the basal layer of human epidermis: A new view based on whole-mount labelling and lineage analysis," *Development*, vol. 126, no. 11, pp. 2409–2418, 1999.

[98] A. K. Langton, H. K. Graham, J. C. McConnell, M. J. Sherratt, C. E. M. Griffiths, and R. E. B. Watson, "Organization of the dermal matrix impacts the biomechanical properties of skin," *Br. J. Dermatol.*, vol. 177, no. 3, pp. 818–827, 2017.

[99] I. L. Kruglikov and P. E. Scherer, "Skin aging as a mechanical phenomenon: The main weak links," *Nutr. Heal. Aging*, vol. 4, no. 4, pp. 291–307, 2018.

[100] Y. S. Doucet, S.-H. Woo, M. E. Ruiz, and D. M. Owens, "The touch dome defines an epidermal niche specialized for mechanosensory signaling," *Cell Rep.*, vol. 3, no. 6, pp. 1759–1765, 2013.

[101] A. K. Langton, P. Halai, C. E. M. Griffiths, M. J. Sherratt, and R. E. B. Watson, "The impact of intrinsic ageing on the protein composition of the dermal-epidermal junction," *Mech. Ageing Dev.*, vol. 156, pp. 14–16, 2016.

[102] Y.-H. Liao *et al.*, "Quantitative analysis of intrinsic skin aging in dermal papillae by in

vivo harmonic generation microscopy," *Biomed. Opt. Express*, vol. 5, no. 9, p. 3266, 2014.

[103] K. Sauermann *et al.*, "Age related changes of human skin investigated with histometric measurements by confocal laser scanning microscopy in vivo," *Ski. Res. Technol.*, vol. 8, no. 1, pp. 52–56, 2002.

[104] T. Hirobe, H. Enami, and A. Nakayama, "The human melanocyte and melanoblast populations per unit area of epidermis in the rete ridge are greater than in the inter-rete ridge," *Int. J. Cosmet. Sci.*, vol. 43, no. 2, pp. 211–217, 2021.

[105] A. Oryan; E. Alemzadeh; A. Moshiri, "Burn wound healing: present concepts, treatment strategies and future directions," *J. Wound Care*, vol. 26, no. 1, pp. 5–19, 2017.

[106] P. Martin, "Wound Healing—Aiming for Perfect Skin Regeneration," *Science (80-.).*, vol. 276, no. April, pp. 1–7, 1997.

[107] L. Cañedo-Dorantes and M. Cañedo-Ayala, "Skin acute wound healing: A comprehensive review," *Int. J. Inflam.*, vol. 2019, 2019.

[108] I. A. Darby, B. Laverdet, F. Bonté, and A. Desmoulière, "Clinical, Cosmetic and Investigational Dermatology Dovepress Fibroblasts and myofibroblasts in wound healing," *Clin. Cosmet. Investig. Dermatol.*, pp. 7–301, 2014.

[109] K. S. Midwood, L. V. Williams, and J. E. Schwarzbauer, "Tissue repair and the dynamics of the extracellular matrix," *Int. J. Biochem. Cell Biol.*, vol. 36, no. 6, pp. 1031–1037, 2004.

[110] P. Bao *et al.*, "The Role of Vascular Endothelial Growth Factor in Wound Healing," *J. Surg. Res.*, vol. 153, no. 2, pp. 347–358, 2009.

[111] A. Rochat, K. Kobayashi, and Y. Barrandon, "Location of stem cells of human hair follicles by clonal analysis," *Cell*, vol. 76, no. 6, pp. 1063–1073, 1994.

[112] S. P. Zhong, Y. Z. Zhang, and C. T. Lim, "Tissue scaffolds for skin wound healing and dermal reconstruction," *Wiley Interdisciplinary Reviews: Nanomedicine and Nanobiotechnology*. 2010.

[113] M. M. M. M. J. Wieduwilt, "The epidermal growth factor receptor family: Biology driving targeted therapeutics," *Cell Mol Life Sci.*, vol. 65, no. 10, pp. 1566–1584, 2008.

[114] B. A. Wenczak, J. B. Lynch, and L. B. Nanney, "Epidermal growth factor receptor distribution in burn wounds. Implications for growth factor-mediated repair," *J. Clin. Invest.*, vol. 90, no. 6, pp. 2392–2401, 1992.

[115] S. B. O. S. M. S. G. H. B. M. Tomic-Canic, "Growth factors and cytokines in wound healing," *Wound Repair Regen.*, vol. 16, pp. 585–601, 2008.

[116] Y. Abramov, E. Hirsch, V. Ilievski, R. P. Goldberg, S. M. Botros, and P. K. Sand, "Expression of platelet-derived growth factor-B mRNA during vaginal vs . dermal incisional wound healing in the rabbit §," *Eur. J. Obstet. Gynecol.*, vol. 162, no. 2, pp. 216–220, 2012.

[117] S. Schreml, R. M. Szeimies, S. Karrer, J. Heinlin, M. Landthaler, and P. Babilas, "The impact of the pH value on skin integrity and cutaneous wound healing," *J. Eur. Acad. Dermatology Venereol.*, vol. 24, no. 4, pp. 373–378, 2010.

[118] A. B. G. Lansdown, "Calcium: A potential central regulator in wound healing in the skin," *Wound Repair Regen.*, vol. 10, no. 5, pp. 271–285, 2002.

[119] S. Guo and L. A. DiPietro, "Critical review in oral biology & medicine: Factors affecting wound healing," *J. Dent. Res.*, vol. 89, no. 3, pp. 219–229, 2010.

[120] B. Sanchez *et al.*, "Impact of human dermal microvascular endothelial cells on primary dermal fibroblasts in response to inflammatory stress," *Front. Cell Dev. Biol.*, vol. 7, no. APR, pp. 1–10, 2019.

[121] J. Neubauer-Geryk, M. Hoffmann, M. Wielicka, K. Piec, G. Kozera, and L. Bieniaszewski, "Current methods for the assessment of skin microcirculation: Part 1," *Adv. Dermatology Allergol.*, vol. 36, no. 3, pp. 247–254, 2019.

[122] I. M. Braverman, "The cutaneous microcirculation," *J. Investig. Dermatology Symp. Proc.*, vol. 5, no. 1, pp. 3–9, 2000.

[123] N. S. Brown and R. Bicknell, "Thymidine phosphorylase, 2-deoxy-D-ribose and

angiogenesis.," *Biochem. J.*, vol. 334 (Pt 1, pp. 1–8, 1998.

[124] J. Rouwkema and A. Khademhosseini, "Vascularization and Angiogenesis in Tissue Engineering: Beyond Creating Static Networks," *Trends Biotechnol.*, vol. 34, no. 9, pp. 733–745, 2016.

[125] J. L. Arbiser, "Angiogenesis and the skin: A primer," *J. Am. Acad. Dermatol.*, vol. 34, no. 3, pp. 486–497, 1996.

[126] M. G. Tonnesen, X. Feng, and R. A. F. Clark, "Angiogenesis in wound healing," *J. Investig. Dermatology Symp. Proc.*, vol. 5, no. 1, pp. 40–46, 2000.

[127] M. W. Laschke and M. D. Menger, "Prevascularization in tissue engineering: Current concepts and future directions," *Biotechnol. Adv.*, vol. 34, no. 2, pp. 112–121, 2016.

[128] J. Rouwkema, N. C. Rivron, and C. van Blitterswijk, "Vascularization in tissue engineering.," *Trends Biotechnol.*, vol. 26, no. 8, pp. 434–41, 2008.

[129] F. S. Frueh, M. D. Menger, N. Lindenblatt, P. Giovanoli, and M. W. Laschke, "Current and emerging vascularization strategies in skin tissue engineering," *Crit. Rev. Biotechnol.*, vol. 37, no. 5, pp. 613–625, 2017.

[130] U. Urs, "Large Scale Time Series Microscopy of Neovessel Growth During Angiogenesis," vol. 91, no. 2, pp. 165–171, 2015.

[131] N. Ferrara and W. J. Henzel, "Pituitary Follicular Cells Secrete a Novel Heparin-binding Factor Specific for Vascular Endothelial Cells," *Biochem. Biophys. Res. Commun.*, vol. 161, no. 2, pp. 851–858, 1989.

[132] D. I. R. Holmes and I. Zachary, "The vascular endothelial growth factor (VEGF) family: Angiogenic factors in health and disease," *Genome Biol.*, vol. 6, no. 2, 2005.

[133] Christopher W Pugh and Peter J Ratcliffe, "Regulation of angiogenesis by hypoxia: role of the HIF system," *Nat. Med.*, vol. 9, no. 6, pp. 677–684, 2003.

[134] N. Ferrara, H.-P. Gerber, and J. LeCouter, "The biology of VEGF and its receptors," *Nat. Med.*, vol. 9, no. 6, pp. 669–676, 2003.

[135] J. Folkman and Y. Shing, "Angiogenesis," *J. Biol. Chem.*, vol. 267, no. 16, pp. 10931–

10934, 1992.

[136] A. O. Afuwape, S. Kiriakidis, and E. M. Paleolog, "The role of the angiogenic molecule VEGF in the pathogenesis of rheumatoid arthritis," *Histol. Histopathol.*, vol. 17, no. 3, pp. 961–972, 2002.

[137] C. S. Abhinand, R. Raju, S. J. Soumya, P. S. Arya, and P. R. Sudhakaran, "VEGF-A/VEGFR2 signaling network in endothelial cells relevant to angiogenesis," *J. Cell Commun. Signal.*, vol. 10, no. 4, pp. 347–354, 2016.

[138] A. K. Pandey *et al.*, "Mechanisms of VEGF (vascular endothelial growth factor) inhibitor-associated hypertension and vascular disease," *Hypertension*, vol. 71, no. 2, pp. E1–E8, 2018.

[139] C. J. Peach *et al.*, "Molecular pharmacology of VEGF-A isoforms: Binding and signalling at VEGFR2," *Int. J. Mol. Sci.*, vol. 19, no. 4, 2018.

[140] M. Lohela, M. Bry, T. Tammela, and K. Alitalo, "VEGFs and receptors involved in angiogenesis versus lymphangiogenesis," *Curr. Opin. Cell Biol.*, vol. 21, no. 2, pp. 154–165, 2009.

[141] A. Bouloumié, V. B. Schini-Kerth, and R. Busse, "Vascular endothelial growth factor up-regulates nitric oxide synthase expression in endothelial cells," *Cardiovasc. Res.*, vol. 41, no. 3, pp. 773–780, 1999.

[142] A. Yilmaztepe *et al.*, "Soluble Vascular Endothelial Growth Factor Receptor-1 (sVEGFR-1) is Decreased in Lung Cancer Patients Showing Progression: A Pilot Study," *Cancer Invest.*, vol. 25, no. 5, pp. 322–327, 2007.

[143] O. Karal-Yilmaz, M. Serhatli, K. Baysal, and B. M. Baysal, "Preparation and in vitro characterization of vascular endothelial growth factor (VEGF)-loaded poly(D,L-lactic-co-glycolic acid) microspheres using a double emulsion/solvent evaporation technique," *J. Microencapsul.*, vol. 28, no. 1, pp. 46–54, 2011.

[144] P. Schumann *et al.*, "Consequences of seeded cell type on vascularization of tissue engineering constructs in vivo," *Microvasc. Res.*, vol. 78, no. 2, pp. 180–190, 2009.

[145] A. Khojasteh *et al.*, "Development of PLGA-coated β-TCP scaffolds containing VEGF for bone tissue engineering," *Mater. Sci. Eng. C*, vol. 69, pp. 780–788, 2016.

[146] G. C. M. Steffens *et al.*, "Modulation of Angiogenic Potential of Tissue-Engineered Peripheral Nerve by Covalent Incorporation of Heparin and Loading with Vascular Endothelial Growth Factor," *Neurosci. Lett.*, vol. 10, no. 9, pp. 1502–1509, 2004.

[147] Z. Wang *et al.*, "Functionalization of electrospun poly(ε-caprolactone) scaffold with heparin and vascular endothelial growth factors for potential application as vascular grafts," *J. Bioact. Compat. Polym.*, vol. 28, no. 2, pp. 154–166, 2013.

[148] A. H. Zisch, M. P. Lutolf, and J. A. Hubbell, "Biopolymeric delivery matrices for angiogenic growth factors," *Cardiovasc. Pathol.*, vol. 12, no. 6, pp. 295–310, 2003.

[149] E. A. Silva and D. J. Mooney, "Effects of VEGF temporal and spatial presentation on angiogenesis," *Biomaterials*, vol. 31, no. 6, pp. 1235–1241, 2010.

[150] S. Ylä-Herttuala, T. T. Rissanen, I. Vajanto, and J. Hartikainen, "Vascular Endothelial Growth Factors. Biology and Current Status of Clinical Applications in Cardiovascular Medicine," *J. Am. Coll. Cardiol.*, vol. 49, no. 10, pp. 1015–1026, 2007.

[151] R. Pola *et al.*, "The morphogen Sonic hedgehog is an indirect angiogenic agent upregulating two families of angiogenic growth factors," *Nat. Med.*, vol. 7, no. 6, pp. 706–711, 2001.

[152] P. Sánchez, J. L. Pedraz, and G. Orive, "Biologically active and biomimetic dual gelatin scaffolds for tissue engineering," *Int. J. Biol. Macromol.*, vol. 98, pp. 486–494, 2017.

[153] L. Wu, L. Chen, and L. Li, "Apelin/APJ system: A novel promising therapy target for pathological angiogenesis," *Clin. Chim. Acta*, vol. 466, pp. 78–84, 2017.

[154] A. Kasai *et al.*, "Apelin is a novel angiogenic factor in retinal endothelial cells," *Biochem. Biophys. Res. Commun.*, vol. 325, no. 2, pp. 395–400, 2004.

[155] M. Sun, Y. He, T. Zhou, P. Zhang, J. Gao, and F. Lu, "Adipose Extracellular Matrix/Stromal Vascular Fraction Gel Secretes Angiogenic Factors and Enhances Skin Wound Healing in a Murine Model," *Biomed Res. Int.*, vol. 2017, 2017.

[156] C. Diniz, J. Suliburska, M. P. Isabel, and L. V. O. Ferreira, "New insights into the antiangiogenic and proangiogenic properties of dietary polyphenols," *Mol. Nutr. Food Res.*, vol. 61, no. 6, pp. 1–17, 2017.

[157] M. Yar *et al.*, "Deoxy-sugar releasing biodegradable hydrogels promote angiogenesis and stimulate wound healing," *Mater. Today Commun.*, vol. 13, no. October, pp. 295–305, 2017.

[158] N. Mangır, C. J. Hillary, C. R. Chapple, and S. MacNeil, "Oestradiol-releasing Biodegradable Mesh Stimulates Collagen Production and Angiogenesis: An Approach to Improving Biomaterial Integration in Pelvic Floor Repair," *Eur. Urol. Focus*, vol. 5, no. 2, pp. 280–289, 2019.

[159] S. Shafaat, N. Mangir, S. R. Regureos, C. R. Chapple, and S. MacNeil, "Demonstration of improved tissue integration and angiogenesis with an elastic, estradiol releasing polyurethane material designed for use in pelvic floor repair," *Neurourol. Urodyn.*, 2018.

[160] S. Dikici, M. Yar, A. J. Bullock, J. Shepherd, S. Roman, and S. Macneil, "Developing wound dressings using 2-deoxy-d-ribose to induce angiogenesis as a backdoor route for stimulating the production of vascular endothelial growth factor," *Int. J. Mol. Sci.*, vol. 22, no. 21, 2021.

[161] D. Vara *et al.*, "Direct Activation of NADPH Oxidase 2 by 2-Deoxyribose-1-Phosphate Triggers Nuclear Factor Kappa B-Dependent Angiogenesis," *Antioxid. Redox Signal.*, vol. 28, no. 2, pp. 110–130, 2018.

[162] H. Uchimiya *et al.*, "Suppression of thymidine phosphorylase-mediated angiogenesis and tumor growth by 2-deoxy-L-ribose," *Cancer Res.*, vol. 62, no. 10, pp. 2834–2839, 2002.

[163] S. I. Akiyama *et al.*, "The role of thymidine phosphorylase, an angiogenic enzyme, in tumor progression," *Cancer Science*, vol. 95, no. 11. pp. 851–857, 2004.

[164] S. A. Shahzad *et al.*, "Synthesis and biological evaluation of novel oxadiazole derivatives: A new class of thymidine phosphorylase inhibitors as potential anti-tumor agents," *Bioorganic Med. Chem.*, vol. 22, no. 3, pp. 1008–1015, 2014.

[165] I. V. Bijnsdorp *et al.*, "Thymidine phosphorylase in cancer cells stimulates human

endothelial cell migration and invasion by the secretion of angiogenic factors," *Br. J. Cancer*, vol. 104, no. 7, pp. 1185–1192, 2011.

[166] S. Dikici, N. Mangir, F. Claeyssens, M. Yar, and S. Macneil, "Exploration of 2-deoxy-D-ribose and 17β-Estradiol as alternatives to exogenous VEGF to promote angiogenesis in tissue-engineered constructs," *Regen. Med.*, vol. 14, no. 3, pp. 179–197, 2019.

[167] N. Mangir, S. Dikici, F. Claeyssens, and S. Macneil, "Using ex Ovo Chick Chorioallantoic Membrane (CAM) Assay to Evaluate the Biocompatibility and Angiogenic Response to Biomaterials," *ACS Biomater. Sci. Eng.*, vol. 5, no. 7, pp. 3190–3200, 2019.

[168] A. Andleeb *et al.*, "Developing affordable and accessible pro-angiogenic wound dressings; incorporation of 2 deoxy D-ribose (2dDR) into cotton fibres and wax-coated cotton fibres," *J. Tissue Eng. Regen. Med.*, vol. 14, no. 7, pp. 973–988, 2020.

[169] S. Dikici, A. J. Bullock, M. Yar, F. Claeyssens, and S. MacNeil, "2-deoxy-D-ribose (2dDR) upregulates vascular endothelial growth factor (VEGF) and stimulates angiogenesis," *Microvasc. Res.*, vol. 131, no. May, p. 104035, 2020.

[170] M. Azam *et al.*, "Addition of 2-deoxy-d-ribose to clinically used alginate dressings stimulates angiogenesis and accelerates wound healing in diabetic rats," *J. Biomater. Appl.*, vol. 34, no. 4, pp. 463–475, 2019.

[171] S. Dikici *et al.*, "Assessment of the Angiogenic Potential of 2-Deoxy-D-Ribose Using a Novel in vitro 3D Dynamic Model in Comparison With Established in vitro Assays," *Front. Bioeng. Biotechnol.*, vol. 7, no. January, pp. 1–20, 2020.

[172] S. Sengupta, L. A. Sellers, H. B. Matheson, and T. P. D. Fan, "Thymidine phosphorylase induces angiogenesis in vivo and in vitro: An evaluation of possible mechanisms," *Br. J. Pharmacol.*, vol. 139, no. 2, pp. 219–231, 2003.

[173] R. K. Dubey and E. K. Jackson, "Genome and Hormones: Gender Differences in Physiology Invited Review: Cardiovascular protective effects of 17ß-estradiol metabolites RAGHVENDRA," *Am. Physiol. Soc.*, vol. 91, pp. 1868–1883, 2001.

[174] M. J. Thornton, "Estrogens and aging skin," *Dermatoendocrinol.*, vol. 5, no. 2, pp. 264–

270, 2013.

[175] J. C. Pence, K. B. H. Clancy, and B. A. C. Harley, "The Induction of Pro-Angiogenic Processes Within a Collagen Scaffold Via Exogenous Estradiol and Endometrial Epithelial Cells," *Biotechnol. Bioeng.*, vol. 112, no. 10, pp. 2185–2194, 2015.

[176] G. Meduri, P. Bausero, and M. Perrot-Applanat, "Expression of vascular endothelial growth factor receptors in the human endometrium: modulation during the menstrual cycle.," *Biol. Reprod.*, vol. 62, no. 2, pp. 439–47, 2000.

[177] M. A. J. Hervé *et al.*, "Regulation of the vascular endothelial growth factor (VEGF) receptor Flk-1/KDR by estradiol through VEGF in uterus," *J. Endocrinol.*, vol. 188, no. 1, pp. 91–99, 2006.

[178] P. Yaşar, G. Ayaz, S. D. User, G. Güpür, and M. Muyan, "Molecular mechanism of estrogen–estrogen receptor signaling," *Reprod. Med. Biol.*, vol. 16, no. 1, pp. 4–20, 2017.

[179] D. Wang *et al.*, "Puerarin Suppresses Invasion and Vascularization of Endometriosis Tissue Stimulated by 17 b -Estradiol," *PLoS One*, vol. 6, no. 9, pp. 1–6, 2011.

[180] M. Shafighi *et al.*, "Topical application of 17β-estradiol (E2) improves skin flap survival through activation of endothelial nitric oxide synthase in rats," *Wound Repair Regen.*, vol. 20, no. 5, pp. 740–747, 2012.

[181] E. D. Albrecht, J. S. Babischkin, Y. Lidor, L. D. Anderson, L. C. Udoff, and G. J. Pepe, "Effect of estrogen on angiogenesis in co-cultures of human endometrial cells and microvascular endothelial cells," *Hum. Reprod.*, vol. 18, no. 10, pp. 2039–2047, 2003.

[182] H. Sekiguchi *et al.*, "Estradiol promotes neural stem cell differentiation into endothelial lineage and angiogenesis in injured peripheral nerve," *Angiogenesis*, vol. 16, no. 1, pp. 45–58, 2013.

[183] C. E. Toutain *et al.*, "Prevention of skin flap necrosis by estradiol involves reperfusion of a protected vascular network," *Circ. Res.*, vol. 104, no. 2, pp. 245–254, 2009.

[184] R. Crompton *et al.*, "Oestrogen promotes healing in a bacterial LPS model of delayed cutaneous wound repair," *Lab. Investig.*, vol. 96, no. 4, pp. 439–449, 2016.

[185] S. Rahman, P. Carter, and N. Bhattarai, "Aloe Vera for Tissue Engineering Applications," *J. Funct. Biomater.*, 2017.

[186] A. A. Maan *et al.*, "The therapeutic properties and applications of Aloe vera : A review," *J. Herb. Med.*, no. January, pp. 1–10, 2018.

[187] K. Eshun and Q. He, "Aloe Vera : A Valuable Ingredient for the Food , Pharmaceutical and Cosmetic Industries - A Review," *Taylor Fr.*, vol. 44, pp. 91–96, 2004.

[188] D. I. Sánchez-Machado, J. López-Cervantes, R. Sendón, and A. Sanches-Silva, "Aloe vera: Ancient knowledge with new frontiers," *Trends in Food Science and Technology*, vol. 61. pp. 94–102, 2017.

[189] A. Bozzi, C. Perrin, S. Austin, and F. Arce Vera, "Quality and authenticity of commercial aloe vera gel powders," *Food Chem.*, vol. 103, no. 1, pp. 22–30, 2007.

[190] J. H. Hamman, "Composition and applications of Aloe vera leaf gel," *Molecules*, vol. 13, no. 8, pp. 1599–1616, 2008.

[191] M. A. Saeed *et al.*, "Aloe vera: a plant of vital significance," *Q. Sci. Vis.*, vol. 2, pp. 1–3, 2003.

[192] S. Simal, C. Rossello, A. Femenia, and E. Sánchez, "Compositional features of polysaccharides from Aloe vera (Aloe barbadensis Miller) plant tissues," *Carbohydr. Polym.*, vol. 39, pp. 109–117, 1999.

[193] R. Maenthaisong, N. Chaiyakunapruk, S. Niruntraporn, and C. Kongkaew, "The efficacy of aloe vera used for burn wound healing: A systematic review," *Burns*, vol. 33, no. 6, pp. 713–718, 2007.

[194] M. Radha and N. Laxmipriya, "Evaluation of biological properties and clinical effectiveness of Aloe vera: A systematic review," *J. Tradit. Complement. Med.*, vol. 5, pp. 21–26, 2015.

[195] F. Nejatzadeh-Barandozi, "Antibacterial activities and antioxidant capacity of Aloe vera," *Org. Med. Chem. Lett.*, vol. 3, no. 1, p. 5, 2013.

[196] S. Suganya, J. Venugopal, S. Ramakrishna, B. S. Lakshmi, and V. R. G. Dev, "Naturally

derived biofunctional nanofibrous scaffold for skin tissue regeneration," *Int. J. Biol. Macromol.*, 2014.

[197] R. Pereira, A. Mendes, and P. Bártolo, "Alginate/Aloe vera hydrogel films for biomedical applications," *Procedia CIRP*, vol. 5, pp. 210–215, 2013.

[198] E. Moon *et al.*, "A novel angiogenic factor derived from Aloe vera gel: B-sitosterol, a plant sterol," *Angiogenesis*, vol. 3, pp. 117–123, 1999.

[199] Q. Pan, H. Pan, H. Lou, Y. Xu, and L. Tian, "Inhibition of the angiogenesis and growth of Aloin in human colorectal cancer in vitro and in vivo," *Cancer Cell Int.*, vol. 13, no. 1, p. 1, 2013.

[200] S. Saeidnia, "The Story of Beta-sitosterol- A Review," *European J. Med. Plants*, vol. 4, no. 5, pp. 590–609, 2014.

[201] S. MacNeil, "Biomaterials for tissue engineering of skin," *Mater. Today*, vol. 11, no. 5, pp. 26–35, 2008.

[202] J. Ho, C. Walsh, D. Yue, A. Dardik, and U. Cheema, "Current Advancements and Strategies in Tissue Engineering for Wound Healing: A Comprehensive Review," *Adv. Wound Care*, vol. 6, no. 6, pp. 191–209, 2017.

[203] E. T. Melkun and J. W. Few, "The use of biosynthetic skin substitute (Biobrane) for axillary reconstruction after surgical excision for hidradenitis suppurativa.," *Plast. Reconstr. Surg.*, vol. 115, no. 5, pp. 1385–1388, Apr. 2005.

[204] H. Cronin and G. Goldstein, "Biologic skin substitutes and their applications in dermatology.," *Dermatologic Surg. Off. Publ. Am. Soc. Dermatologic Surg.*, vol. 39, no. 1 Pt 1, pp. 30–34, Jan. 2013.

[205] M. N. Nicholas and J. Yeung, "Current status and future of skin substitutes for chronic wound healing," *J. Cutan. Med. Surg.*, vol. 21, no. 1, pp. 23–30, 2017.

[206] O. B. Hughes, A. Rakosi, F. MacQuhae, I. Herskovitz, J. D. Fox, and R. S. Kirsner, "A review of cellular and acellular matrix products: Indications, techniques, and outcomes," *Plast. Reconstr. Surg.*, vol. 138, no. 3, pp. 138S-147S, 2016.

[207] J. Schneider *et al.*, "Matriderm® versus Integra®: A comparative experimental study," *Burns*, vol. 35, no. 1, pp. 51–57, 2009.

[208] A. Ring *et al.*, "Enhanced neovascularization of dermis substitutes via low-pressure plasma-mediated surface activation," *Burns*, vol. 36, no. 8, pp. 1222–1227, 2010.

[209] S. S. Scherer *et al.*, "Poly-N-Acetyl glucosamine nanofibers: A new bioactive material to enhance diabetic wound healing by cell migration and angiogenesis," *Ann. Surg.*, vol. 250, no. 2, pp. 322–330, 2009.

[210] J. Pu, F. Yuan, S. Li, and K. Komvopoulos, "Electrospun bilayer fibrous scaffolds for enhanced cell infiltration and vascularization in vivo," *Acta Biomater.*, vol. 13, pp. 131–141, 2015.

[211] Y. Miyagi, L. L. Y. Chiu, M. Cimini, R. D. Weisel, M. Radisic, and R. K. Li, "Biodegradable collagen patch with covalently immobilized VEGF for myocardial repair," *Biomaterials*, vol. 32, no. 5, pp. 1280–1290, 2011.

[212] A. Perets, Y. Baruch, F. Weisbuch, G. Shoshany, G. Neufeld, and S. Cohen, "Enhancing the vascularization of three-dimensional porous alginate scaffolds by incorporating controlled release basic fibroblast growth factor microspheres," *J. Biomed. Mater. Res. - Part A*, vol. 65, no. 4, pp. 489–497, 2003.

[213] D. J. Margolis *et al.*, "Phase I study of H5.020CMV.PDGF-β to treat venous leg ulcer disease," *Mol. Ther.*, vol. 17, no. 10, pp. 1822–1829, 2009.

[214] T. M. Crombleholme, "Adenoviral-mediated gene transfer in wound healing," *Wound Repair Regen.*, vol. 8, no. 6, pp. 460–472, 2000.

[215] S. Michael *et al.*, "Tissue Engineered Skin Substitutes Created by Laser-Assisted Bioprinting Form Skin-Like Structures in the Dorsal Skin Fold Chamber in Mice," *PLoS One*, vol. 8, no. 3, 2013.

[216] D. R. Griffin, W. M. Weaver, P. O. Scumpia, D. Di Carlo, and T. Segura, "Accelerated wound healing by injectable microporous gel scaffolds assembled from annealed building blocks," *Nat. Mater.*, vol. 14, no. 7, pp. 737–744, 2015.

[217] P. L. Tremblay, V. Hudon, F. Berthod, L. Germain, and F. A. Auger, "Inosculation of tissue-engineered capillaries with the host's vasculature in a reconstructed skin transplanted on mice," *Am. J. Transplant.*, vol. 5, no. 5, pp. 1002–1010, 2005.

[218] I. Montaño *et al.*, "Formation of Human Capillaries *In Vitro* : The Engineering of Prevascularized Matrices," *Tissue Eng. Part A*, vol. 16, no. 1, pp. 269–282, 2010.

[219] F. J. O'Brien, "Biomaterials & scaffolds for tissue engineering," *Mater. Today*, vol. 14, no. 3, pp. 88–95, 2011.

[220] H. K. Makadia and S. J. Siegel, "Poly Lactic-co-Glycolic Acid (PLGA) as biodegradable controlled drug delivery carrier," *Polymers (Basel).*, vol. 3, no. 3, pp. 1377–1397, 2011.

[221] F. Alexis, "Factors affecting the degradation and drug-release mechanism of poly(lactic acid) and poly[(lactic acid)-co-(glycolic acid)]," *Polymer International*, vol. 54, no. 1. pp. 36–46, 2005.

[222] J. S. Constant *et al.*, "Lactate elicits vascular endothelial growth factor from macrophages: A possible alternative to hypoxia," *Wound Repair Regen.*, vol. 8, no. 5, pp. 353–360, 2000.

[223] P. E. Porporato *et al.*, "Lactate stimulates angiogenesis and accelerates the healing of superficial and ischemic wounds in mice," *Angiogenesis*, vol. 15, no. 4, pp. 581–592, 2012.

[224] T. N. Milovanova *et al.*, "Lactate Stimulates Vasculogenic Stem Cells via the Thioredoxin System and Engages an Autocrine Activation Loop Involving Hypoxia-Inducible Factor 1," *Mol. Cell. Biol.*, vol. 28, no. 20, pp. 6248–6261, 2008.

[225] G. Chen, T. Sato, H. Ohgushi, T. Ushida, T. Tateishi, and J. Tanaka, "Culturing of skin fibroblasts in a thin PLGA-collagen hybrid mesh," *Biomaterials*, vol. 26, no. 15, pp. 2559–2566, 2005.

[226] X. Hu, S. Liu, G. Zhou, Y. Huang, Z. Xie, and X. Jing, "Electrospinning of polymeric nanofibers for drug delivery applications," *Journal of Controlled Release*. 2014.

[227] Y. Wang *et al.*, "Degradable PLGA Scaffolds with Basic Fibroblast Growth Factor," pp.

89–97.

[228] F. R. Formiga *et al.*, "Sustained release of VEGF through PLGA microparticles improves vasculogenesis and tissue remodeling in an acute myocardial ischemia-reperfusion model," *J. Control. Release*, vol. 147, no. 1, pp. 30–37, 2010.

[229] M. V. Jose, V. Thomas, K. T. Johnson, D. R. Dean, and E. Nyairo, "Aligned PLGA/HA nanofibrous nanocomposite scaffolds for bone tissue engineering," *Acta Biomater.*, vol. 5, no. 1, pp. 305–315, 2009.

[230] K. A. Blackwood *et al.*, "Development of biodegradable electrospun scaffolds for dermal replacement," *Biomaterials*, vol. 29, no. 21, pp. 3091–3104, 2008.

[231] J. Hu *et al.*, "Highly Aligned Electrospun Collagen/Polycaprolactone Surgical Sutures with Sustained Release of Growth Factors for Wound Regeneration," *ACS Appl. Bio Mater.*, vol. 3, no. 2, pp. 965–976, 2020.

[232] T. Patrício, M. Domingos, A. Gloria, and P. Bártolo, "Characterisation of PCL and PCL/PLA scaffolds for tissue engineering," *Procedia CIRP*, vol. 5, pp. 110–114, 2013.

[233] N. M. Al-Namnam, K. H. Kim, W. L. Chai, K. O. Ha, C. H. Siar, and W. C. Ngeow, "A biocompatibility study of injectable poly(caprolactone-trifumarate) for use as a bone substitute material," *Front. Life Sci.*, vol. 8, no. 3, pp. 215–222, 2015.

[234] A. J. Reid *et al.*, "Long term peripheral nerve regeneration using a novel PCL nerve conduit," *Neurosci. Lett.*, vol. 544, pp. 125–130, 2013.

[235] C. W. Macosko *et al.*, "A novel degradable polycarbonate networks for tissue engineering," *Biomaterials*, vol. 24, pp. 801–808, 2003.

[236] T. Hayashi, "Biodegradable polymers for biomedical uses," *Prog. Polym. Sci.*, vol. 19, no. 4, pp. 663–702, 1994.

[237] L. Pastorino, F. Pioli, M. Zilli, A. Converti, and C. Nicolini, "Lipase-catalyzed degradation of poly(ε-caprolactone)," *Enzyme Microb. Technol.*, vol. 35, no. 4, pp. 321–326, 2004.

[238] B. Azimi, P. Nourpanah, M. Rabiee, and S. Arbab, "Poly (ε-caprolactone) fiber: An

overview," *J. Eng. Fiber. Fabr.*, vol. 9, no. 3, pp. 74–90, 2014.

[239] A. Martins *et al.*, "Surface modification of electrospun polycaprolactone nanofiber meshes by plasma treatment to enhance biological performance," *Small*, vol. 5, no. 10, pp. 1195–1206, 2009.

[240] N. Recek *et al.*, "Cell Adhesion on Polycaprolactone Modified by Plasma Treatment," *Int. J. Polym. Sci.*, vol. 2016, 2016.

[241] C. M. Chan, T. M. Ko, and H. Hiraoka, "Polymer surface modification by plasmas and photons," *Surf. Sci. Rep.*, vol. 24, no. 1–2, pp. 1–54, 1996.

[242] C. Chong, Y. Wang, A. Fathi, R. Parungao, P. K. Maitz, and Z. Li, "Skin wound repair: Results of a pre-clinical study to evaluate electropsun collagen–elastin–PCL scaffolds as dermal substitutes.," *Burns*, vol. 45, no. 7, pp. 1639–1648, 2019.

[243] K. W. Ng, H. N. Achuth, S. Moochhala, T. C. Lim, and D. W. Hutmacher, "In vivo evaluation of an ultra-thin polycaprolactone film as a wound dressing," *J. Biomater. Sci. Polym. Ed.*, vol. 18, no. 7, pp. 925–938, 2007.

[244] J. G. Merrell *et al.*, "Curcumin Loaded Poly(ε-Caprolactone) Nanofibers: Diabetic Wound Dressing with Antioxidant and Anti-inflammatory Properties NIH Public Access Author Manuscript," *Clin Exp Pharmacol Physiol*, vol. 36, no. 12, pp. 1149–1156, 2009.

[245] B. Joseph, R. Augustine, N. Kalarikkal, S. Thomas, B. Seantier, and Y. Grohens, "Recent advances in electrospun polycaprolactone based scaffolds for wound healing and skin bioengineering applications," *Mater. Today Commun.*, vol. 19, no. October 2018, pp. 319–335, 2019.

[246] P. Weiss and B. Garber, "Shape and Movement of Mesenchyme Cells as Functions of the Physical Structure of the Medium: Contributions to a Quantitative Morphology," *Proc. Natl. Acad. Sci.*, vol. 38, no. 3, pp. 264–280, 1952.

[247] A. S. G. Curtis and M. Varde, "Control of Cell Behavior : Topological Factors," *J Nat Cancer*, vol. 33, no. 1, pp. 15–26, 1964.

[248] J. J. Blaker, J. C. Knowles, and R. M. Day, "Novel fabrication techniques to produce

microspheres by thermally induced phase separation for tissue engineering and drug delivery," *Acta Biomater.*, vol. 4, no. 2, pp. 264–272, 2008.

[249] S. G. Priya, H. Jungvid, and A. Kumar, "Skin Tissue Engineering for Tissue Repair and Regeneration," *Tissue Eng. Part B Rev.*, vol. 14, no. 1, pp. 105–118, 2008.

[250] J. Xue, T. Wu, Y. Dai, and Y. Xia, "Electrospinning and electrospun nanofibers: Methods, materials, and applications," *Chem. Rev.*, vol. 119, no. 8, pp. 5298–5415, 2019.

[251] A. Repanas, S. Andriopoulou, and B. Glasmacher, "The significance of electrospinning as a method to create fibrous scaffolds for biomedical engineering and drug delivery applications," *J. Drug Deliv. Sci. Technol.*, vol. 31, pp. 137–146, 2016.

[252] T. J. Sill and H. A. von Recum, "Electrospinning: Applications in drug delivery and tissue engineering," *Biomaterials*, vol. 29, no. 13, pp. 1989–2006, 2008.

[253] N. Bhardwaj and S. C. Kundu, "Electrospinning: A fascinating fiber fabrication technique," *Biotechnol. Adv.*, vol. 28, no. 3, pp. 325–347, 2010.

[254] M. Buzgo, A. Mickova, M. Rampichova, and M. Doupnik, "Blend electrospinning, coaxial electrospinning, and emulsion electrospinning techniques," in *Core-shell nanostructures for drug delivery and theranostics*, Elsevier, 2018, pp. 325–347.

[255] S. Chen, R. Li, X. Li, and J. Xie, "Electrospinning: An enabling nanotechnology platform for drug delivery and regenerative medicine," *Adv. Drug Deliv. Rev.*, vol. 132, pp. 188–213, 2018.

[256] H. S. Yoo, T. G. Kim, and T. G. Park, "Surface-functionalized electrospun nanofibers for tissue engineering and drug delivery," *Adv. Drug Deliv. Rev.*, vol. 61, no. 12, pp. 1033–1042, 2009.

[257] S. Fahimirad and F. Ajalloueian, "Naturally-derived electrospun wound dressings for target delivery of bio-active agents," *Int. J. Pharm.*, vol. 566, no. May, pp. 307–328, 2019.

[258] X. Yan, M. Yu, S. Ramakrishna, S. J. Russell, and Y. Z. Long, "Advances in portable electrospinning devices for: In situ delivery of personalized wound care," *Nanoscale*, vol. 11, no. 41, pp. 19166–19178, 2019.

[259] A. A. Dongargaonkar, G. L. Bowlin, and H. Yang, "Electrospun blends of gelatin and gelatin-dendrimer conjugates as a wound-dressing and drug-delivery platform," *Biomacromolecules*, vol. 14, no. 11, pp. 4038–4045, 2013.

[260] J. Mašek *et al.*, "Multi-layered nanofibrous mucoadhesive films for buccal and sublingual administration of drug-delivery and vaccination nanoparticles - important step towards effective mucosal vaccines," *J. Control. Release*, vol. 249, pp. 183–195, 2017.

[261] A. Rohani Shirvan, A. Bashari, and N. Hemmatinejad, "New insight into the fabrication of smart mucoadhesive buccal patches as a novel controlled-drug delivery system," *Eur. Polym. J.*, vol. 119, no. July, pp. 541–550, 2019.

[262] B. W. Streeter, J. Xue, Y. Xia, and M. E. Davis, "Electrospun Nanofiber-Based Patches for the Delivery of Cardiac Progenitor Cells," *ACS Appl. Mater. Interfaces*, vol. 11, no. 20, pp. 18242–18253, 2019.

[263] X. Liu *et al.*, "Electrospinnability of Poly Lactic-co-glycolic Acid (PLGA): the Role of Solvent Type and Solvent Composition," *Pharm. Res.*, vol. 34, no. 4, pp. 738–749, 2017.

[264] K. Hirowatari, "Real three dimensional micro fabrication using stereo lithography and metal molding," *Proc. IEEE Micro Electro Mech. Syst.*, pp. 42–47, 1993.

[265] M. Vaezi, H. Seitz, and S. Yang, "A review on 3D micro-additive manufacturing technologies," *International Journal of Advanced Manufacturing Technology*. 2013.

[266] R. Gauvin *et al.*, "Microfabrication of complex porous tissue engineering scaffolds using 3D projection stereolithography," *Biomaterials*, vol. 33, no. 15, pp. 3824–3834, 2012.

[267] A. K. Nguyen and R. J. Narayan, "Two-photon polymerization for biological applications," *Mater. Today*, vol. 20, no. 6, pp. 314–322, 2017.

[268] T. Matsuda, M. Mizutani, and S. C. Arnold, "Molecular design of photocurable liquid biodegradable copolymers. 1. Synthesis and photocuring characteristics," *Macromolecules*, vol. 33, no. 3, pp. 795–800, 2000.

[269] Í. Ortega, A. J. Ryan, P. Deshpande, S. MacNeil, and F. Claeyssens, "Combined microfabrication and electrospinning to produce 3-D architectures for corneal repair,"

Acta Biomater., vol. 9, no. 3, pp. 5511–5520, 2013.

[270] T. E. Paterson, S. N. Beal, M. E. Santocildes-Romero, A. T. Sidambe, P. V. Hatton, and I. O. Asencio, "Selective laser melting-enabled electrospinning: Introducing complexity within electrospun membranes," *Proc. Inst. Mech. Eng. Part H J. Eng. Med.*, vol. 231, no. 6, pp. 565–574, 2017.

[271] I. Ortega Ascensio, S. Mittar, C. Sherborne, A. Raza, F. Claeyssens, and S. MacNeil, "A methodology for the production of microfabricated electrospun membranes for the creation of new skin regeneration models," *J. Tissue Eng.*, vol. 9, p. 204173141879985, 2018.

[272] A. Theron, E. Zussman, and A. L. Yarin, "Electrostatic field-assisted alignment of electrospun nanofibres," *Nanotechnology*, vol. 12, pp. 384–390, 2001.

[273] D. Li, G. Ouyang, J. T. Mccann, and Y. Xia, "Collecting Electrospun Nanofibers with Patterned Electrodes," *Nanoletters*, vol. 5, no. 5, pp. 913–916, 2005.

[274] B. Ma, J. Xie, J. Jiang, and J. Wu, "Sandwich-type fiber scaffolds with square arrayed microwells and nanostructured cues as microskin grafts for skin regeneration," *Biomaterials*, vol. 35, no. 2, pp. 630–641, 2014.

[275] M. Tallawi *et al.*, "Novel PGS/PCL electrospun fiber mats with patterned topographical features for cardiac patch applications," *Mater. Sci. Eng. C*, vol. 69, pp. 569–576, 2016.

[276] H. L. Kwang *et al.*, "Hydrophilic electrospun polyurethane nanofiber matrices for hMSC culture in a microfluidic cell chip," *J. Biomed. Mater. Res. - Part A*, vol. 90, no. 2, pp. 619–628, 2009.

[277] A. R. Brunelle, C. B. Horner, K. Low, G. Ico, and J. Nam, "Electrospun thermosensitive hydrogel scaffold for enhanced chondrogenesis of human mesenchymal stem cells," *Acta Biomater.*, vol. 66, pp. 166–176, 2018.

[278] G. Lammers *et al.*, "Construction of a Microstructured Collagen Membrane Mimicking the Papillary Dermis Architecture and Guiding Keratinocyte Morphology and Gene Expression," *Macromol. Biosci.*, vol. 12, no. 5, pp. 675–691, 2012.

[279] T. Okuda, K. Tominaga, and S. Kidoaki, "Time-programmed dual release formulation by multilayered drug-loaded nanofiber meshes," *J. Control. Release*, vol. 143, no. 2, pp. 258–264, 2010.

[280] F. J. Bye *et al.*, "Development of bilayer and trilayer nanofibrous/microfibrous scaffolds for regenerative medicine," *Biomater. Sci.*, vol. 1, no. 9, p. 942, 2013.

[281] T. Yao, M. B. Baker, and L. Moroni, "Strategies to improve nanofibrous scaffolds for vascular tissue engineering," *Nanomaterials*, vol. 10, no. 5, 2020.

[282] S. Heydarkhan-Hagvall *et al.*, "Three-dimensional electrospun ECM-based hybrid scaffolds for cardiovascular tissue engineering," *Biomaterials*, vol. 29, no. 19, pp. 2907–2914, 2008.

[283] S. Politi *et al.*, "Smart ECM-based electrospun biomaterials for skeletal muscle regeneration," *Nanomaterials*, vol. 10, no. 9, pp. 1–19, 2020.

[284] B. M. Gillette *et al.*, "Engineering extracellular matrix structure in 3D multiphase tissues," *Biomaterials*, vol. 32, no. 32, pp. 8067–8076, 2011.

[285] Y. Xu *et al.*, "ECM-inspired micro/nanofibers for modulating cell function and tissue generation," *Sci. Adv.*, vol. 6, no. 48, pp. 1–18, 2020.

[286] C. M. Rogers *et al.*, "A novel technique for the production of electrospun scaffolds with tailored three-dimensional micro-patterns employing additive manufacturing," *Biofabrication*, vol. 6, no. 3, 2014.

[287] A. Luraghi, F. Peri, and L. Moroni, "Electrospinning for drug delivery applications: A review," *J. Control. Release*, vol. 334, pp. 463–484, 2021.

[288] J. M. Cornejo Bravo, L. J. Villarreal Gómez, and A. Serrano Medina, "Electrospinning for Drug Delivery Systems: Drug Incorporation Techniques," in *Electrospinning - Material, Techniques, and Biomedical Applications*, 2016, pp. 141–155.

[289] V. Pillay *et al.*, "A review of the effect of processing variables on the fabrication of electrospun nanofibers for drug delivery applications," *J. Nanomater.*, vol. 2013, 2012.

[290] Í. Ortega, P. Deshpande, A. A. Gill, S. Macneil, and F. Claeyssens, "Development of a

microfabricated artificial limbus with micropockets for cell delivery to the cornea," *Biofabrication*, vol. 5, no. 2, 2013.

[291] D. H. Ramos-Rodriguez, S. MacNeil, F. Claeyssens, and I. Ortega Asencio, "Fabrication of Topographically Controlled Electrospun Scaffolds to Mimic the Stem Cell Microenvironment in the Dermal-Epidermal Junction.," *ACS Biomater. Sci. Eng.*, vol. 7, no. 6, 2021.

[292] C. A. Schneider, W. S. Rasband, and K. W. Eliceiri, "NIH Image to ImageJ: 25 years of Image Analysis HHS Public Access," *Nat. Methods*, vol. 9, no. 7, pp. 671–675, 2012.

[293] J. Patterson and C. Mura, "Rapid Colorimetric Assays to Qualitatively Distinguish RNA and DNA in Biomolecular Samples," *J. Vis*, vol. Exp. (72), no. e50225, 2013.

[294] Y. You, S. J. Lee, B. M. Min, and W. H. Park, "Effect of solution properties on nanofibrous structure of electrospun poly(lactic-co-glycolic acid)," *J. Appl. Polym. Sci.*, vol. 99, no. 3, pp. 1214–1221, 2006.

[295] J. H. Yu, S. V. Fridrikh, and G. C. Rutledge, "The role of elasticity in the formation of electrospun fibers," *Polymer (Guildf).*, vol. 47, no. 13, pp. 4789–4797, 2006.

[296] M. O. Christen and F. Vercesi, "Polycaprolactone: How a well-known and futuristic polymer has become an innovative collagen-stimulator in esthetics," *Clin. Cosmet. Investig. Dermatol.*, vol. 13, pp. 31–48, 2020.

[297] "International Council for Harmonisation Guideline Q3C (R7) on Impurities: Guideline for Residual Solvents.," *European Medicines Agency*, 2018. [Online]. Available: https://healthdocbox.com/Substance_Abuse/127287345-Ich-guideline-q3c-r7-on-impurities-guideline-for-residual-solvents.html.

[298] J. Yang, T. A. Marzan, W. Ye, C. D. Sommers, J. D. Rodriguez, and D. A. Keire, "A Cautionary Tale: Quantitative LC-HRMS Analytical Procedures for the Analysis of N-Nitrosodimethylamine in Metformin," *AAPS J.*, vol. 22, no. 4, pp. 1–8, 2020.

[299] Ameeduzzafar *et al.*, "Improvement of ocular efficacy of levofloxacin by bioadhesive Chitosan coated PLGA nanoparticles: Box-behnken design, in-vitro characterization, antibacterial evaluation and scintigraphy study," *Iran. J. Pharm. Res.*, vol. 19, no. 1, pp.

292–311, 2020.

[300] D. S. Villanueva Navarrete, "Design and fabrication of microstructured and mechanically-controlled electrospun corneal membranes," The University of Sheffield, 2020.

[301] B. Azimi, P. Nourpanah, M. Rabiee, and S. Arbab, "Poly(lactide-co-glycolide) Fiber : An Overview," *J. Eng. Fiber. Fabr.*, vol. 9, no. 1, pp. 47–66, 2014.

[302] I. Cantón *et al.*, "Development of an Ibuprofen-releasing biodegradable PLA/PGA electrospun scaffold for tissue regeneration," *Biotechnol. Bioeng.*, vol. 105, no. 2, pp. 396–408, 2010.

[303] A. R. Sadeghi, S. Nokhasteh, A. M. Molavi, M. Khorsand-Ghayeni, H. Naderi-Meshkin, and A. Mahdizadeh, "Surface modification of electrospun PLGA scaffold with collagen for bioengineered skin substitutes," *Mater. Sci. Eng. C*, 2016.

[304] H. J. Shin *et al.*, "Electrospun PLGA nanofiber scaffolds for articular cartilage reconstruction: Mechanical stability, degradation and cellular responses under mechanical stimulation in vitro," *J. Biomater. Sci. Polym. Ed.*, vol. 17, no. 1, pp. 103–119, 2006.

[305] Q. Yao *et al.*, "Aloe/poloxamer hydrogel as an injectable β-estradiol delivery scaffold with multi-therapeutic effects to promote endometrial regeneration for intrauterine adhesion treatment," *Eur. J. Pharm. Sci.*, vol. 148, no. December 2019, p. 105316, 2020.

[306] Y. Liu, Y. Ji, K. Ghosh, R. A. F. Clark, L. Huang, and M. H. Rafailovich, "Effects of fiber orientation and diameter on the behavior of human dermal fibroblasts on electrospun PMMA scaffolds," *J. Biomed. Mater. Res. - Part A*, vol. 90, no. 4, pp. 1092–1106, 2009.

[307] T. Sun, D. Norton, R. J. McKean, J. W. Haycock, A. J. Ryan, and S. MacNeil, "Development of a 3D Cell Culture System for Investigating Cell Interactions With Electrospun Fibers," *Biotechnol. Bioeng.*, vol. 97, no. 5, pp. 1378–1328, 2006.

[308] P. Carter, S. M. Rahman, and N. Bhattarai, "Facile fabrication of aloe vera containing PCL nanofibers for barrier membrane application," *J. Biomater. Sci. Polym. Ed.*, vol. 27, no. 7, pp. 692–708, 2016.

[309] S. Suganya, J. Venugopal, S. Agnes Mary, S. Ramakrishna, B. S. Lakshmi, and V. R. Giri

Dev, "Aloe vera incorporated biomimetic nanofibrous scaffold: A regenerative approach for skin tissue engineering," *Iran. Polym. J. (English Ed.*, vol. 23, no. 3, pp. 237–248, 2014.

[310] İ. Uslu, S. Keskin, A. Gül, T. C. Karabulut, and M. L. Aksu, "Preparation and Properties of Electrospun Poly (vinyl alcohol) Blended Hybrid Polymer with Aloe vera and HPMC as Wound Dressing," *Hacettepe J. Biol. Chem.*, vol. 38, no. 1, pp. 19–25, 2010.

[311] S. Agnes Mary and V. R. Giri Dev, "Electrospun herbal nanofibrous wound dressings for skin tissue engineering," *J. Text. Inst.*, vol. 106, no. 8, pp. 886–895, 2015.

[312] L. L. Lima, A. C. K. Bierhalz, and Â. M. Moraes, "Influence of the chemical composition and structure design of electrospun matrices on the release kinetics of Aloe vera extract rich in aloin," *Polym. Degrad. Stab.*, vol. 179, 2020.

[313] F. R. Isfahani, H. Tavanai, and M. Morshed, "Release of aloe vera from electrospun aloe vera-PVA nanofibrous pad," *Fibers Polym.*, vol. 18, no. 2, pp. 264–271, 2017.

[314] A. R. Unnithan *et al.*, "Electrospun polyurethane-dextran nanofiber mats loaded with Estradiol for post-menopausal wound dressing," *Int. J. Biol. Macromol.*, vol. 77, pp. 1–8, 2015.

[315] C. Steffi *et al.*, "Estradiol-Loaded Poly(ϵ-caprolactone)/Silk Fibroin Electrospun Microfibers Decrease Osteoclast Activity and Retain Osteoblast Function," *ACS Appl. Mater. Interfaces*, vol. 10, no. 12, pp. 9988–9998, 2018.

[316] M. A. Weber, M. H. Kleijn, M. Langendam, J. Limpens, M. J. Heineman, and J. P. Roovers, "Local oestrogen for pelvic floor disorders: A systematic review," *PLoS One*, vol. 10, no. 9, 2015.

[317] W. S. Ramsey, W. Hertl, E. D. Nowlan, and N. T. Binkowski, "Surface Treatments and Cell Attachment," *Vitr. Biol.*, vol. 20, no. 10, pp. 802–808, 1984.

[318] A. M. Sandoval-Castellanos, F. Claeyssens, and J. W. Haycock, "Biomimetic surface delivery of NGF and BDNF to enhance neurite outgrowth," *Biotechnol. Bioeng.*, vol. 117, no. 10, pp. 3124–3135, 2020.

[319] A. Sakudo, Y. Yagyu, and T. Onodera, "Disinfection and sterilization using plasma technology: Fundamentals and future perspectives for biological applications," *Int. J. Mol. Sci.*, vol. 20, no. 20, p. 5216, 2019.

[320] K. Bialik-Wąs, K. Pluta, D. Malina, M. Barczewski, K. Malarz, and A. Mrozek-Wilczkiewicz, "Advanced SA/PVA-based hydrogel matrices with prolonged release of Aloe vera as promising wound dressings," *Mater. Sci. Eng. C*, no. August, p. 111667, 2020.

[321] M. Naseri-Nosar, S. Farzamfar, M. Salehi, A. Vaez, R. Tajerian, and M. Azami, "Erythropoietin/aloe vera-releasing wet-electrospun polyvinyl alcohol/chitosan sponge-like wound dressing: In vitro and in vivo studies," *J. Bioact. Compat. Polym.*, vol. 33, no. 3, pp. 269–281, 2018.

[322] K. S. Ahlawat and B. S. Khatkar, "Processing, food applications and safety of aloe vera products: A review," *J. Food Sci. Technol.*, vol. 48, no. 5, pp. 525–533, 2011.

[323] J. Zeng *et al.*, "Influence of the drug compatibility with polymer solution on the release kinetics of electrospun fiber formulation," *J. Control. Release*, vol. 105, no. 1–2, pp. 43–51, 2005.

[324] F. H. Silver, "Wound dressings and skin replacement," in *Biomaterials, medical devices and tissue engineering: An integrated approach*, Springer, 1994, pp. 46–91.

[325] R. B. Trinca, C. B. Westin, J. A. F. da Silva, and Â. M. Moraes, "Electrospun multilayer chitosan scaffolds as potential wound dressings for skin lesions," *Eur. Polym. J.*, vol. 88, pp. 161–170, 2017.

[326] A. Cipitria, A. Skelton, T. R. Dargaville, P. D. Dalton, and D. W. Hutmacher, "Design, fabrication and characterization of PCL electrospun scaffolds - A review," *J. Mater. Chem.*, vol. 21, no. 26, pp. 9419–9453, 2011.

[327] F. Gassner and A. J. Owen, "Physical properties of poly(β-hydroxybutyrate)-poly(ε-caprolactone) blends," *Polymer (Guildf).*, vol. 35, no. 10, pp. 2233–2236, 1994.

[328] C. Ru, F. Wang, M. Pang, L. Sun, R. Chen, and Y. Sun, "Suspended, Shrinkage-Free, Electrospun PLGA Nanofibrous Scaffold for Skin Tissue Engineering," *ACS Appl. Mater.*

Interfaces, vol. 7, no. 20, pp. 10872–10877, 2015.

[329] Y. J. Liu, H. L. Jiang, Y. Li, and K. J. Zhu, "Control of dimensional stability and degradation rate in electrospun composite scaffolds composed of poly(D,L-lactide-co-glycolide) and poly(ε-caprolactone)," *Chinese J. Polym. Sci. (English Ed.*, vol. 26, no. 1, pp. 63–71, 2008.

[330] S. Sharma, D. Gupta, S. Mohanty, M. Jassal, A. K. Agrawal, and R. Tandon, "Surface-modified electrospun poly(ε-Caprolactone) scaffold with improved optical transparency and bioactivity for damaged ocular surface reconstruction," *Investig. Ophthalmol. Vis. Sci.*, vol. 55, no. 2, pp. 899–907, 2014.

[331] S. Sharma, S. Mohanty, D. Gupta, M. Jassal, A. K. Agrawal, and R. Tandon, "Cellular response of limbal epithelial cells on electrospun poly-ε- caprolactone nanofibrous scaffolds for ocular surface bioengineering: A preliminary in vitro study," *Mol. Vis.*, vol. 17, no. November, pp. 2898–2910, 2011.

[332] M.-A. Campeau *et al.*, "Effect of manufacturing and experimental conditions on the mechanical and surface properties of silicone elastomer scaffolds used in endothelial mechanobiological studies," *Biomed. Eng. Online*, vol. 16, no. 1, pp. 1–23, 2017.

[333] S. Kobel and M. P. Lutolf, "High-throughput methods to define complex stem cell niches," *Biotechniques*, vol. 48, no. 4, pp. ix–xxii, 2010.

[334] C. R. Toh, T. A. Fraterman, D. A. Walker, and R. C. Bailey, "Direct biophotolithographic method for generating substrates with multiple overlapping biomolecular patterns and gradients," *Langmuir*, vol. 25, no. 16, pp. 8894–8898, 2009.

[335] M. L. Cuchiara, K. L. Horter, O. A. Banda, and J. L. West, "Covalent immobilization of stem cell factor and stromal derived factor 1α for in vitro culture of hematopoietic progenitor cells," *Acta Biomater.*, vol. 9, no. 12, pp. 9258–9269, 2013.

[336] B. P. Mahadik, S. Pedron Haba, L. J. Skertich, and B. A. C. Harley, "The use of covalently immobilized stem cell factor to selectively affect hematopoietic stem cell activity within a gelatin hydrogel," *Biomaterials*, vol. 67, pp. 297–307, 2015.

[337] Y. P. Xia, B. Li, D. Hylton, M. Detmar, G. D. Yancopoulos, and J. S. Rudge, "Transgenic

delivery of VEGF to mouse skin leads to an inflammatory condition resembling human psoriasis," *Blood*, vol. 102, no. 1, pp. 161–168, 2003.

[338] A. Luengas-martinez and J. Hardman-smart, "Vascular Endothelial Growth Factor Blockade Induces Dermal Endothelial Cell Apoptosis in a Clinically Relevant Skin Organ Culture Model (Journal of Physical Chemistry (2020) 33 (170-177) DOI: 10.1159/000508344)," *Skin Pharmacol. Physiol.*, vol. 33, pp. 170–177, 2020.

[339] F. Larcher, R. Murillas, M. Bolontrade, C. J. Conti, and J. L. Jorcano, "VEGF/VPF overexpression in skin of transgenic mice induces angiogenesis, vascular hyperpermeability and accelerated tumor development," *Oncogene*, vol. 17, no. 3, pp. 303–311, 1998.

[340] K. E. Johnson and T. A. Wilgus, "Multiple Roles for VEGF in Non-Melanoma Skin Cancer: Angiogenesis and Beyond," *J. Skin Cancer*, vol. 2012, pp. 1–6, 2012.

[341] J. W. Zhu, X. J. Wu, D. Luo, Z. F. Lu, S. Q. Cai, and M. Zheng, "Activation of VEGFR-2 signaling in response to moderate dose of ultraviolet B promotes survival of normal human keratinocytes," *Int. J. Biochem. Cell Biol.*, vol. 44, no. 1, pp. 246–256, 2012.

[342] B. Beck *et al.*, "A vascular niche and a VEGF-Nrp1 loop regulate the initiation and stemness of skin tumours," *Nature*, vol. 478, no. 7369, pp. 399–403, 2011.

[343] I. Marech *et al.*, "Classical and non-classical proangiogenic factors as a target of antiangiogenic therapy in tumor microenvironment," *Cancer Lett.*, vol. 380, no. 1, pp. 216–226, 2016.

[344] B. A. Bunnell, M. Flaat, C. Gagliardi, B. Patel, and C. Ripoll, "Adipose-derived stem cells: Isolation, expansion and differentiation," *Methods*, vol. 45, no. 2, pp. 115–120, 2008.

[345] S. Verdier-Sevrain, M. Yaar, J. Cantatore, A. Traish, and B. A. Gilchrest, "Estradiol induces proliferation of keratinocytes via receptor- mediated mechanisms," *FASEB J.*, vol. 18, no. 11, pp. 1252–1254, 2004.

[346] S. Stevenson, L. D. Nelson, D. T. Sharpe, and M. J. Thornton, "17β-Estradiol regulates the secretion of TGF-β by cultured human dermal fibroblasts," *J. Biomater. Sci. Polym.*

Ed., vol. 19, no. 8, pp. 1097–1109, 2008.

[347] E. Makrantonaki, K. Vogel, S. Fimmel, M. Oeff, H. Seltmann, and C. C. Zouboulis, "Interplay of IGF-I and 17β-estradiol at age-specific levels in human sebocytes and fibroblasts in vitro," *Exp. Gerontol.*, vol. 43, no. 10, pp. 939–946, 2008.

[348] M. Hormozi, R. Assaei, and M. B. Boroujeni, "The effect of aloe vera on the expression of wound healing factors (TGFβ1 and bFGF) in mouse embryonic fibroblast cell: In vitro study," *Biomed. Pharmacother.*, vol. 88, pp. 610–616, 2017.

[349] M. Zandi, M. Masoumian, A. Shariatinia, and M. R. Sanjabi, "Optimal Concentrations and Synergistic Effects of Some Herbal Extracts on Viability of Dermal Fibroblasts," *Gene, Cell Tissue*, vol. 3, no. 4, 2016.

[350] D. Ribatti, A. Vacca, L. Roncali, and F. Dammacco, "The chick embryo chorioallantoic membrane as a model for in vivo research on anti-angiogenesis.," *Curr. Pharm. Biotechnol.*, vol. 1, no. 1, pp. 73–82, 1996.

[351] N. Mangir, A. Raza, J. W. Haycock, C. Chapple, and S. Macneil, "An improved in vivo methodology to visualise tumour induced changes in vasculature using the chick chorionic allantoic membrane assay," *In Vivo (Brooklyn).*, vol. 32, no. 3, pp. 461–472, 2018.

[352] K. Norrby, "In vivo models of angiogenesis," *J. Cell. Mol. Med.*, vol. 10, no. 3, pp. 588–612, 2006.

[353] M. M. Ghosh, S. Boyce, C. Layton, E. Freedlander, and S. Mac Neil, "A comparison of methodologies for the preparation of human epidermal- dermal composites," *Ann. Plast. Surg.*, vol. 39, no. 4, pp. 390–404, 1997.

[354] J. G. Rheinwald and H. Green, "Serial cultivation of strains of human epidermal keratinocytes: The formation of keratinizing colonies from single cells," *Cell*, vol. 6, pp. 331–344, 1975.

[355] M. H. Elfarnawany, "Signal Processing Methods for Quantitative Power Doppler Microvascular Angiography," *Electron. Thesis Diss. Repos.*, vol. 3106, pp. 1–192, 2015.

[356] P. Bainbridge, "Wound healing and the role of fibroblasts," *J. Wound Care*, vol. 22, no. 8,

pp. 407–412, 2013.

[357] N. A. Bondarenko *et al.*, "Effect of Vascular Endothelial Growth Factor and Erythropoietin on Functional Activity of Fibroblasts and Multipotent Mesenchymal Stromal Cells," *Bull. Exp. Biol. Med.*, vol. 160, no. 4, pp. 498–501, 2016.

[358] B.-X. Yan *et al.*, "Comparative expression of PEDF and VEGF in human epidermal keratinocytes and dermal fibroblasts: from normal skin to psoriasis," *Discov. Med.*, vol. 25, no. 136, pp. 47–56, 2018.

[359] C. Hammerberg, G. J. Fisher, J. J. Voorhees, and K. D. Cooper, "Elevated thymidine phosphorylase activity in psoriatic lesions accounts for the apparent presence of an epidermal 'growth inhibitor,' but is not in itself growth inhibitory," *J. Invest. Dermatol.*, vol. 97, no. 2, pp. 286–290, 1991.

[360] D. Creamer, R. Jaggar, M. Allen, R. Bicknell, and J. Barker, "Overexpression of the angiogenic factor platelet-derived endothelial cell growth factor/thymidine phosphorylase in psoriatic epidermis," *Br. J. Dermatol.*, vol. 137, no. 6, pp. 851–855, 1997.

[361] X. Xie, Y. Wang, Y. Xia, and Y. Mao, "Overexpressed vascular endothelial growth factor in adipose derived stem cells attenuates fibroblasts and skin injuries by ultraviolet radiation," *Biosci. Rep.*, vol. 39, no. 7, pp. 1–13, 2019.

[362] J. H. Kim, M. Jung, H. S. Kim, Y. M. Kim, and E. H. Choi, "Adipose-derived stem cells as a new therapeutic modality for ageing skin," *Exp. Dermatol.*, vol. 20, no. 5, pp. 383–387, 2011.

[363] K. M. Moon *et al.*, "The effect of secretory factors of adipose-derived stem cells on human keratinocytes," *Int. J. Mol. Sci.*, vol. 13, no. 1, pp. 1239–1257, 2012.

[364] S.-Y. Song, H.-M. Chung, and J.-H. Sung, "The pivotal role of VEGF in adipose-derived-stem-cell-mediated regeneration," *Expert Opin. Biol. Ther.*, vol. 10, no. 11, pp. 1529–1537, 2010.

[365] F. Yu *et al.*, "Human adipose-derived stem cells enriched with VEGF-modified mRNA promote angiogenesis and long-term graft survival in a fat graft transplantation model," *Stem Cell Res. Ther.*, vol. 11, no. 1, pp. 1–20, 2020.

[366] S. J. Baek, S. K. Kang, and J. C. Ra, "In vitro migration capacity of human adipose tissue-derived mesenchymal stem cells reflects their expression of receptors for chemokines and growth factors," *Exp. Mol. Med.*, vol. 43, no. 10, pp. 596–603, 2011.

[367] J. I. Hye Kim, S. Gyu Park, W. Kim, S. U. Song, and J. Sung, "Functional regulation of adipose-derived stem cells by PDGF-D," *Stem Cells*, vol. 33, no. 2, pp. 542–556, 2015.

[368] A. Surazynski, K. Jarzabek, J. Haczynski, P. Laudanski, J. Palka, and S. Wolczynski, "Differential effects of estradiol and raloxifene on collagen biosynthesis in cultured human skin fibroblasts.," *Int. J. Mol. Med.*, vol. 12, no. 5, pp. 803–809, Nov. 2003.

[369] S. Trompezinski, I. Pernet, D. Schmitt, and J. Viac, "UV radiation and prostaglandin E2 up-regulate vascular endothelial growth factor (VEGF) in cultured human fibroblasts," *Inflamm. Res.*, vol. 50, no. 8, pp. 422–427, 2001.

[370] G. S. Ashcroft *et al.*, "Estrogen accelerates cutaneous wound healing associated with an increase in TGF-β1 levels," *Nat. Med.*, vol. 3, no. 11, pp. 1209–1215, 1997.

[371] S. Liarte, Á. Bernabé-García, and F. J. Nicolás, "Role of TGF-β in Skin Chronic Wounds: A Keratinocyte Perspective," *Cells*, vol. 9, no. 2, 2020.

[372] J. W. Penn, A. O. Grobbelaar, and K. J. Rolfe, "The role of the TGF-β family in wound healing, burns and scarring: a review.," *Int. J. Burns Trauma*, vol. 2, no. 1, pp. 18–28, 2012.

[373] S. Zhang *et al.*, "Prostaglandin E2 hydrogel improves cutaneous wound healing via M2 macrophages polarization," *Theranostics*, vol. 8, no. 19, pp. 5348–5361, 2018.

[374] A. Parekh *et al.*, "Prostaglandin E2 differentially regulates contraction and structural reorganization of anchored collagen gels by human adult and fetal dermal fibroblasts," *Wound Repair Regen.*, vol. 17, no. 1, pp. 88–98, 2009.

[375] R. G. Richards and S. M. Hartman, "Human dermal fibroblast cells express prolactin in vitro," *J. Invest. Dermatol.*, vol. 106, no. 6, pp. 1250–1255, 1996.

[376] K. Foitzik, E. A. Langan, and R. Paus, "Prolactin and the skin: A dermatological perspective on an ancient pleiotropic peptide hormone," *J. Invest. Dermatol.*, vol. 129, no.

5, pp. 1071–1087, 2009.

[377] N. Kanda and S. Watanabe, "17β-Estradiol Inhibits Oxidative Stress-Induced Apoptosis in Keratinocytes by Promoting Bcl-2 Expression," *J. Invest. Dermatol.*, vol. 121, no. 6, pp. 1500–1509, 2003.

[378] R. Urano, K. Sakabe, K. Seiki, and M. Ohkido, "Female sex hormone stimulates cultured human keratinocyte proliferation and its RNA- and protein-synthetic activities," *J. Dermatol. Sci.*, vol. 9, no. 3, pp. 176–184, 1995.

[379] V. Peržeiová *et al.*, "Pharmacological activation of estrogen receptors-αand-β differentially modulates keratinocyte differentiation with functional impact on wound healing," *Int. J. Mol. Med.*, vol. 37, no. 1, pp. 21–28, 2016.

[380] H. S. Young *et al.*, "Interaction between genetic control of vascular endothelial growth factor production and retinoid responsiveness in psoriasis," *J. Invest. Dermatol.*, vol. 126, no. 2, pp. 453–459, 2006.

[381] S. Jettanacheawchankit, S. Sasithanasate, P. Sangvanich, W. Banlunara, and P. Thunyakitpisal, "Acemannan stimulates gingival fibroblast proliferation; expressions of keratinocyte growth factor-1, vascular endothelial growth factor, and type I collagen; and wound healing," *J. Pharmacol. Sci.*, vol. 109, no. 4, pp. 525–531, 2009.

[382] P. Chithra, G. B. Sajithlal, and G. Chandrakasan, "Influence of Aloe vera on the glycosaminoglycans in the matrix of healing dermal wounds in rats," *J. Ethnopharmacol.*, vol. 59, no. 3, pp. 179–186, 1998.

[383] S. Shafaie, S. Andalib, H. Shafaei, A. Montaseri, and M. Tavakolizadeh, "Differential Biological Behavior of Fibroblasts and Endothelial Cells under Aloe vera Gel Culturing," *Int. J. Mol. Cell. Med.*, vol. 9, no. 3, pp. 234–245, 2020.

[384] S. T. Andreadis, K. E. Hamoen, M. L. Yarmush, and J. R. Morgan, "Keratinocyte growth factor induces hyperproliferation and delays differentiation in a skin equivalent model system," *FASEB J.*, vol. 15, no. 6, pp. 898–906, 2001.

[385] D. Popadic *et al.*, "Aloe-emodin inhibits proliferation of adult human keratinocytes in vitro," *J. Cosmet. Sci.*, vol. 63, no. 5, pp. 297–302, 2012.

[386] M. Moriyama *et al.*, "Beneficial effects of the genus Aloe on wound healing, cell proliferation, and differentiation of epidermal keratinocytes," *PLoS One*, vol. 11, no. 10, pp. 1–15, 2016.

[387] S. W. Choi, B. W. Son, Y. S. Son, Y. I. Park, S. K. Lee, and M. H. Chung, "The wound-healing effect of a glycoprotein fraction isolated from aloe vera," *Br. J. Dermatol.*, vol. 145, no. 4, pp. 535–545, 2001.

[388] M. Takahashi, D. Kitamoto, Y. Asikin, K. Takara, and K. Wada, "Liposomes Encapsulating Aloe vera Leaf Gel Extract Significantly Enhance Proliferation and Collagen Synthesis in Human Skin Cell Lines," *J. Oleo Sci.*, vol. 650, no. 12, pp. 643–650, 2009.

[389] H. Leng, L. Pu, L. Xu, X. Shi, J. Ji, and K. Chen, "Effects of aloe polysaccharide, a polysaccharide extracted from Aloe vera, on TNF-a-induced HaCaT cell proliferation and the underlying mechanism in psoriasis," *Mol. Med. Rep.*, vol. 18, no. 3, pp. 3537–3543, 2018.

[390] P. Gentile, V. Chiono, I. Carmagnola, and P. V. Hatton, "An overview of poly(lactic-co-glycolic) Acid (PLGA)-based biomaterials for bone tissue engineering," *International Journal of Molecular Sciences*, vol. 15, no. 3. pp. 3640–3659, 2014.

[391] H. Baharvand, S. M. Hashemi, S. K. Ashtiani, and A. Farrokhi, "Differentiation of human embryonic stem cells into hepatocytes in 2D and 3D culture systems in vitro," *Int. J. Dev. Biol.*, vol. 50, no. 7, pp. 645–652, 2006.

[392] M. Kapałczyńska *et al.*, "2D and 3D cell cultures – a comparison of different types of cancer cultures," *Arch. Med. Sci.*, vol. 14, no. 4, pp. 910–919, 2016.

[393] C. Jensen and Y. Teng, "Is It Time to Start Transitioning From 2D to 3D Cell Culture?," *Front. Mol. Biosci.*, vol. 7, no. March, pp. 1–15, 2020.

[394] A. Pupovac, B. Senturk, C. Griffoni, K. Maniura-Weber, M. Rottmar, and S. L. McArthur, "Toward Immunocompetent 3D Skin Models," *Adv. Healthc. Mater.*, vol. 7, no. 12, pp. 1–11, 2018.

[395] H. Niehues, J. A. Bouwstra, A. El Ghalbzouri, J. M. Brandner, P. L. J. M. Zeeuwen, and

E. H. van den Bogaard, "3D skin models for 3R research: The potential of 3D reconstructed skin models to study skin barrier function," *Exp. Dermatol.*, vol. 27, no. 5, pp. 501–511, 2018.

[396] S. H. Mathes, H. Ruffner, and U. Graf-Hausner, "The use of skin models in drug development," *Adv. Drug Deliv. Rev.*, vol. 69–70, pp. 81–102, 2014.

[397] B. Kinikoglu, "A Comparison of Scaffold-free and Scaffold-based Reconstructed Human Skin Models as Alternatives to Animal Use," *ATLA Altern. to Lab. Anim.*, vol. 45, no. 6, pp. 309–316, 2017.

[398] A. K. Dabrowska *et al.*, "Materials used to simulate physical properties of human skin," *Ski. Res. Technol.*, vol. 22, no. 1, pp. 3–14, 2016.

[399] J. Chen, H. Yang, J. Li, J. Chen, Y. Zhang, and X. Zeng, "The development of an artificial skin model and its frictional interaction with wound dressings," *J. Mech. Behav. Biomed. Mater.*, vol. 94, no. January, pp. 308–316, 2019.

[400] C. A. Brohem, L. B. Da Silva Cardeal, M. Tiago, M. S. Soengas, S. B. De Moraes Barros, and S. S. Maria-Engler, "Artificial skin in perspective: Concepts and applications," *Pigment Cell Melanoma Res.*, vol. 24, no. 1, pp. 35–50, 2011.

[401] D. Y. Lee, H. T. Ahn, and K. H. Cho, "A new skin equivalent model: Dermal substrate that combines de-epidermized dermis with fibroblast-populated collagen matrix," *J. Dermatol. Sci.*, vol. 23, no. 2, pp. 132–137, 2000.

[402] E. H. Van Den Bogaard *et al.*, "Crosstalk between keratinocytes and T cells in a 3D microenvironment: A model to study inflammatory skin diseases," *J. Invest. Dermatol.*, vol. 134, no. 3, pp. 719–727, 2014.

[403] S. Gibbs, S. Murli, G. De Boer, A. A. T. Mulder, A. Mieke Mommaas, and M. Ponec, "Melanosome capping of keratinocytes in pigmented reconstructed epidermis - Effect of ultraviolet radiation and 3-isobutyl-1-methyl-xanthine on melanogenesis," *Pigment Cell Res.*, vol. 13, no. 6, pp. 458–466, 2000.

[404] J. Z. Yu, E. Korkmaz, M. I. Berg, P. R. LeDuc, and O. B. Ozdoganlar, "Biomimetic scaffolds with three-dimensional undulated microtopographies," *Biomaterials*, vol. 128,

pp. 109–120, 2017.

[405] Z. Shen *et al.*, "Construction of tissue-engineered skin with rete ridges using co-network hydrogels of gelatin methacrylated and poly(ethylene glycol) diacrylate," *Mater. Sci. Eng. C*, vol. 129, no. August, p. 112360, 2021.

[406] H. T. Ong *et al.*, "Paracrine Activity from Adipose-Derived Stem Cells on in Vitro Wound Healing in Human Tympanic Membrane Keratinocytes," *Stem Cells Dev.*, vol. 26, no. 6, pp. 405–418, 2017.

[407] K. H. Chakrabarty *et al.*, "Development of autologous human dermal-epidermal composites based on sterilized human allodermis for clinical use," *Br. J. Dermatol.*, vol. 141, no. 5, pp. 811–823, 1999.

[408] C. A. Harrison *et al.*, "Use of an in vitro model of tissue-engineered skin to investigate the mechanism of skin graft contraction," *Tissue Eng.*, vol. 12, no. 11, pp. 3119–3133, 2006.

[409] A. Giangreco, S. J. Goldie, V. Failla, G. Saintigny, and F. M. Watt, "Human skin aging is associated with reduced expression of the stem cell markers β1 integrin and MCSP," *J. Invest. Dermatol.*, vol. 130, no. 2, pp. 604–608, 2010.

[410] K. Kretzschmar and F. M. Watt, "Markers of Epidermal Stem Cell Subpopulations," *Cold Spring Harb Perspect Med*, vol. 4, no. 10, pp. 1–14, 2014.

[411] H.-R. Choi, S.-Y. Byun, S.-H. Kwon, and K.-C. Park, "Niche interactions in epidermal stem cells," *World J. Stem Cells*, vol. 7, no. 2, pp. 495–501, 2015.

[412] S. J. Ellis and G. Tanentzapf, "Integrin-mediated adhesion and stem-cell-niche interactions," *Cell Tissue Res.*, vol. 339, no. 1, pp. 121–130, 2010.

[413] K. Kühn, "Basement membrane (type IV) collagen," *Matrix Biol.*, vol. 14, no. 6, pp. 439–445, 1995.

[414] K. Zhou *et al.*, "Nanoscaled and microscaled parallel topography promotes tenogenic differentiation of asc and neotendon formation in vitro," *Int. J. Nanomedicine*, vol. 13, pp. 3867–3881, 2018.

[415] D. H. Ramos-Rodriguez, S. MacNeil, F. Claeyssens, and I. Ortega Asencio, "Delivery of

Bioactive Compounds to Improve Skin Cell Responses on Microfabricated Electrospun Microenvironments," *Bioengineering*, vol. 8, no. 8, 2021.

[416] C. H. Lin *et al.*, "Regeneration of rete ridges in Lanyu pig (Sus scrofa): Insights for human skin wound healing," *Exp. Dermatol.*, vol. 28, no. 4, pp. 472–479, 2019.

[417] B. N. Blackstone, M. M. Malara, M. E. Baumann, K. L. McFarland, D. M. Supp, and H. M. Powell, "Fractional CO2 laser micropatterning of cell-seeded electrospun collagen scaffolds enables rete ridge formation in 3D engineered skin," *Acta Biomater.*, vol. 102, pp. 287–297, 2020.

[418] S. Dhivya, V. V. Padma, and E. Santhini, "Wound dressings - A review," *Biomed.*, vol. 5, no. 4, pp. 24–28, 2015.

[419] S. P. Miguel *et al.*, "Electrospun polymeric nanofibres as wound dressings: A review," *Colloids Surfaces B Biointerfaces*, vol. 169, pp. 60–71, 2018.

[420] P. Zahedi, I. Rezaeian, S. O. Ranaei-Siadat, S. H. Jafari, and P. Supaphol, "A review on wound dressings with an emphasis on electrospun nanofibrous polymeric bandages," *Polym. Adv. Technol.*, vol. 21, no. 2, pp. 77–95, 2010.

[421] M. Madaghiele, C. Demitri, A. Sannino, and L. Ambrosio, "Polymeric hydrogels for burn wound care: Advanced skin wound dressings and regenerative templates," *Burn. Trauma*, vol. 2, no. 4, pp. 153–161, 2014.

[422] E. M. Tottoli, R. Dorati, I. Genta, E. Chiesa, S. Pisani, and B. Conti, "Skin wound healing process and new emerging technologies for skin wound care and regeneration," *Pharmaceutics*, vol. 12, no. 8, pp. 1–30, 2020.

[423] C. C. Compton, J. M. Gill, D. A. Bradford, S. Regauer, G. G. Gallico, and N. E. O'Connor, "Skin regenerated from cultured epithelial autografts on full-thickness burn wounds from 6 days to 5 years after grafting. A light, electron microscopic and immunohistochemical study.," *Lab. Invest.*, vol. 60, no. 5, pp. 600–612, 1989.

[424] D. A. Medalie, S. A. Eming, M. E. Collins, R. G. Tompkins, M. L. Yarmush, and J. R. Morgan, "Differences in Dermal Analogs Influence Subsequent Pigmentation, Epidermal Differentiation, Basement Membrane, and Rete Ridge Formation of Transplanted

Composite Skin Grafts1," *Transplantation*, vol. 64, no. 3, pp. 454–465, 1997.

[425] S. M. Dellatore, A. S. Garcia, and W. M. Miller, "Mimicking stem cell niches to increase stem cell expansion," *Curr. Opin. Biotechnol.*, vol. 19, no. 5, pp. 534–540, 2008.

[426] K. F. Eichholz and D. A. Hoey, "Mediating human stem cell behaviour via defined fibrous architectures by melt electrospinning writing," *Acta Biomater.*, vol. 75, pp. 140–151, 2018.

[427] H. Jahani, S. Kaviani, M. Hassanpour-Ezatti, M. Soleimani, Z. Kaviani, and Z. Zonoubi, "The effect of aligned and random electrospun fibrous scaffolds on rat mesenchymal stem cell proliferation," *Cell J.*, vol. 14, no. 1, pp. 31–38, 2012.

[428] M. Ventre, V. Coppola, C. F. Natale, and P. A. Netti, "Aligned fibrous decellularized cell derived matrices for mesenchymal stem cell amplification," *J. Biomed. Mater. Res. - Part A*, vol. 107, no. 11, pp. 2536–2546, 2019.

[429] N. Goonoo and A. Bhaw-Luximon, "Nanomaterials combination for wound healing and skin regeneration," in *Advanced 3D-printed systems and nanosystems for drug delivery and tissue engineering*, Elsevier, 2020, pp. 159–217.

[430] H. J. Lee and W. G. Koh, "Hydrogel micropattern-incorporated fibrous scaffolds capable of sequential growth factor delivery for enhanced osteogenesis of hMSCs," *ACS Appl. Mater. Interfaces*, vol. 6, no. 12, pp. 9338–9348, 2014.

[431] A. N. Annaidh, M. Ottenio, K. Bruyère, M. Destrade, and M. D. Gilchrist, "Mechanical properties of excised human skin," in *6th World Congress of Biomechanics (WCB 2010). August 1-6, 2010 Singapore*, 2010, pp. 1000–1003.

[432] N. T. Hiep and B. T. Lee, "Electro-spinning of PLGA/PCL blends for tissue engineering and their biocompatibility," *J. Mater. Sci. Mater. Med.*, vol. 21, no. 6, pp. 1969–1978, 2010.

[433] S. F. Chou and K. A. Woodrow, "Relationships between mechanical properties and drug release from electrospun fibers of PCL and PLGA blends," *J. Mech. Behav. Biomed. Mater.*, vol. 65, no. September 2016, pp. 724–733, 2017.

[434] C. Shen, T. Tsuda, S. Fushiki, H. Mizutani, and K. Yamanishi, "The expression of p63 during epidermal remodeling in psoriasis," *J. Dermatol.*, vol. 32, no. 4, pp. 236–242, 2005.

[435] Z. Yuan, J. Zhao, W. Zhu, Z. Yang, and B. Li, "Ibuprofen-loaded electrospun fibrous scaffold doped with sodium bicarbonate for responsively inhibiting inflammation and promoting muscle wound healing in vivo," *Biomater. Sci.*, vol. 2, pp. 502–511, 2014.

[436] A. J. Singer and S. T. Boyce, "Burn Wound Healing and Tissue Engineering," *J. Burn Care Res.*, 2017.

[437] O. O. Agarry, M. T. Olaleye, and C. O. Bello-Michael, "Comparative antimicrobial activities of aloe vera gel and leaf," *African J. Biotechnol.*, vol. 4, no. 12, pp. 1413–1414, 2005.